

R-04-61

**Groundwater flow and
radionuclide transport modelling
using CONNECTFLOW in support
of the SR Can assessment**

Lee Hartley, Ian Cox, David Holton,
Fiona Hunter, Steve Joyce
Serco Assurance

Björn Gylling, Maria Lindgren
Kemakta Konsult

September 2004

Svensk Kärnbränslehantering AB

Swedish Nuclear Fuel
and Waste Management Co
Box 5864
SE-102 40 Stockholm Sweden
Tel 08-459 84 00
+46 8 459 84 00
Fax 08-661 57 19
+46 8 661 57 19



ISSN 1402-3091

SKB Rapport R-04-61

Groundwater flow and radionuclide transport modelling using CONNECTFLOW in support of the SR Can assessment

Lee Hartley, Ian Cox, David Holton,
Fiona Hunter, Steve Joyce
Serco Assurance

Björn Gylling, Maria Lindgren
Kemakta Konsult

September 2004

Summary

Nuclear waste in Sweden is handled by the Swedish Nuclear Fuel and Waste Management Co, SKB. Within SKB's programme for spent nuclear fuel management, an interim storage facility and a transportation system are already in operation. SKB's concept for the final stage of the nuclear fuel cycle, based on several decades of research and development, is to place spent fuel inside a cast iron insert inside copper canisters. These are then deposited in a repository, about 500 m deep in saturated, granitic rock, with the canisters surrounded by bentonite clay. This concept is referred to as the KBS-3 method.

Two principal remaining tasks in SKB's programme are to locate, build and operate i) the deep repository and ii) an encapsulation plant in which the spent fuel will be emplaced in canisters to be deposited in the deep repository.

SKB is currently pursuing site investigations for a deep repository in the municipalities of Östhammar and Oskarshamn. The investigations are conducted in two stages; an initial phase followed, if the expected site suitability is confirmed, by a complete site investigation phase. The aim is to build a deep repository at one of these candidate sites, provided that the bedrock and other relevant conditions are found to be suitable. An application to build a deep repository will be made at the end of 2008 according to the current timetable.

The favoured alternative for the location of the encapsulation plant is at Oskarshamn, where it would operate in conjunction with the existing interim storage facility. An application to build an encapsulation plant will be made in 2006.

These two planning applications will each require a report on the long-term safety of the deep repository. This is an obvious requirement for the application to build the repository. In the case of the encapsulation plant, such a report will demonstrate that a repository for the sealed canisters (to be delivered by the encapsulation plant) will meet the requirements on long-term safety set up by the Swedish authorities. The two safety reports will be referred to as SR-Can and SR-Site, for the encapsulation plant and repository, respectively. SR-Can will be based on site data from the initial site investigation phase and SR-Site on data from the complete site investigation.

The first stage of the SR-Can project is to demonstrate the methodology that will be used in preparing for the planning application for the encapsulation plant. The methodology, which has evolved from that used in SKB's previous assessment, SR 97 /1/, will be reported and reviewed prior to its use in the final assessments. Also, the preliminary safety evaluations for each site, as envisaged in Reference /2/, will be carried out as sub-tasks within the SR-Can project. The main purposes of those evaluations are to:

- Determine whether earlier judgements of the suitability of the candidate area for a deep repository with respect to long-term safety holds up in the light of borehole data;
- Provide feed-back to continued site investigations and site-specific repository design.

A proposed methodology for the SR-Can assessment has been published in SKB Technical Report TR-03-08, 'Planning Report for the Safety Assessment SR-Can' /3/. The methodology envisaged the use of both continuum porous medium (CPM) and discrete fracture network (DFN) models on a range of scales to investigate the groundwater flow and radionuclide transport from a deep disposal facility to the biosphere. The modelling must address the effects of variable groundwater density and transients. Transients occur

naturally as a consequence of changes in climate states (temperate, periglacial and glacial) and during the operational and immediate post-closure phases of the repository. Key outputs from the modelling will be the groundwater flux, the definition of flow paths and values for parameters describing the transport of radionuclides along the paths. Ultimately, the results from the groundwater flow modelling will feed into biosphere calculations of radiological risks to man.

SKB's methodology refers to three scales of modelling, these being 'Regional' (~10 km), local (~1 km) and 'repository/block' (10–100 m). Using models at these scales it is necessary to simulate the transient, variable-density groundwater flow in sufficient detail to enable the groundwater flux and radionuclide transport paths to be determined. For example, flows from deposition holes into adjacent small-scale fractures represent one release route for radionuclides into the geosphere. Further transport through fractures of increasing size, up to regional-scale fracture zones, is the most likely route to the biosphere. Research into ways of coupling the geosphere and biosphere through near-surface and surface hydrology models is ongoing within the SKB programme.

The focus of the project reported here has been to illustrate and test the geosphere methodology for the post-closure phase of the safety assessment, that is, between the present and 10,000 years after present (AP). The initial data for the Forsmark site Version 1.1 has been used as an example. However, some of the key input relating to the fracture interpretation was revised as part of the Version 1.1 site description as this project was being carried out. Hence, two sets of fracture parameterisations were used to construct DFN models corresponding to the original and updated Forsmark Version 1.1 site descriptions.

In order to demonstrate the groundwater flow and transport methodology outlined by SKB in TR-03-08 /2/, a set of nested models has been constructed using Serco Assurance's CONNECTFLOW software in order to assess issues on various key scales. These nested models are:

- a regional-scale CPM model containing representations of deterministic large-scale fracture zones, with site-scale hydrogeological properties based on and consistent with an underlying DFN data description. This model has been provided from the ongoing Forsmark hydrogeological modelling study undertaken jointly by Kemakta Konsult, Serco Assurance and Golder Associates. The purpose of this model is to study transients and provide boundary conditions for models on smaller-scales;
- a local-scale DFN model nested within a regional-scale CPM model to assess far-field transport pathways, but also capture the detailed transport pathways through the DFN immediately around the repository tunnels;
- a CPM representation of the deposition holes, engineered damage zone (EDZ) and deposition tunnels nested within a canister-scale DFN model. This model is used to perform detailed calculations of groundwater fluxes in the DFN adjacent to canisters and in the EDZ, for input to near-field source term models.

Output from these models has been used to calculate performance measures (PMs) such as canister flux, travel time, and exit locations that are required as input to performance safety assessment (PSA) calculations. Since the above set of models offer greater resolution of both near-field parameters such as flows in the fractures intersecting a deposition hole and far-field parameters such as F-quotient through a DFN, then new concepts are required for how such information can be incorporated in the PSA calculations. Hence, consideration is also given to how PSA calculations should be performed using the COMP23 and FARF31 programs, based on output from CONNECTFLOW. This illustrates the capacity

of CONNECTFLOW to integrate with SKB's existing software in order to provide an overall methodology for the groundwater flow and PSA calculations.

The study has shown the development of the complete model chain from fracture network data, fracture conceptual model analysis, regional-scale paleo-hydrogeology to the use of detailed nested models to obtain performance measures for the near-field, far-field and biosphere as required by safety assessment. The methodology has shown to be tractable and to yield more realistic and detailed distribution of PMs than has been possible in the past. A number of scenarios have been considered including release from canisters at different times, different backfill properties, and quite distinct interpretations of the underlying fracture network data. This demonstrates the robustness and flexibility of the approach.

For the original DFN interpretation the fracture network connectivity is relatively good and may be analogous to the situation at Oskarshamn to some extent. The general conclusions for this data are:

- A cut-off in fracture length about 50 m can be used for deriving the equivalent CPM permeability distribution for 100 m blocks;
- Fractures down to about 3 m have to be included on the canister-scale to consider the near-field flows;
- Natural transients have a significant affect on PMs due to differences in head and salinity at 2,500 AD and 12,000 AD. Future freshwater conditions imply shorter paths and hence greater risk;
- At 2,500 AD paths discharge vertically above repository or on the sea bed for nested model, whereas in the CPM the longer paths towards sea dominates;
- At 12,000 AD all paths in the nested model discharge close to the repository (coast retreated to NE);
- DFN modelling gives greater probability of many canisters being in 'safe' areas away from high-K features. CPM uses average properties and hence all canisters are in an 'averagely safe' area. Generally lower equivalent flow-rates, Q_{eq} , for the nested model;
- Far-field PMs for Path_f (starting in the fracture) and Path_t (starting in the tunnel) are similar. Presumably this is because for the base case, fractures are the dominant pathway and so particles starting in the tunnel tend to enter the fracture system after only a short distance.
- Five realisations of the DFN model show no major differences in path behaviour;
- Higher hydraulic conductivity backfill focuses more flow through repository, reflected in higher Q_{eq} values for Path_t, and hence higher risk.

For the updated DFN interpretation the fracture network connectivity is relatively poor and represents a distinct case. The general conclusions for this data are:

- A cut-off in fracture length about 20 m can be used for deriving the equivalent CPM permeability distribution for 100 m blocks;
- Fractures down to about 1 m have to be included on the canister-scale to consider the near-field flows;
- Natural transients have a secondary effect on PMs. Flow-rates and pathways are more dominated by the local fracture connectivity around the deposition tunnels;

- The tunnel provides a dominant local pathway for transport even with a low backfill conductivity of 10^{-10} m/s. As well as providing a major conduit for flow, the tunnels also connect up localised fracture clusters that would otherwise be inaccessible to site-scale flows;
- Only about 60% of canisters are intersected by the connected fracture network;
- There is little difference between Path_t and Path_f in terms of the far-field PMs for the opposite reason to the original DFN. That is, now the tunnel pathway dominates so particles entering the fracture system tend to enter a tunnel.
- DFN modelling gives greater probability of many canisters being in 'safe' areas away from high-K features compared to a low-resolution CPM model. CPM uses average properties and hence all canisters are in an 'averagely safe' area. Generally lower equivalent flow-rates, Q_{eq} , for the nested model;
- Higher hydraulic conductivity backfill focuses more flow through repository, reflected in higher Q_{eq} values for Path_t, and significantly lower travel times and F-quotients.
- The dominance of the tunnels as a pathway in this case demands an explicit treatment of retention in the safety assessment for this case.

The methodology as developed should not be viewed as entirely complete. A number of issues have arisen as the project has proceeded and some approximations were made during this initial phase. It is suggested that in the next phase of SR-can the following issues should be addressed:

- The EDZ should be modelled explicitly in the canister-scale model and greater mesh resolution should be used to resolve transport in the tunnels especially for poorly connected networks where the tunnel dominates. Other repository design features such as plugs could be considered also;
- The canister-scale models should include all canisters explicitly;
- Consideration has to be given to alternative fracture conceptual models and interpretations;
- The sensitivity to the structural model in terms of confidence of structures needs to be addressed;
- A verification of the pathways and transport statistics against a refined CPM model of the local-scale would be valuable to support the approximation of solving for constant density in the DFN model but coupled to environmental pressure;
- The effects of channelisation of transport within fractures needs to be modelled more explicitly;
- An approach needs to be found that is more robust for handling transport in dead-end fracture clusters that occur for sparse networks;
- If CPM models are still to be propagated through the safety assessment then the spatial distribution of fracture porosity and flow-wetted surface area should be derived from upscaling DFN models in a similar way to permeability.

Contents

1	Introduction	9
2	Fracture conceptual model analysis	13
2.1	Introduction and objectives	13
2.2	Approach	13
2.3	Fracture network data sources	14
2.3.1	Orientations	14
2.3.2	Fracture intensity P32 and fracture length	14
2.3.3	Fracture transmissivity and transport aperture	16
2.3.4	Transport and channelisation	26
2.3.5	Representation of deposition tunnels, and engineered damage zone (EDZ)	27
3	Nested regional-scale CPM/DFN model for the temperate climatic period (2,000–12,000 years AD)	29
3.1	Objective	29
3.2	Approach	29
3.3	Model properties – sources of information	30
3.4	Model grid	32
3.5	Permeability upscaling	34
3.6	CPM model: groundwater flow and particle tracking	41
3.6.1	Grid modification	41
3.6.2	Boundary conditions	44
3.6.3	Pressure and salt transport calculations	45
3.6.4	Particle tracking	54
3.7	Nested CPM/DFN model: groundwater flow and particle tracking	62
3.7.1	CPM/DFN grid	62
3.7.2	Pressure calculations	70
3.7.3	Particle tracking calculations	73
4	Nested canister-scale DFN/CPM model	77
4.1	Objective	77
4.2	Approach	77
4.3	Model grid	77
4.4	Pressure calculation	83
4.5	Particle tracking	84
5	Performance measures and recommendations for performance assessment	95
5.1	Inputs to safety assessment calculations using PROPER	95
5.1.1	Path definitions	95
5.1.2	Groundwater parameters	97
5.1.3	Equivalent flow rate	97
5.1.4	Parameter distributions	99

6	Updated DFN model for Forsmark SDM 1.1	125
6.1	Fracture conceptual model analysis	125
6.1.1	Modifications to fracture parameterisation	125
6.1.2	Permeability upscaling and fracture length cut-offs	126
6.2	Regional-scale CPM modelling	132
6.2.1	Permeability upscaling	132
6.2.2	Pressure and salt transport calculations	134
6.2.3	Particle tracking calculations	136
6.3	Regional-scale nested CPM/DFN model	138
6.3.1	CPM/DFN model	138
6.3.2	Flow calculations	142
6.3.3	Particle tracking calculations	146
6.4	Nested canister-scale DFN/CPM model	150
6.4.1	CPM/DFN model	150
6.4.2	Flow calculations	152
6.4.3	Particle tracking calculations	153
6.5	Performance measures	153
6.5.1	Base case – low backfill conductivity and release at 2,500 AD	154
7	Conclusions	169
	References	171

1 Introduction

Nuclear waste in Sweden is handled by the Swedish Nuclear Fuel and Waste Management Co, SKB. Within SKB's programme for spent nuclear fuel management, an interim storage facility and a transportation system are already in operation. SKB's concept for the final stage of the nuclear fuel cycle, based on several decades of research and development, is to place spent fuel inside a cast iron insert inside copper canisters. These are then deposited in a repository, about 500 m deep in saturated, granitic rock, with the canisters surrounded by bentonite clay. This concept is referred to as the KBS-3 method.

Two principal remaining tasks in SKB's programme are to locate, build and operate i) the deep repository and ii) an encapsulation plant in which the spent fuel will be emplaced in canisters to be deposited in the deep repository.

SKB is currently pursuing site investigations for a deep repository in the municipalities of Östhammar and Oskarshamn. The investigations are conducted in two stages; an initial phase followed, if the expected site suitability is confirmed, by a complete site investigation phase. The aim is to build a deep repository at one of these candidate sites, provided that the bedrock and other relevant conditions are found to be suitable. An application to build a deep repository will be made at the end of 2008 according to the current timetable.

The favoured alternative for the location of the encapsulation plant is at Oskarshamn, where it would operate in conjunction with the existing interim storage facility. An application to build an encapsulation plant will be made in 2006.

These two planning applications will each require a report on the long-term safety of the deep repository. This is an obvious requirement for the application to build the repository. In the case of the encapsulation plant, such a report will demonstrate that a repository for the sealed canisters (to be delivered by the encapsulation plant) will meet the requirements on long-term safety set up by the Swedish authorities. The two safety reports will be referred to as SR-Can and SR-Site, for the encapsulation plant and repository, respectively. SR-Can will be based on site data from the initial site investigation phase and SR-Site on data from the complete site investigation.

The first stage of the SR-Can project is to demonstrate the methodology that will be used in preparing for the planning application for the encapsulation plant. The methodology, which has evolved from that used in SKB's previous assessment, SR 97 /1/, will be reported and reviewed prior to its use in the final assessments. Also, the preliminary safety evaluations for each site, as envisaged in Reference /2/, will be carried out as sub-tasks within the SR-Can project. The main purposes of those evaluations are to:

- Determine whether earlier judgements of the suitability of the candidate area for a deep repository with respect to long-term safety holds up in the light of borehole data;
- Provide feed-back to continued site investigations and site-specific repository design.

A proposed methodology for the SR-Can assessment has been published in SKB Technical Report TR-03-08, 'Planning Report for the Safety Assessment SR-Can' /3/. The methodology envisaged the use of both continuum porous medium (CPM) and discrete fracture network (DFN) models on a range of scales to investigate the groundwater flow and radionuclide transport from a deep disposal facility to the biosphere. The modelling must address the effects of variable groundwater density and transients. Transients occur

naturally as a consequence of changes in climate states (temperate, periglacial and glacial) and during the operational and immediate post-closure phases of the repository. Key outputs from the modelling will be the groundwater flux, the definition of flow paths and values for parameters describing the transport of radionuclides along the paths. Ultimately, the results from the groundwater flow modelling will feed into biosphere calculations of radiological risks to man.

SKB's methodology refers to three scales of modelling, these being 'Regional' (~10 km), local (~1 km) and 'repository/block' (10–100 m). Using models at these scales it is necessary to simulate the transient, variable-density groundwater flow in sufficient detail to enable the groundwater flux and radionuclide transport paths to be determined. For example, flows from deposition holes into adjacent small-scale fractures represent one release route for radionuclides into the geosphere. Further transport through fractures of increasing size, up to regional-scale fracture zones, is the most likely route to the biosphere. Research into ways of coupling the geosphere and biosphere through near-surface and surface hydrology models is ongoing within the SKB programme.

The focus of the project reported here has been to illustrate and test the geosphere methodology for the post-closure phase of the safety assessment, that is, between the present and 10,000 years after present (AP). The initial data for the Forsmark site Version 1.1 has been used as an example. However, some of the key input relating to the fracture interpretation was revised as part of the Version 1.1 site description as this project was being carried out. Hence, two sets of fracture parameterisations were used to construct DFN models corresponding to the original and updated Forsmark Version 1.1 site descriptions.

In order to demonstrate the groundwater flow and transport methodology outlined by SKB in TR-03-08 /3/, a set of nested models has been constructed using Serco Assurance's CONNECTFLOW software in order to assess issues on various key scales. These nested models are:

- a regional-scale CPM model containing representations of deterministic large-scale fracture zones, with site-scale hydrogeological properties based on and consistent with an underlying DFN data description. This model has been provided from the ongoing Forsmark hydrogeological modelling study undertaken jointly by Kemakta Konsult, Serco Assurance and Golder Associates. The purpose of this model is to study transients and provide boundary conditions for models on smaller-scales;
- a local-scale DFN model nested within a regional-scale CPM model to assess far-field transport pathways, but also capture the detailed transport pathways through the DFN immediately around the repository tunnels;
- a CPM representation of the deposition holes, engineered damage zone (EDZ) and deposition tunnels nested within a canister-scale DFN model. This model is used to perform detailed calculations of groundwater fluxes in the DFN adjacent to canisters and in the EDZ, for input to near-field source term models.

Output from these models has been used to calculate performance measures such as canister flux, travel time, and exit locations that are required as input to performance safety assessment (PSA) calculations. Since the above set of models offer greater resolution of both near-field parameters such as flows in the fractures intersecting a deposition hole and far-field parameters such as F-quotient through a DFN, then new concepts are required for how such information can be incorporated in the PSA calculations. Hence, consideration is also given to how PSA calculations should be performed using the COMP23 and FARF31 programs, based on output from CONNECTFLOW. This illustrates the capacity of CONNECTFLOW to integrate with SKB's existing software in order to provide an overall

methodology for the groundwater flow and PSA calculations. Figure 1-1 shows a schematic illustration of the model chain for the groundwater flow and transport calculations developed for SR-Can and how these feed into the PSA calculations. The arrows show the flow of information (direction and type) between the various models.

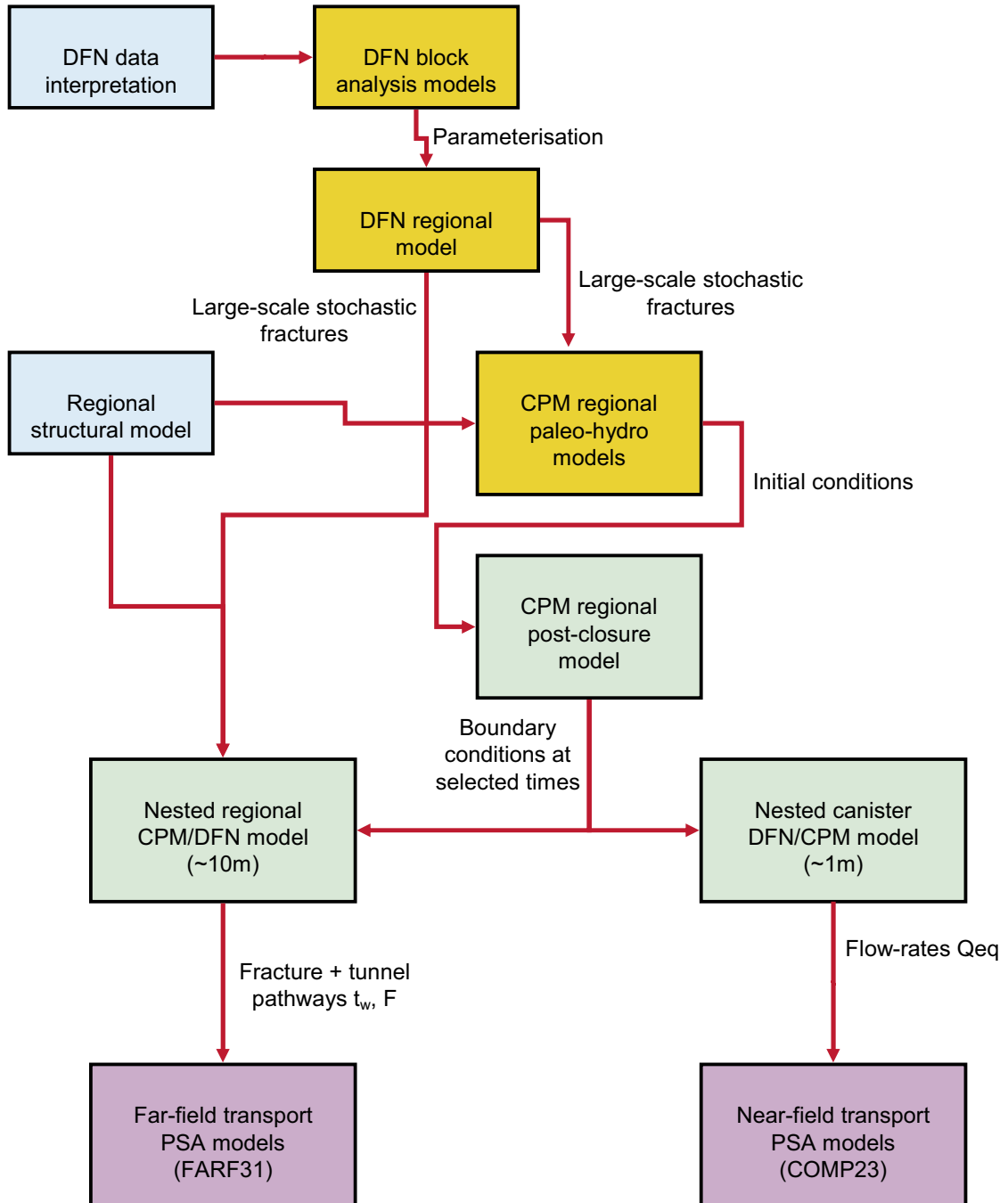


Figure 1-1. Schematic illustration of model chain developed for the SR-Can methodology. Models coloured blue were supplied as part of the Site Descriptive Modelling (SDM) 1.1 Exercise. Models coloured orange were an overlap between work within SDM and SR-Can. Models coloured green have been created solely within SR-Can. Models coloured purple relate to the PSA modelling phase of SR-Can.

The remainder of this report describes the models that have been set up and the results obtained. Section 2 addresses the analysis of the conceptual models for the fracture network at Forsmark. Sections 3 and 4 then describe the nested CPM/DFN models used to simulate the regional-scale and canister-scale flow and transport respectively. In Section 5, the performance measures and recommendations for how to use these measures in PSA calculations are presented.

2 Fracture conceptual model analysis

2.1 Introduction and objectives

A conceptual model and data description of fracture properties of the Forsmark site Version 1.1 have been used in this study. In this Section, an analysis is made of the original DFN interpretation only. The conceptual model describes a hierarchy of fracturing on a range of scales. Consideration has been given to the applicability of the concepts to both the groundwater flow and transport modelling at the necessary fracture length scales – canister (0.5 m to 10 m), local (10–100 m), and regional (100–1,000 m). These considerations include: what are the appropriate scales of models to give an adequate representation of key issues like canister fluxes and F-quotient, and practical issues such as the size of the numerical models (number of fractures and/or elements).

The data interpretation for Forsmark V1.1 was based primarily on data from a single borehole, KFM01A. Therefore, at this stage, the emphasis is on methodology development rather than on site-specific concepts. Hence, it is appropriate to consider the robustness of any conclusions drawn. The approach taken is to use the Forsmark V1.1 data as an illustration of the proposed methodology and to carry that through to its end-point in terms of predicting performance measures for safety assessment calculations, but to consider what might be the effects of changes in the DFN conceptual model. A re-interpreted DFN parameterisation is also defined in SKB Report R-04-15 /4/ with a lower fracture intensity, but higher transmissivity, based on a re-assessment of the intensity of conductive fractures. This alternative DFN model will be assessed as an amendment to this study, and to an extent provides a test of the robustness of the methodology.

The objective of this section then is to provide a practical strategy for the rest of the study, and in particular to make suggestions for the following issues:

1. How does the equivalent permeability (mean and variance) vary with scale, and how is this affected by truncation of length/transmissivity distributions?
2. What scale of fracturing needs to be considered for flow calculations around the deposition holes?
3. What size of DFN model is possible for nesting within a regional-scale CPM model?
4. How much of the repository can be modelled for canister-scale flows?
5. How does the F-quotient vary depending on the scale of fractures considered, and how can an F-quotient be applied in the CPM model consistent with the underlying DFN?
6. How should sensitivity to varying confidence in the characterisation of large-scale structures be addressed?

2.2 Approach

The main emphasis of this task is to consider the implications of DFN parameterisation for groundwater flow and transport calculations. A number of calculations have been performed using DFN models generated within simple blocks on a variety of scales to assess the scale-dependent flow and transport rates and how sensitive these quantities are to truncations of the DFN parameter distributions. This helps guide choices about sizes of models and provides a basis for making any simplifying assumptions, such as PDF truncation.

2.3 Fracture network data sources

A description of the DFN parameterisation was delivered in December 2003 prior to its publication in SKB Report R-04-15 /4/. In addition, the repository layout has been provided, which specifies the deposition hole dimensions and spacing, layout of repository, canister positions, and backfill parameters. The design data is required for the model feasibility study.

2.3.1 Orientations

Five fracture sets were identified based on orientation. The original version 1.1 data was fitted by a statistical model using the Univariate Fisher distribution to give the orientation parameters listed in Table 2-1.

Table 2-1. Orientation parameters for 5 fractures sets at Forsmark.

	NE	NW	NS	EW	SubH
Mean strike	223.9	126.0	175.5	97.9	240.2
Mean dip	88.7	87.5	87.6	87.0	10.7
Fisher concentration	19.7	22.8	21.0	37.3	11.8

2.3.2 Fracture intensity P32 and fracture length

A key parameter in any DFN model is the intensity of open fractures that are potential hydraulic conductors. There are several ways of measuring fracture intensity such as image-logs (borehole-TV), core characterisation, and flow-logs. In addition, there are several measures of fracture intensity that can be used, such as fracture count per unit length (P10), or fracture surface area per unit volume (P32). P32 is convenient since it is independent of fracture length and orientation. For the original version 1.1 DFN, fractures were picked from core analysis and it was assumed that all natural cuts correspond to open conductive fractures. Figure 2-1 shows the distribution of open fractures with depth. This distribution was interpreted as a piecewise constant distribution with a distinct step at 400 m depth. Hence, a P32 value was given for above 400 m depth, and below 400 m depth.

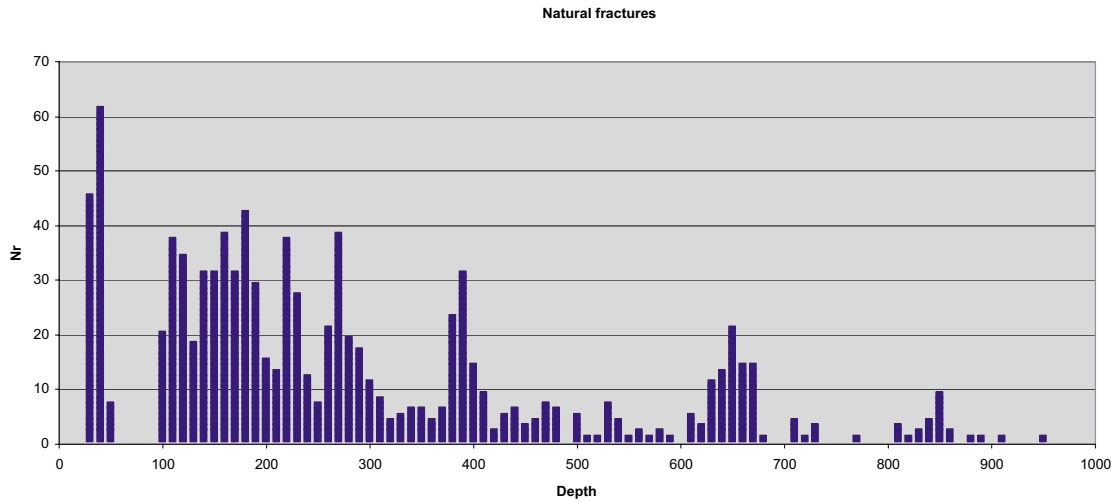


Figure 2-1. Distribution of natural (open) fractures based on original interpretation for KFM01A. The axes are numbers of fractures per 10 m against depth.

Table 2-2 gives the P32 values for each fracture set above 400 m depth. The corresponding values for the rock below 400 m are given in Table 2-3. On the basis of fracture mapping on outcrops and linked to lineament length distribution, a power-law distribution for fracture length was interpreted with an exponent for the CCDF of $k_1 = 2.97$. For the purposes of this study, fractures need to be considered on a range of scales, and so it is necessary to calculate the fracture intensity for various lengths of fractures. For the power-law distribution Equation 2-1 can be used to calculate the P32 for a truncated range of lengths between L_{min} and L_{max} .

$$P_{32}[L_{min}, L_{max}] = P_{32}[L \geq L_0] \left(L_{max}^{[2-k_L]} - L_{min}^{[2-k_L]} \right) / \left(-L_0^{[2-k_L]} \right) \quad \text{Equation 2-1}$$

Here, $L_0 = 0.5$ m is the minimum length used for the “untruncated” intensities, $P_{32}[L \geq L_0]$, $K_L = 2.97$ is the slope of the fracture length distribution in the CCDF. In Table 2-2 and Table 2-3 P32 values are given for fractures with lengths 100–1,000 m (regional-scale), 10–100 m (local-scale), and 1–10 m (canister-scale).

Table 2-2. P32 (fracture area per unit volume) for fractures within 400 m of ground surface for each of the 5 fracture sets. P32 values for different fracture length ranges are also given.

	NE	NW	NS	EW	SubH	P32 total
P32 Intensity	2.2254	0.5525	1.2564	0.0634	1.8450	5.9426
ratio	0.3745	0.0930	0.2114	0.0107	0.3105	
P32 1 m to 10 m	1.0143	0.2518	0.5727	0.0289	0.8410	2.7087
P32 10 m to 100 m	0.1087	0.0270	0.0614	0.0031	0.0901	0.2902
P32 100 m to 1,000 m	0.0116	0.0029	0.0066	0.0003	0.0097	0.0311

Table 2-3. P32 (fracture area per unit volume) for fractures below 400 m deep for each of the 5 fracture sets. P32 values for different fracture length ranges are also given.

	NE	NW	NS	EW	SubH	P32 total
P32 Intensity ratio	0.2269	0.06626	0.1507	0.0076	0.2213	0.7127
P32 1 m to 10 m	0.1217	0.0302	0.0687	0.0035	0.1009	0.3249
P32 10 m to 100 m	0.0130	0.0032	0.0074	0.0004	0.0108	0.0348
P32 100 m to 1,000 m	0.0014	0.0003	0.0008	0.0000	0.0012	0.0037

The proposed depth for a repository at Forsmark is 400 m. This corresponds exactly with the depth chosen for a step change in fracture density, and would lead to features such as fewer small-scale fractures intersecting the deposition holes slightly below $z = -400$ m than the deposition tunnels slightly above. Hence, rather than having a discontinuity in P32 coincident with the repository, an extra layer was interpreted around the repository. Based on Figure 2-1, a layer between 300 m and 500 m depth was chosen with an average P32 calculated as the mean of the values from the layers above and below.

It should be noted that in using a power-law fracture length distribution the correct exponent was used for calculating the distribution of P32 with length, but the sampling of a length for individual length fractures was sampled from a PDF with exponent 2.97 rather than the value specified in the SDM of 3.97. This leads to a moderate shift towards slightly more large fractures in each length range, but the P32 in each length range is as interpreted.

2.3.3 Fracture transmissivity and transport aperture

For version 1.1 there is a hypothesis that fracture transmissivity (T) is directly correlated to length using the following relationship

$$T = a L^b. \quad \text{Equation 2-2}$$

The parameters a and b were obtained in the site description by matching numerical simulations of a DFN around a borehole with the observed average transmissivity from the Posiva flow-log. For the original model this gave

$$T = 2.47 \cdot 10^{-12} L^{1.791}. \quad \text{Equation 2-3}$$

The coupling between fracture transmissivity and size expressed by Equation 2-3 leads to a flow system that on each scale of consideration is governed by the largest feature on that scale. The rationale for such a model is of course that large features are the main contributors to the fracture network connectivity. Moreover, large features are generally both wider and thicker than small features. Expected characteristics of a DFN model with this transmissivity/length coupling are that any large fractures will dominate flow locally, while the much denser small fractures provide the background hydraulic conductivity. That is, the model corresponds to a concept where there is a background of small-scale fractures that give rise to a relatively low background conductivity, but with an occasional large feature that gives a local conductivity-spike that is orders of magnitude higher than the background. This is consistent with the profile of conductivity seen in both the double packer-tests and the Posiva flow-log data. As b is increased, the contrast between large

features and the background, and hence the degree of heterogeneity, is increased. Hence, the result is that flow and transport tend to be channelled toward the larger fractures. Particles released into such a network get channelled toward the larger fractures that carry higher flow rates such that transport follows a dendritic pattern. These characteristics will be demonstrated in the results of this study.

In theory, other relationships between fracture transmissivity and size may exist, including no relationship at all. On the basis of our current understanding, however, the absence of a relationship between fracture transmissivity and size would lead to lower connectivity between high transmissivity fractures and hence lower overall conductivity. Also, transport would be more diffuse than the dendritic channelling that occurs with a correlation. Therefore, the current conceptual model of a T/L correlation is thought to be somewhat pessimistic.

The final key fracture parameter is the transport aperture, which when combined with fracture area gives the volume of the fracture accessed by transport. Again, a correlation is assumed between aperture and transmissivity, and hence length, with the relationship:

$$\alpha_t = 0.4 T^{0.5}. \quad \text{Equation 2-4}$$

The transport aperture is used in calculating travel time and F-quotient along particle tracks in the DFN model. It can also be used to calculate an equivalent kinematic porosity for the CPM models. The effects of channelisation within individual fractures may act to decrease this transport aperture by some factor, but also reduce the accessible flow width of fracture flow channels.

Figure 2-2 illustrates one realisation of the fracture network for the zone above -400 m, based on fractures with a length between 100 m and 1,000 m. Flux-based upscaling techniques were used to calculate the equivalent CPM permeability tensor on specified scales. The technique involves generating a DFN model within some large region, 1 km for example, and then subdividing the region into a regular array of sub-blocks of scale 100 m, for example. For each sub-block, the fractures cutting each block are identified, and then flow calculations are carried out for flow through the block parallel to each of the coordinate axes. An equivalent permeability tensor is then fitted to the resulting array of flux values /8/. The equivalent upscaled permeabilities corresponding to Figure 2-2 for 100x100x100 m blocks, are shown in Figure 2-3.

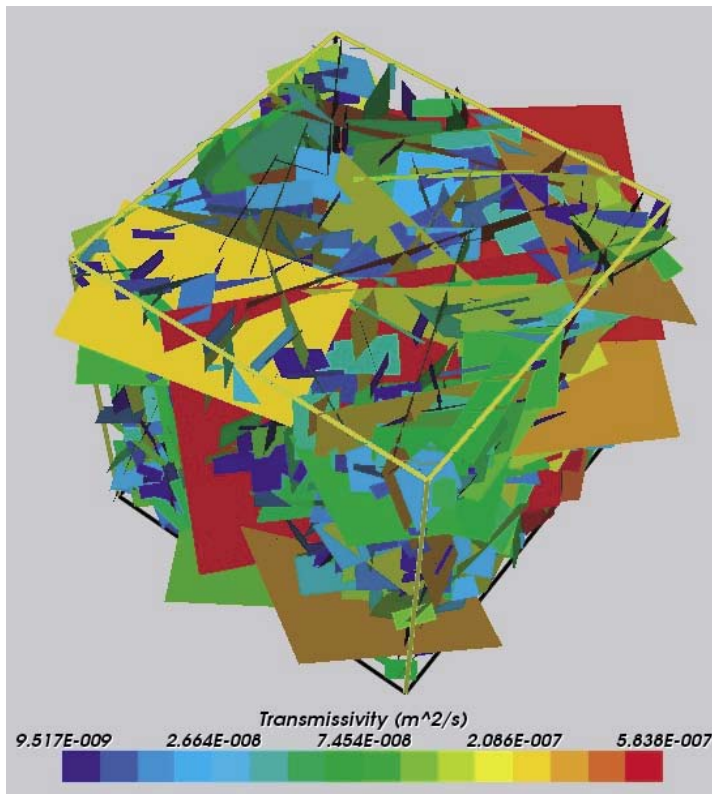
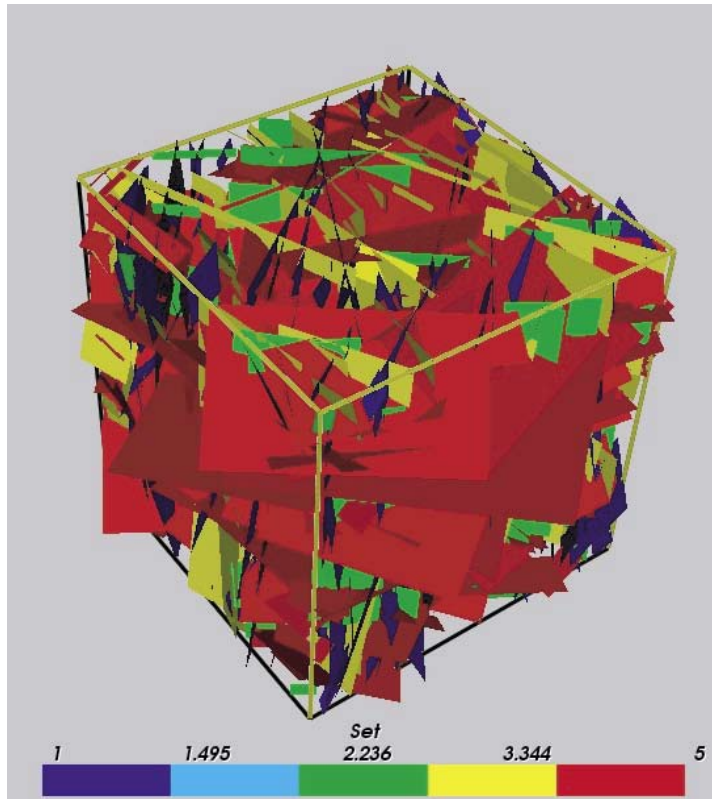


Figure 2-2. Fracture network for the zone above -400 m for Forsmark V 1.1 in a 1 km block, containing fractures with lengths between 100 m and 1,000 m. Fractures are coloured by set (top), and by transmissivity (bottom).

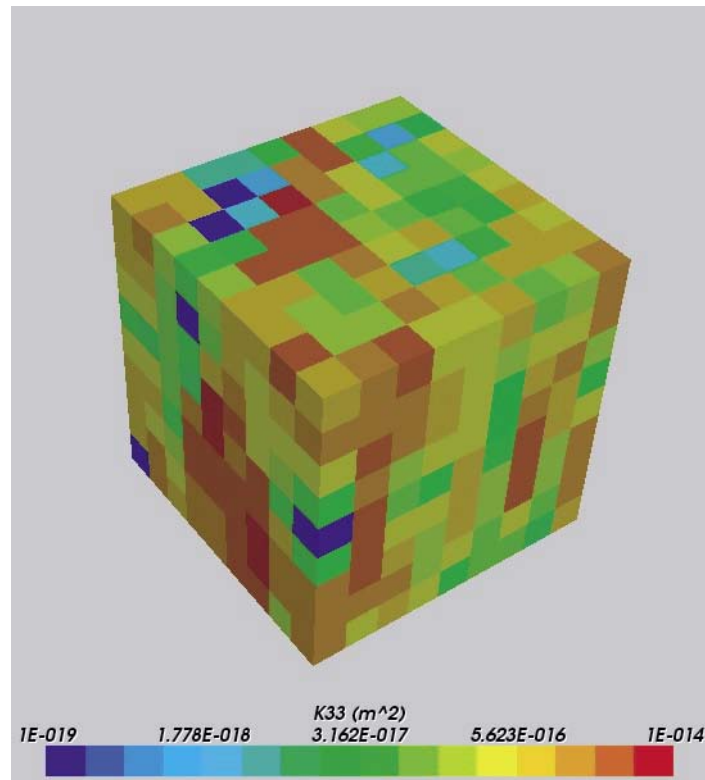


Figure 2-3. Equivalent CPM model based on upscaled vertical permeability (K_{33}) for 100 m cubes of the fracture network illustrated in Figure 2-2.

Note, for water the conversion factor between hydraulic conductivity and permeability is a factor of about 10^7 to go from permeability to a conductivity.

A 100 m scale was chosen since permeabilities on this scale are required for repository design issues and it is appropriate for construction of a CPM regional-scale model. In order to understand how the equivalent permeability on a 100 m scale is affected by fractures on various scales, upscaling was performed for various cut-offs in the fracture length distribution. As a rough approximation, permeability will scale in proportion to P_{32} times T . Based on Equation 2-1 and Equation 2-2, permeability will scale with L in proportion to $L^{(2-k+1+b)}$, which in this case equals $L^{0.8}$, or a near linear increase with fracture length. Hence, it can be expected that even if smaller and smaller fractures are added to a model then the equivalent permeability for a block will eventually converge. In the first instance, the upscaled permeability was calculated for all fractures with lengths between 100 m–1,000 m, and then for all fractures with lengths between 10 m–1,000 m. For both these cases permeabilities were calculated for a 9x9x9 array of 100 m blocks. The reason that there are only 9 blocks in each direction is a result of the way the upscaling was performed. For accuracy it has been found that groundwater flow should be calculated through a fracture network region larger than the block required for upscaling, but then to calculate the flux and equivalent permeability through a block in the centre of the required size. The additional volume of DFN model around the block is called a ‘guard zone’ and its purpose is to ensure that the flows calculated in the central block are representative of flows through an in-situ network. Without a guard zone there is a risk that permeability will be over-estimated because a large fracture may cut across a corner or edge linking two boundary conditions, and hence give much higher flow-rates than are seen in the central fracture network. In this study, flows were calculated through a 200 m block, but the fluxes were calculated through the central 100 m block to fit an equivalent permeability, so there is a 50 m thick guard zone around the 100 m block. 50 m was chosen as the half length of a

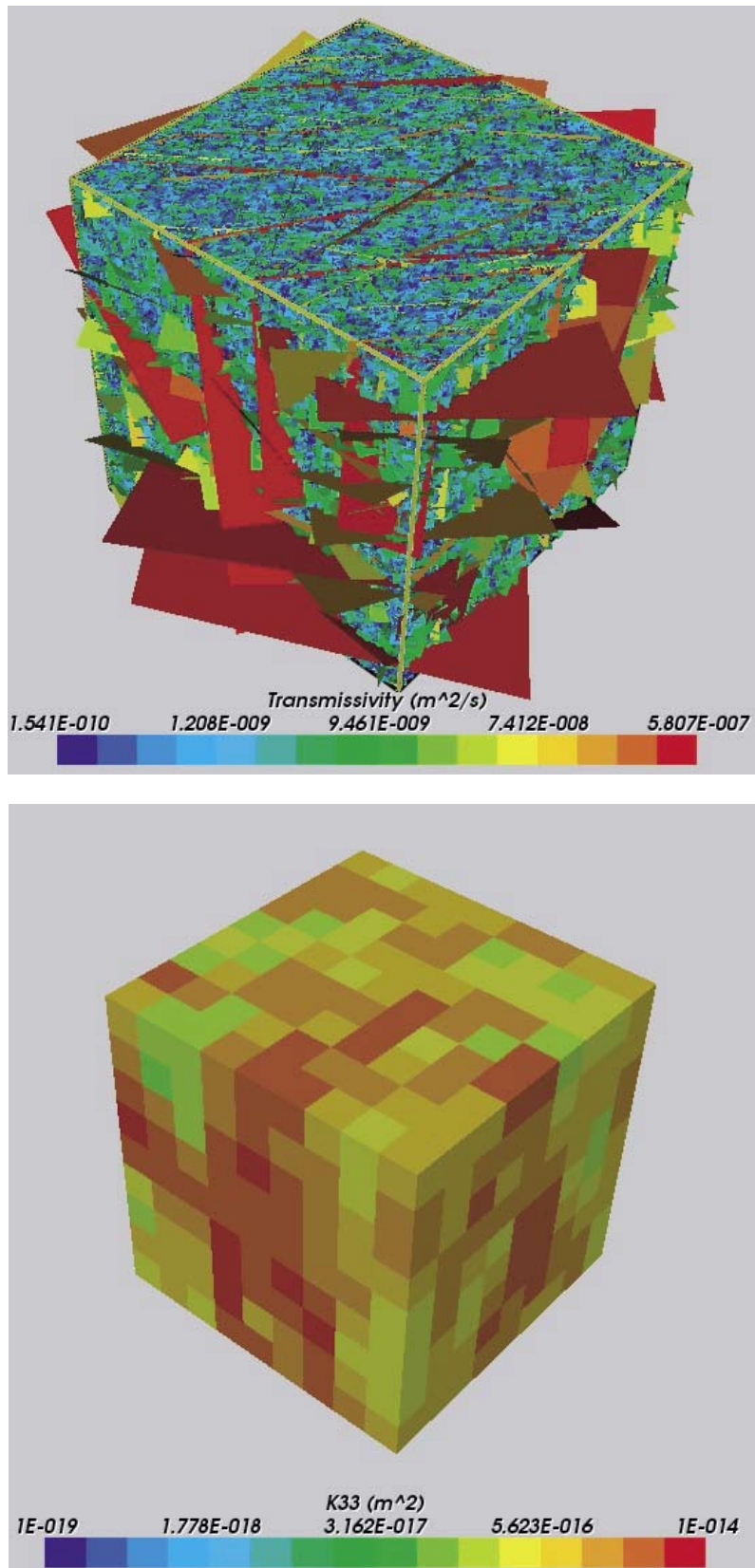


Figure 2-4. Fracture network for the zone above -400 m for Forsmark V1.1 on a 1 km block, containing fractures with lengths between 10 m and 1,000 m. Fractures are coloured by transmissivity (top). The upscaled equivalent vertical permeability for 100 m cubes is shown (bottom).

100 m fracture. Figure 2-4 shows the fracture network and corresponding upscaled vertical permeability for the upper 400 m of rock with fractures down to 10 m. Compared with Figure 2-3 the permeability is similar in magnitude, but more homogeneous because the small-scale fractures enhance the background permeability.

The enhancement of the background permeability by fractures with lengths between 10 m and 100 m means that the permeability is never less than about 10^{-17} m² (see Figure 2-4), whereas with only fractures greater than 100 m, some cells are not crossed by a large fracture and so essentially have zero permeability (see Figure 2-3). The equivalent cases for the DFN below a depth of 400 m are shown in Figure 2-5. Here the network has greater sparsity with many cells having zero permeability even when the 10–100 m fractures are added. This suggests that the network is around or below the percolation threshold.

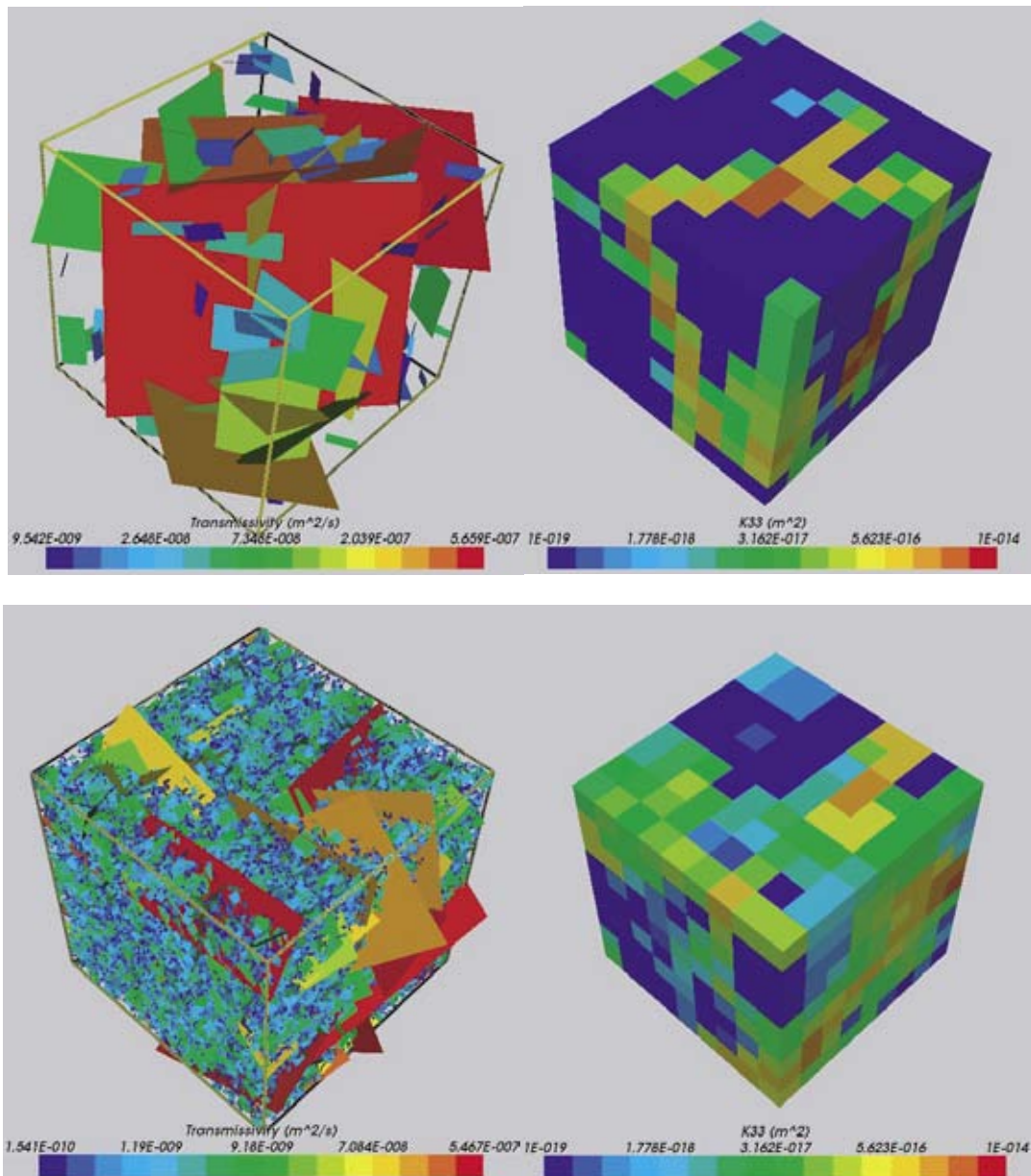


Figure 2-5. Fracture network for the zone below -400 m for Forsmark V1.1, containing fractures with lengths between 100 m and 1,000 m (top), and between 10 m and 1,000 m (bottom). Fractures are coloured by transmissivity. The corresponding upscaled equivalent vertical permeability ($K33$) for 100 m cubes are shown to the right.

Particular attention was paid to the network properties around the repository layer which was used between 300 m and 500 m depth and that had the mean P32 from layers characterised above and below 400 m depth. Figure 2-6 shows the DFN block models constructed for this layer with fracture lengths ranging from 10 m–1,000 m. The corresponding upscaled permeability is all above $5 \cdot 10^{-18} \text{ m}^2$ without zero values suggesting the network is above the percolation threshold. Another measure of fracture connectivity is the directional matrix block size. This is defined as the average spacing between fractures in the connected network. It is calculated by removing fractures that are isolated, drilling an array of parallel hypothetical cores through the block, and then calculating the total length of core divided by the number of connected fractures intersected. An example of the matrix block size in the E-W direction is shown at the bottom of Figure 2-6.

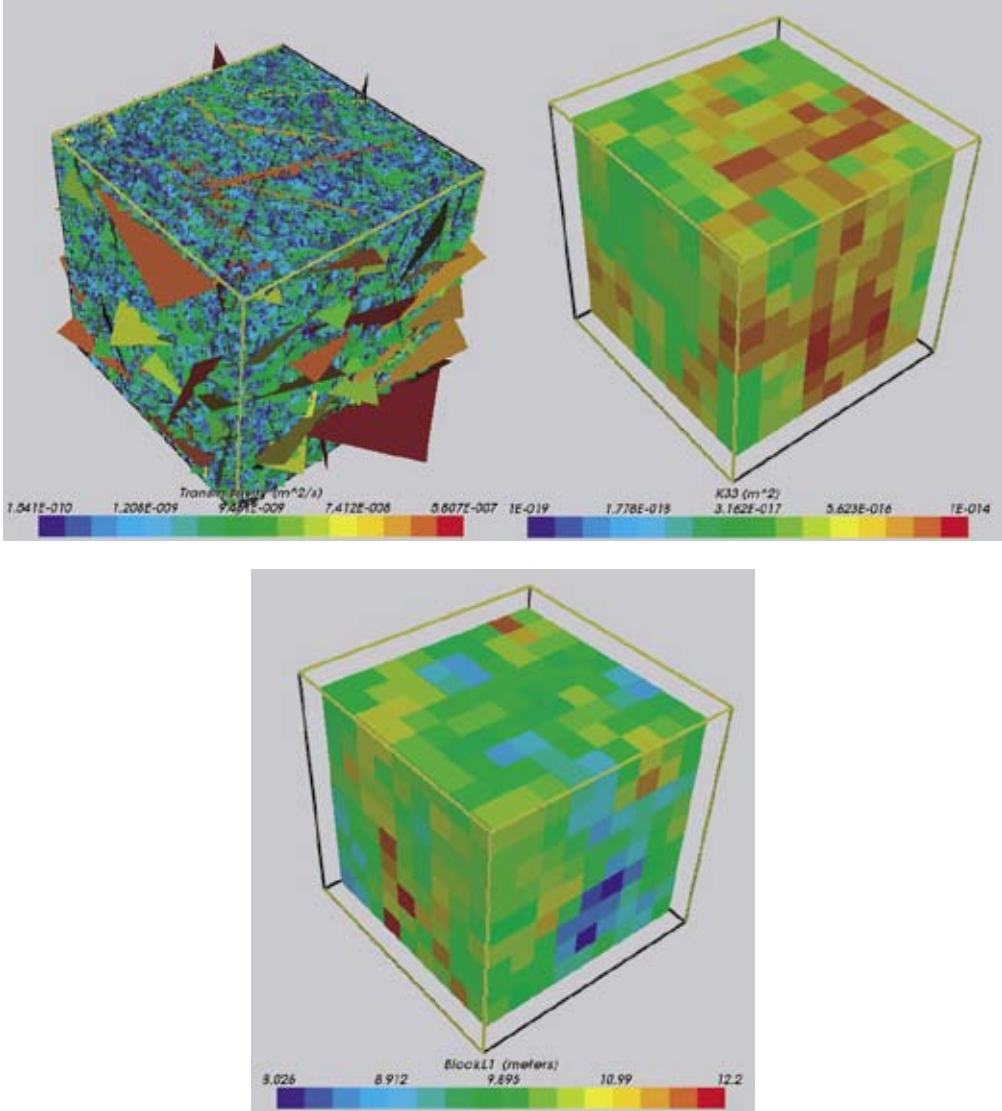


Figure 2-6. Fracture network for the repository layer between –500 m and –300 m for Forsmark V 1.1, containing fractures with lengths between 10 m and 1,000 m. Fractures are coloured by transmissivity (top-left). The corresponding upscaled equivalent vertical permeability (K33) for 100 m cubes is shown (top-right) and the upscaled matrix block size in the E-W direction is shown (bottom).

The sensitivity to truncating the DFN length distribution was studied by quantifying the distribution of upscaled permeability and matrix block size. Two criteria were put on the choice of an appropriate cut-off in fracture length:

- The distribution of upscaled permeability for an array of 100 m blocks should be converged, so that spatial distribution of permeability in a regional CPM model of 100 m elements is correct;
- The matrix block size should be smaller than the 100 m block to ensure that there is a network of fractures within each block.

Figure 2-7 shows the equivalent plots to Figure 2-6 for the repository layer but with a cut-off of fracture length at 50 m rather than 10 m. As can be seen the upscaled permeability and matrix block size are very similar to the case with smaller fractures (down to 10 m) included, which suggests a cut-off around 50 m is acceptable.

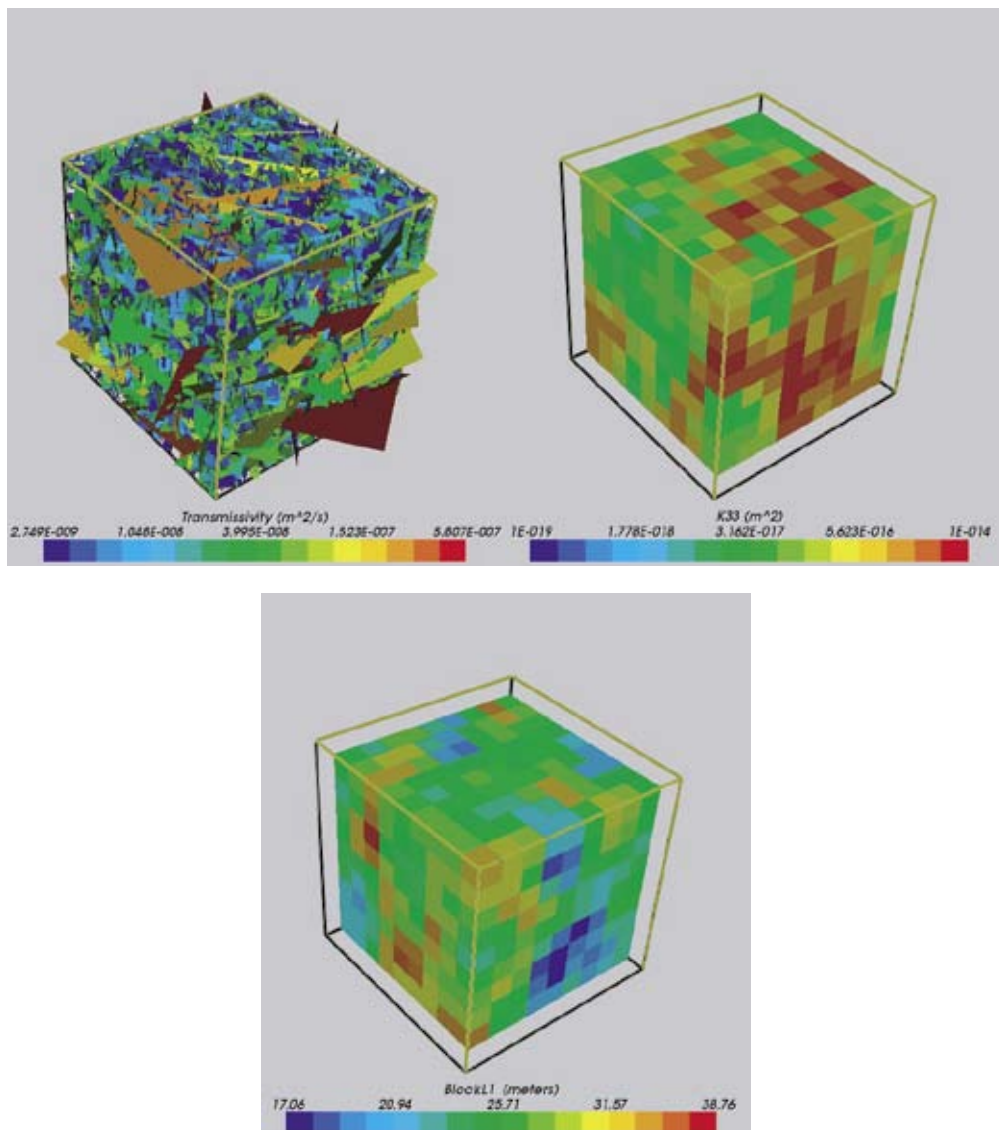


Figure 2-7. Fracture network for the repository layer between –500 m and –300 m for Forsmark V 1.1, containing fractures with lengths between 50 m and 1,000 m. Fractures are coloured by transmissivity (top-left). The corresponding upscaled equivalent vertical permeability (K33) for 100 m cubes is shown (top-right) and the upscaled matrix block size in the E-W direction is shown (bottom).

These results are summarised below in the form of histograms for permeability based on the data for a 9x9x9 array of 100 m blocks (i.e. 729 values). The upscaled permeability is calculated in the form of a tensor (directional permeability), which allows for directional anisotropy. However, for the purposes of illustration, the geometric mean permeability has been used here as a scalar measure of permeability for comparison purposes. Figure 2-8 shows the distribution of the geometric mean permeability for the layer above 300 m depth for a cut-off at 100 m and at 10 m. This shows a clear difference with a long tail toward low values when a cut-off of 100 m is used just because some blocks are not crossed by a large fracture. The extra connectivity provided by including the small-scale fractures gives a much tighter and homogeneous distribution. Clearly, then if a regional-scale CPM model were constructed based on a cut-off of 100 m it would have too high a degree of heterogeneity. The corresponding distribution for the layer below 500 m depth is shown in Figure 2-9. Here, the distribution is very heterogeneous even when fractures down to 10 m are included. When a cut-off of 100 m is used, then about 60% of cells have zero permeability. For the repository layer, 300 m to 500 m depth, the histogram in Figure 2-10 is shown for cut-offs of 10 m, 50 m and 100 m. This demonstrates that a cut-off of about 50 m is sufficient to reproduce the distribution when smaller scale fractures are included.

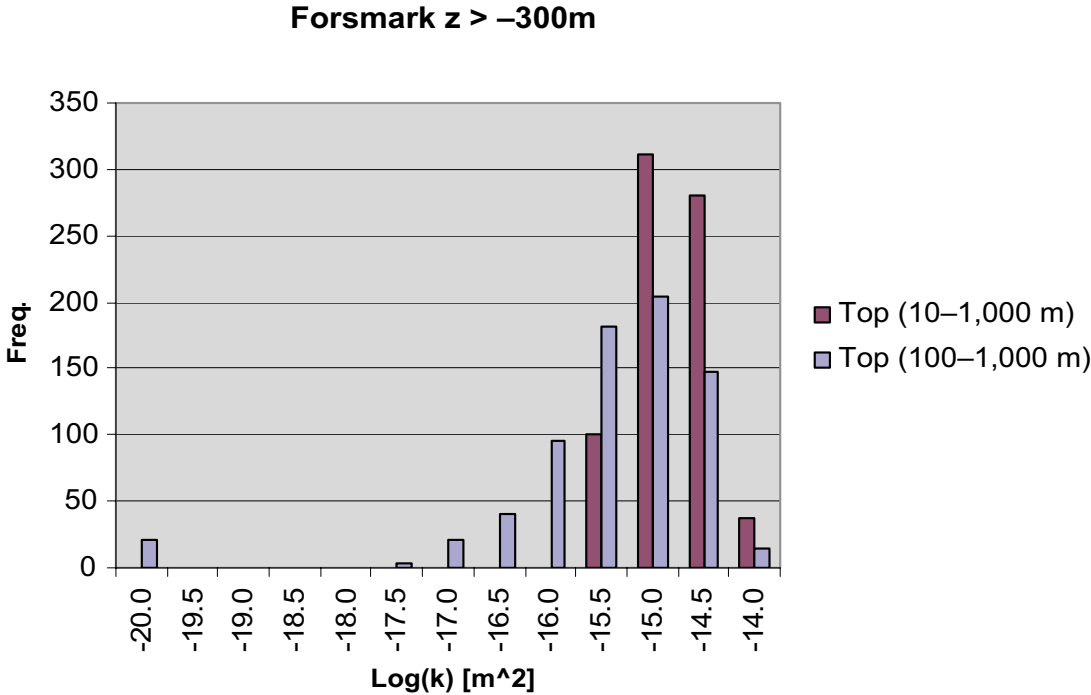


Figure 2-8. Distribution of upscaled permeability for the top of the DFN model above $z = -300\text{ m}$ on 100 m blocks (based on a total of 729 blocks i.e. 9x9x9). Here, the geometric mean permeability is used as a scalar quantity. Two series of data are shown for the cases with all fractures of lengths 10–1,000 m, and for fractures between 100–1,000 m.

Forsmark $z < -500\text{m}$

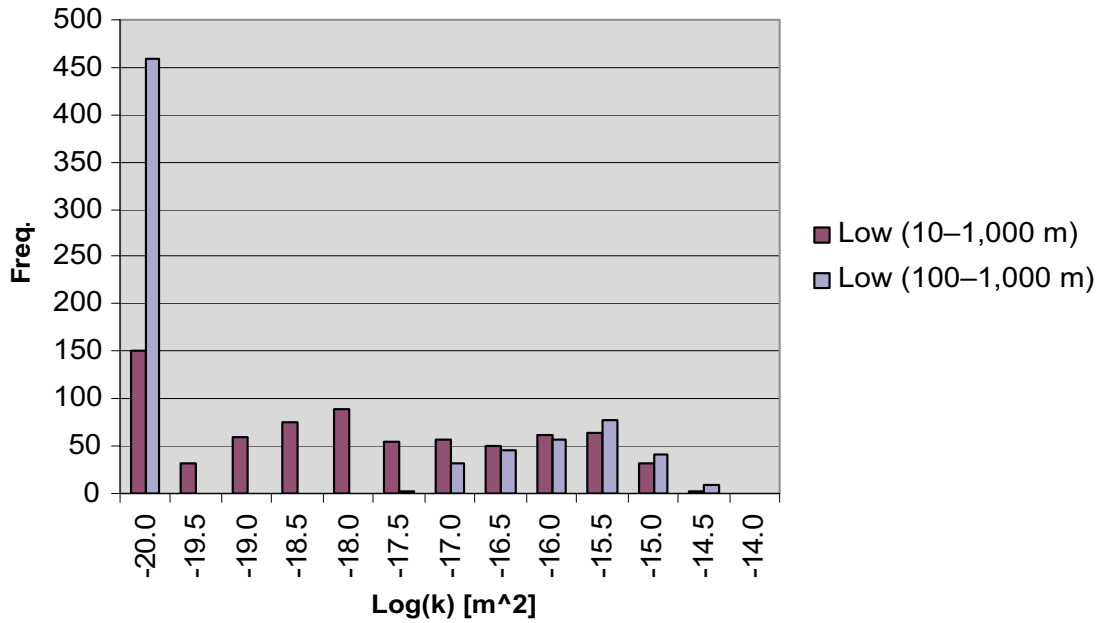


Figure 2-9. Distribution of upscaled permeability for the bottom of the DFN model below $z = -500\text{ m}$ on 100 m blocks (based on a total of 729 blocks i.e. $9 \times 9 \times 9$). Here, the geometric mean permeability is used as a scalar quantity. Two series of data are shown for the cases with all fractures of lengths 10–1,000 m, and for fractures between 100–1,000 m.

Forsmark $z = -300\text{ to }-500\text{m}$

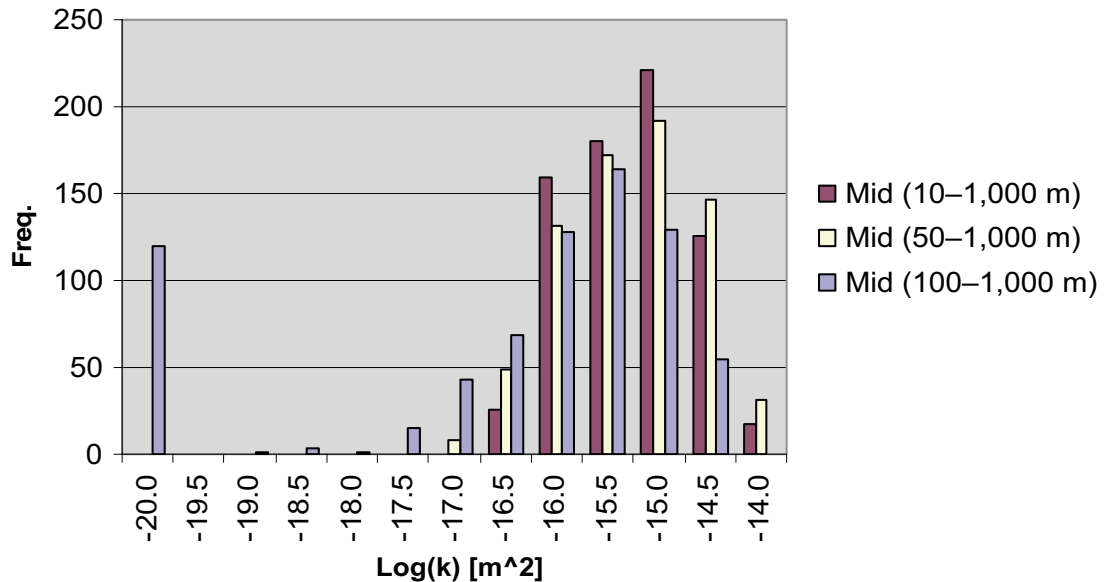


Figure 2-10. Distribution of upscaled permeability for the middle of the DFN model between $z = -500\text{ m}$ and $z = -300\text{ m}$ on 100 m blocks (based on a total of 729 blocks i.e. $9 \times 9 \times 9$). Here, the geometric mean permeability is used as a scalar quantity. Three series of data are shown for the cases with all fractures of lengths 10–1,000 m, for 50–1,000 m, and for 100–1,000 m.

For the repository layer, the matrix block size was also calculated for a variety of length scale cut-offs. Table 2-4 gives the directional matrix block sizes for each of the coordinate directions (x = E-W, y = N-S, z = vertical) for cut-offs of 10 m, 50 m and 100 m. The matrix block size is smallest in the x-direction and about the same in the y and z directions. There is a marked difference between a cut-off at 50 m and 100 m suggesting that the adding in the extra fractures to 50 m has a big effect on connectivity. Also, the values for a 50 m cut-off are a third of the 100 m block size, suggesting a network of fractures in each block whereas for a 100 m cut-off the 100 m blocks are just randomly sampling individual large fractures. Based on these results it was concluded that a cut-off in the length distribution of 50 m was sufficient for parameterising a regional model. It can also be concluded that it should be feasible to create a nested DFN local-scale model for a site area of about 1 km in size.

Table 2-4. Matrix block size statistics in the three coordinate directions for the middle of the DFN model between z = -500 m and z = -300 m on 100 m blocks (based on a total of 729 blocks i.e. 9x9x9). This is a measure of the directional spacings between fractures in the connected network. The first figure is the mean value. The value in brackets is the standard deviation over the ensemble of blocks.

Fracture length range (m)	MBSx (m)	MBSy (m)	MBSz (m)
100–1,000	105 (34)	136 (39)	133 (39)
50–1,000	26 (2)	32 (4)	36 (3)
10–1,000	10 (0.5)	13 (0.8)	15 (0.5)

It should be noted that such conclusions are dependent on the distributions of P32, length and transmissivity, and hence these conclusions are specific to the current DFN model. However, it is recommended that the general methodology be followed for other DFN models or variants.

When issues on other scales are considered such as flow around the deposition tunnels and holes then smaller scale fractures need to be considered. For this DFN, the approach is to include fractures from 1,000 m to 50 m in the regional-scale and local-scale models, but then to include smaller scale fractures within a layer around the repository structures for the nested models. The thickness of this layer must be at least the size of the matrix block size for a 50 m cut-off i.e. >36 m thick. For the canister-scale nested model even smaller fractures will need to be included to ensure there is at least one fracture cutting each canister. Appropriate limits for fracture sizes and extent will be determined based on practical criteria in terms of what sizes of models can be simulated. For the current conceptual DFN, the use of power-laws means that reducing the length cut-off leads to a large increase in the number of fractures included in the model.

2.3.4 Transport and channelisation

In this phase of modelling the details of the heterogeneity within an individual fracture will not be represented explicitly. Instead it needs to be accounted for by appropriate factors multiplying travel-time, t_w , and F-quotient. In DFN model, transport takes place in fractures along paths between pairs of fracture intersections. The travel time between these intersections is calculated as:

$$t_w = \frac{A_f \alpha_t}{Q}, \quad \text{Equation 2-5}$$

- A_f is the fracture area accessed by this flow channel in the fracture [m^2];
- Q is the flux between a pair of fracture [m^3/yr];
- α_t is the transport aperture of the fracture [m].

The F-quotient is given by

$$F = \frac{2t_w}{\alpha_t} . \quad \text{Equation 2-6}$$

Channelisation within the plane of a fracture will lead to a reduction in the accessible fracture area by some factor $A'_f = \beta \times A_f$, say 0.1. This will lead to

$$t'_w = \beta \times t_w \quad \text{and} \quad F' = \beta \times F . \quad \text{Equation 2-7}$$

Channelisation within the cross-section of a fracture due to Gouge material or roughness will lead to a reduction in the transport aperture by some factor $\alpha'_t = \lambda \times \alpha_t$ will lead to

$$t'_w = \lambda \times t_w \quad \text{and} \quad F' = F . \quad \text{Equation 2-8}$$

2.3.5 Representation of deposition tunnels, and engineered damage zone (EDZ)

The fractured rock at Forsmark is very tight. Therefore, it is possible that, under a range of engineering concepts, the backfill material may be more transmissive than the ‘background’ host rock. Hence, a suitable representation of the effect of the repository on hydraulic properties post-closure is required for the PSA calculations. There are several ways of representing the deposition tunnels. For a CPM model, the tunnels can be represented using the Implicit Fracture Zone (IFZ) method which modifies the permeability of elements the tunnel goes through to represent the combined flow in the tunnel and rock. However, as the cross-sectional area of a tunnel is of around 10 m^2 compared to an element cross-sectional area of about 10^4 m^2 so for the tunnel to have an effect on element properties we either have to use a more refined mesh or have backfill with a hydraulic conductivity over a thousand times that of the background rock. In a DFN model, the tunnels can be represented in an explicit way as fractures with an effective transmissivity equal to the width of the tunnel times the hydraulic conductivity of the backfill. For a nested canister-scale model, the deposition tunnels and deposition holes can be represented explicitly by a CPM finite-element model nested with a repository scale DFN model.

In this interim study the EDZ is not represented explicitly. Instead the representation of tunnel is taken to include the combined effect of the tunnel and EDZ. The transmissivity of the tunnel is a function of the cross-sectional area and hydraulic conductivity of the tunnel while for the EDZ it is a function of the extent type of damage caused during construction. For transport, the porosity of the tunnel is likely to be high around 0.1, while for the EDZ it is likely to be much smaller around 10^{-4} to 10^{-3} .

3 Nested regional-scale CPM/DFN model for the temperate climatic period (2,000–12,000 years AD)

3.1 Objective

The overall objective is to build a regional CPM model with a nested DFN repository model in order to assess transport pathways at a number of start times in a transient flow field. It is appropriate to make best use of the transient saline CPM model of the palaeo-hydrogeology at Forsmark set up by the CONNECTFLOW Team as part of the PFM 1.1 Site Descriptive Modelling (SDM). This covers the past from 8,000 BC to present. For the post-closure assessment modelling this model has to be run until 12,000 AD.

3.2 Approach

The approach has been to set up a CONNECTFLOW model based on the SDM 1.1 CPM model, with a regional-scale DFN model 1,000 m thick, and with extra local-scale fractures in a 60 m thick layer around the repository footprint. 60 m was used since it is significantly larger than the vertical matrix block size calculated in Table 2-4 for fractures down to 10 m, and hence would constitute a network containing several matrix blocks. Quasi-steady-state flow is computed in the nested model using a salinity distribution interpolated from the fully transient CPM model at a number of discrete times. Initially, a model was set up to compute flow on a purely steady-state freshwater model based on the present hydraulic boundary conditions. The second stage model involved computing the salinity distribution in the CPM region from a snapshot of the salinity at a set of appropriate times in the future (2,500 AD and 12,000 AD), and then using this to calculate the flow-field in the nested model based on the appropriate salinity and boundary conditions for that time.

The density of water in the DFN part was taken as a constant. This is a restriction of the current DFN implementation. In the CPM part, the groundwater density was held fixed at the value calculated at that time in the pure CPM model. The salinity, and water density, were therefore fixed distributions in the CPM part, but pressure, and hence flow, were recalculated in the nested model. Pressure and mass flux were continuous at the interface. However, to ensure that the correct driving force for flow, or potential, was used in the DFN part, the continuity equation at the CPM/DFN interface was modified to account for variable density. The modification was to equate the residual pressure in the DFN model to the environmental pressure in the CPM model at the interface. That is,

$$P^E = P^R - \int_z^{z_0} (\rho - \rho_0) g dz, \quad \text{Equation 3-1}$$

where

- P^E is the environmental pressure [N/m²];
- P^R is the residual pressure [N/m²];
- ρ is fluid density [kg/m³];

- ρ_0 is freshwater density [kg/m^3];
- g is gravitational acceleration;
- z_0 is a reference elevation (usually sea-level) [m].

The fluid density was calculated based on the salinity distribution in the CPM model at the required time.

A number of times were considered to assess the sensitivity of transport pathways as time evolves. The important idea was to identify ‘critical’ times when either repository fluxes or transport pathways show a significant change, e.g. flow in the repository is predominantly up instead of down, or the saline interface drops below the repository. It was found that suitable times were an early time just after the operational period at which saline conditions prevailed in the repository (2,500 AD was used), and a much later time at which freshwater had displaced much of the salinity around the repository (12,000 AD was used).

3.3 Model properties – sources of information

The framework for the modelling of version 1.1 of Forsmark is given by the Task Description 1.1 for Forsmark Version 1.1 /5/.

The geometric information on fracture zones is obtained from the Forsmark Version 1.1 XML files created by RVS, HCD1.xml and HCD2.xml. These files are stored in the restricted on-line database Simone, 2003.

The region to be modelled is illustrated in Figure 3-1, which shows the zone for which 50 m topographic data are available (largest insert box), the zone for which 10 m topographic data are available (smaller insert box) and the approximate area covered by the regional-scale model (red outline). This figure also shows the regional water divides.

Model property data were delivered in the Excel file PFM_V.1.1_Data_delivery_PS1 /6/. Data were then updated in the addendum to Task Description PFM V1.1 /7/. The regional-scale deterministic fracture zones (mapped and inferred features), as provided in Reference /6/, are shown in Figure 3-2. These features have varying confidence associated with their existence, which is a reflection of a mixture of data acquisition methods used and the available data, as described in Reference /4/.

The properties for fracture zones, rock mass and overburden are given in the above-discussed data deliveries /6, 7/. The same data deliveries specified the inferred DFN parameters. Also, the layered structure of the model is defined in the deliveries. In Version 1.1 of the Forsmark data, the fracture zones have a much more varying set of properties compared to the previous version.

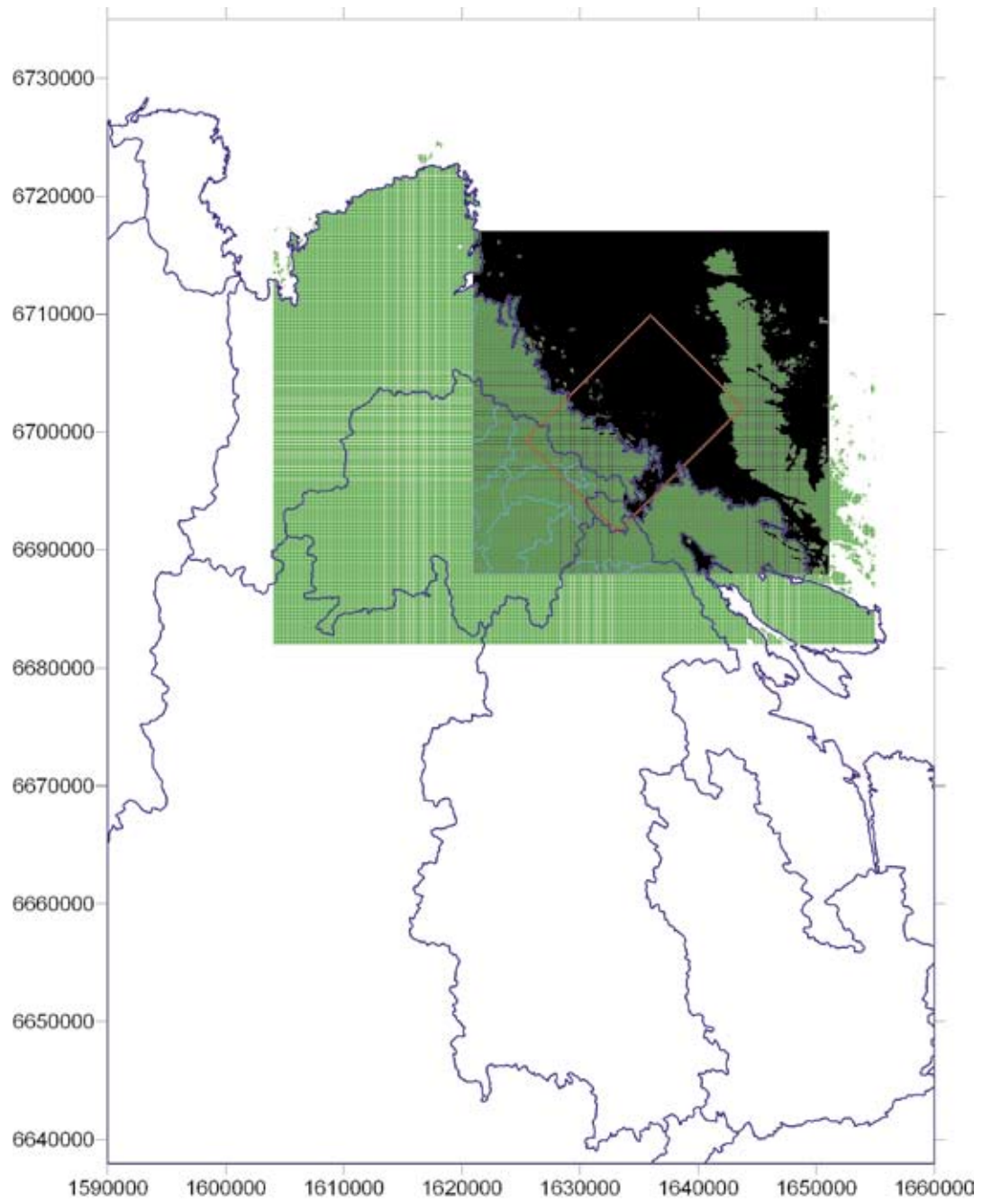


Figure 3-1. Overview of available data, i.e. 10 m data, 50 m data and regional water divides.

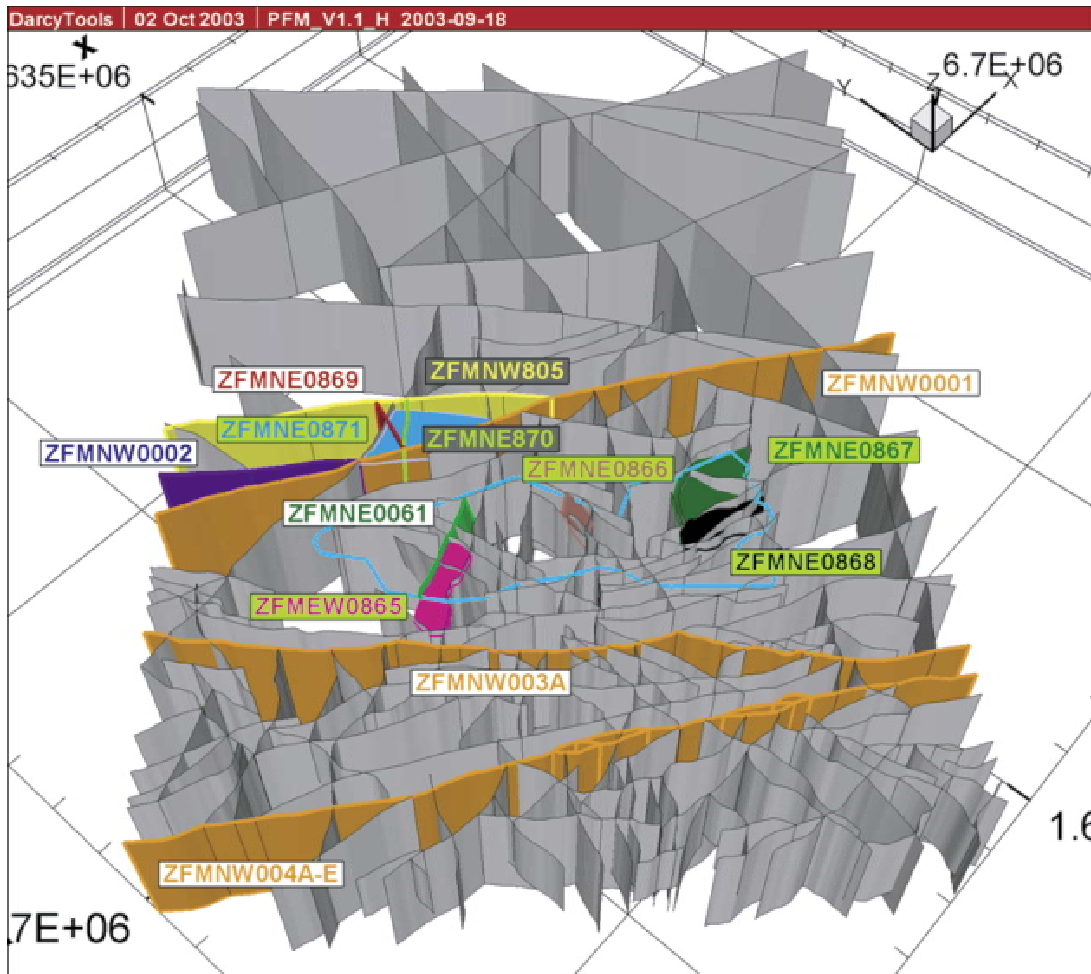


Figure 3-2. Regional deterministic fracture zones HCD1 (from Reference /6/). The coloured features are judged to have a high confidence of occurrence, whereas the grey features are judged to have a medium or low confidence of occurrence.

3.4 Model grid

The lateral boundaries of the model follow hydraulic boundaries, such as topographic surface water divides and major fracture zones. In addition, below the present sea level, the boundaries of the model also follow areas along which the sea floor has the lowest topographic elevation. The position of lateral boundaries of the model is presented in Figure 3-3, which also shows the topography of the modelled region. In general, the modelled area can be described as a low-lying coastal region, rising to the south-west to a maximum elevation of about 30 m above mean sea level, with the coastline running roughly north-west to south-east through the model. The deepest areas modelled offshore are along the north-eastern boundary of the model, where the maximum depth attained is -40 m below mean sea level.

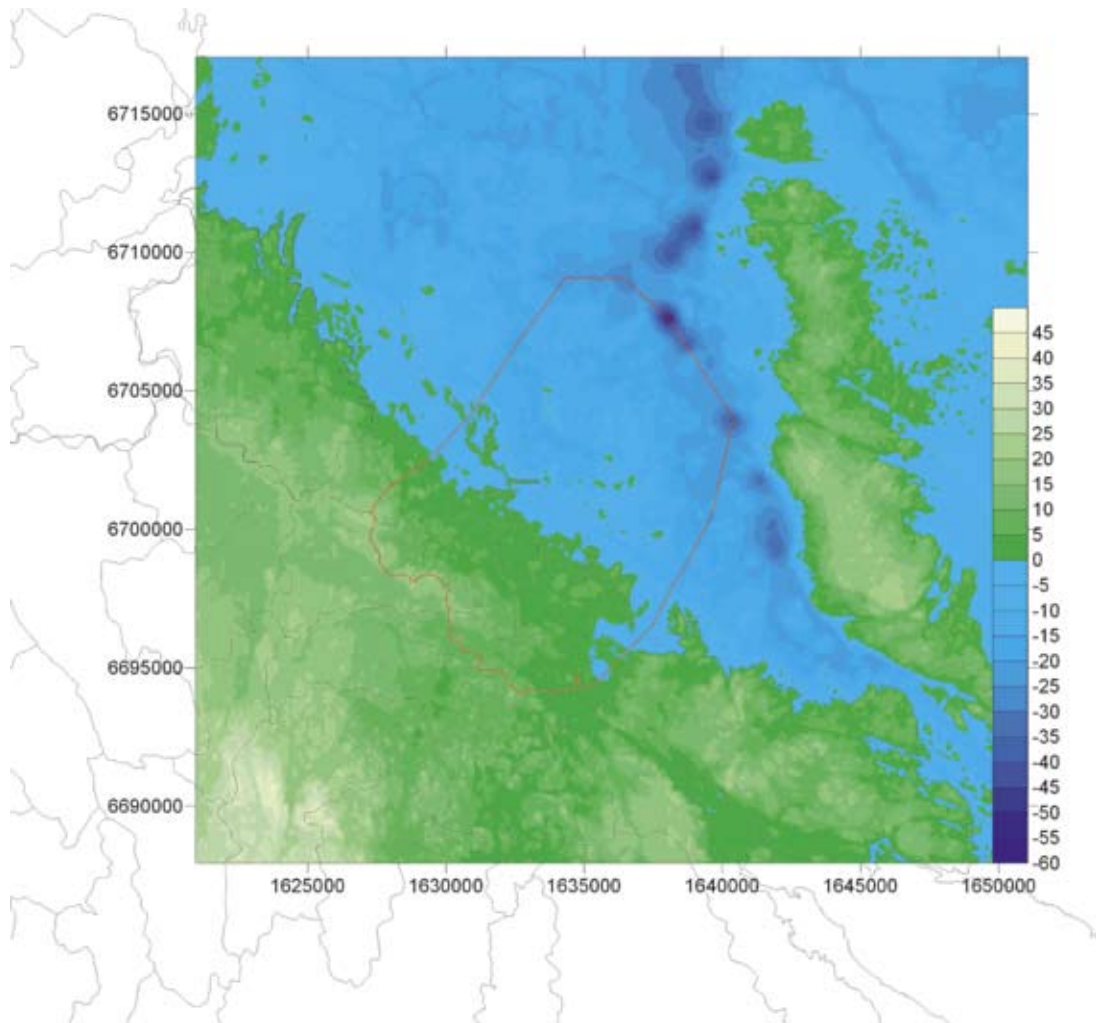


Figure 3-3. Topography (m above mean sea level), lateral boundary of model (red line) and water divides.

The surface of the Forsmark CPM model follows the topography, as shown in Figure 3-4. The different layers of elements follow the topographic undulation down to a depth of 400 m, after which the layers are horizontal. For all cases, the model extends down to a depth of 2,300 m. As defined in the task description, the size of the elements is 100x100x100 m, except at the top and base of the model, where a more refined vertical discretisation is used. The smallest vertical discretisation is 3 m at the top of the model to represent the quaternary cover.

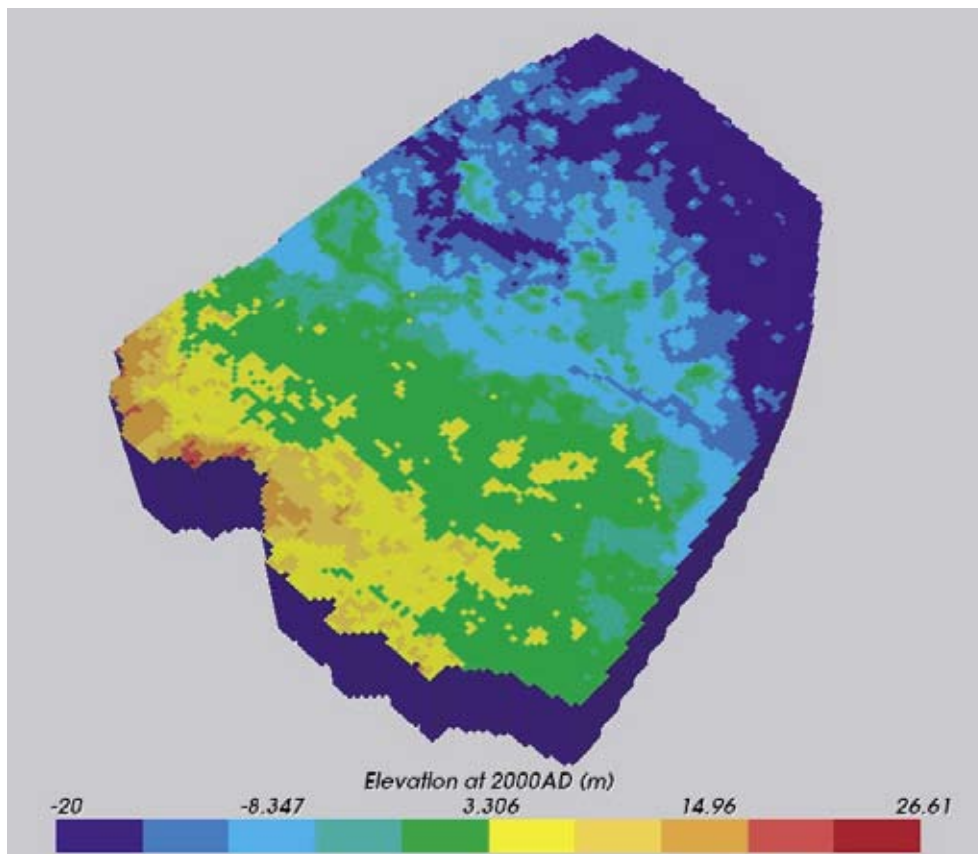


Figure 3-4. Surface elevation for the regional model.

3.5 Permeability upscaling

In order to parameterise the CPM model using the fracture data provided, it was necessary to build a regional-scale DFN model populated with stochastically-generated fractures, but that also included the identified deterministic features (Figure 3-2). The model representation of the latter is illustrated in Figure 3-5 (note the different model orientation compared with Figure 3-2).

The upscaling calculations were carried out for a rectangular region that was slightly larger than the regional-scale area shown within the model boundary in Figure 3-3. For these calculations, only the stochastically-generated fractures were included in the model; the deterministic features were superimposed on the CPM model later, before carrying out groundwater flow and transport calculations. For these latter calculations, the modelled region was the smaller area shown in Figure 3-3. The cells required for this reduced-volume model were selected from those within the upscaling model using a ‘nearest neighbour’ interpolation. This procedure ensures that individual cells are in the same location in each model and is equivalent to discarding those cells that fall outside the defined model boundary.

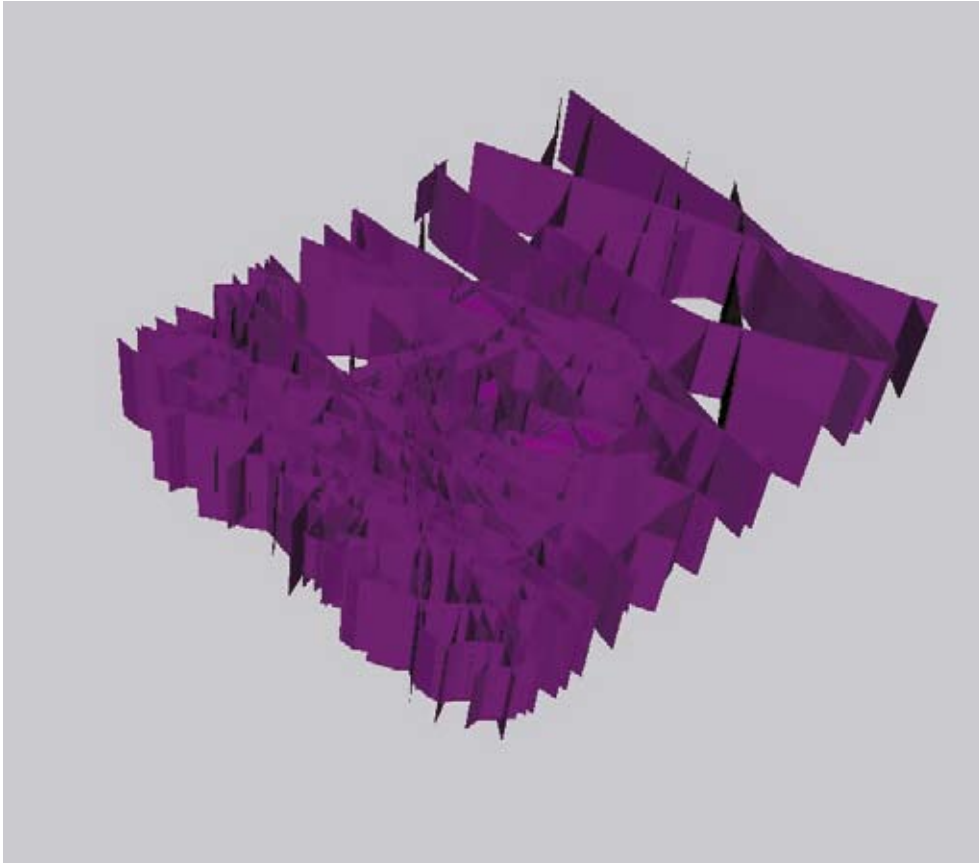


Figure 3-5. *Deterministic fracture zones defined for the Forsmark 1.1 structural model. (cf the geological model shown in Figure 3-2.)*

Representations of the stochastic DFN model, including the superimposed deterministic features, are given in Figure 3-6 and Figure 3-7. The former includes fractures with a length scale from 1,000 m down to 50 m, whereas the latter shows only the fractures with a length greater than 100 m. It is noticeable that the smaller fractures shown in Figure 3-6 also tend to be of relatively low transmissivity, hence the preponderance of blue-coloured fracture planes compared with Figure 3-7. However, as noted in Section 2, the smaller-scale fractures provide connectivity between the larger fractures and can be important in determining the overall value for upscaled permeability in a CPM model.

The horizontal sections shown in Figure 3-8 are taken from the model containing fractures in the length range 50 m to 1,000 m (Figure 3-6). The sections are at depths of -100 m, -400 m and $-1,000$ m, the second of these being at the proposed repository depth. The repository footprint has been superimposed on each of the sections to illustrate the different fracture intensities at each depth. As can be seen, the fracture intensity, and hence connectivity, reduces significantly in the deeper fractured rock below $z = -500$ m.

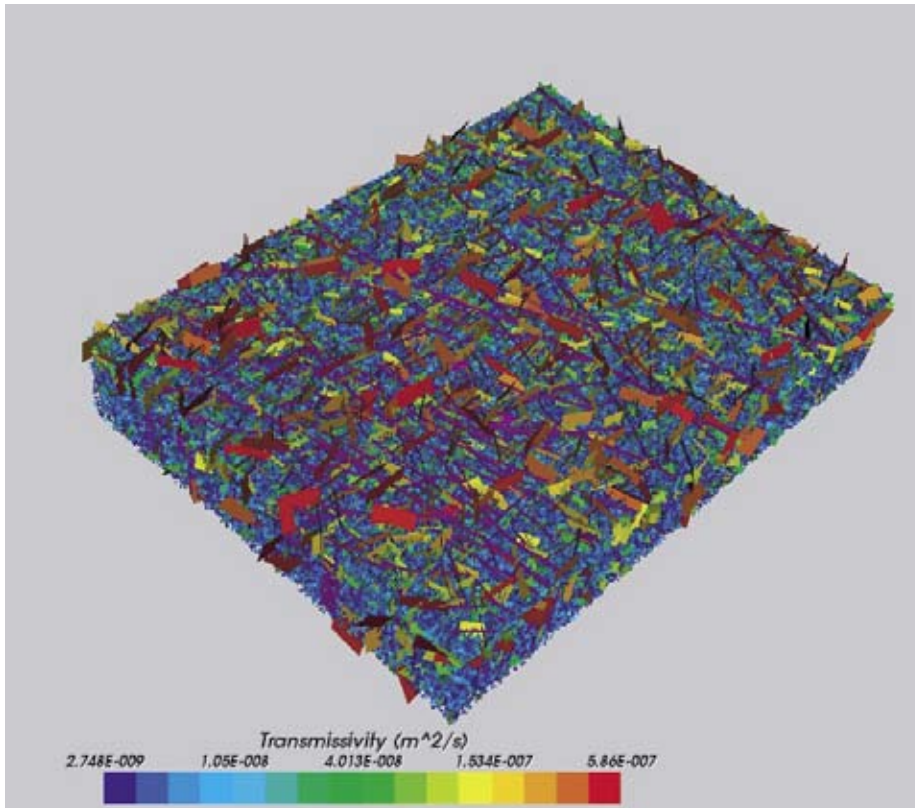


Figure 3-6. The stochastic DFN model for the regional model of fracture lengths between 50–1,000 m with the deterministic zones superimposed.

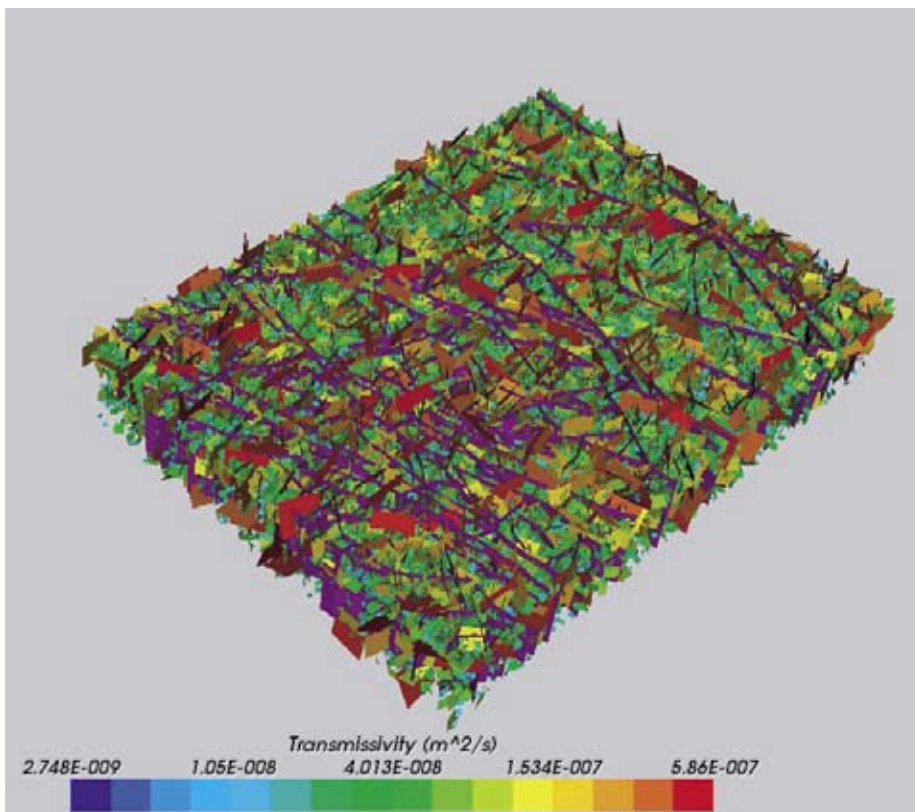


Figure 3-7. The stochastic DFN model for the regional model showing only fractures with lengths between 100–1,000 m with the deterministic zones superimposed.

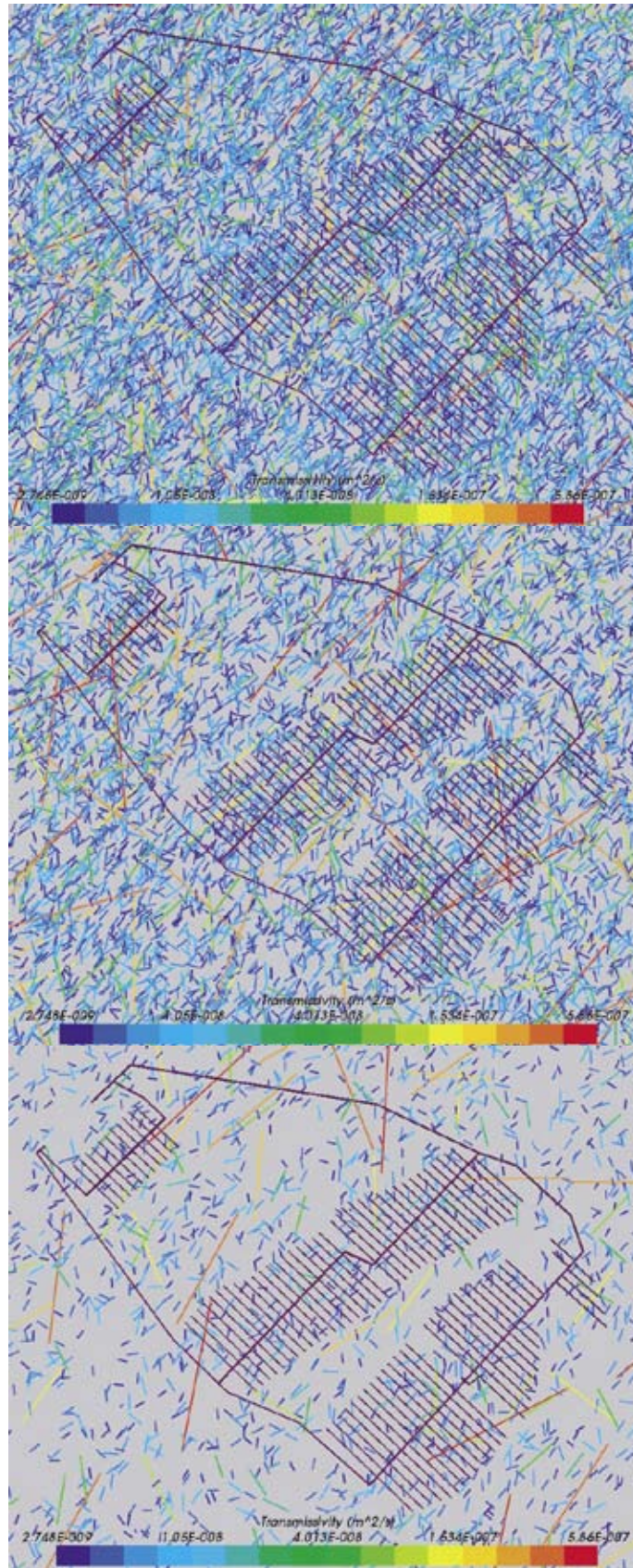


Figure 3-8. Horizontal slice through the regional DFN model for fractures lengths between 50–1,000 m for $z = -100$ m (top), $z = -400$ m (middle), and $z = -1,000$ m (bottom). The repository footprint is superimposed on each slice for illustration.

The effect of this depth dependency is reflected in the upscaled vertical permeabilities, k_{33}^1 , calculated for the CPM model (Figure 3-9). The top surface of the model shows elements with vertical permeability almost exclusively in the range 10^{-15} to 10^{-17} m² (red to green coloration). However, inspection of the vertical model boundaries reveals a decreasing likelihood of elements having a k_{33} value at the upper end of this range as the element depth increases, and an increasing likelihood that the k_{33} value will lie in the range 10^{-17} to 10^{-19} m² (green to blue coloration). This observation is also clear in the cross sections at -400 m and -1,000 m presented in Figure 3-10. (Note that the permeability range for the latter figure extends to 10^{-14} m² at the upper limit.)

The correlation between the derived CPM vertical permeability and the presence of the larger fractures is illustrated in Figure 3-11. The upper plot shows the upscaled k_{33} value for a section of the grid (composed of 100 m blocks). The lower plot depicts the same information but with the larger fractures from the corresponding DFN model superimposed. Together the data show how the presence of the larger fractures correlates with the presence of higher k_{33} values.

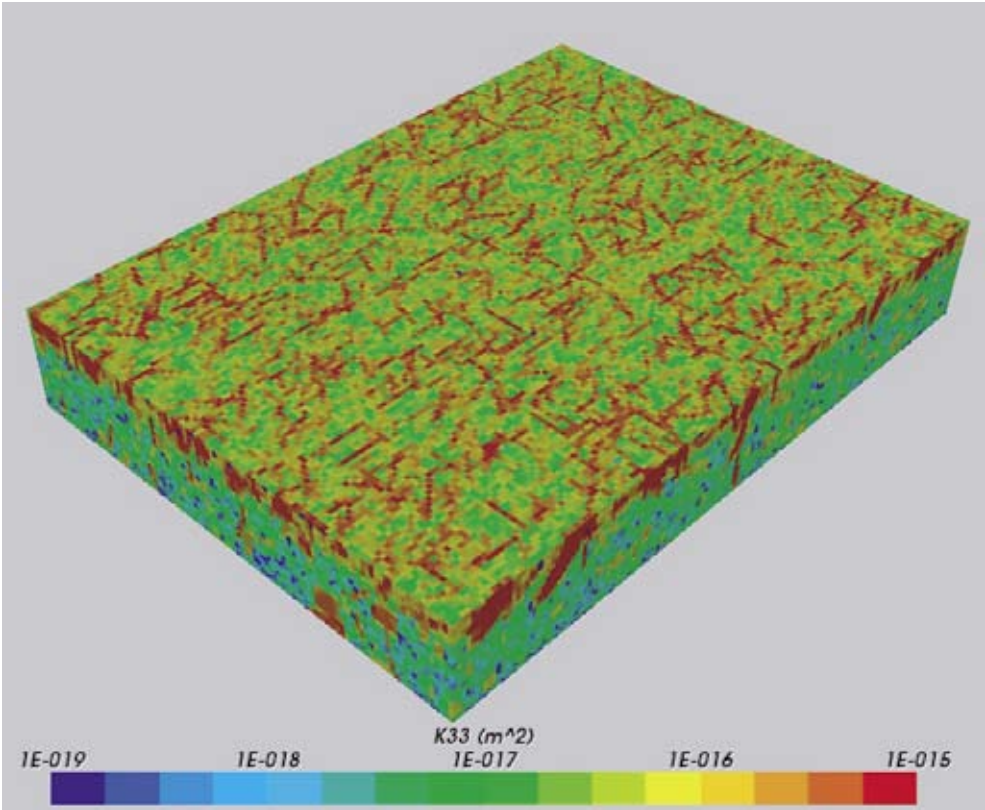


Figure 3-9. The distribution of vertical permeability k_{33} for the regional model based on upscaling the stochastic DFN model.

¹ The vertical permeability is referred to as either k_{33} or k_{zz} in this report.

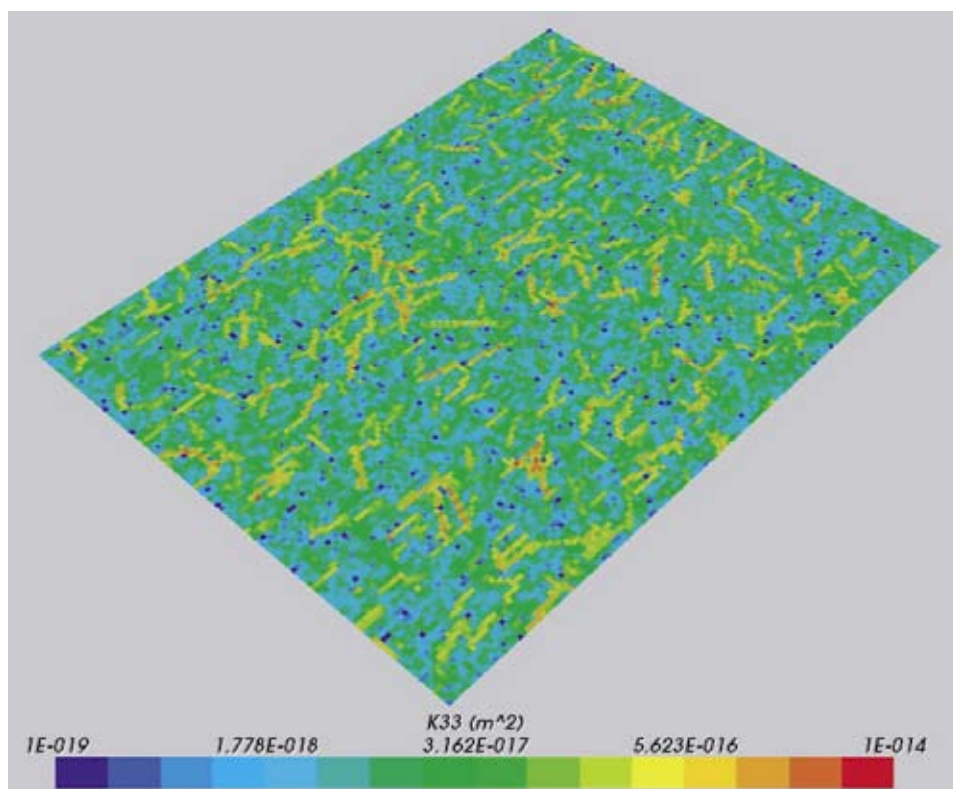
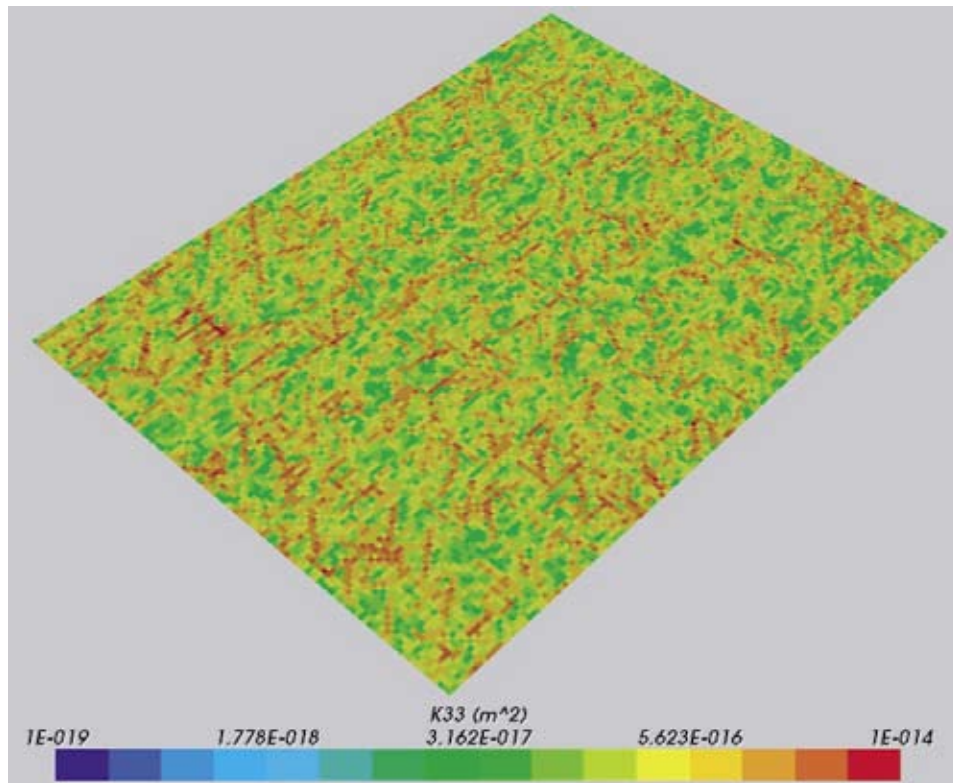


Figure 3-10. The distribution of vertical permeability k_{33} for the regional model based on upscaling the stochastic DFN model for a horizontal slice at $z = -400$ m (top), $z = -1,000$ m (bottom).

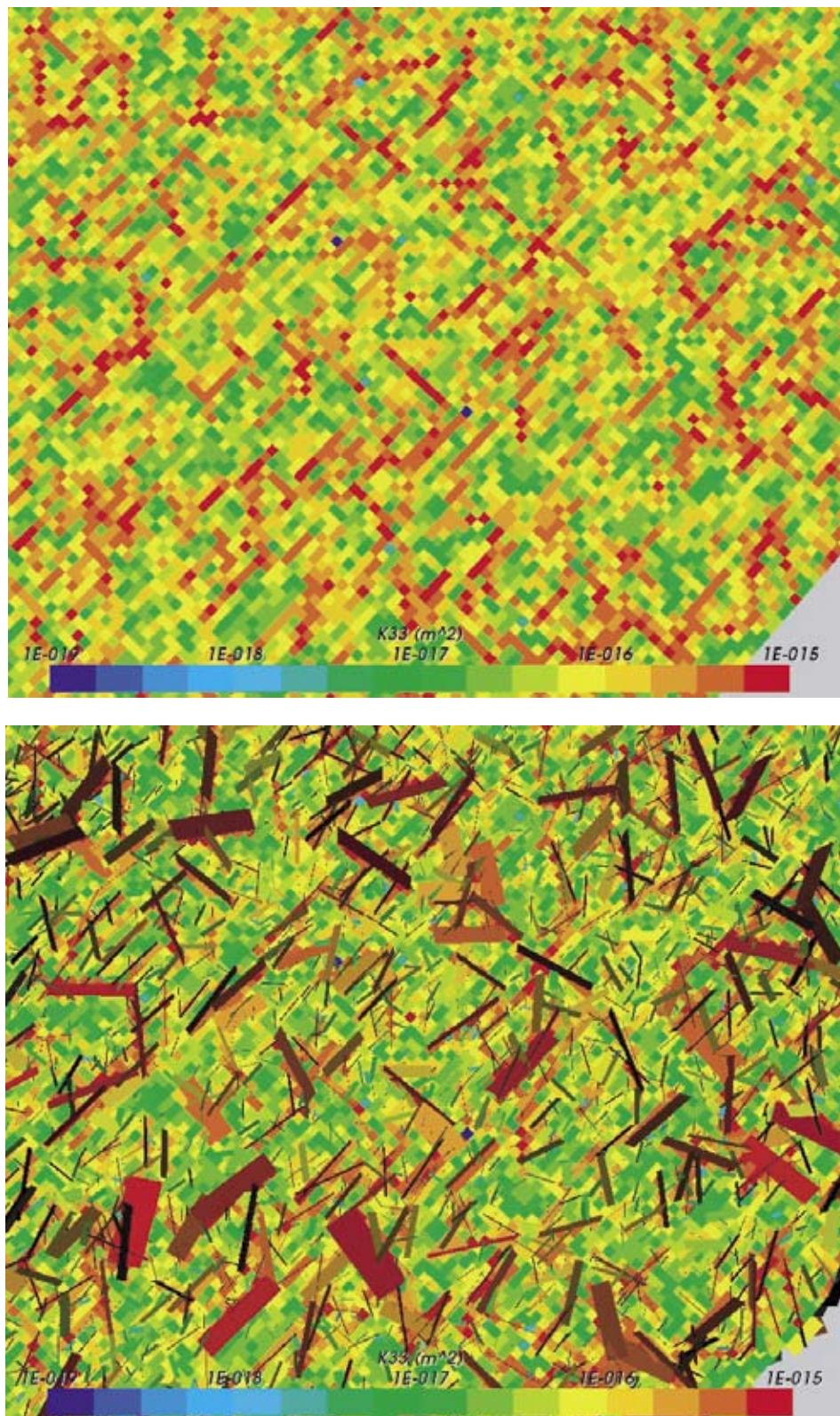


Figure 3-11. An illustration of the DFN derived regional permeability (vertical component k_{33}) showing the permeability on the 100 m grid (top), and the permeability with the DFN superimposed (bottom).

3.6 CPM model: groundwater flow and particle tracking

3.6.1 Grid modification

Having calculated the upscaled permeabilities for the CPM model based on the stochastic DFN model, the grid was modified to that required for the groundwater flow and transport calculations. This transformation consisted of three stages:

1. Reduction to the correct areal extent (i.e. the boundary shown in Figure 3-3) by selection of the cells that lie within the defined regional model boundary;
2. Superposition of the effects of the regional-scale deterministic fracture zones (Figure 3-5) on the permeabilities of the cells in the model;
3. Introduction of a 3 m thick layer of homogeneous Quaternary deposits over the entire model, and a further 10 m layer below that. Each of these layers has a higher conductivity than the fractured rock beneath.

The effects of the transformation are shown in Figure 3-12, which depicts the vertical permeability component (k_{zz}) for the CPM model cells. The boundary is now seen to be irregular, matching the definition shown in Figure 3-3. The uniform top surface permeability reflects the high value associated with the Quaternary deposits ($1.5 \cdot 10^{-12} \text{ m}^2$), with a 10 m layer of permeability $2.0 \cdot 10^{-14} \text{ m}^2$ below that. The vertical boundaries show high permeability structures penetrating the full depth of the model, these being the deterministic features identified in Reference /6/ and shown in DFN form in Figure 3-5. Figure 3-13 and Figure 3-14 illustrate how the CPM vertical permeability components for cells near the surface (but below the Quaternary deposits) and at a depth of $z = -1,000 \text{ m}$ correlate with the positions of the deterministic features.

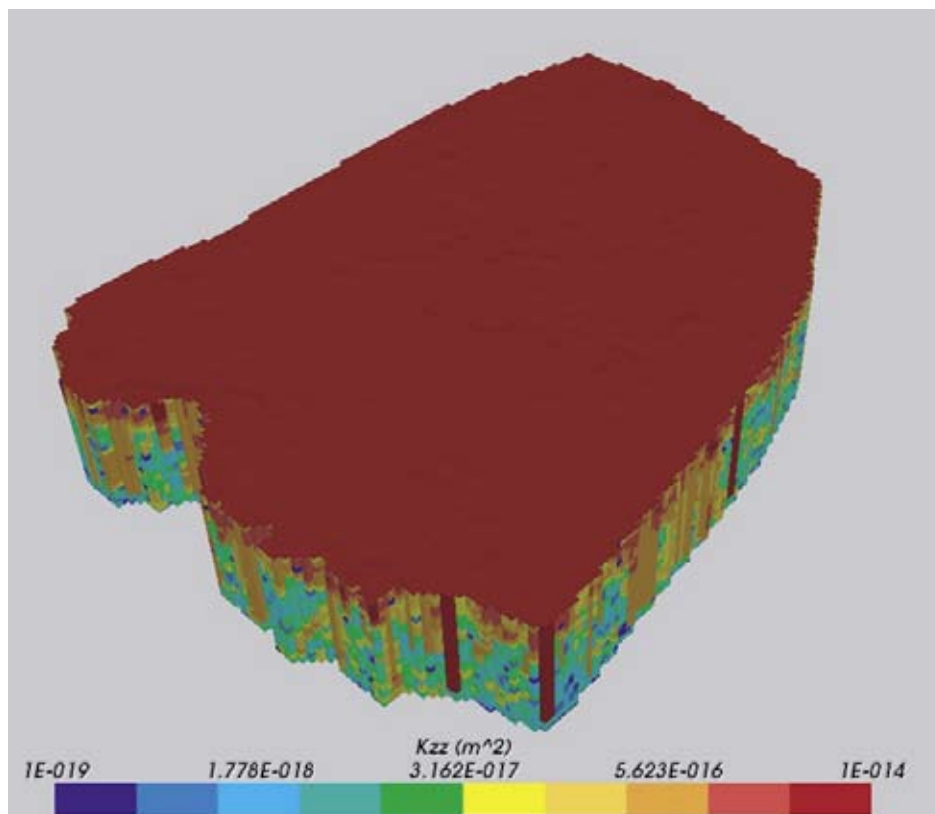


Figure 3-12. Distribution of permeability (vertical component k_{zz}) in the regional model. A 3 m layer of Quaternary deposits on top has a permeability of $1.5 \cdot 10^{-12} \text{ m}^2$.

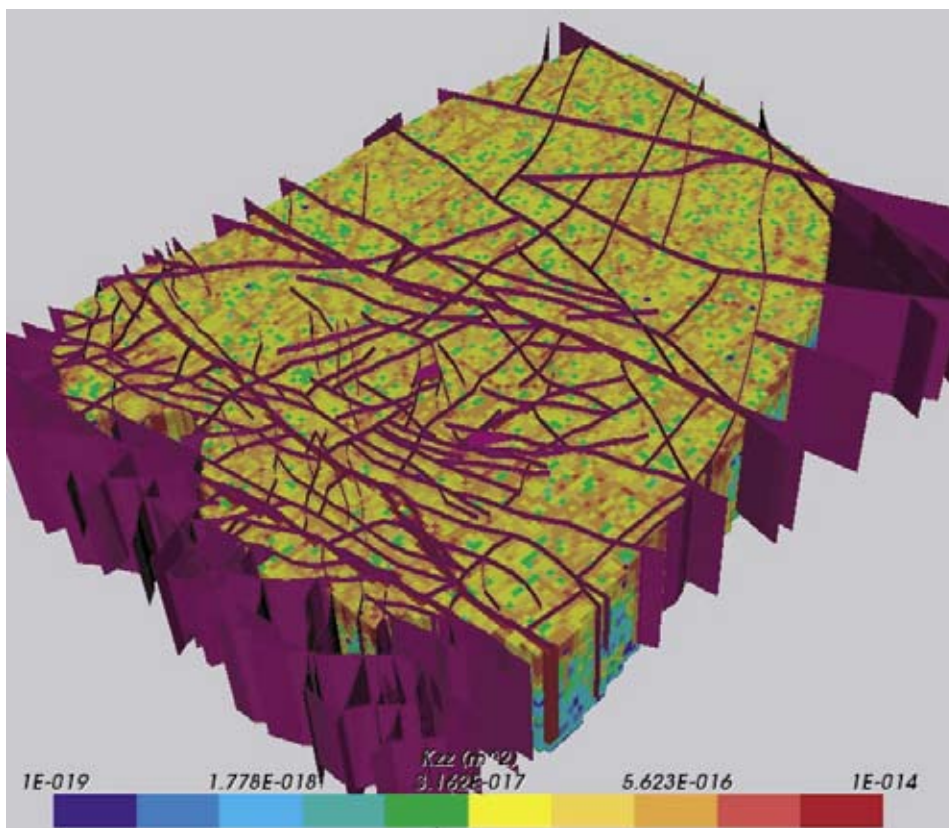
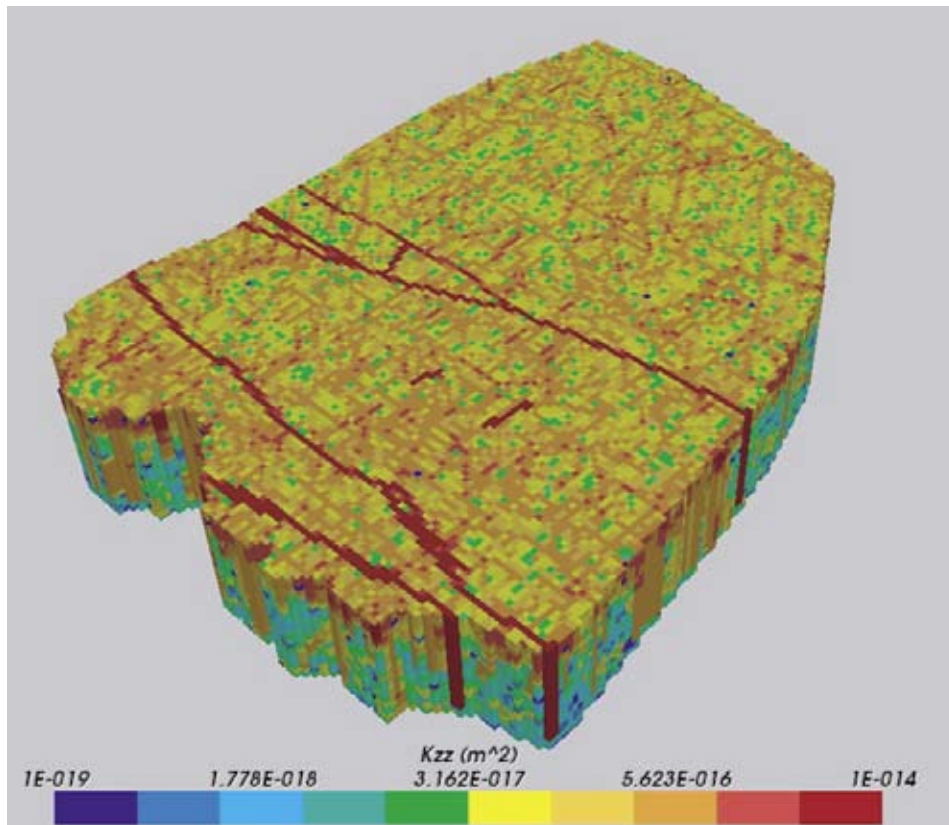


Figure 3-13. Distribution of permeability (vertical component k_{zz}) in the regional model with the top 2 layers removed. The distribution of permeability (top), and the same plot with the deterministic fracture zones superimposed (bottom).

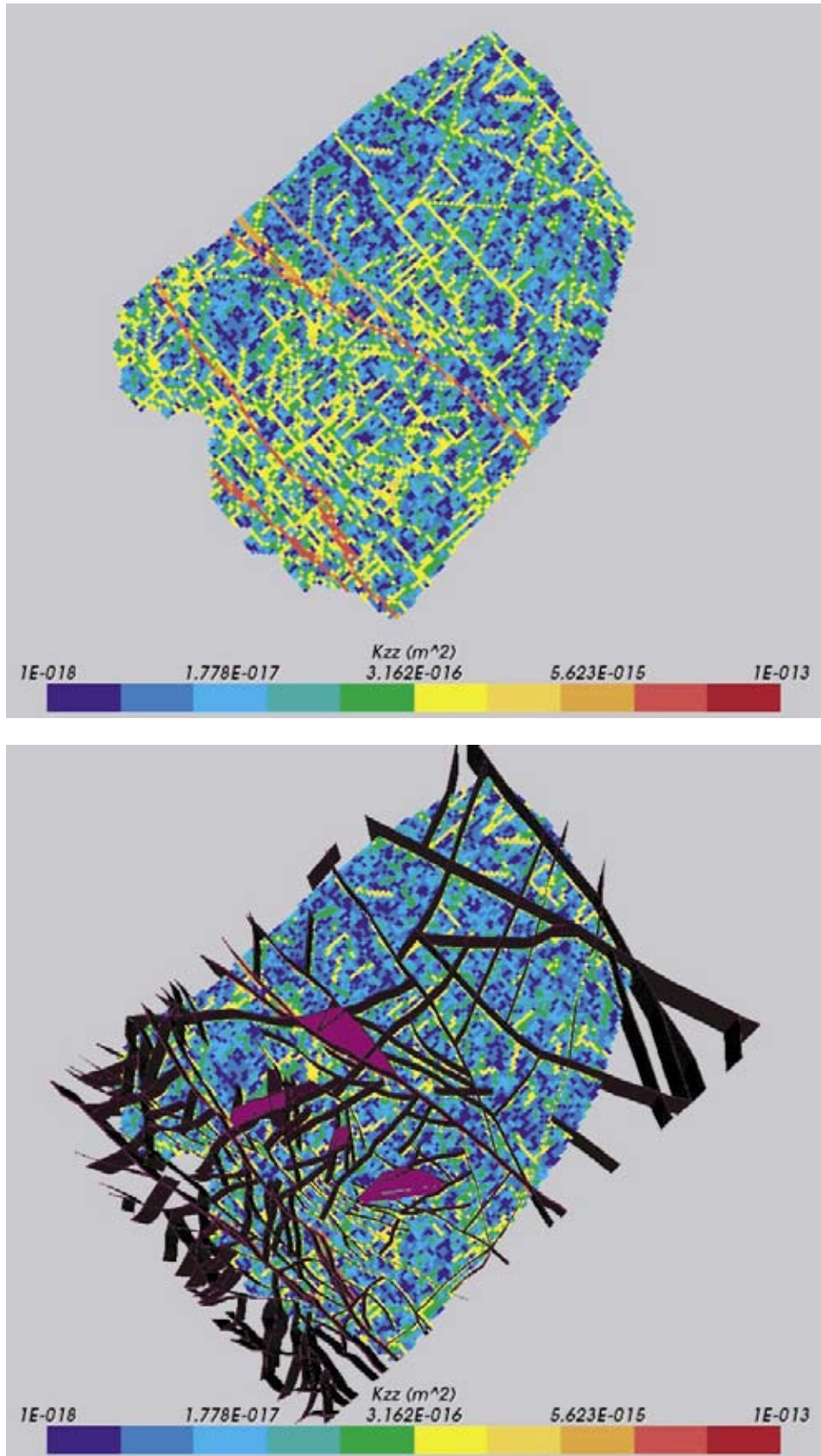


Figure 3-14. Distribution of permeability (vertical component k_{zz}) in the regional model at $z = -1,000$ m. The distribution of permeability (top), and the same plot with the deterministic fracture zones superimposed (bottom).

3.6.2 Boundary conditions

(a) Outer vertical boundary – lateral boundaries

The outer vertical boundary of the model (lateral boundaries) coincides with various important hydrogeological structures, such as (i) water divides on-shore, (ii) major fracture zones of the domain located offshore or (iii) deep sections of the domain located offshore (by offshore we mean offshore at present, 2,000 AD). The lateral boundaries of the model are illustrated in Figure 3-3.

It is assumed that the structures used as the lateral model boundaries are also boundaries for the groundwater flow; accordingly, in the model, the lateral boundaries are defined as no-flow boundaries such that no groundwater flow (or surface water flow) can pass these boundaries.

This assumption is based on the observations that:

- (i) Surface water divides are along significant topographic ridges and it is not likely that large amounts of groundwater will flow across a significant topographic ridge.
- (ii) Regional fracture zones are used as lateral boundaries in the model below the present sea; these zones are along low lying parts of the topography (including the sub-sea topography), and as such are important discharge areas. It is not likely that large amounts of groundwater will flow across a significant discharge area.
- (iii) A regional valley is an important discharge area for groundwater, and it is not likely that large amounts of groundwater will flow across a significant discharge area.

Nevertheless, it is possible that in reality some groundwater flow may take place across the surfaces that are defined as the model's lateral boundaries. It is, however, likely that such flows are very small.

(b) Boundary at base of model

The base level of the model is defined at a certain depth below the ground surface. The model extends to a depth of 2,300 m. The fracture zones extend down to a depth of 2,100 m. Along the base of the model, the model is assigned a no-flow boundary condition, with a specified salinity. The specified salinity is set to 10% (salt mass fraction). No groundwater can flow across this boundary, but salinity may cross by diffusion. The salinity along the base of the model is the highest salinity level in the model.

(c) Boundary condition along the top of the model

Two different boundary conditions have been used along the top of the model, one for regions below the sea and the other for areas of dry land.

Below the sea

A specified pressure condition is used below the sea, representing the elevation of the sea water surface. The specified pressure condition is of atmospheric pressure at the sea surface, which will produce a varying pressure along the sea floor dependent on the varying sea-bed topography.

A specified salinity condition is also used below the sea. If inflow of seawater to the groundwater system takes place along the sea floor, the salinity of this water corresponds to

that of the Baltic Sea. In the model, the salinity of the Baltic Sea varies with time according to an assumed salinity evolution. Discharge of groundwater may take place along the sea floor; the salinity of such groundwater may vary according to the distribution in the model, which will vary with time. Therefore, no specified salinity is assigned to the discharge.

Above the sea

A specified pressure condition is used above the coastline, representing the varying elevation of the topography. The specified pressure condition is of atmospheric pressure at ground surface.

A specified salinity condition is also used above the coastline. If groundwater recharge takes place, the inflowing water carries zero salinity, i.e. above the coastline, freshwater will recharge the model. Where discharge of groundwater occurs, the salinity may vary according to the distribution in the model.

Note that the boundary condition along the model's top boundary changes with the coastline evolution (moving sea water level). Between 8,000 BC and approximately 1,000 BC, the whole of the model will be below the sea, at 2,000 AD, approximately one third of the model will be above the sea, and at 12,000 AD the whole top surface of the model is above sea-level.

3.6.3 Pressure and salt transport calculations

The CPM model was used to calculate groundwater flows based on the boundary conditions described above, and assuming fully saturated conditions. Figure 3-15 shows the regional distribution of residual pressure² for current (2,000 AD) conditions. Two observations about these results are worth recording. Firstly, it is clear from the distribution of residual pressure on the top surface, that the driving gradient is from the higher land at the south-western model boundary north-east towards the coast and the Baltic Sea. This is as would be expected given the topography of the area.

The second observation is that the residual pressure increases with depth, as can be seen from the vertical boundaries. However, this does not necessarily mean that the driving forces are creating an upward flow throughout the model. The main reason for the increasing residual pressure with depth is that the groundwater salinity (and hence density) increases with depth, as shown in Figure 3-16, but the calculation of residual pressure assumes a constant density water column. The salt mass fraction (density) distribution shown in the figure clearly illustrates the presence of fresh water near land surface and slightly saline water beneath the Baltic. The imposed salinity boundary conditions then produce an increasing salt mass fraction with depth, up to 10% at the bottom boundary. (Note that the scale for Figure 3-16 is a gradation between the minimum and maximum in the model, and does not show the actual salt mass fraction.)

² Residual pressure is defined as the total pressure at a point minus the pressure that would be exerted by a column of fresh water from that point up to the water table.

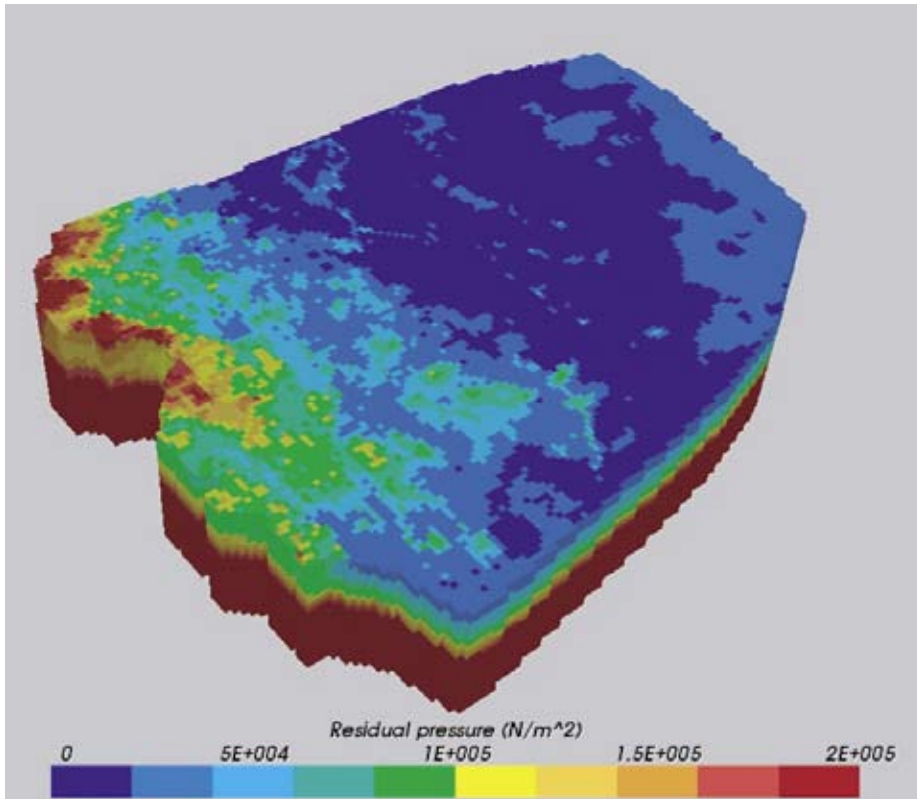


Figure 3-15. Distribution of residual pressure in the CPM model at 2,000 AD.

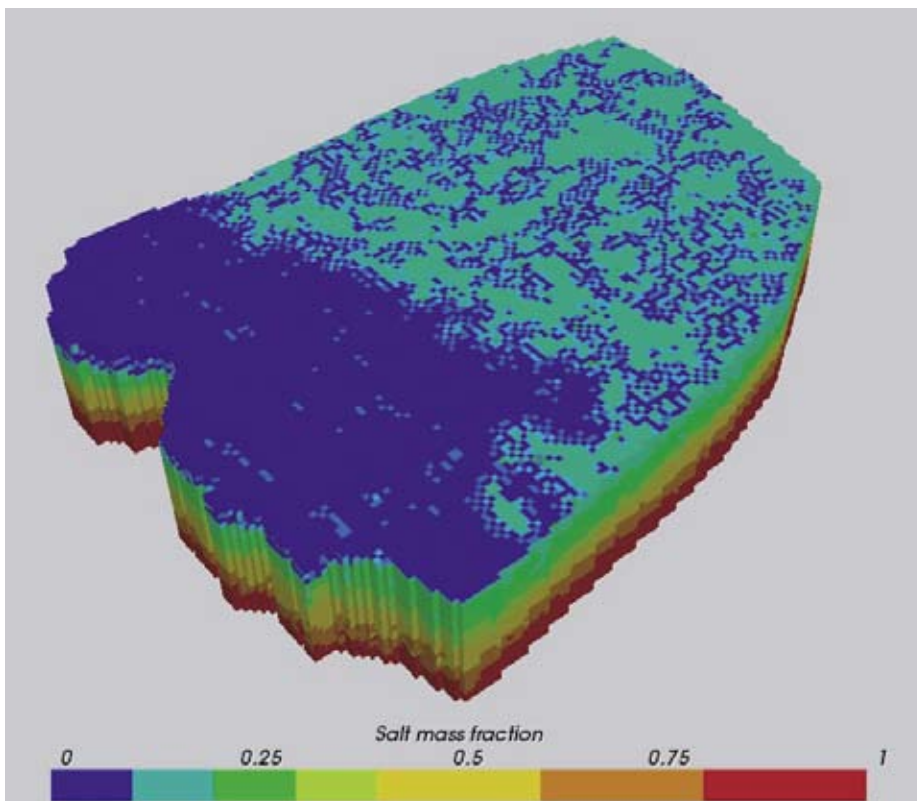


Figure 3-16. Distribution of salt mass fraction in the CPM model at 2,000 AD.

A more meaningful picture of the driving forces in the system can be obtained by plotting the environmental pressure³ instead of the residual pressure, which then takes account of the variable density in the model. The equivalent plot for environmental pressure (see Equation 3-1) is shown in Figure 3-17. Again, this figure indicates that the main driving head in the system originates from the higher land to the south-west of the model and is generating flows down-gradient to the north-east, i.e. towards the Baltic. However, unlike Figure 3-15, the distribution of environmental pressure with depth shows that the driving head at all depths is greatest in the south-west and decreases towards the north-east. Therefore, it is clear that the predominant driving force is not upwards but seawards at all depths.

Closer inspection of Figure 3-17 indicates that the steepest pressure gradients occur in the extreme south-west corner of the model where the topography changes most rapidly. Over much of the model, the preponderance of blue shading indicates relatively low gradients for driving flow. Given this distribution, it would be expected that the groundwater fluxes would be largest in the south-west corner of the model, decreasing to both the south-east and north-east.

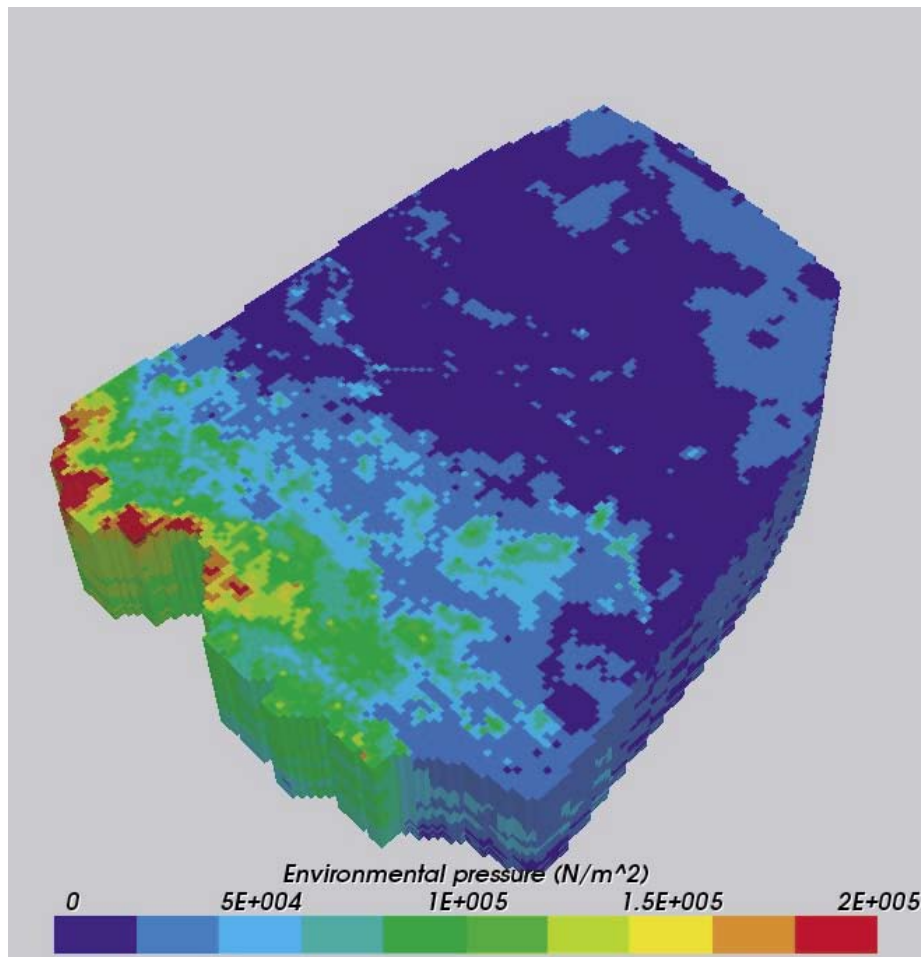


Figure 3-17. Distribution of environmental pressure in the CPM model at 2,000 AD.

³ Environmental pressure is defined as the total pressure at a point minus the pressure exerted by a variable-density water column from that point up to the water table.

It is also evident from Figure 3-17 that, although the overall head gradient is from south-west to north-east, there will be some local variations in flow direction. For example, the islands in the Baltic are local high points topographically, and therefore generate pressure gradients in all directions (approximately radially). Also, along the southern boundary of the model, the lakes form local lows in the topography and will therefore act as groundwater discharge locations for local flows.

The future evolution of the pressure (and hence flow) distribution was investigated by rerunning the CPM model using appropriate boundary conditions, i.e. moving the coastline further to the north-east and modifying the top surface boundary conditions accordingly. Two future times were simulated in the nested model, these being 2,500 AD and 12,000 AD, but plots for 7,000 AD were also produced from the CPM model. The environmental pressure plots at these three future times are shown in Figure 3-18, Figure 3-19 and Figure 3-20.

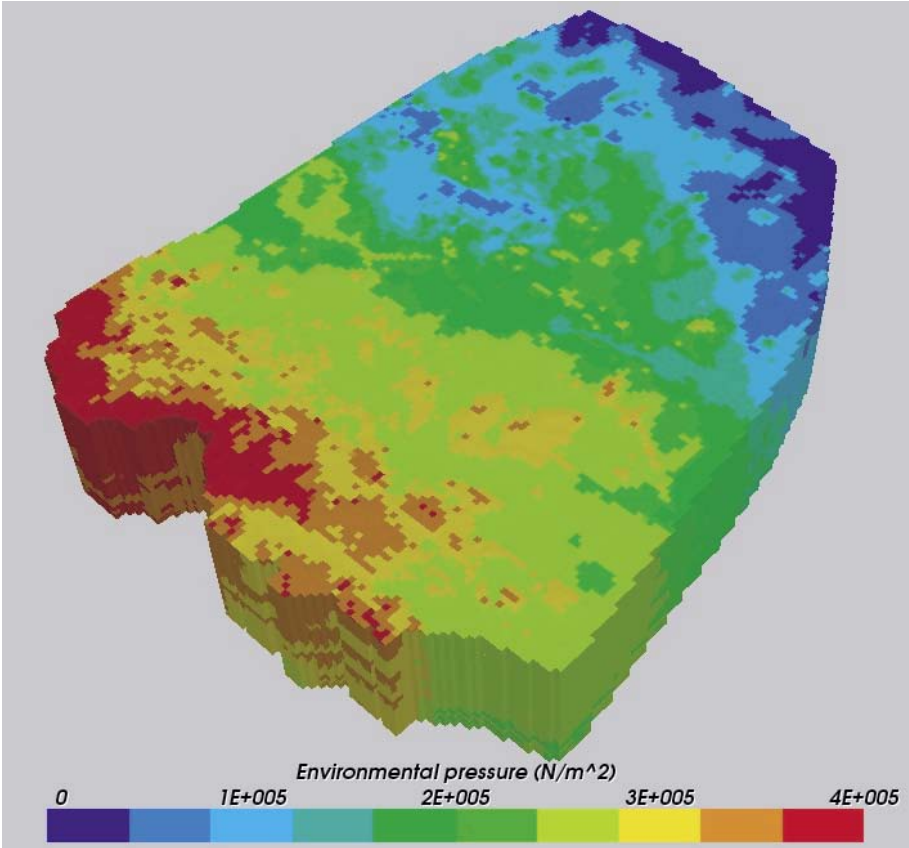


Figure 3-18. Distribution of environmental pressure in the CPM model at 2,500 AD.

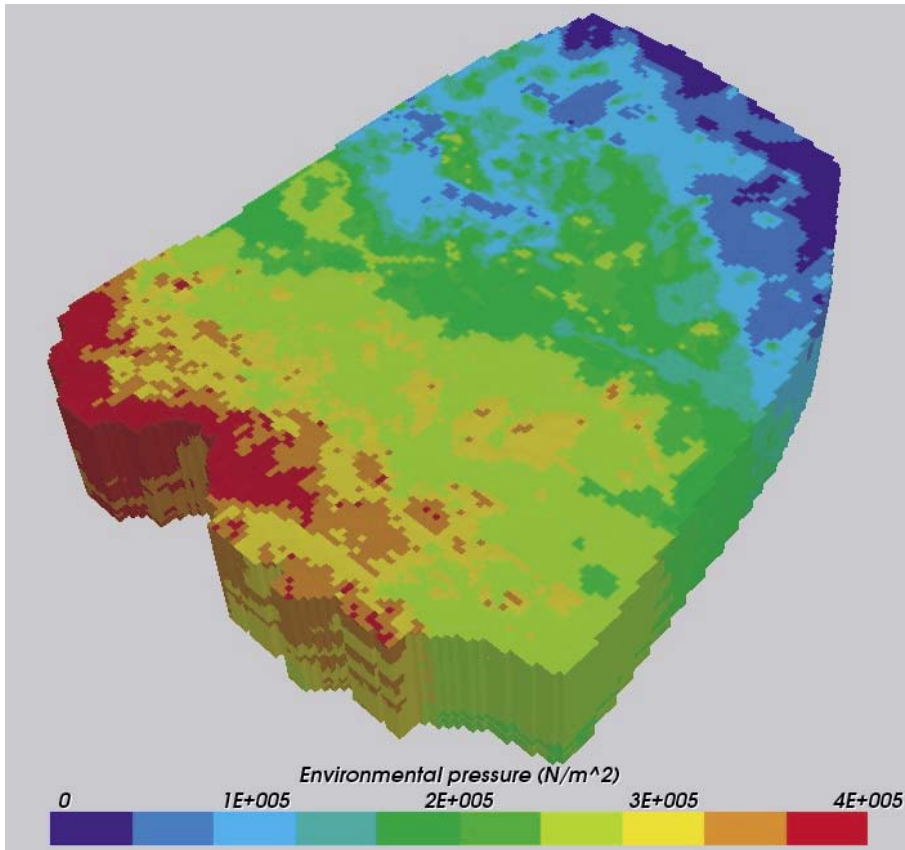


Figure 3-19. Distribution of environmental pressure in the CPM model at 7,000 AD.

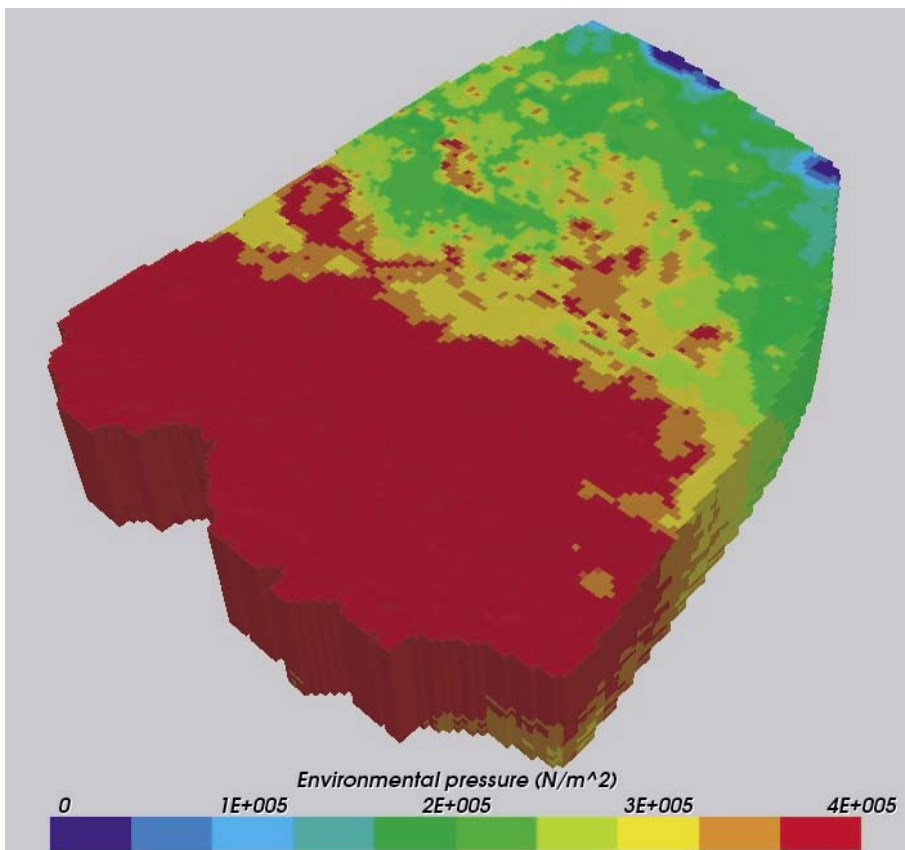


Figure 3-20. Distribution of environmental pressure in the CPM model at 12,000 AD.

The overall picture from these three figures is one of increasing environmental pressure in the southern half of the model, even though the topography has not been modified. The reason for this is that the datum for elevations is mean sea level, so that, as the sea level drops and the coast recedes north-eastwards, the high land becomes higher relative to the datum. It is clear from the figures, though, that the general pressure gradient remains from south-west to north-east throughout the modelled timeframe.

The other effect produced by the receding coastline is an increase in the area over which freshwater recharge can occur to the groundwater system. This results in salinity being flushed out of the rocks over time, an effect that can be seen in Figure 3-21, Figure 3-22 and Figure 3-23 for times of 2,500 AD, 7,000 AD and 12,000 AD respectively. These figures show the salt mass fraction plotted on 4 vertical slices through the model domain. The effect of freshwater flushing is particularly noticeable when comparing Figure 3-21 (2,500 AD) with Figure 3-22 (7,000 AD), with substantial flushing evident over the entire model area and to a significant depth in the latter. Because the salinity boundary condition on the base of the model does not vary with time, the ingress of fresh water at the surface results in increased vertical salinity gradients for the later plots.

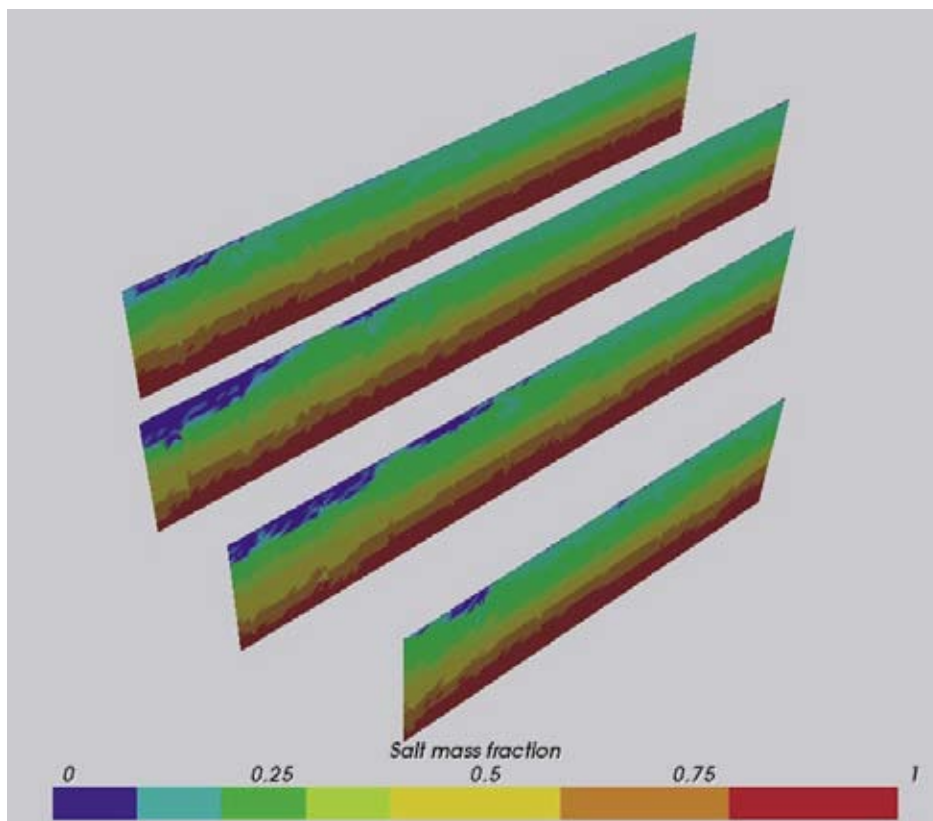


Figure 3-21. Salt mass fraction on 4 vertical slices in the CPM model at 2,500 AD.

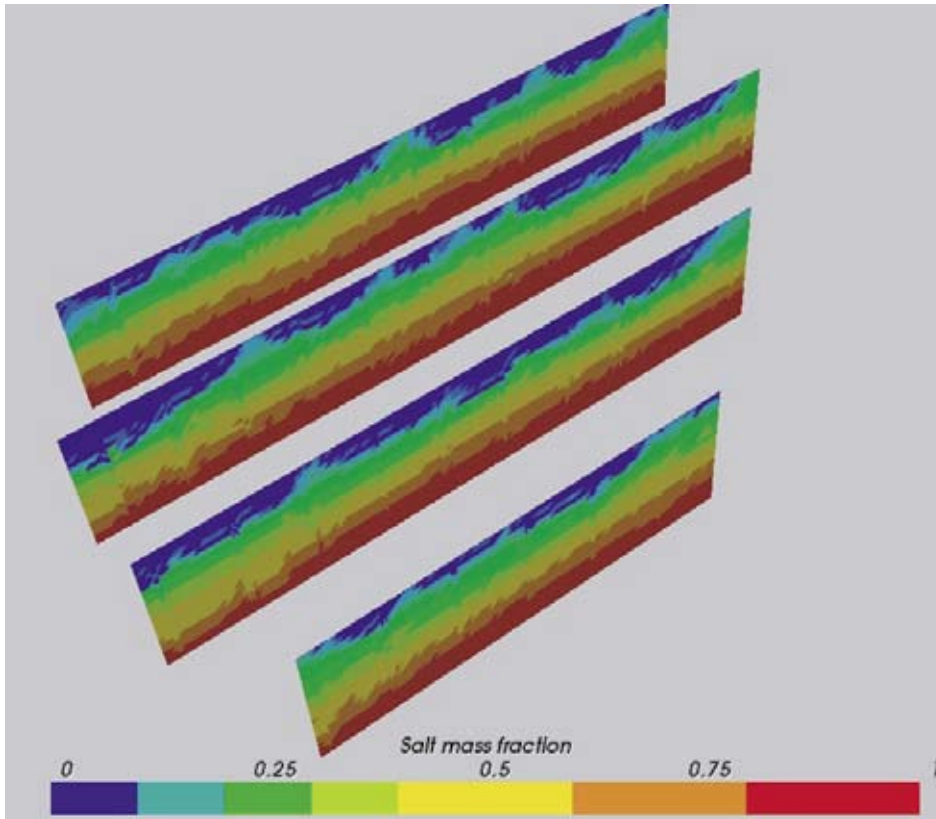


Figure 3-22. Salt mass fraction on 4 vertical slices in the CPM model at 7,000 AD.

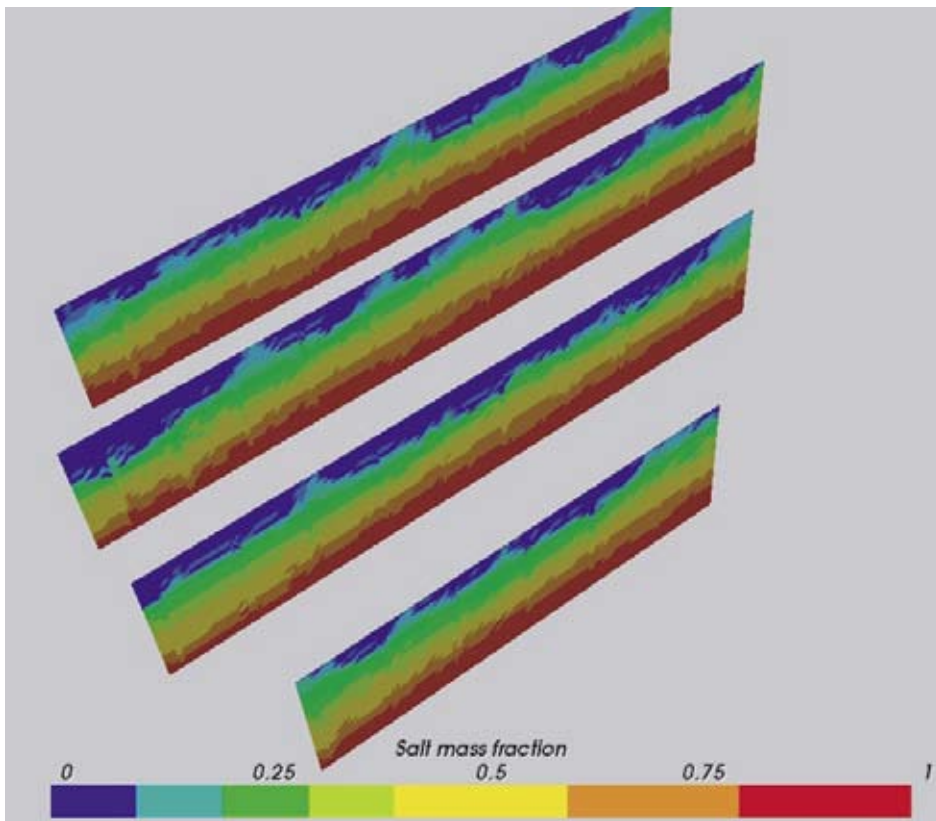


Figure 3-23. Salt mass fraction on 4 vertical slices in the CPM model at 12,000 AD.

The figures presented so far have concentrated on the regional-scale pressure and salt distributions in order to give an overview of the evolution of the groundwater system as a whole. However, within the regional CPM model, it is possible to focus on the repository zone as the specific area of interest.

Figure 3-24 illustrates the distribution of environmental pressure at repository depth at times of 2,500 AD and 12,000 AD. The repository structure is depicted to aid interpretation of the plots. In common with the regional-scale plots, these local figures show an increase in the absolute magnitude of the environmental pressure. However, it is clear from the scale maximum and minimum for the two plots in Figure 3-24 that the overall pressure gradient across the repository is similar in both. However, changes can be detected; for example, the environmental pressures in the north-western and central parts of the repository are relatively lower at the later time (in particular, between the two sets of tunnels in the southern part of the repository), whereas the pressure to the south-east of the repository is relatively higher. From these changes it can be inferred that flows along the length of the repository tunnels will be higher at 12,000 AD than at 2,500 AD, because the gradient is more aligned with the tunnel structure.

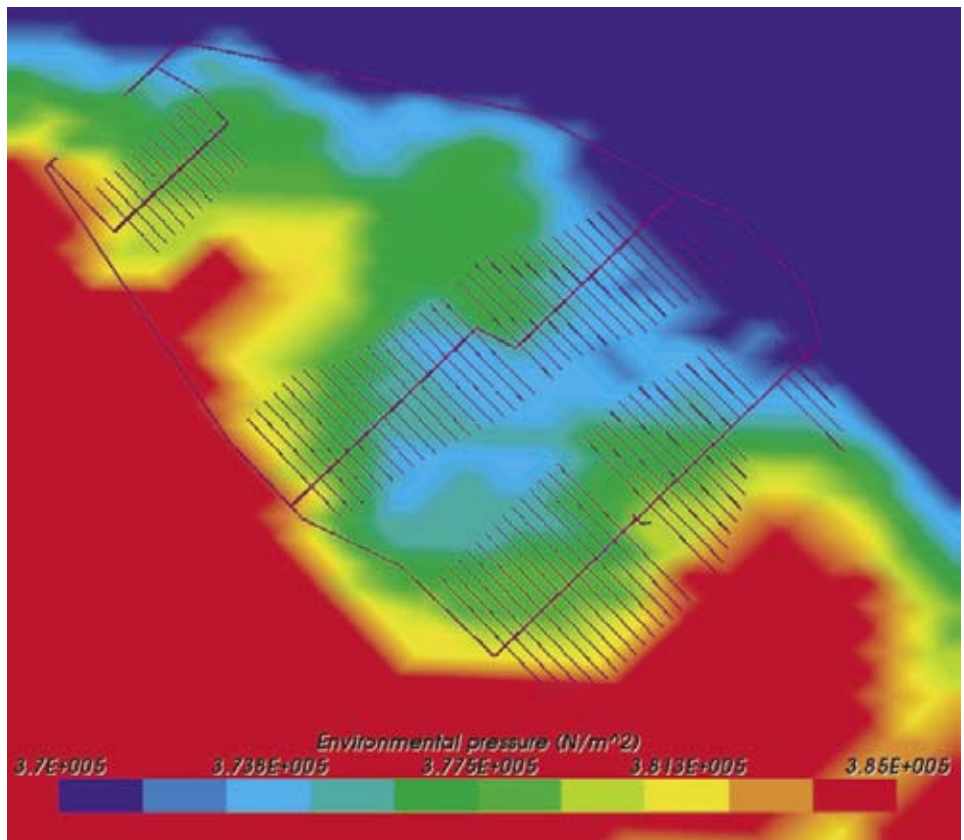
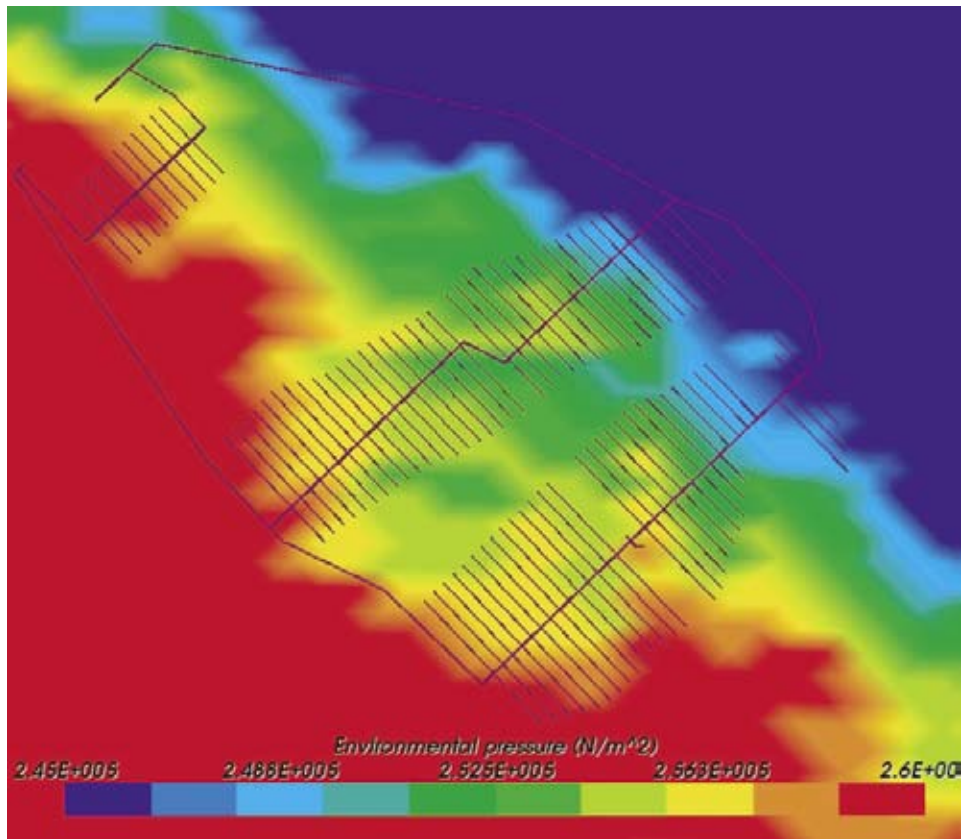


Figure 3-24. Distribution of environmental pressure in the CPM model near the repository at 2,500 AD (top) and 12,000 AD (bottom).

3.6.4 Particle tracking

Having determined the driving heads for flows at a number of representative times during the evolution of the Forsmark site, it is possible to undertake particle tracking calculations for the CPM model. In order to demonstrate the methodology, a sample of 604 canister locations was used for the starting points for released particles. These locations were within the south-eastern sector of the repository, as shown in Figure 3-25.

The particles were released into the flow field calculated for 2,500 AD and tracked to the model boundaries. The exit points for the particles and the complete pathlines from repository to boundary are shown in Figure 3-26 and Figure 3-27, respectively. The exit point plot (Figure 3-26) shows that, although there is some linear clustering of exit points along high permeability features, there is also quite a wide area over which the pathlines discharge. There is also a significant range of travel times from release to discharge for the 604 paths, from approximately 1,000 years up to around 100,000 years, as shown in Figure 3-27.

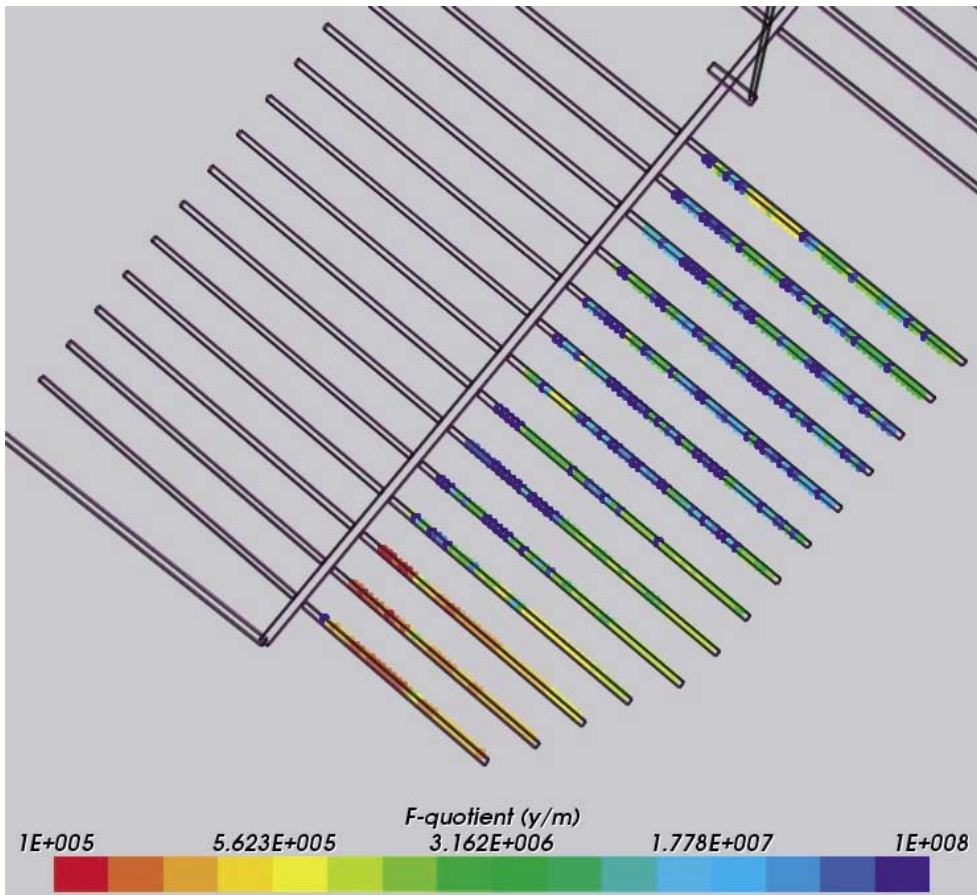


Figure 3-25. Start locations for particle tracks in the CPM model for the south-east corner of the repository. Here, the 604 canister locations are coloured by the total F-quotient for pathlines in the CPM model and tracked through the flow-field at 2,500 AD.

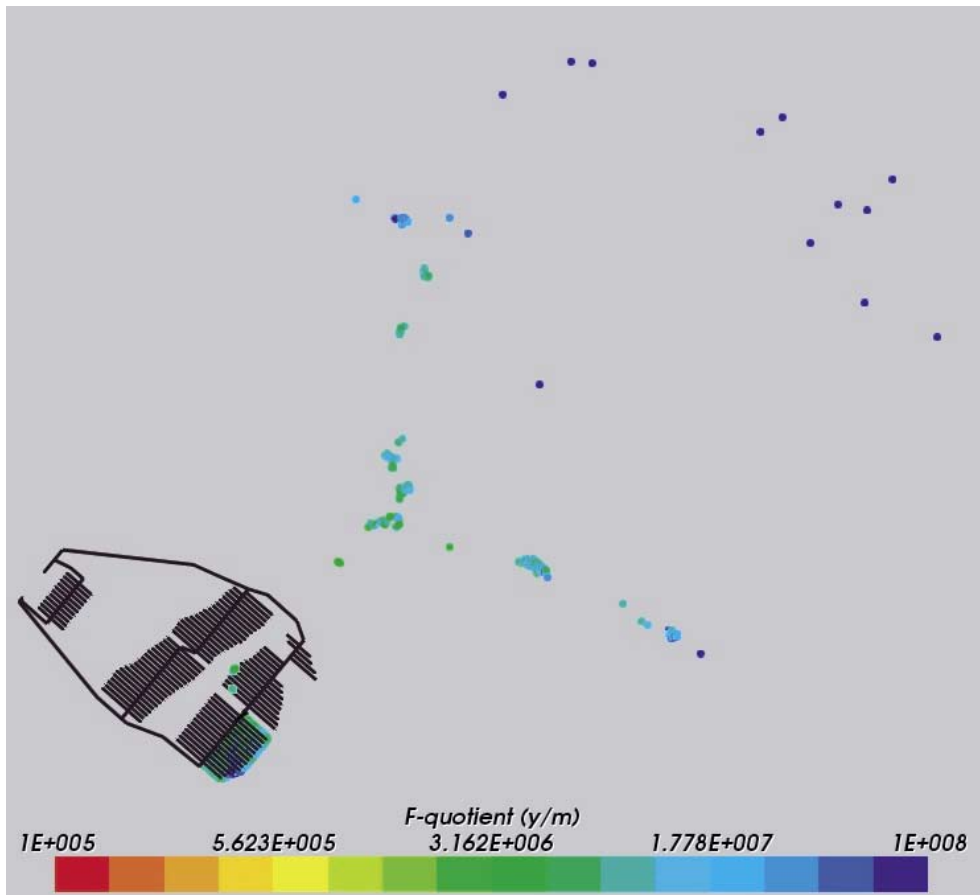


Figure 3-26. Exit locations for particle tracks in the CPM model for the south-east corner of the repository. The 604 exit locations are coloured by the total F-quotient for pathlines in the CPM model and tracked through the flow-field at 2,500 AD.

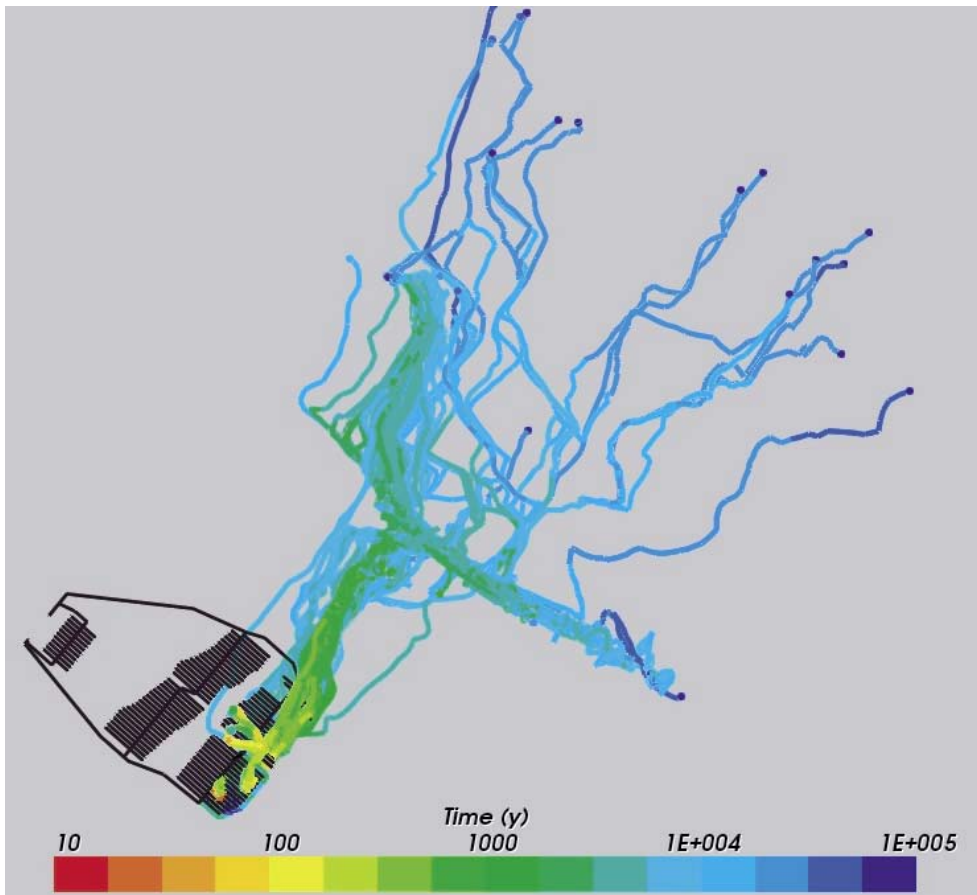


Figure 3-27. Particle tracks in the CPM model for the south-east corner of the repository. The pathlines are coloured by travel time along the path for pathlines in the CPM model and tracked through the flow-field at 2,500 AD.

As noted above, the high permeability linear features that have been included in the model exert a noticeable influence on the particle tracks. This is illustrated by Figure 3-28, which shows the pathlines from Figure 3-27 superimposed on the deterministic fracture zones that were used to determine the CPM permeability values. This figure demonstrates that the particle tracks spread out along one of the main fracture zones (just below the centre of the figure) and that this feature provides an exit route for the linear clusters of particles identified previously (compare Figure 3-26 and Figure 3-28).

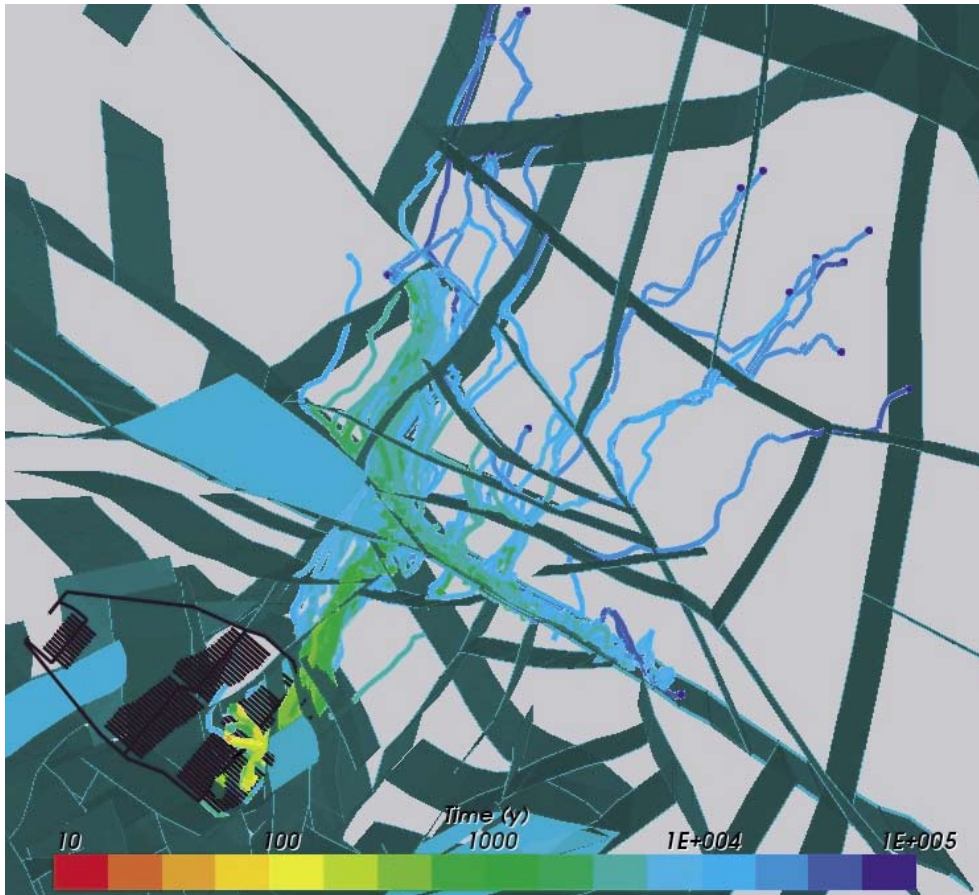


Figure 3-28. Particle tracks in the CPM model for the south-east corner of the repository. The pathlines are coloured by travel time along the path for pathlines in the CPM model and tracked through the flow-field at 2,500 AD.

A similar particle tracking calculation was undertaken using the flow field calculated for 12,000 AD. The same set of 604 particle release points was used (Figure 3-29), and the particles were tracked through the geosphere to their release points at the model boundary (Figure 3-30). Compared with the exit points at 2,500 AD (Figure 3-26);

- there is an increased likelihood that the particles will discharge directly above the repository (cluster above the south-east repository corner);
- the influence of the linear fracture zone is still evident, albeit with fewer particle exit points;
- there are more particle exit points spread out to the north-east of the repository.

The full pathlines, superimposed on the deterministic fracture zones, are shown in Figure 3-31.

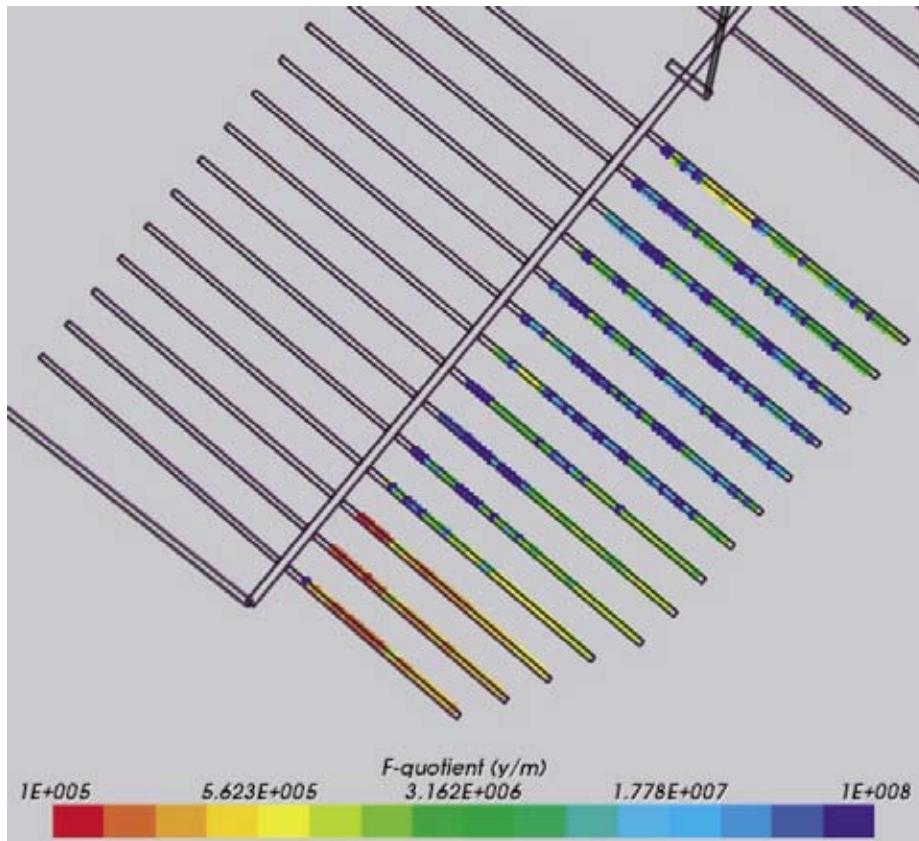


Figure 3-29. Start locations for particle tracks in the CPM model for the south-east corner of the repository. Here, the 604 canister locations are coloured by the total F-quotient for pathlines in the CPM model and are tracked through the flow-field at 12,000 AD.

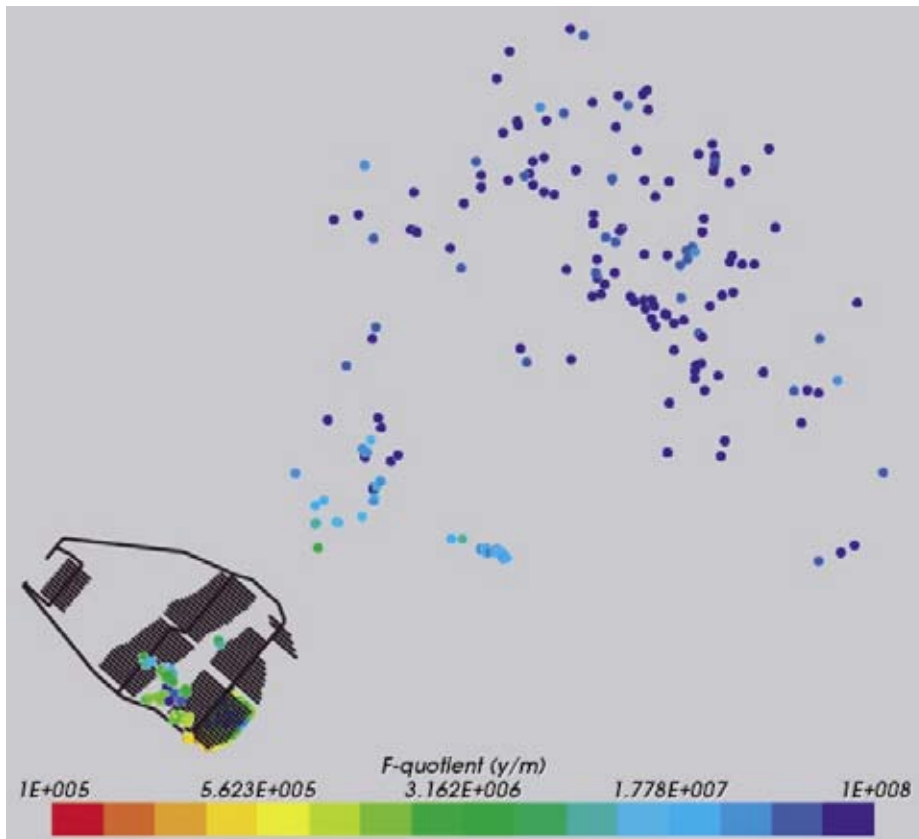


Figure 3-30. Exit locations for particle tracks in the CPM model for the south-east corner of the repository. The 604 exit locations are coloured by the total F-quotient for pathlines in the CPM model and tracked through the flow-field at 12,000 AD.

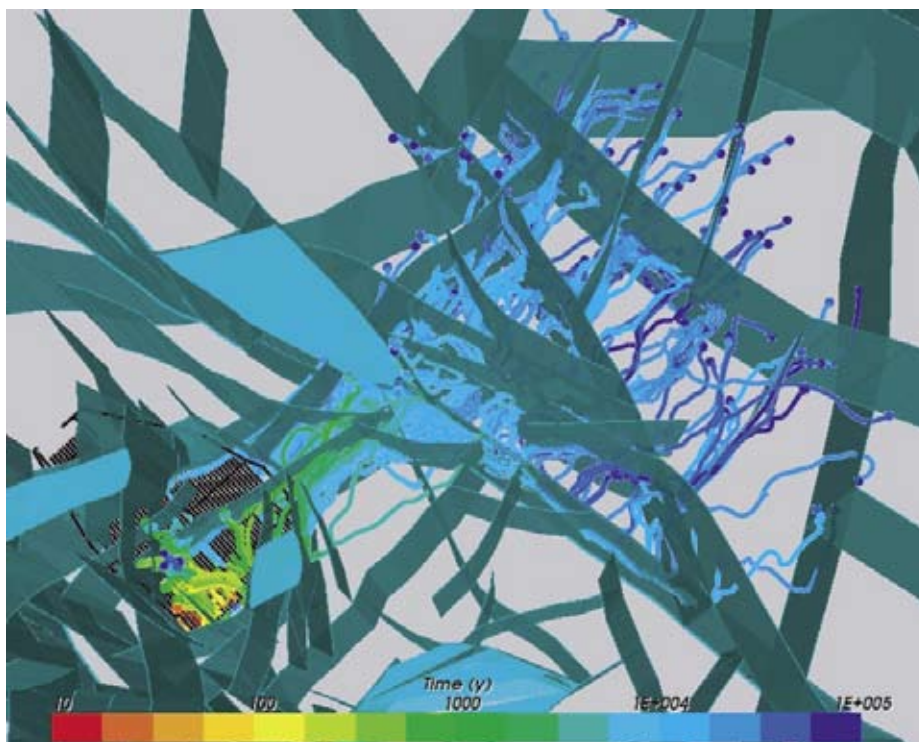


Figure 3-31. Particle tracks in the CPM model for the south-east corner of the repository. The pathlines are coloured by travel time along the path for pathlines in the CPM model and are tracked through the flow-field at 12,000 AD.

The results presented thus far have all been obtained using the same implementation of the CPM model. However, due to the stochastic nature of the DFN model from which the CPM properties were determined, it is possible that upscaling from a different set of DFN realisations would produce a CPM model with different flow and transport properties. To test this uncertainty, a second realisation of the CPM model was generated and used for particle tracking calculations. The results for times of 2,500 AD and 12,000 AD are shown in Figure 3-32, which depicts pathlines at each time superimposed on the deterministic fracture zones.

Although the location and properties of the deterministic features are identical for both realisations of the CPM model, the upscaled permeabilities from the regional-scale DFN model will vary between realisations. Therefore, the superposition of the deterministic features on the upscaled CPM properties will lead to specific cells within a deterministic feature having different properties in each realisation. This will be reflected in the pressure distribution (for identical boundary conditions) and will therefore affect the particle tracks.

This is indeed seen to be the case in Figure 3-32, where the deterministic feature in the centre of the plots can be seen to capture less of the particle tracks, which have a greater tendency to move further north-east before reaching a discharge point than was the case for the first realisation.

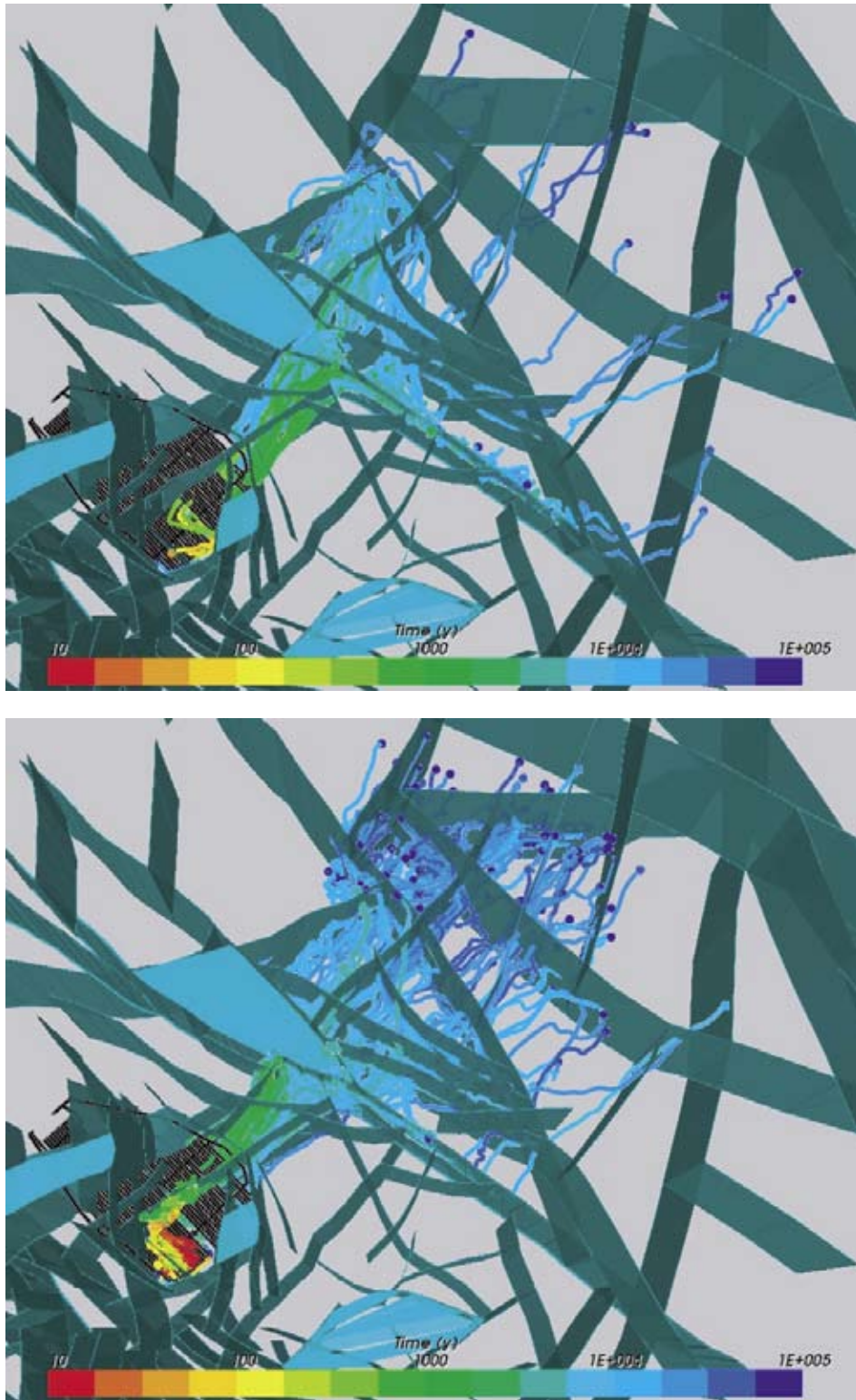


Figure 3-32. Particle tracks in the CPM model for the south-east corner of the repository using the second realisation of the CPM model. The pathlines are coloured by travel time along the path for pathlines in the CPM model and tracked through the flow-field at 2,500 AD (top) and 12,000 AD (bottom).

3.7 Nested CPM/DFN model: groundwater flow and particle tracking

3.7.1 CPM/DFN grid

In order to improve the representation of flows and particle tracks in the region immediately surrounding the repository, part of the CPM model was replaced with a local DFN model, as shown in Figure 3-33. The DFN model had dimensions of about 3,800x5,200x1,000 m, encompassing all of the repository footprint, and included regional-scale fractures with length ranging from 1000 m down to 50 m. In addition, extra local-scale fractures with lengths between 50 m and 12.5 m were added in a 60 m thick layer around the repository. The repository tunnels were included in the DFN region as vertical fractures with an equivalent transmissivity to represent a backfilled tunnel of specified hydraulic conductivity and cross-sectional area. These ‘tunnel fractures’ will exchange flow with the surrounding fracture network. Using this representation, it is possible to track particles released from designated areas of the repository, initially through the fractures close to the repository and then through the equivalent CPM portion of the grid.

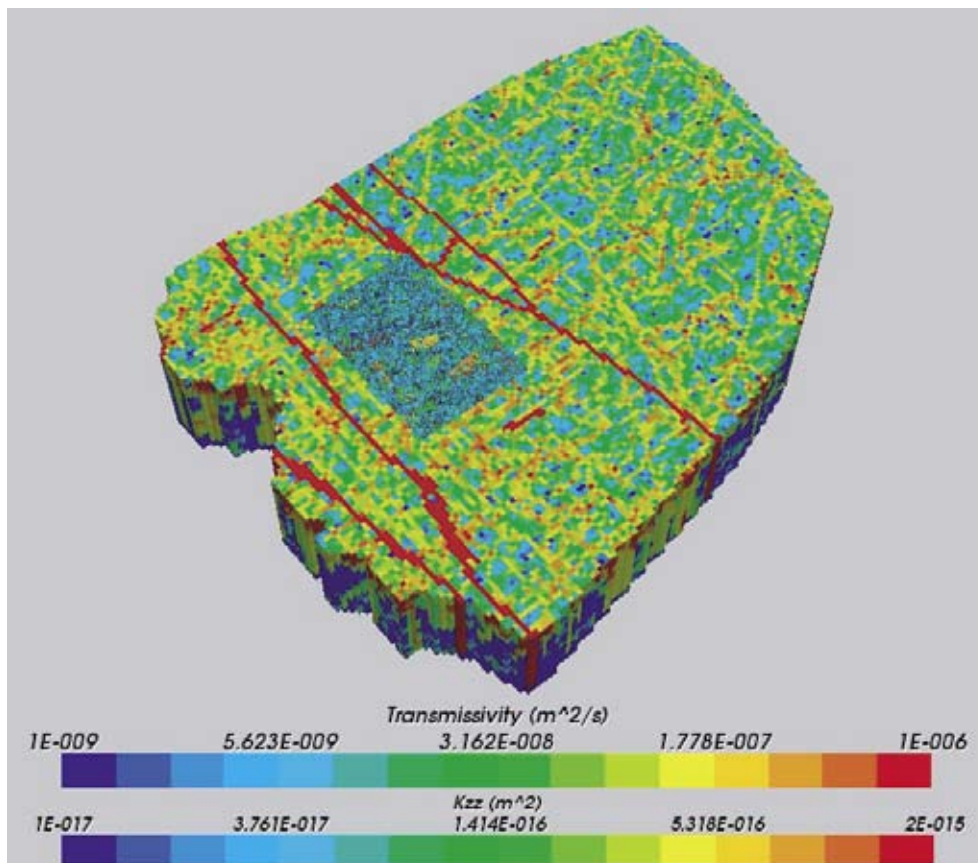


Figure 3-33. The regional nested model with the top 2 layers removed to show the central local-scale DFN sub-area. The CPM model is coloured by vertical permeability (k_{zz}). For the DFN model, fractures are coloured by transmissivity.

Figure 3-34 shows the nested CPM/DFN model with the deterministic fracture zones superimposed. As can be seen, the red-coloured CPM permeability features that extend across the model from south-east to north-west all correspond to deterministic features. The repository-scale DFN model lies between these features, but is crossed by a number of other deterministic fracture zones, which are included in the DFN model (Figure 3-35).

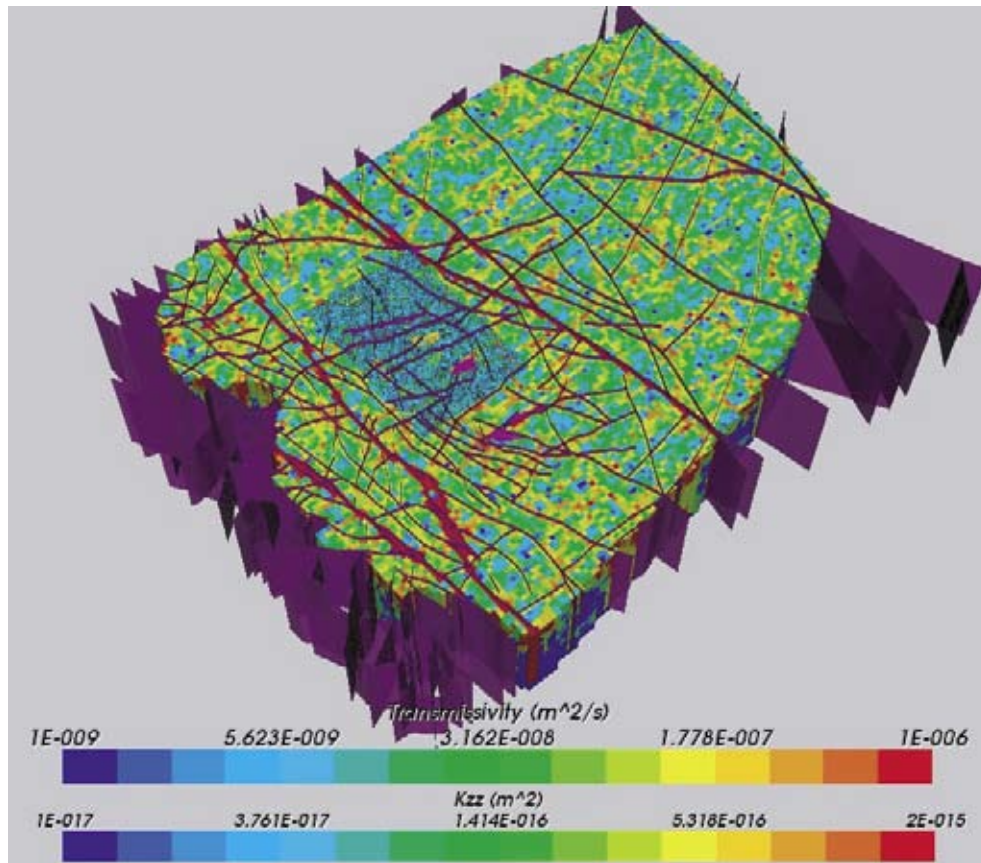


Figure 3-34. The regional nested model with the top 2 layers removed to show the central local-scale DFN sub-area with the deterministic fracture zones superimposed. The CPM model is coloured by vertical permeability (k_{zz}). For the DFN model, fractures are coloured by transmissivity.

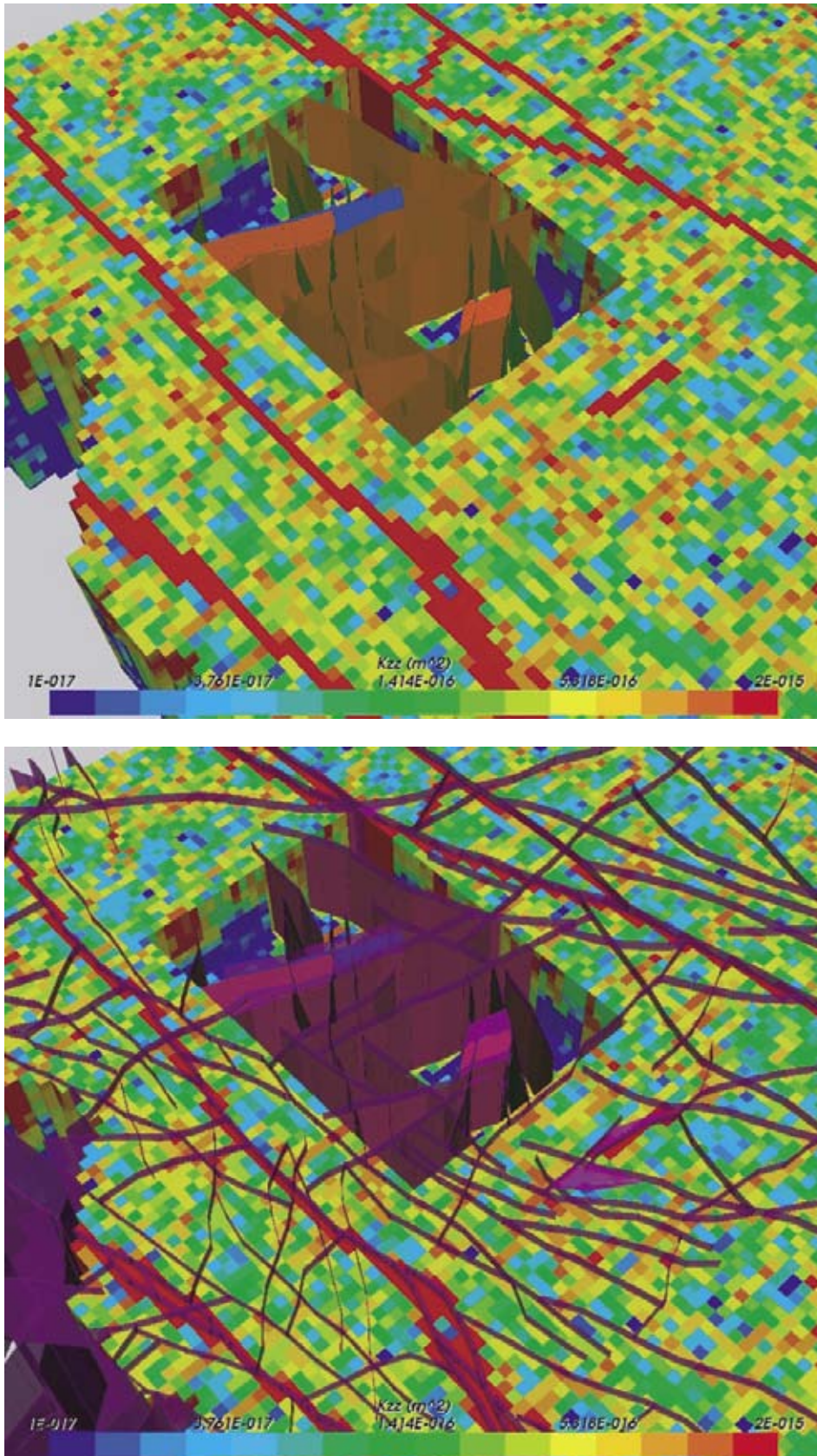


Figure 3-35. The regional nested model showing how the deterministic fracture zones are represented in the DFN model and their continuity into the surrounding CPM. In the bottom plot the deterministic fractures zones are superimposed. The CPM model is coloured by vertical permeability (kzz). For the DFN model, fractures are coloured by transmissivity.

Figure 3-36 shows an enlarged view of the repository-scale DFN model nested within the CPM grid. It is evident from the shading of the fractures within the DFN model that the majority are small features with relatively low transmissivity (blue shading). However, some of the larger, more transmissive fractures (green/orange/red shading) are also clearly visible.

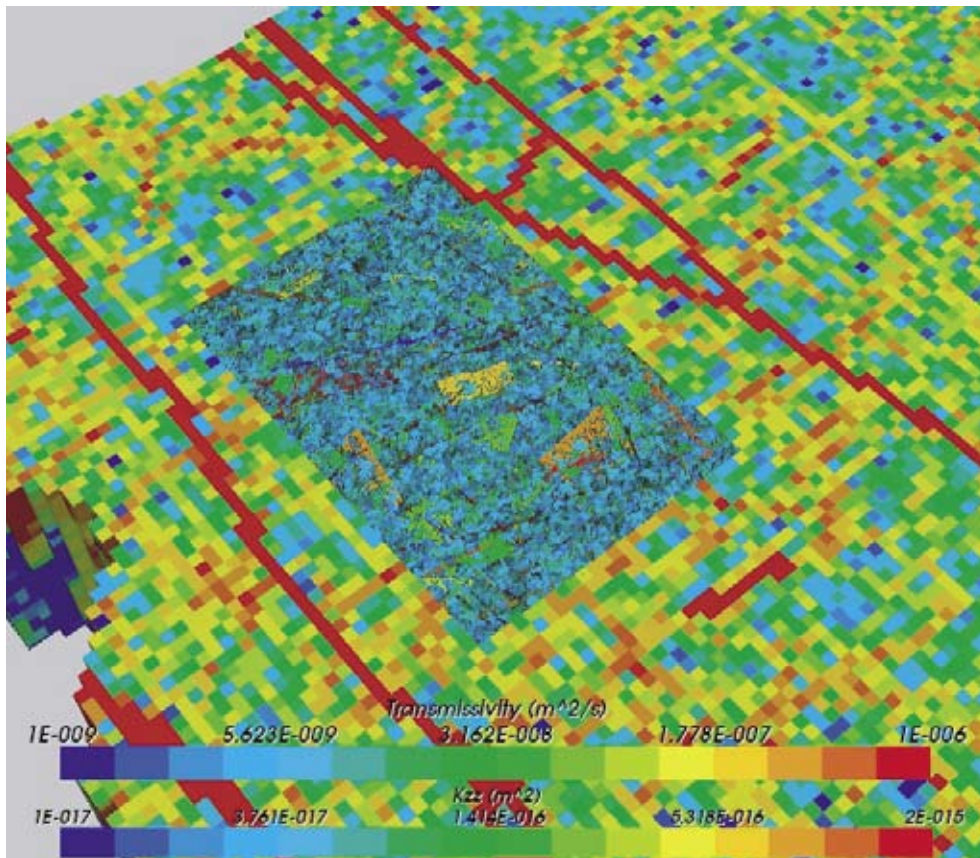


Figure 3-36. The regional nested model with the top 2 layers removed and focused on the central local-scale DFN sub-area. The CPM model is coloured by vertical permeability (k_{zz}). For the DFN model, fractures are coloured by transmissivity.

Looking more closely again at the DFN model, Figure 3-37 shows how the deterministic features intersect the repository structure. From this figure it is clear that many of the repository tunnels are intersected by deterministic fracture zones, which are relatively large-scale objects. By inference, there would be many more intersections between the more numerous, smaller-scale fractures and the tunnels. Therefore, to provide an improved representation of particle movement local to the tunnels and deposition holes, a refined fracture specification was included for a zone within the DFN model close to the tunnels. This zone is shown in Figure 3-38 (and in more detail in Figure 3-39), and contains the fracture network specified for the whole of the nested DFN model, plus local-scale fractures to improve the connectivity to the repository structure. This refined zone covers a limited vertical region of the DFN model (60 m thick) as well as a restricted areal extent. In this way, particle migration can be tracked from the release points, through the smaller fractures (down to 12.5 m length) to intermediate and then large fractures, into the deterministic fracture zones and ultimately into and through the CPM model to the exit points. (Note that the CPM grid cells in Figure 3-38 and Figure 3-39 are 100x100 m, giving some indication of the fracture length scales involved.)

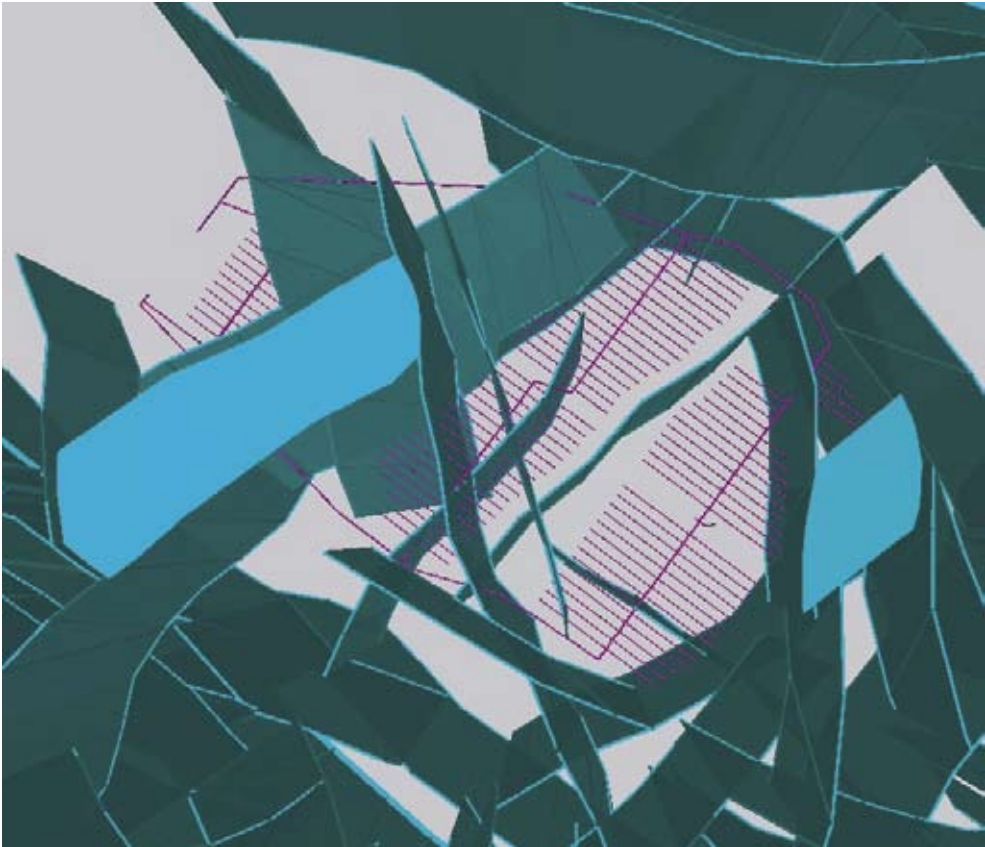


Figure 3-37. *The repository layout with the deterministic fracture zones superimposed (semi-transparent).*

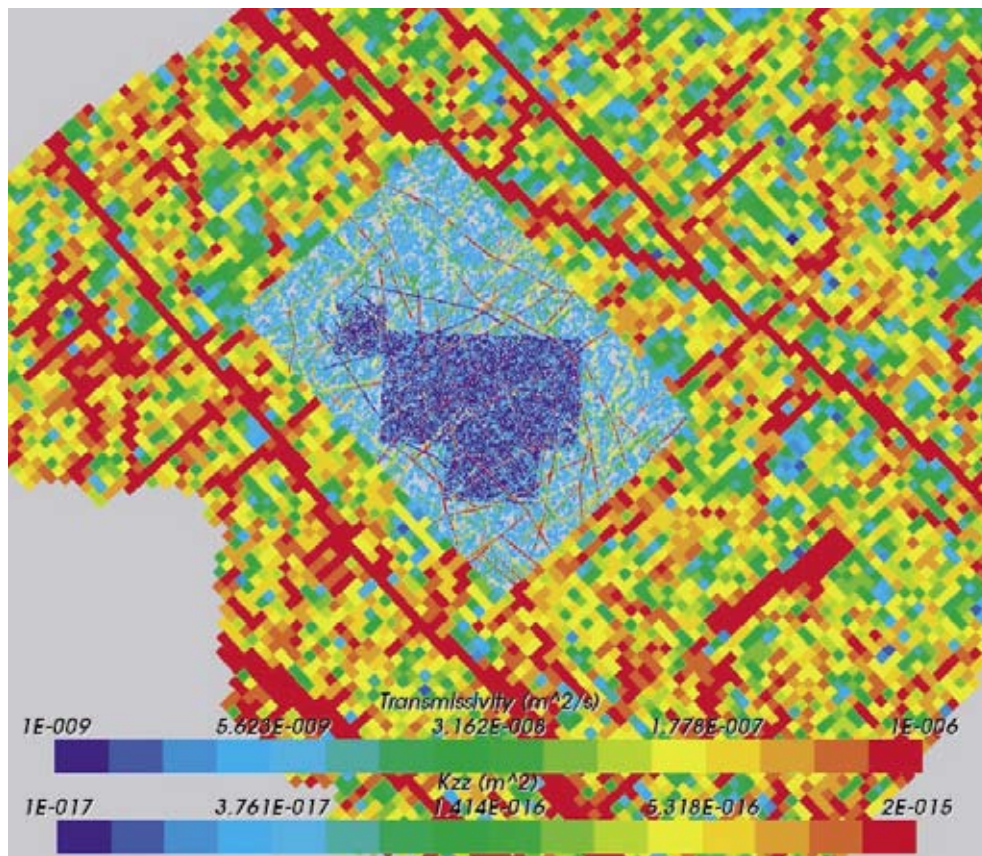


Figure 3-38. A horizontal slice through the regional nested model at repository depth ($z = -400$ m). The DFN area is in the centre and shows the extra small-scale fractures around the repository. The CPM model is coloured by vertical permeability (k_{zz}). For the DFN model, fractures are coloured by transmissivity.

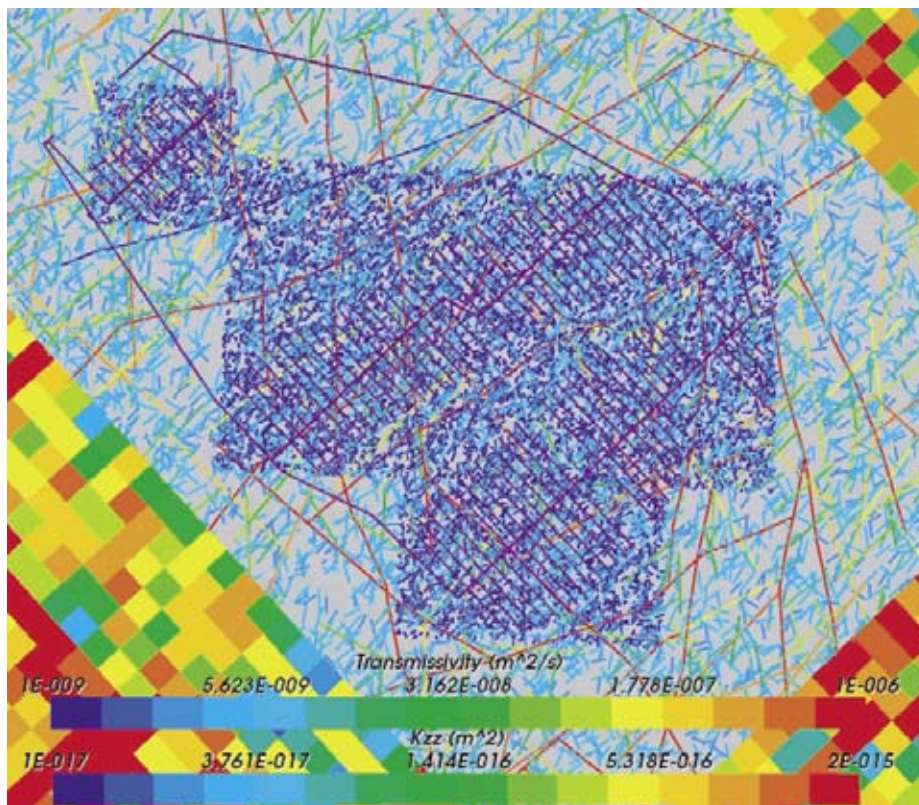
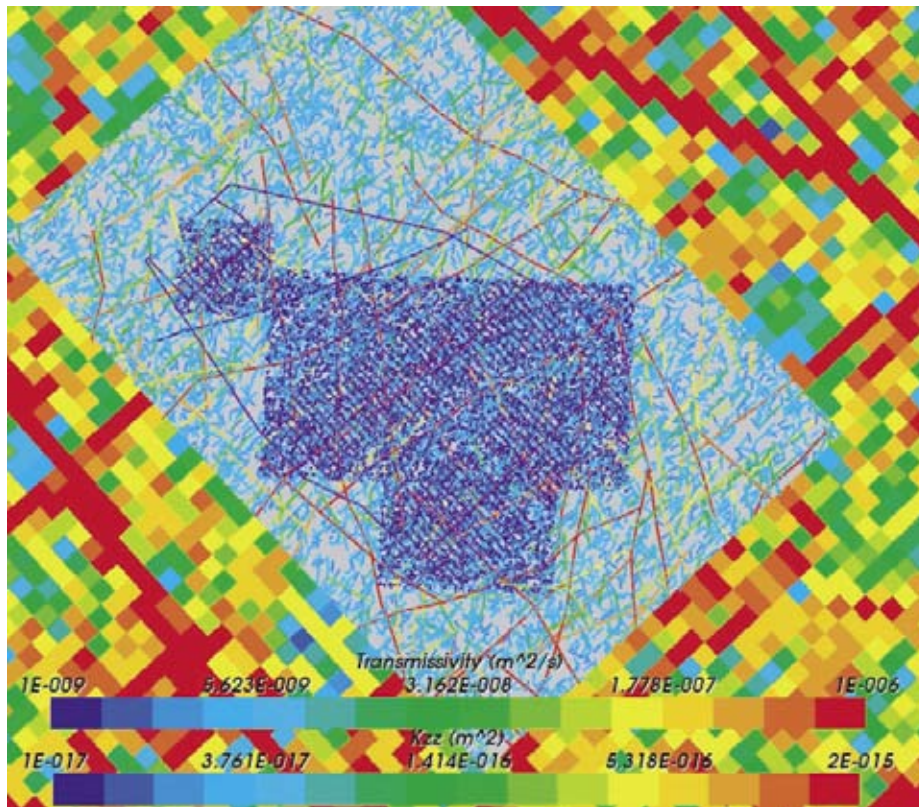


Figure 3-39. A horizontal slice through the regional nested model at repository depth ($z = -400$ m). Showing the DFN area (top), and the repository area (bottom). The CPM model is coloured by vertical permeability (k_{zz}). For the DFN model, fractures are coloured by transmissivity.

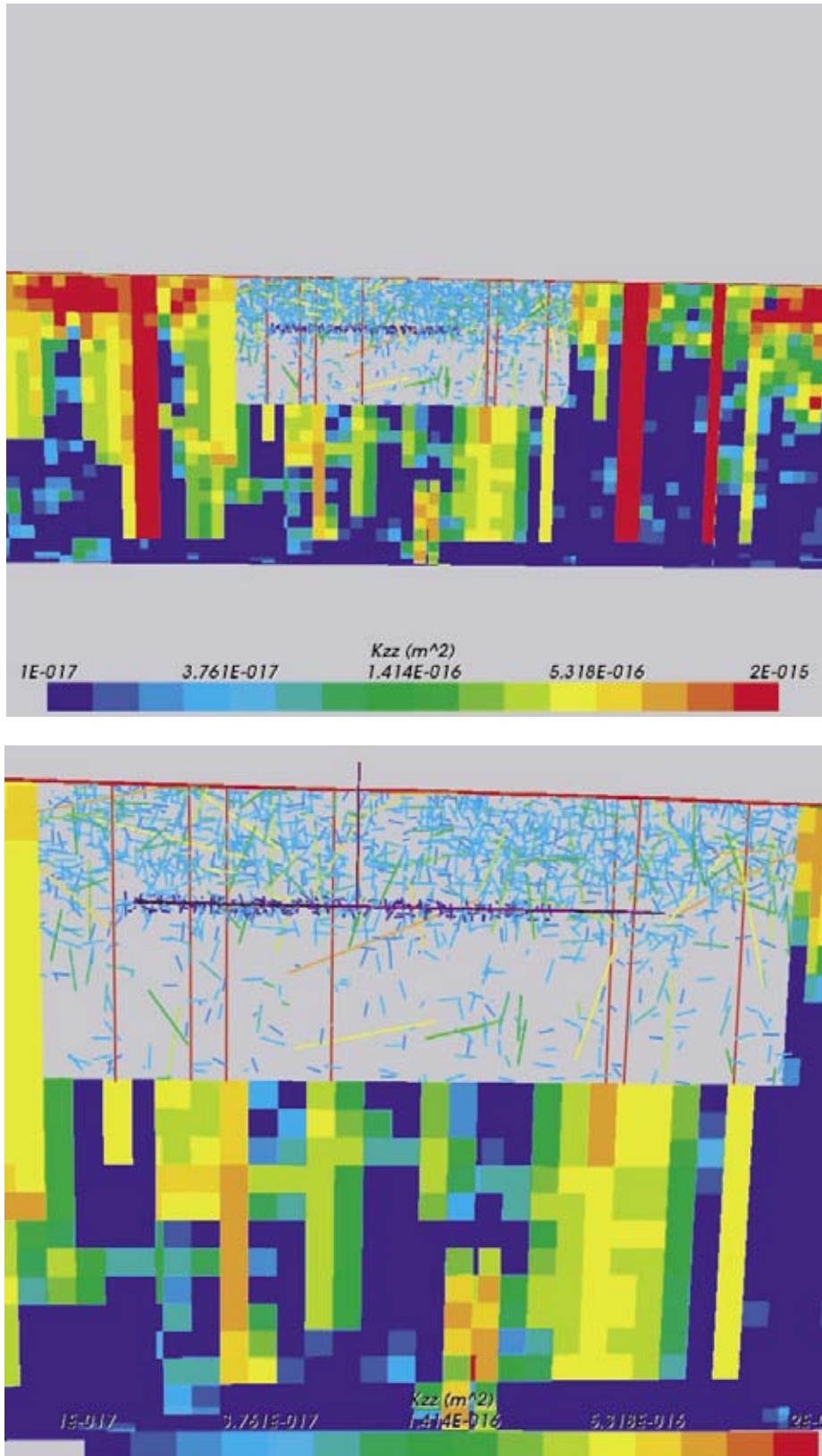


Figure 3-40. A vertical slice through the regional nested model cutting through the repository from SW (left) to NE (right). Showing the CPM and DFN area (top), and around the DFN (bottom). The CPM model is coloured by vertical permeability (k_{zz}). For the DFN model, fractures are coloured by transmissivity. The vertical red lines are fracture zones. The horizontal purple line is the repository.

Figure 3-40 shows a cross section through the regional CPM/DFN model that intersects the repository. Both plots in this figure illustrate the limited extent of the refined DFN representation close to the repository (band of dark blue fractures), and the difference in overall fracture intensity above and below the repository. This latter point is reflected both by the lower numbers of fractures shown in the DFN model and by the increased occurrence of blue-shaded (low permeability) CPM cells below repository depth.

3.7.2 Pressure calculations

Having defined the model, it was then used to calculate pressure distributions for the combined CPM/DFN grid. The salt mass fraction distribution was interpolated onto the CPM part of the grid from the regional-scale CPM model to give the groundwater density distribution and so that flow calculated in the CPM sub-model would include the effect of the spatial variation in density. It should be noted that the DFN part of the model can only simulate constant density groundwater flow. However, because environmental pressure accounts for density variations, applying an environmental pressure boundary condition on the exterior of the DFN model will induce the correct constant-density groundwater flows through the fracture network. CONNECTFLOW automatically ensures continuity of pressure and conservation of mass flux across the boundary between the CPM and DFN grids.

The result of the groundwater flow calculation in the nested regional-scale model for flows at 2,500 AD are presented in Figure 3-41 for the model with the top two layers removed. As can be seen, the distribution of pressure is continuous across the CPM/DFN boundary, for example, at the south-west corner and along the north-eastern boundary of the DFN model. Compare with Figure 3-24 for the equivalent plot in a coarse CPM model at the same time.

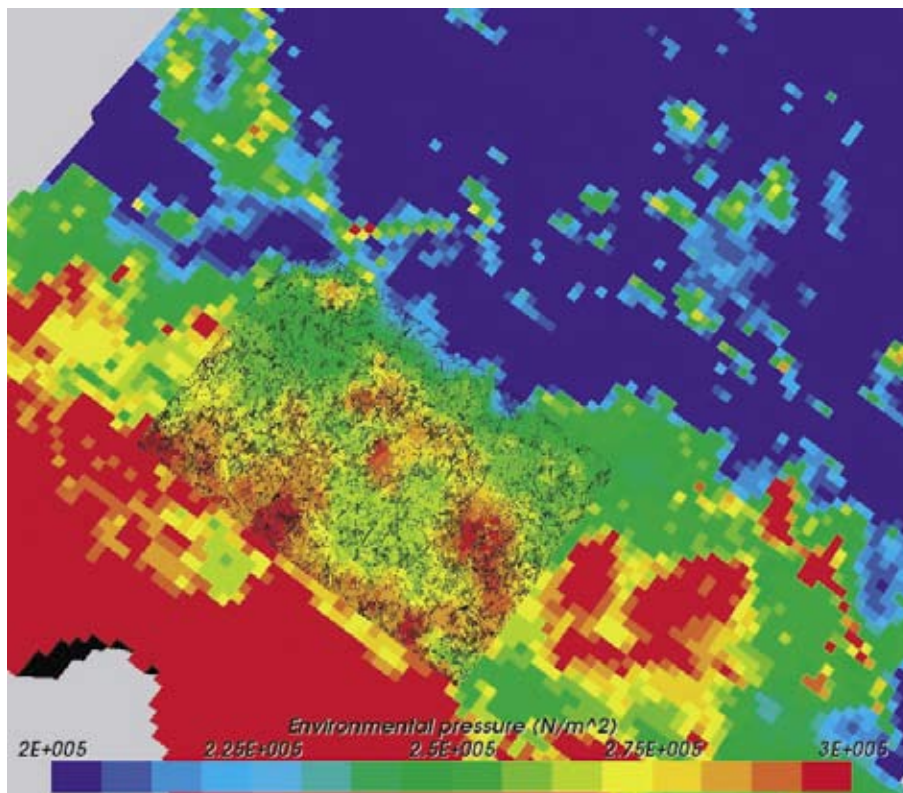


Figure 3-41. Distribution of environmental pressure in the nested regional-scale model near the top of the model with the top two layers removed. For the CPM sub-model, the average environmental pressure in the finite-element is used. For the DFN sub-model, the average residual pressure in the fracture is used.

The corresponding pressure distributions at repository depth (-400 m) and at -700 m are shown in Figure 3-42. Again continuity of pressure across the DFN model boundaries is observed, but it is clear that the network is more sparse at the greater depth.

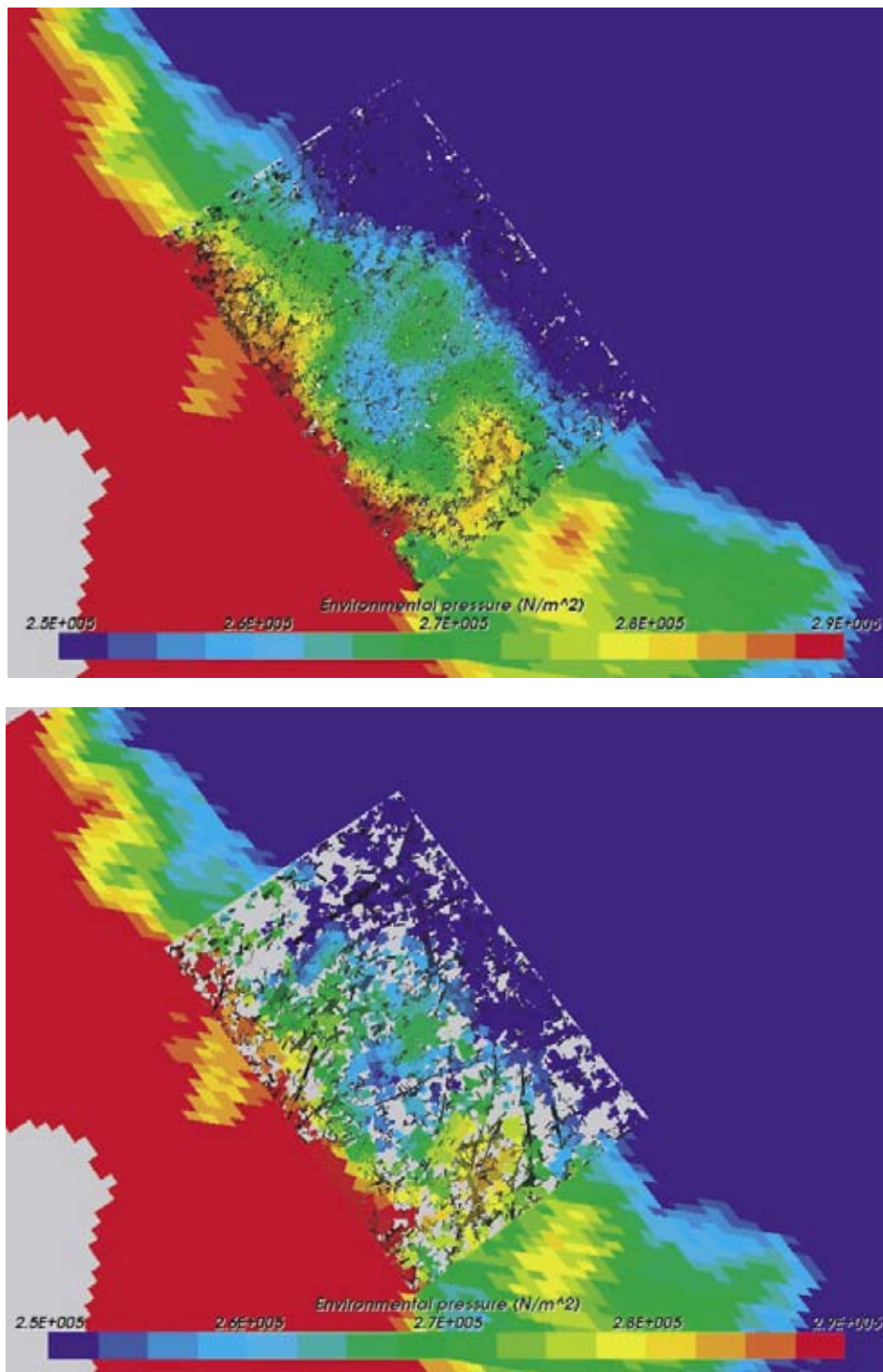


Figure 3-42. Distribution of environmental pressure in the nested regional-scale model at $z = -400$ m (top), and $z = -700$ m (bottom). For the CPM sub-model, the average environmental pressure in the finite-element is used. For the DFN sub-model, the average residual pressure in the fracture is used.

A more detailed view of the refined DFN grid and repository is shown in Figure 3-43, which depicts the pressure distribution at 2,500 AD. Comparison with the upper plot of Figure 3-24 shows the similarity between the pressure distributions in the purely CPM and the nested CPM/DFN models although there is greater resolution here.

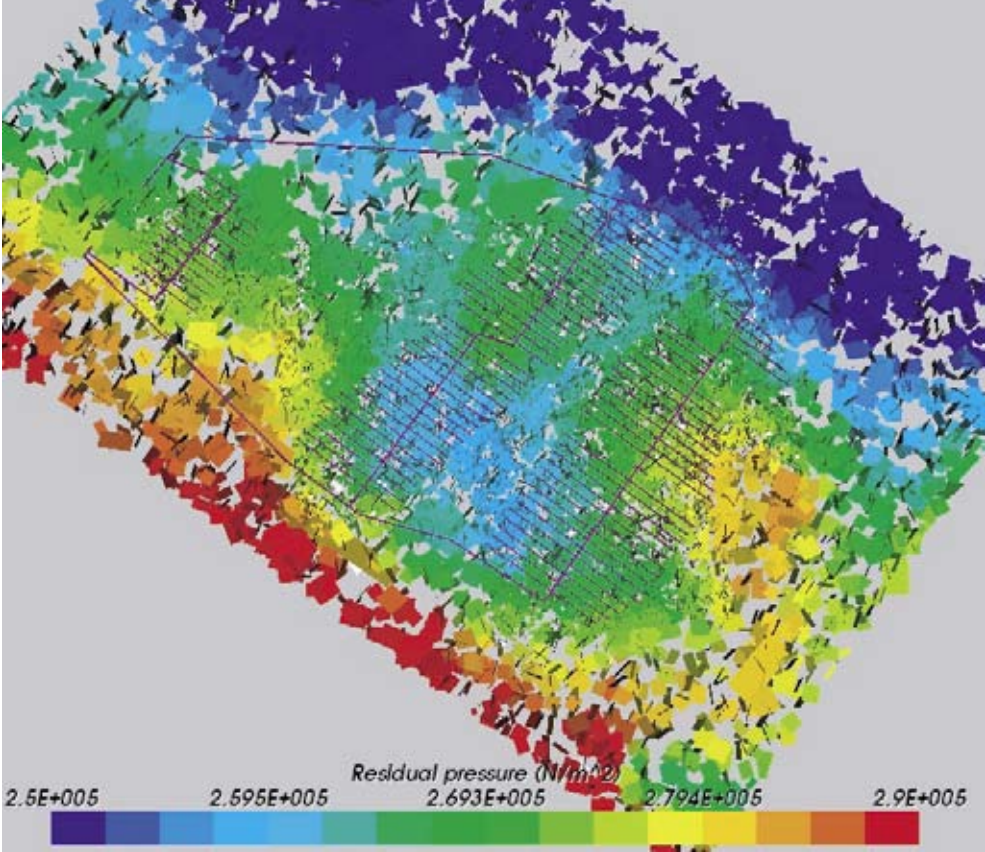


Figure 3-43. Distribution of residual pressure in the DFN sub-model of the nested regional-scale model in a horizontal layer around repository depth ($z = -400$ m). Fractures are coloured by the average residual pressure. The repository is superimposed.

3.7.3 Particle tracking calculations

The regional-scale nested CPM/DFN model described above was also used to carry out particle tracking calculations for a full set of 5,026 canister locations. The particle release points are shown in Figure 3-44, and are coloured according to their associated F-quotient in the model. It should be noted that the release points correspond to the fracture intersection nearest to the deposition-hole location and may therefore be up to a few metres from the actual deposition hole. It is important, to note that both the travel time and F-quotient spent in the deposition tunnels has intentionally been removed from the transport PMs. Retention in the tunnel is an issue that will be treated in future safety assessments.

The corresponding track exit points are shown in Figure 3-45. As with the earlier particle tracking results, the influence of the deterministic fracture zones is evident in the distribution of particle exit points (Figure 3-45). (Note that no plot for the complete pathlines is presented here; the sheer number of paths would make interpretation of such a figure impossible.)

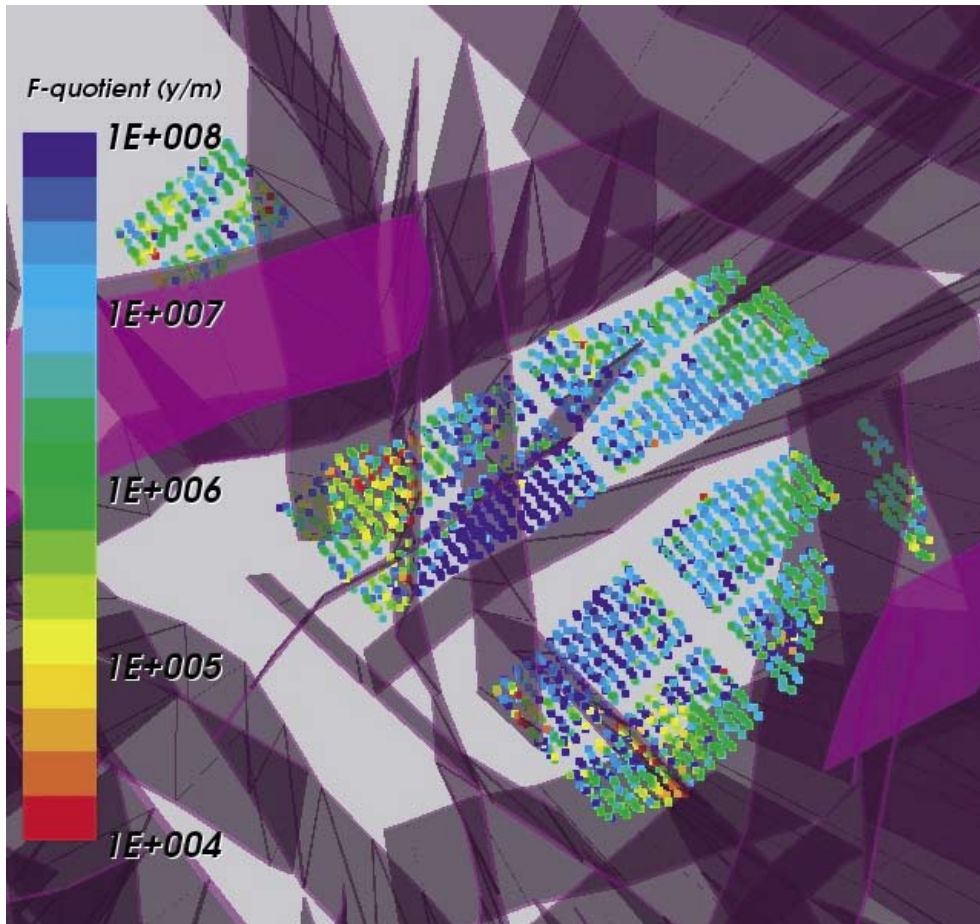


Figure 3-44. Start locations for particle tracks in the regional-scale nested model for the whole repository. Here, the 5,026 canister locations are coloured by the F-quotient for pathlines in the regional-scale model and tracked through the flow-field at 2,500 AD.

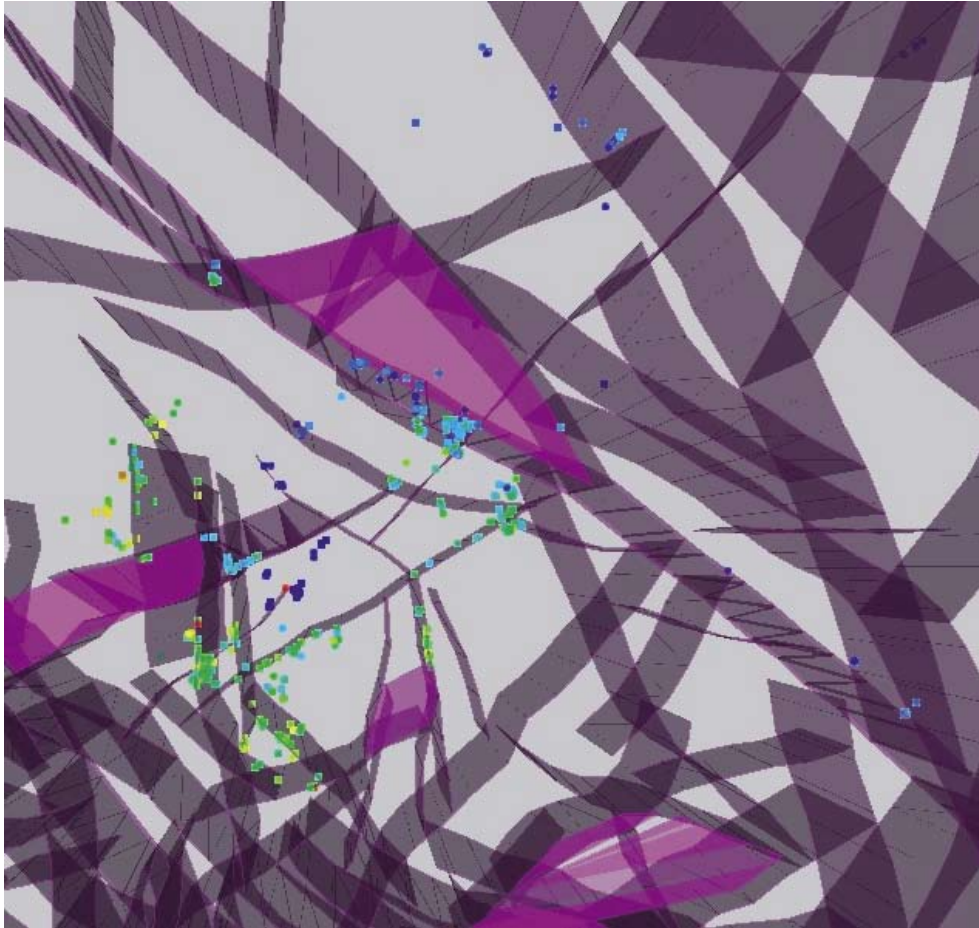


Figure 3-45. Exit locations for particle tracks in the regional-scale nested model for the whole repository. Here, the exit locations for pathlines from 5,026 canister locations are coloured by the F-quotient for pathlines in the regional-scale model and tracked with the flow-field at 2,500 AD.

Histograms for the 5,026 particle tracks are presented in Figure 3-46, Figure 3-47 and Figure 3-48, these being for Qeq1, travel time and F-quotient, respectively.

As noted above, the particle release point was at the nearest fracture intersection to each deposition-hole. Given the truncation of the length scale for fractures included in the regional-scale model (12.5 m), this could result in the release point being several metres from the deposition hole. This distance, which in reality particles would traverse in smaller-scale (lower transmissivity) fractures, has not been included in the calculation of particle track data. It is therefore possible that the travel time and F-quotient are underestimated in the following figures.

5026 cans; v2r1_path1

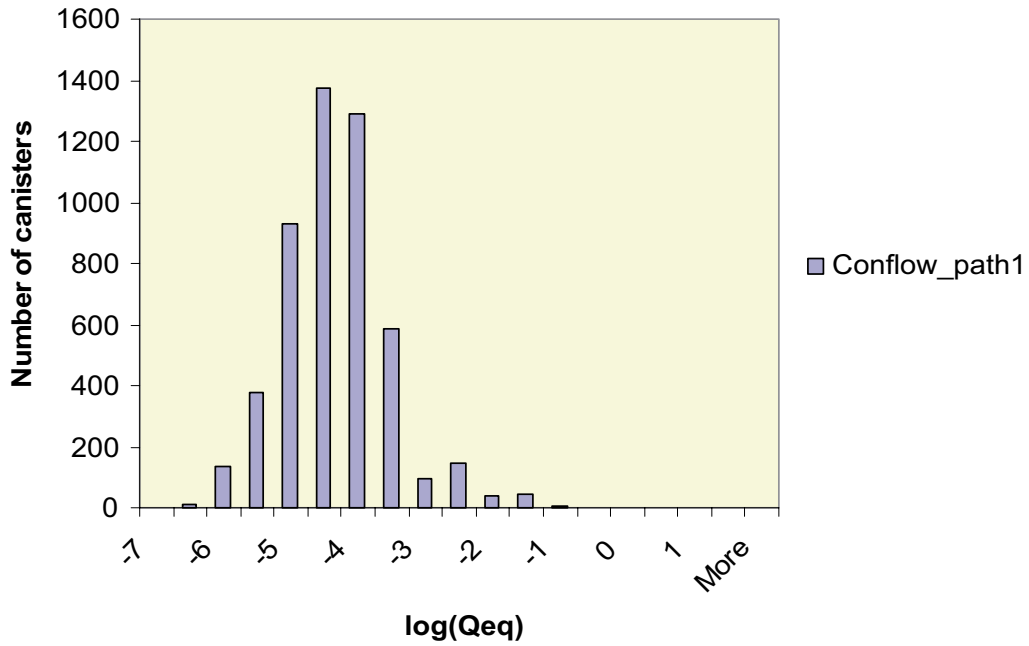


Figure 3-46. Distribution of Q_{eq1} in the regional-scale nested model with a release from 5,026 canisters into the nearest fracture intersection. The case shown is for a release after 2,500 AD and for a backfill conductivity of 10^{-10} ms^{-1} .

5026 cans; path1

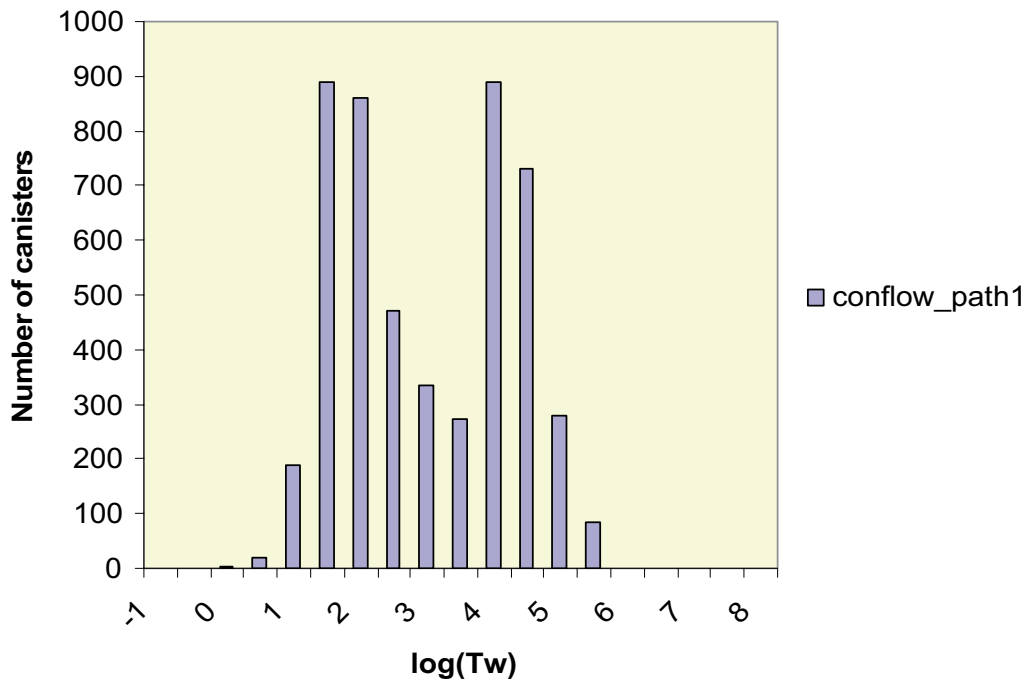


Figure 3-47. Distribution of travel time in the regional-scale nested model with a release from 5,026 canisters into the nearest fracture intersection. The case shown is for a release after 2,500 AD and for a backfill conductivity of 10^{-10} ms^{-1} .

5026 cans; path1

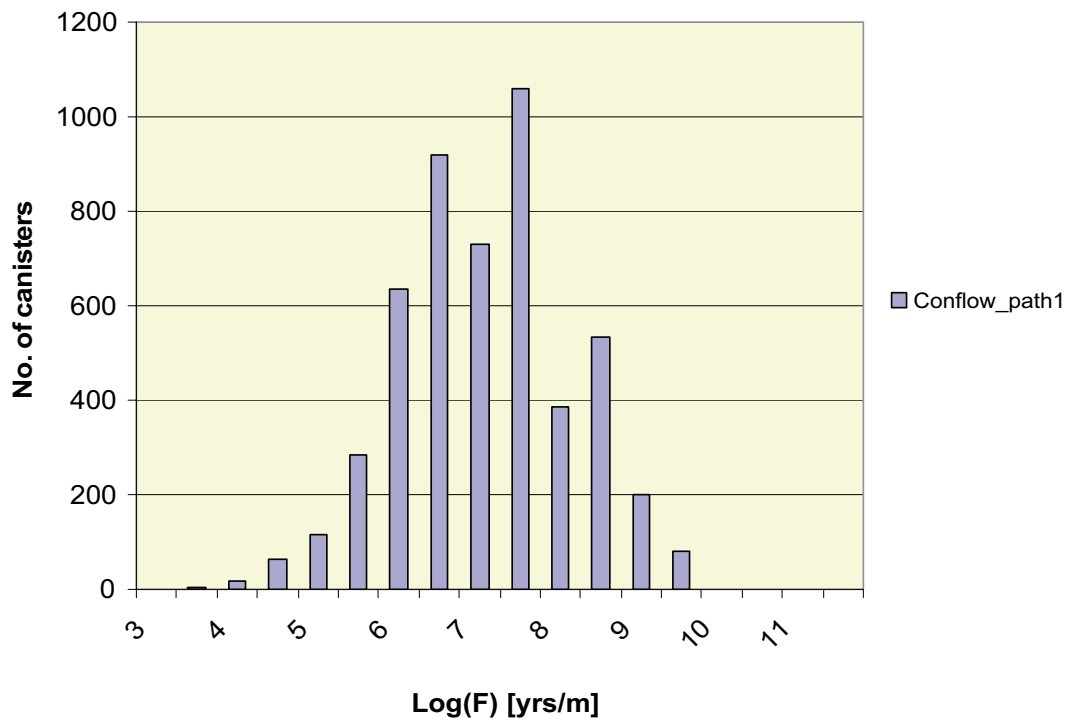


Figure 3-48. Distribution of F-quotient in the regional-scale nested model with a release from 5,026 canisters into the nearest fracture intersection. The case shown is for a release after 2,500 AD and for a backfill conductivity of 10^{-10} ms^{-1} .

4 Nested canister-scale DFN/CPM model

4.1 Objective

The objective of this task is to construct a canister-scale DFN model with a nested CPM representation of tunnels, deposition holes and the EDZ. In order to demonstrate the methodology, the DFN model has been restricted to a sub-region of the repository at the south-eastern corner containing 604 canisters. The CONNECTFLOW model consists of a CPM model describing the repository structures (tunnel, deposition holes) within a DFN model of the fractures down to a length scale of 3.5 m that intersect canisters. The purpose is to calculate two pathways for each canister: one starting in a fracture intersecting the deposition hole (denoted Path_f), and one in the tunnel immediately above the canister (denoted Path_t). For each path initial velocities are calculated and then transformed into the equivalent flow-rates Qeq1 (fracture intersecting the deposition hole), Qeq2 (fracture intersecting the EDZ) and Qeq3 (fracture intersecting the tunnel) for individual canisters, and flow path statistics from these locations are calculated. Only a section of the repository was considered here since it would have been time consuming to construct a mesh for the entire repository given the non-uniformity of the tunnel layout that has been used to avoid fracture zones, and was considered unnecessary for this methodology phase. The overall objective for the next phase of SR-Can is to be able to provide an approach capable of capturing the full repository, that is 5,026 canister locations.

4.2 Approach

The modelling is based on steady-state calculations, but with environmental pressure boundary conditions transferred from the regional transient CPM model at appropriate times. The entire model is 100 m thick and covers an area of 590x410 m.

The key issue with this model is to develop an understanding of the canister-fluxes (Qs) and their variability for the selected canister locations. Careful consideration will be given to particle releases, i.e. taking into consideration releases from multiple fracture intersections and possible backfill release (per canister). In addition, the relative position of the release from the canister and angle of fracture intersecting the canister location will be computed. Statistical analysis of these results, i.e. separating the various release pathways, will attempt to identify the relative importance of these pathways.

4.3 Model grid

The mesh for the repository structure is illustrated at two scales in Figure 4-1, and the CPM representation of an access tunnel, deposition tunnels and canister locations is shown in Figure 4-2. There are 14 deposition tunnels and 604 canister locations in this section of the repository. Here, each deposition hole is represented as a single finite-element and extends down from the floor of the deposition tunnel. The bentonite and canister are not represented explicitly, instead a low conductivity 10^{-10} m/s is assigned to the deposition hole finite-elements. Similarly, the engineered damaged zone (EDZ) was not modelled explicitly,

but can be included implicitly within the properties assigned to the deposition tunnel. In later phases of SR-Can more detailed meshes can be constructed fairly straightforwardly to include the geometry properties of the EDZ.

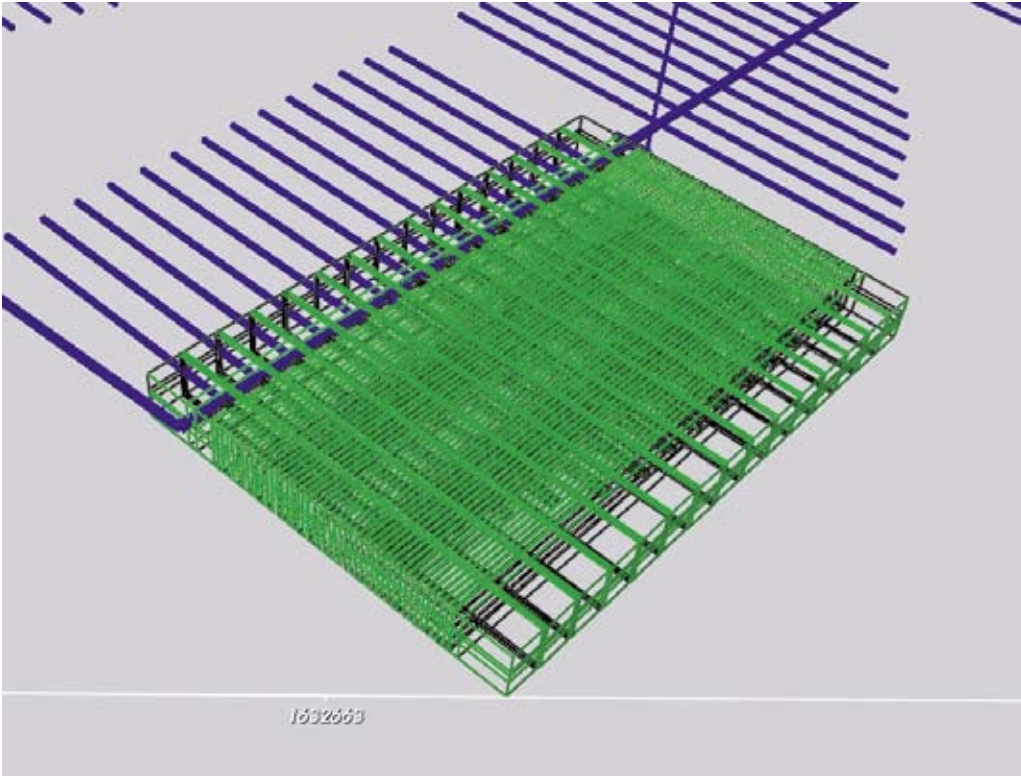
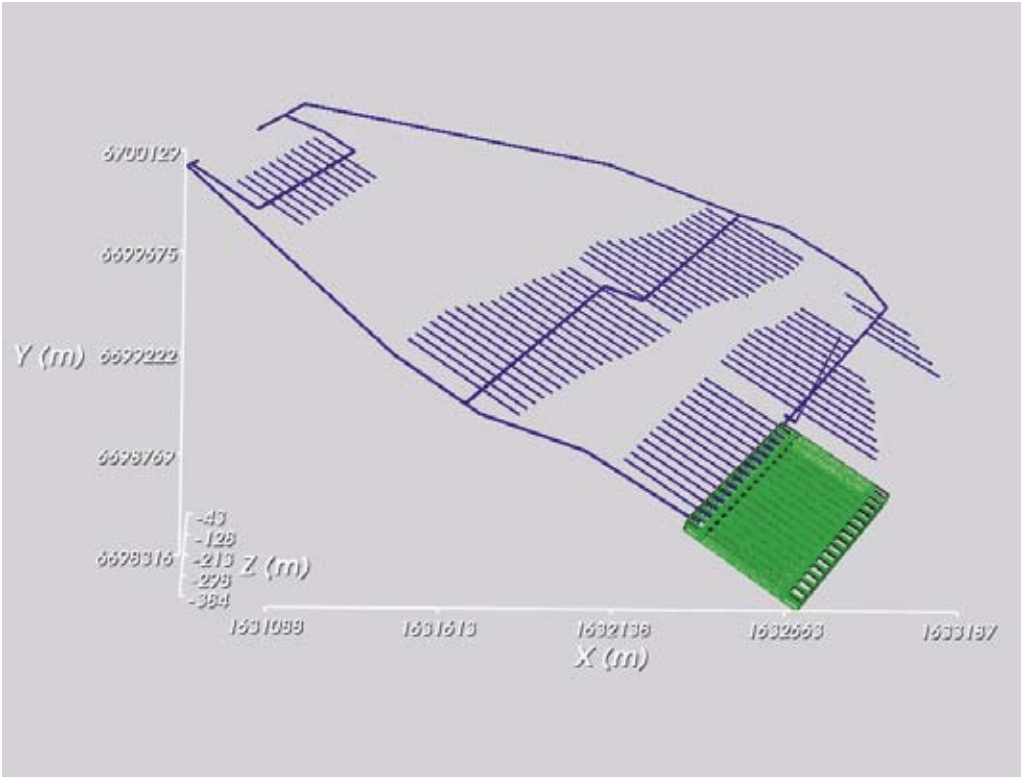


Figure 4-1. The south-east corner of the repository chosen for the illustration of canister-scale modelling. The mesh of the deposition tunnels and canisters is shown in green. The whole repository is shown in blue.

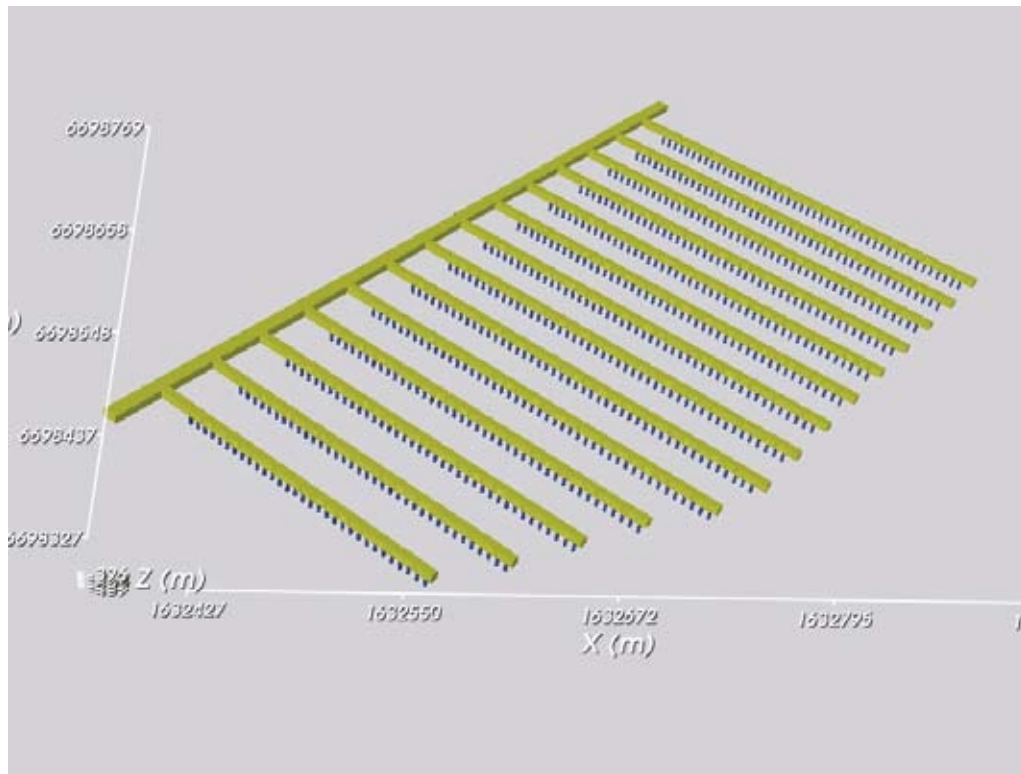


Figure 4-2. An access tunnel, 14 deposition tunnels and 604 canisters represented in the canister-scale model. This part of the model is represented by a CPM sub-model nested with a surrounding DFN model.

The repository structures shown in Figure 4-2 are surrounded by a local DFN model (the canister-scale model) as shown in Figure 4-3, which shows the full volume of the DFN model with fractures down to 3.5 m in length. As with the DFN plots given in Section 3, the fractures are coloured according to transmissivity, the more transmissive features in any plot being coloured red, with progressively lower transmissivities being shown shaded through orange, yellow and green to blue. All deterministic and stochastic fractures generated in the nested regional-scale model that cut the canister-scale model area are imported directly into this model. Hence, all fractures with lengths greater than 12.5 m are imported from the site-scale DFN model. Extra fractures are added in a 60 m thick slab between $z = -370$ m and $z = -430$ m with length scales between 3.5 m and 12.5 m. This provides consistency with the larger model scales described in Section 3.

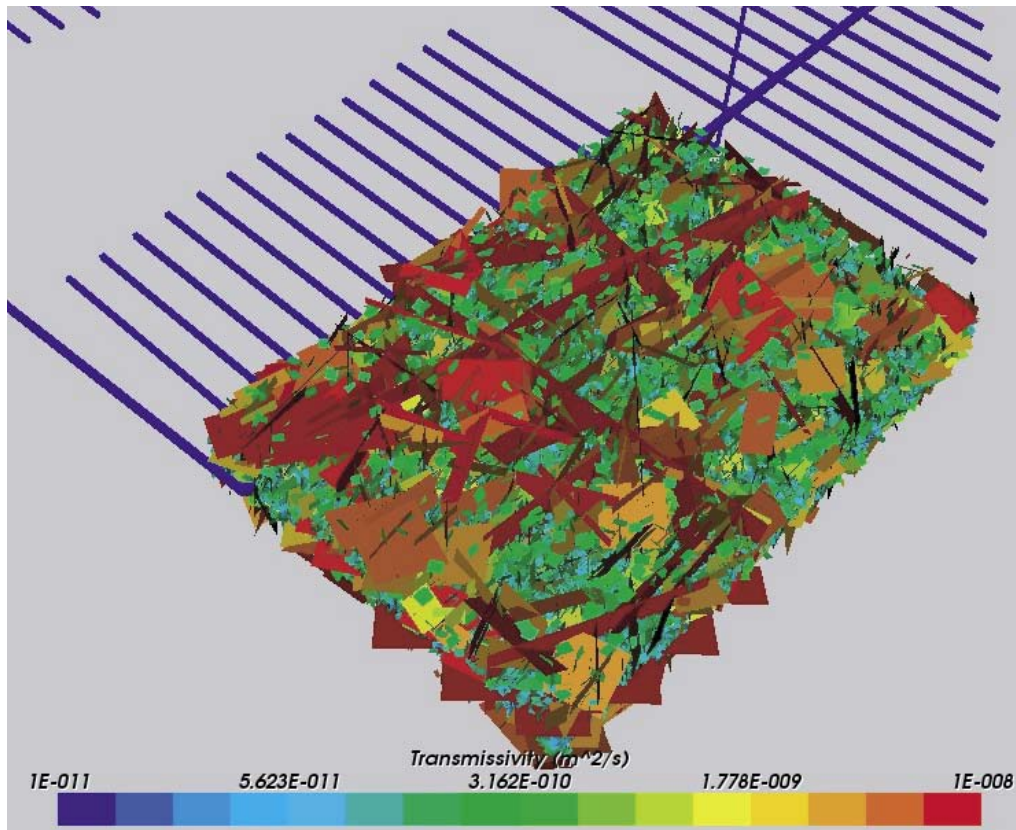


Figure 4-3. The DFN sub-model for the nested canister-scale model. The fractures are coloured by transmissivity, and part of the repository tunnels is shown in the background.

An alternative view of the canister-scale DFN model is provided in Figure 4-4, which presents a horizontal section through the model at repository depth. This figure illustrates the fracture density in the model and, in particular, the lower plot shows individual fracture traces intersecting with the repository structures. From this figure it is clear that the model is representing a large number of repository/fracture intersections. This observation is reinforced by Figure 4-5, in which individual fractures and canisters are shown. In plotting this figure, all model elements above $z = -400$ m have been removed so that the interaction between canisters and fractures is clear. From this figure it can be inferred that very few of the canisters will have no intersections with the local fracture network, which has fractures ranging in size down to 3.5 m.

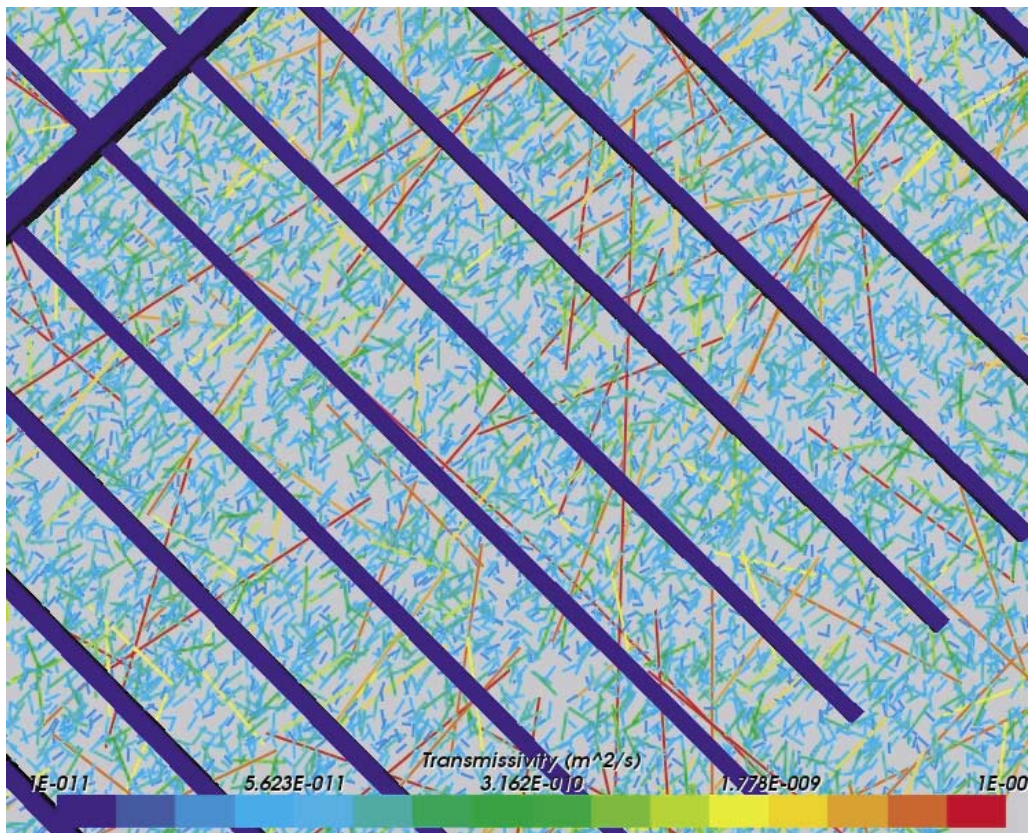
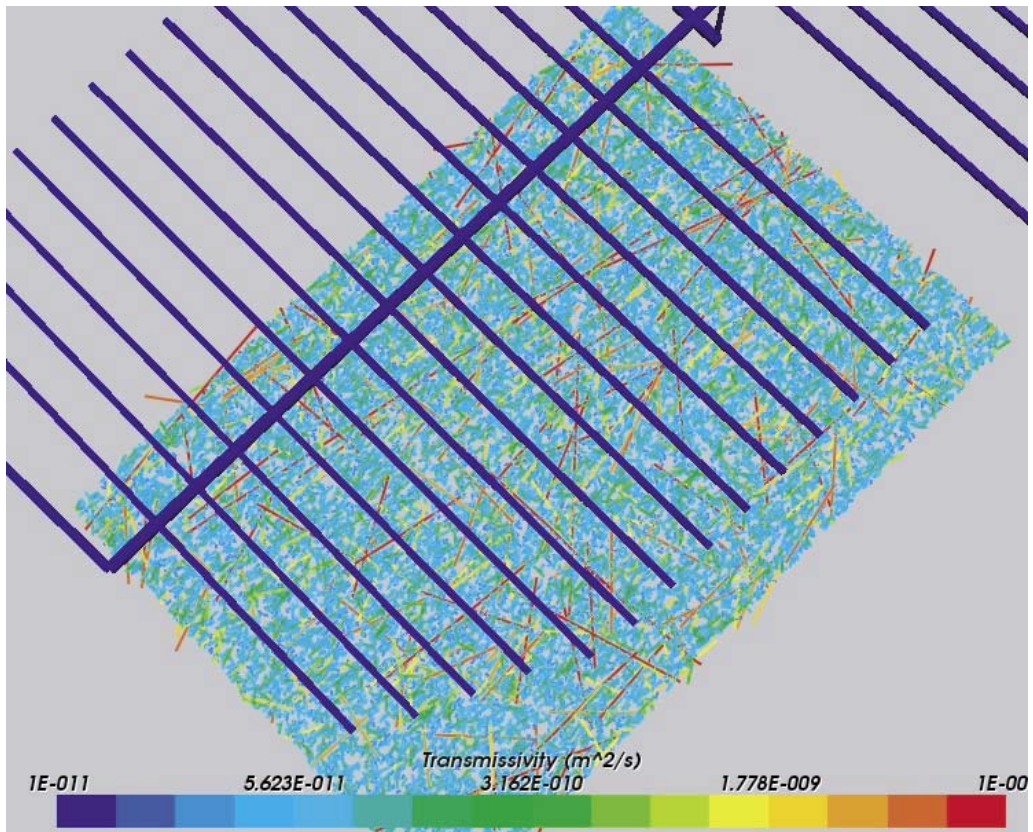


Figure 4-4. The DFN sub-model for the nested canister-scale model on a horizontal slice at $z = -400$ m. The fractures are coloured by transmissivity, and part of the repository tunnel system is shown in the background.

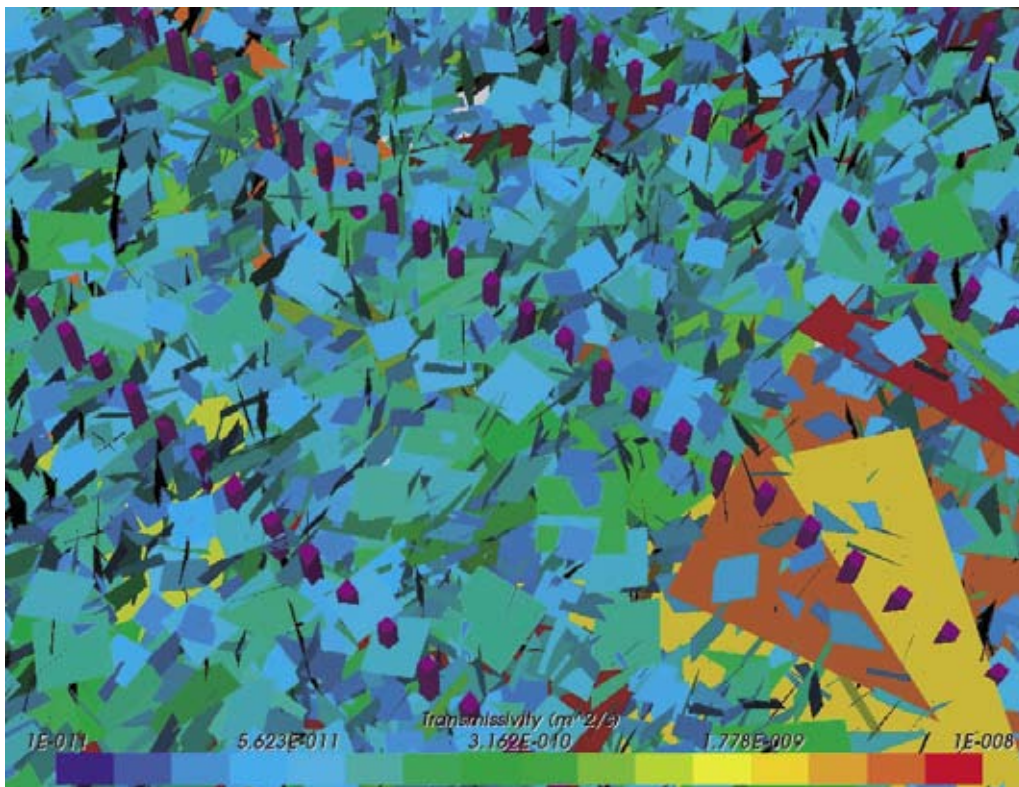
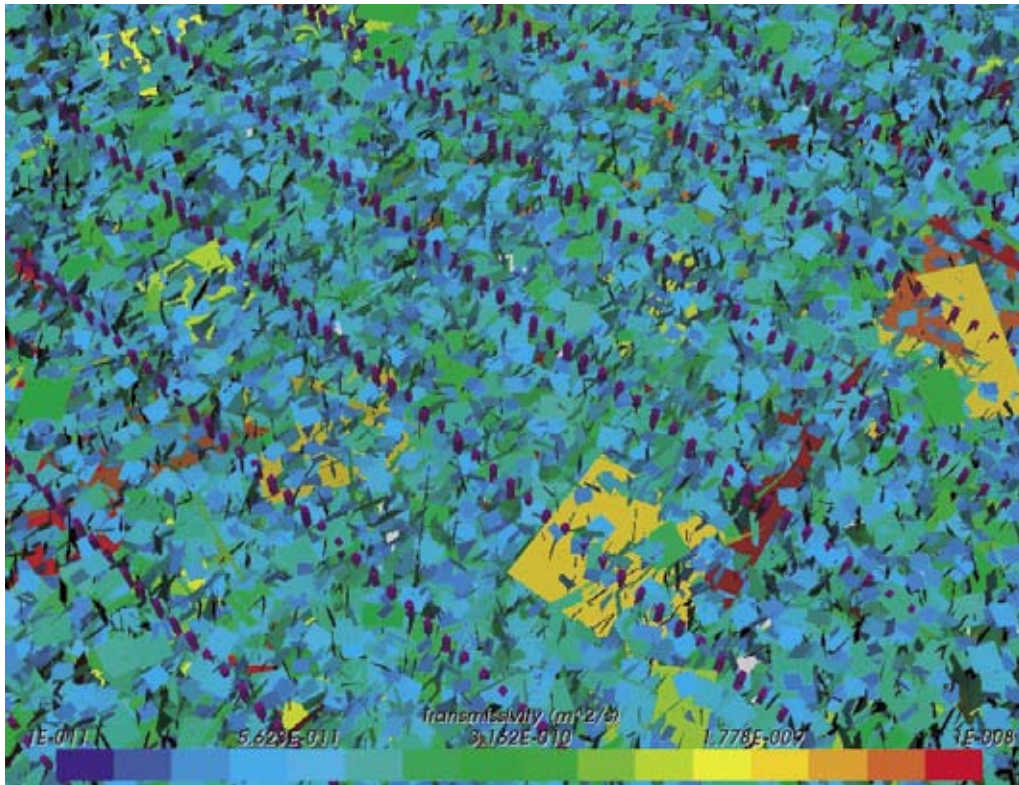


Figure 4-5. Fractures network surrounding the canisters in the nested canister-scale model. The canisters are coloured purple, and the fractures are coloured by transmissivity. The tunnels and fractures above $z = -400$ m have been removed. Far viewpoint (top), closer viewpoint (bottom).

4.4 Pressure calculation

The model described in subsection 4.3 was used to calculate groundwater flow for various times, using boundary conditions interpolated from the environmental pressure in the regional CPM model for all 6 external faces of the model. The results for the environmental pressure distribution at 2,500 AD are presented in Figure 4-6 for a section through the repository tunnels. It is evident from this figure that the pressure distribution is continuous throughout the model, with no discontinuities introduced by the DFN/CPM boundaries. The corresponding results for only the CPM part of the model are shown in Figure 4-7.

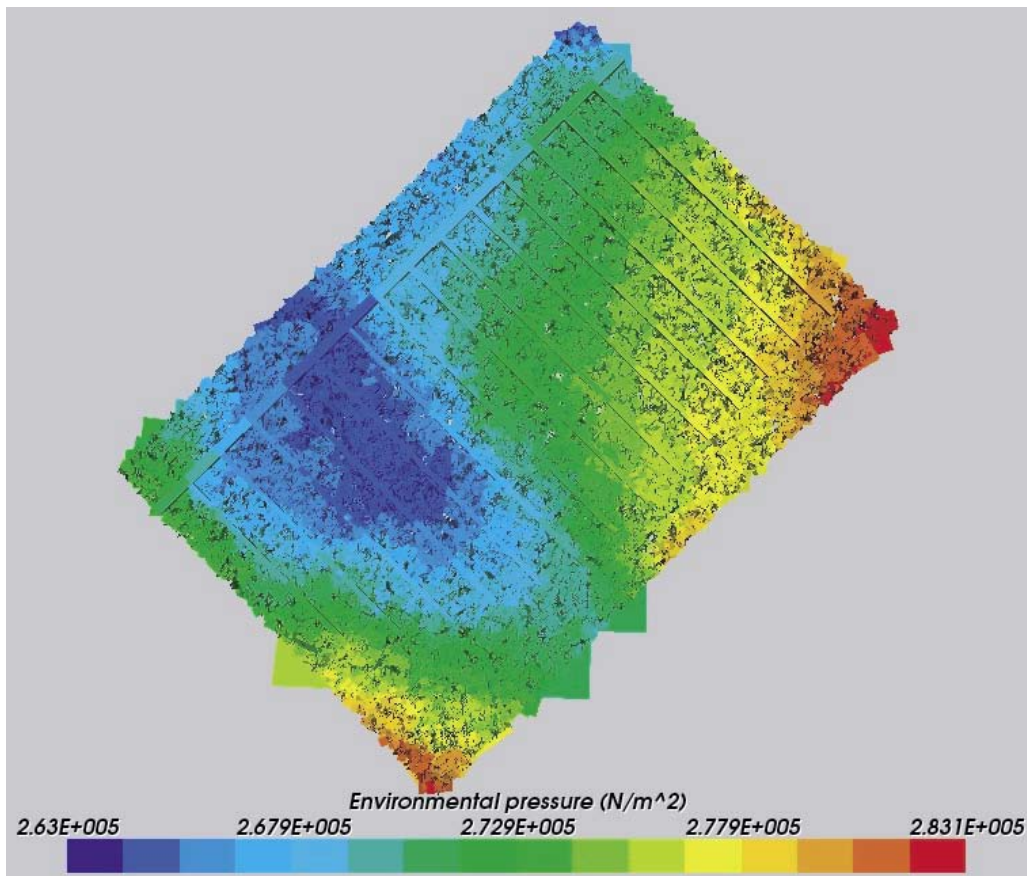


Figure 4-6. The distribution of environmental pressure in the nested canister-scale model at $z = -400$ m. The pressure is continuous through the fractures and tunnels.

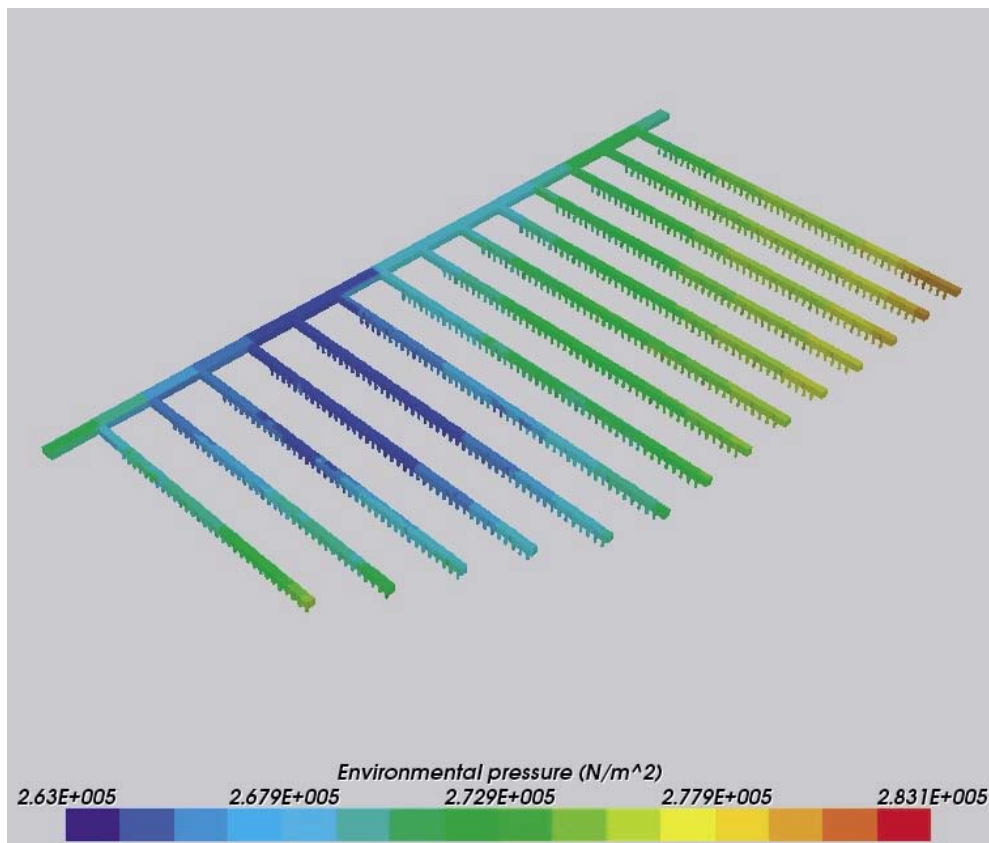


Figure 4-7. The distribution of environmental pressure in the CPM sub-model of the nested canister-scale model including the tunnels and canisters.

4.5 Particle tracking

The results from the groundwater flow calculations, i.e. the pressure distributions, were used to calculate particle tracks through the canister-scale model. A total of 604 particles were released, one for each canister location. These release points are shown in Figure 4-8. The particles were tracked through the model to the canister-scale model boundaries using the flow field calculated for 2,500 AD. The particles were then restarted from their canister-scale exit points (or nearest fracture) in the regional-scale model (as described in Section 3) for 2,500 AD and again were tracked to the model boundary. Unless the particle is within a deterministic feature when it reaches the boundary of the canister-scale model, the process of restarting the particle tracks introduces small discontinuities in them, as shown in Figure 4-9 (dark blue track). In terms of the overall particle track, from release point to boundary of the regional-scale model, these discontinuities are small (of the order of a few metres) and do not significantly affect the parameters describing the tracks, i.e. track length and travel time. Again, both travel time and F-quotient in the tunnels and canisters have intentionally been removed from the transport PMs.

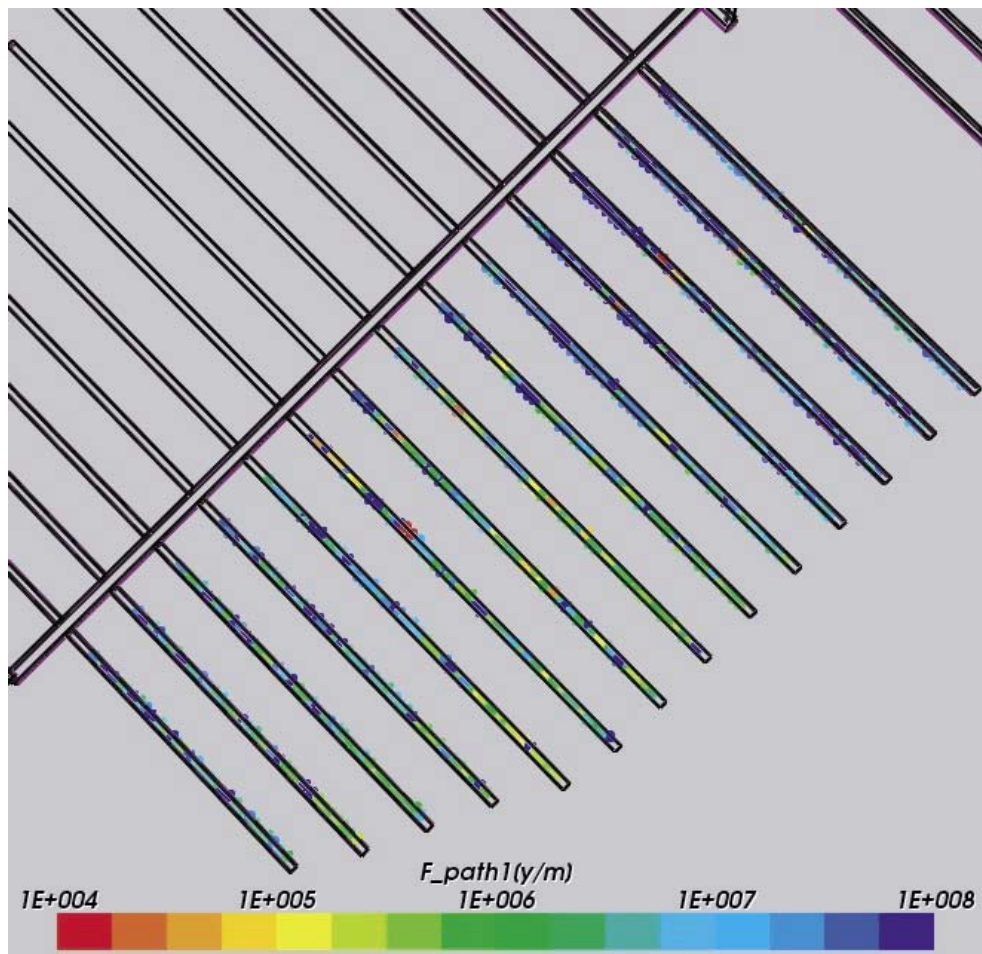


Figure 4-8. Start locations for particle tracks in the nested model for the south-east corner of the repository. Here, the 604 canister locations are coloured by the F -quotient for pathlines in the nested model (canister-scale + regional-scale) and tracked with the flow-field at 2,500 AD.

The plots in Figure 4-9 show the influence of the deterministic fractures (high transmissivity) on the paths followed by the particles. In the upper plot, it is clear that sections of the paths are fairly straight; in particular, there is a location towards the bottom of the plot where all five paths are following a route that is sub-parallel with the deposition tunnels. From the lower plot, this can be seen to coincide with one of the deterministic fractures. Similarly, from the lower plot, the green particle track can be seen to follow several deterministic fracture alignments during its journey through the model.

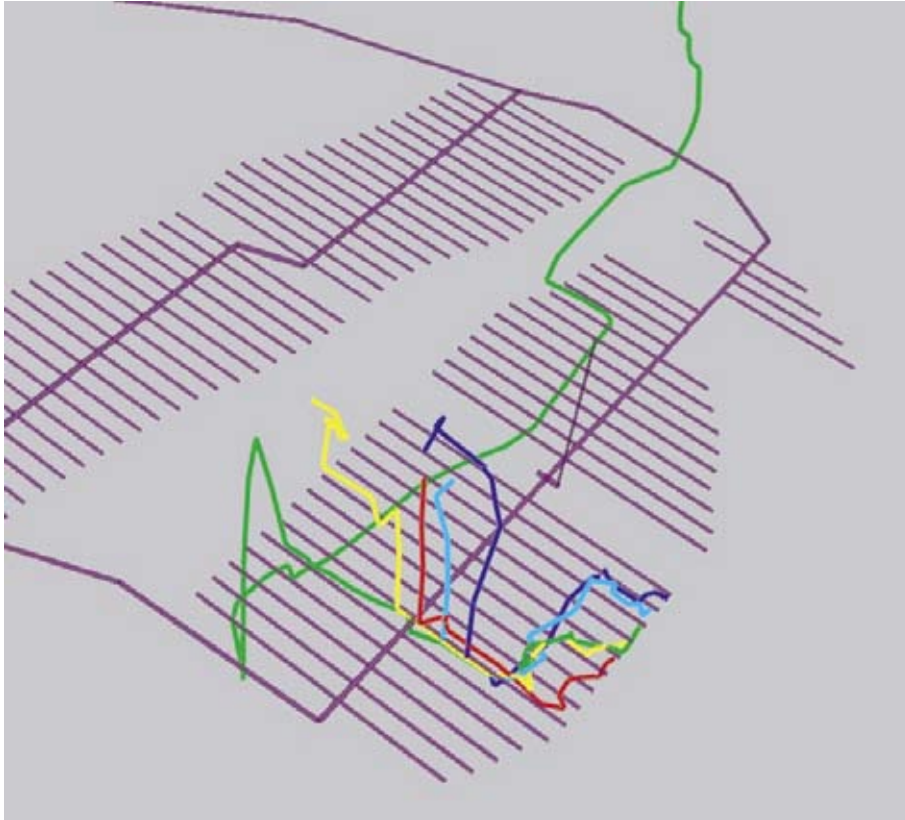


Figure 4-9. Five particle tracks in the nested model for the south-east corner of the repository. The paths are coloured by particle number and show the continuity of the particles through both the canister-scale and regional-scale nested models. An oblique view (top), and map view with the deterministic fracture zones (bottom).

Figure 4-10 shows a plot of particle tracks for particles released at all 604 canister locations and transported by the flow field calculated for 2,500 AD. The tracks are coloured according to travel time in the regional-scale nested model. The plots show two broad groups of pathlines arising from the south-east corner of the repository. The first group comprises paths that rise almost vertically to the surface, discharging above the repository in less than 100 years (red coloured paths in the south-east of the plot). The second group comprises paths that are transported a significant distance within the fracture network, eventually discharging to the sea bed after of the order of 10,000 to 100,000 years (blue paths to the north of the model). Again the lower plot indicates the strong influence of the large deterministic fractures. A few tracks indicate a discharge location above the repository to the west of the particle origins (predominantly yellow paths).

A similar pattern of discharge points is shown in Figure 4-11 for paths originating in the deposition tunnels above the canister locations (again tracked through the flow field for 2,500 AD). The most significant difference compared with Figure 4-10 appears to the north of the repository, where two paths discharge quite separate from the main group, in particular the path that appears at the north-eastern edge of the model. This indicates that different parts of the fracture network are being accessed by these paths, and gives an impression of the true area over which discharge of water originating in the repository could occur.

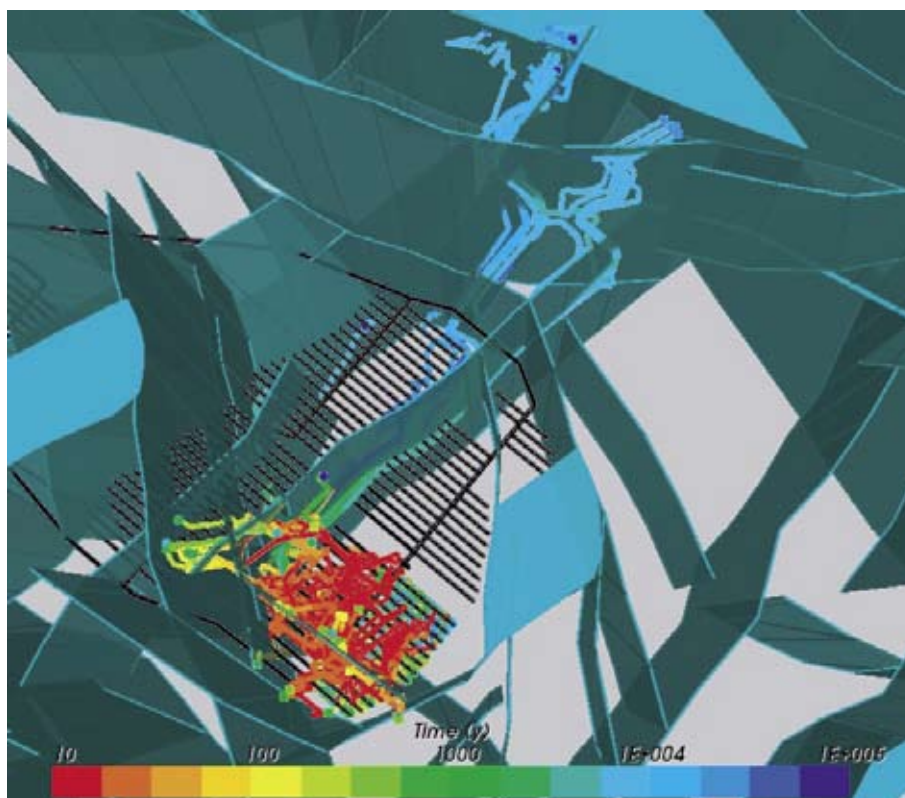
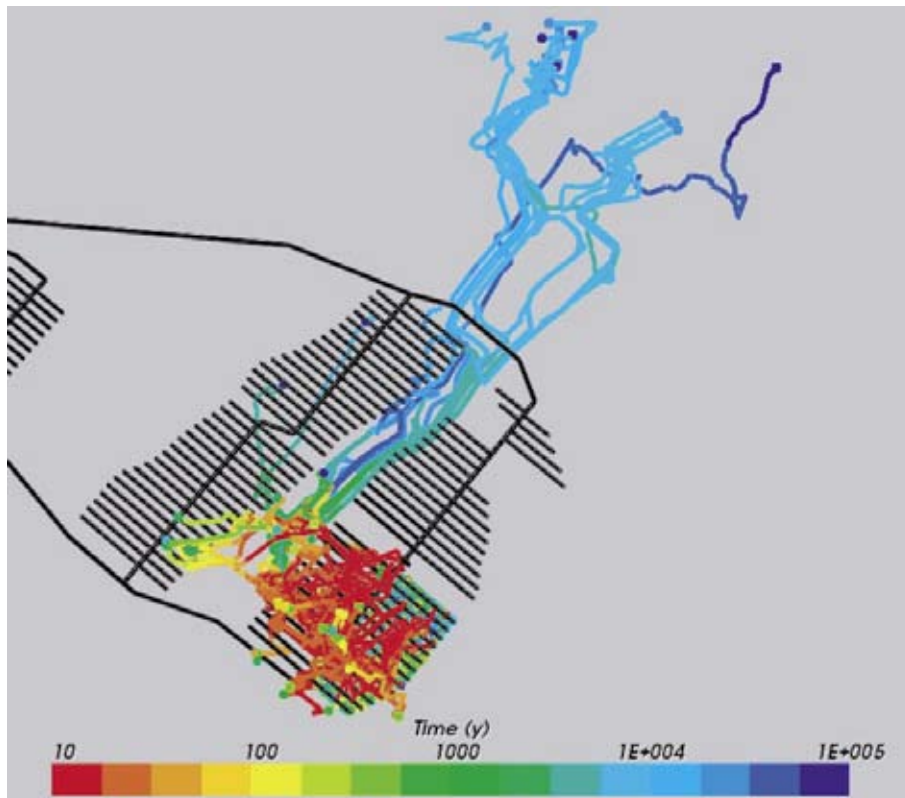


Figure 4-10. Particle tracks in the nested model for particles starting in the 604 canisters in the south-east corner of the repository. The paths are coloured by travel time along the path in the regional-scale nested model. A map view (top), and with the deterministic fracture zones superimposed (bottom). This case is for a release at 2,500 AD.

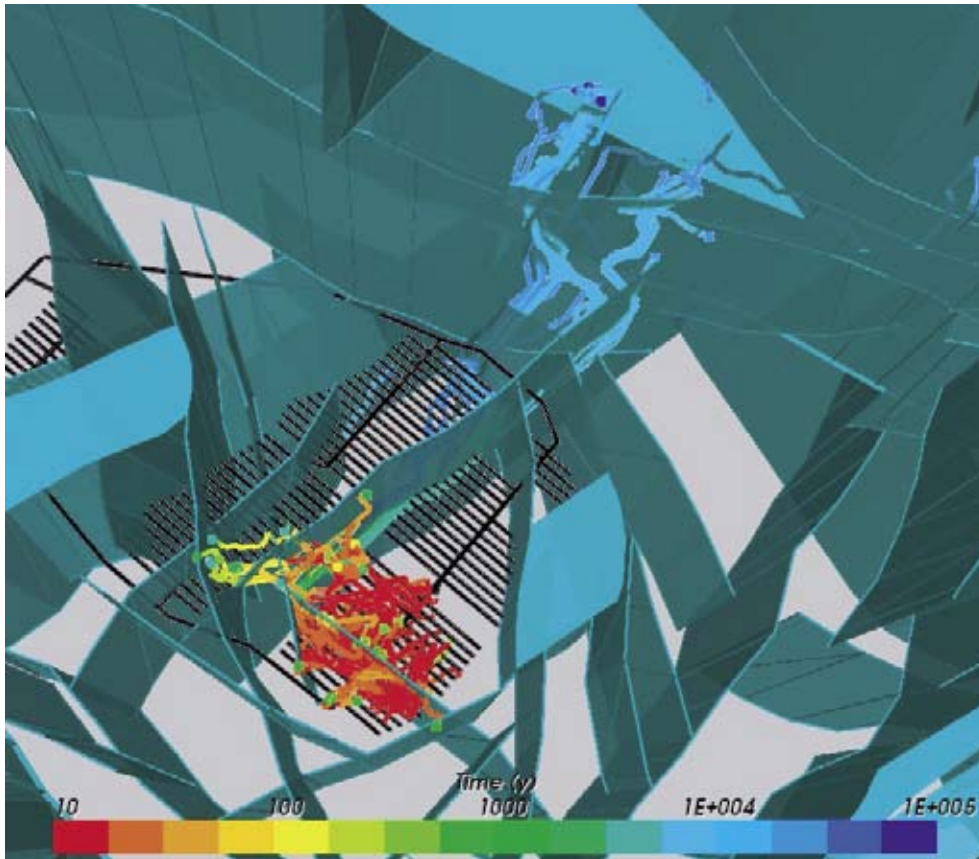


Figure 4-11. Particle tracks in the nested model for particles starting in the tunnel above the 604 canisters in the south-east corner of the repository. The paths are coloured by travel time along the path in the regional-scale nested model. The deterministic fracture zones are superimposed. This case is for a release at 2,500 AD.

A second set of particle tracks was calculated for the flow field at 12,000 AD, when the coastline would have receded beyond the north-east extent of the model. The path origins are shown in Figure 4-12, and are coloured by F-quotient for the whole model.

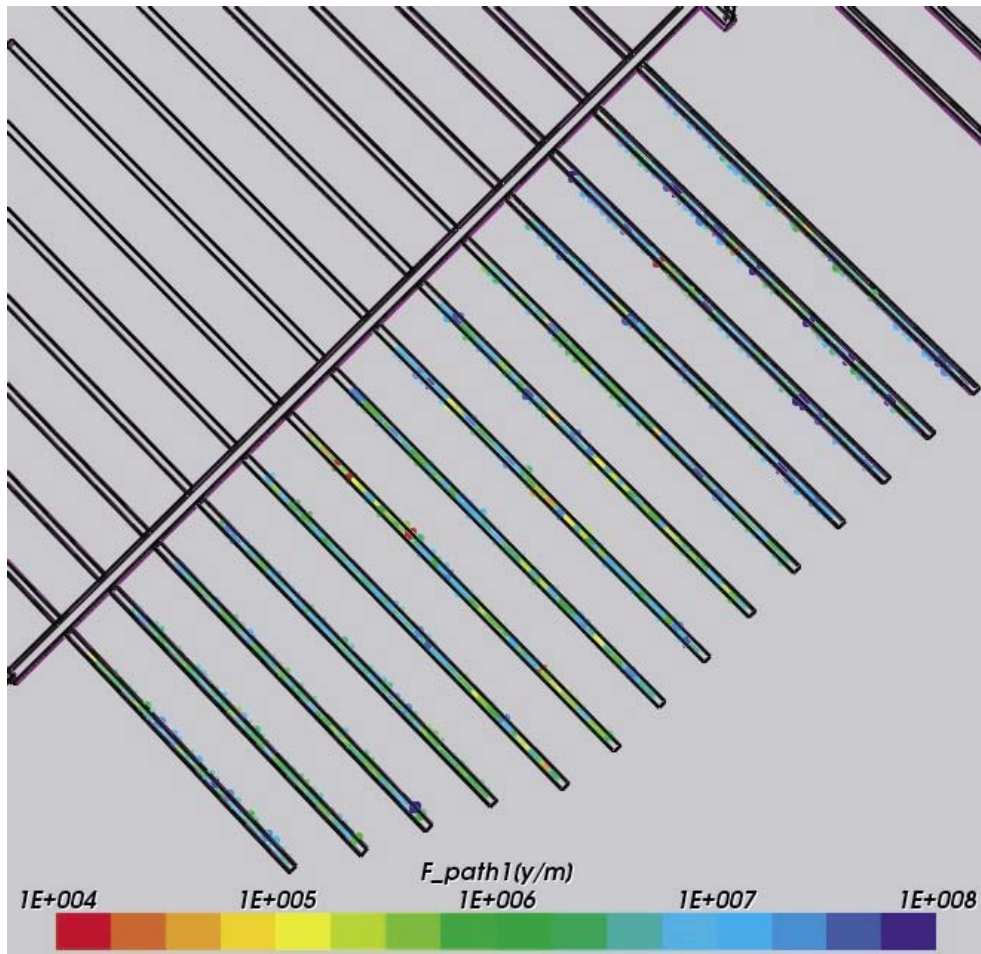


Figure 4-12. Start locations for particle tracks in the nested model for the south-east corner of the repository. Here, the 604 canister locations are coloured by the total F -quotient for pathlines in the nested model (canister-scale + regional-scale) and tracked with the flow-field at 12,000 AD.

The resulting particle tracks for release points in the tunnels above the canisters are shown in Figure 4-13. By comparison with Figure 4-11 it is clear that the flow field has altered significantly between 2,500 AD and 12,000 AD. At the latter time, there is no discharge in the northern region of the model, where the sea existed at 2,500 AD. Instead all of the tracks discharge at land surface above the repository, the great majority within 1,000 years of release.

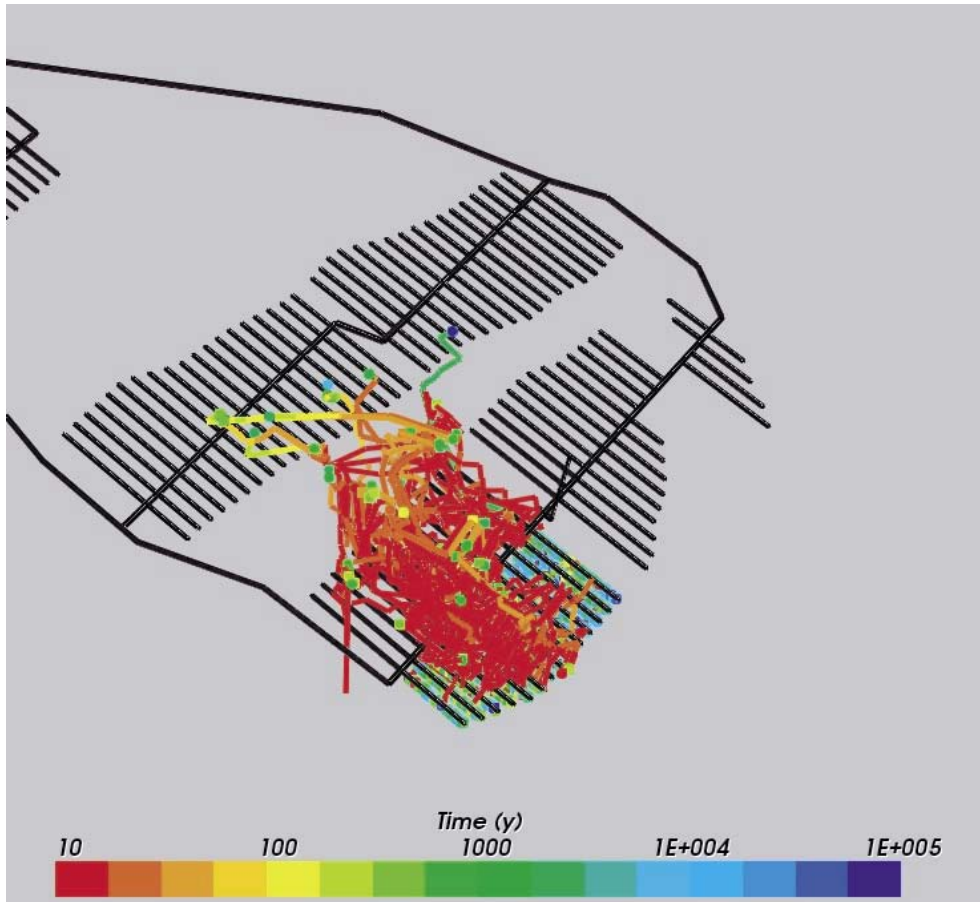


Figure 4-13. Particle tracks in the nested model for particles starting in the tunnel above the 604 canisters in the south-east corner of the repository. The paths are coloured by travel time along the path in the regional-scale nested model. This case is for a release at 12,000 AD.

The results presented above are for a repository backfill with a hydraulic conductivity of 10^{-10} m/s. To test the effect of the backfill permeability on the particle tracks, a set of calculations for 2,500 AD (pressure and transport) was undertaken for a higher backfill conductivity (10^{-8} m/s). The results from the particle tracking calculations are presented in Figure 4-14, where the upper plot shows the tracks for particles released in the canisters, and the lower plot is for particles released in the tunnels above the canisters. These plots are comparable with Figure 4-10 and Figure 4-11 for the lower conductivity backfill.

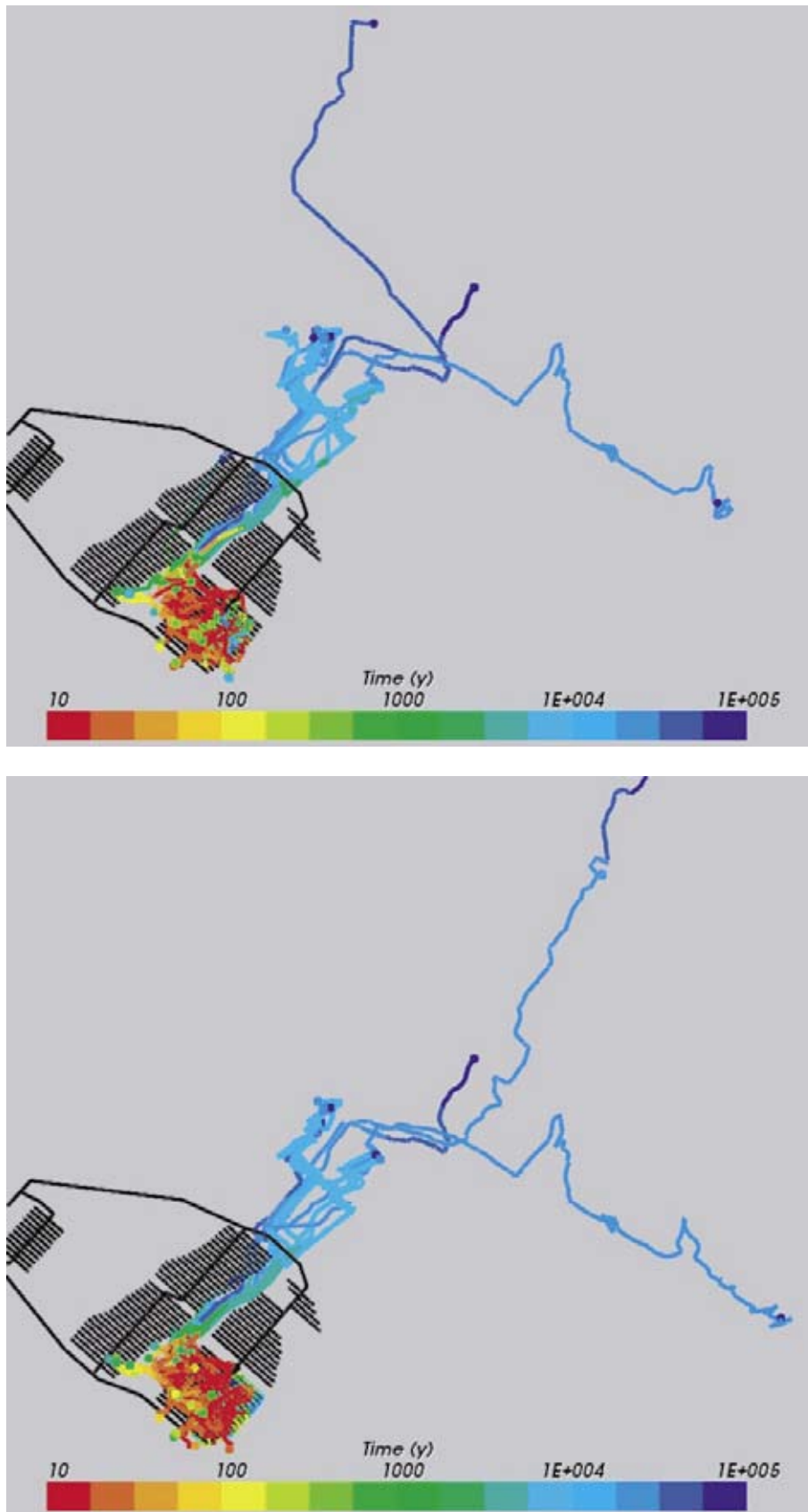


Figure 4-14. Particle tracks in the nested model in the south-east corner of the repository. This case is for higher back-fill conductivity and for a release at 2,500 AD. The paths are coloured by travel time along the path in the regional-scale nested model. Particles start in the 604 canisters (top) and in the tunnel above the canister (bottom).

Comparison of the figures shows that the greatest impact of the backfill permeability is to extend the region over which discharge occurs offshore. Both plots in Figure 4-14 show a small number of particle tracks that discharge to the sea bed further north and/or east than tracks in the corresponding lower-permeability backfill case. This indicates greater spreading of the discharge plume from the repository, with consequent reduction of contaminant concentration in some areas of the model. The main discharge locations, and the order-of-magnitude travel times associated with them, are very similar for both backfill permeability values. The pathlines in the vicinity of the repository are shown at two scales in Figure 4-15.

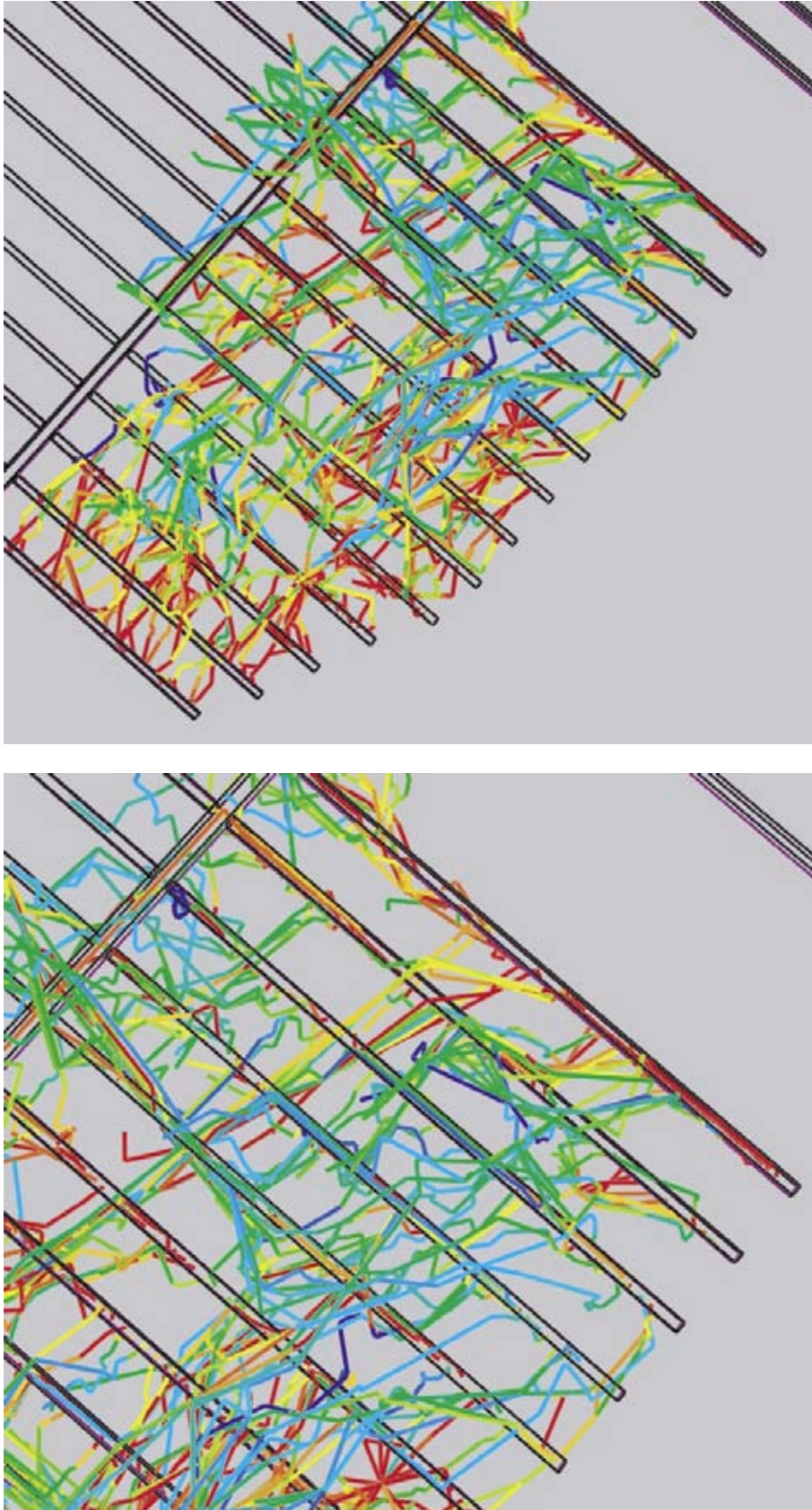


Figure 4-15. Particle tracks in the canister-scale model for particles starting in the 604 canisters in the south-east corner of the repository. This case is for higher back-fill conductivity and for a release at 2,500 AD. The paths are coloured by travel time along the path in the regional-scale nested model. The repository is superimposed.

5 Performance measures and recommendations for performance assessment

5.1 Inputs to safety assessment calculations using PROPER

The primary goal of the modelling described so far is to illustrate how input parameters can be obtained for safety assessment calculations. These parameters include flow rates in and around the repository structures for near-field modelling, transport pathway characteristics for far-field modelling and discharge areas for biosphere considerations. This section considers how to provide appropriate transport performance measures (PMs) as input to PROPER (Q, Tw and F-quotient) to ensure the results from Sections 3 and 4 can be used appropriately. The main objective is to demonstrate the viability of the proposed methodology in terms of using detailed flow calculations from canister-scale modelling and discrete transport models on the site-scale to derive PMs for essentially every canister.

5.1.1 Path definitions

The methodology for calculating transport within the nested model is to consider two possible flow routes that both consider pathways through firstly the canister-scale model and then the regional-scale model (a 'relay' approach from the canister-scale model to the regional-scale model). The first path (Path_f) allows release of radionuclides through a fracture in the rock intersecting the deposition hole that contains the canister. The second path (Path_t) considers release of radionuclides into both the engineered disturbed zone (EDZ) around the base of the tunnel and release into a fracture zone intersecting the deposition tunnel. In terms of the near-field model, Path_t considers transport of radionuclides through the backfill and/or EDZ associated with the deposition tunnel, whereas Path_f considers transport of radionuclides solely through the bentonite.

In addition, transport is calculated for Path_c in a purely CPM regional model. Path_c allows release of radionuclides through a fracture in the rock intersecting the deposition hole that contains the canister and considers release of radionuclides into both the EDZ around the base of the tunnel and release into a fracture intersecting the deposition tunnel. However, this model is cruder since it does not resolve the detailed groundwater flow and transport around individual canisters. It only calculates bulk flow velocities on a scale of 100 m.

In terms of the input for COMP23, the Qeq values are required for three pathways (Figure 5-1). In the nested model, path_Q1 is based on the value from Path_f, while path_Q2 and path_Q3 are based on the values from Path_t. For the pure CPM model, path_Q1, path_Q2 and path_Q3 are based on values from Path_c.

In summary, the definitions of the various paths are as follows:

- Path_f – is a pathway through the nested model for a release at a fracture that intersects a canister;
- Path_t – is a pathway through the nested model for a release in the tunnel above a canister;

- Path_c – is a pathway through the CPM model for a release in the flow field located at a position that corresponds to the canister;
- path_Q1 is the outflow from a COMP23 model corresponding to flow into a fracture at the top of the canister (compartment C-6);
- path_Q2 is the outflow from a COMP23 model corresponding to flow into the EDZ (compartment B-6);
- path_Q3 is the outflow from a COMP23 model corresponding to flow into the tunnel (compartments C-1 to C-3).

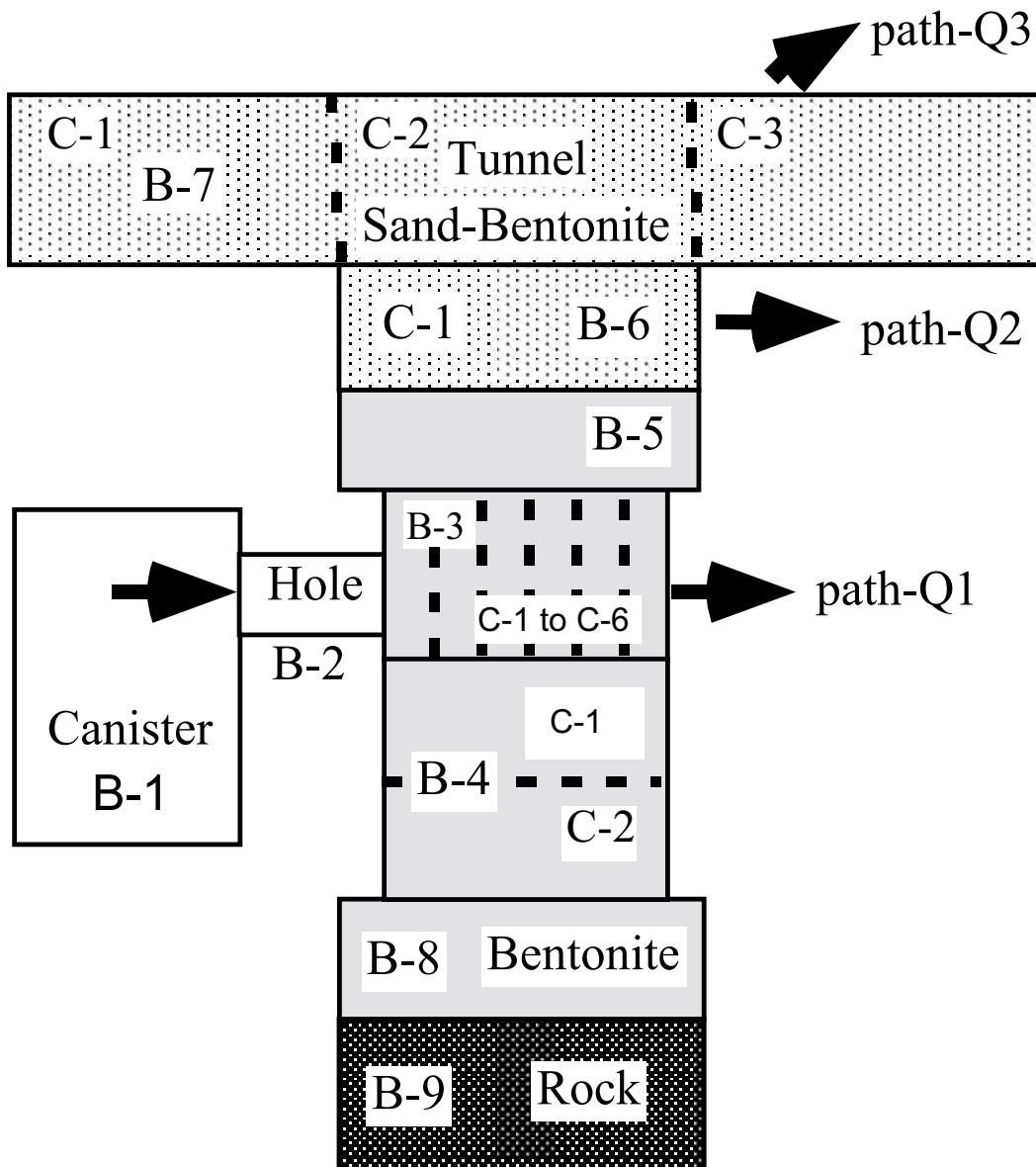


Figure 5-1. Schematic of model compartments of KBS3 repository.

5.1.2 Groundwater parameters

Groundwater flow conditions for each canister were computed using either a nested model or a CPM model. The parameters computed are the equivalent flow rate (Q_{eq} , $m^3 yr^{-1}$), the groundwater Darcy velocity (U_0 , $m yr^{-1}$), the groundwater travel time migration path (T_w , yr), and the F-quotient (F , $yr m^{-1}$). The equivalent flow rate and the groundwater Darcy velocity are input parameters to the near-field model, while the groundwater travel time and F-quotient are input parameters to the far-field model. Retention of radionuclides in fractured rock has been found to depend strongly on the relation between the flow wetted surface and the water flow rate. This may be taken into account using the F-quotient. For an individual fracture, the F-quotient is defined as twice the advective travel time divided by the transport aperture. The cumulative F-quotient for a pathway to the surface is the sum of the values for the individual fractures accessed by each path. COMP23, uses a derived parameter: the flow wetted surface per unit volume of water, A_w ($m^2 m^{-3}$). This can be derived as the F-quotient divided by the groundwater travel time in the transport pathway (F/t_w). These data are entered as a PTABLE, each row in the PTABLE representing a separate set of groundwater flow conditions for each canister.

5.1.3 Equivalent flow rate

As discussed in subsection 5.1.1, there are several pathways that release radionuclides from the near-field into the far-field (Figure 5-2). This release can be visualised as the diffusion of dissolved species from the bentonite into flowing water in the near-field fracture network (equivalent flow rate or Q_{eq}). The equivalent flow rate has been derived by solving the boundary layer theory equations for diffusive transport into flowing water. The value of Q_{eq} depends on the geometry of the contact area, the water flux, the flow porosity and the water diffusivity. There are three different calculations that consider the release pathways. Firstly, $Q_{eq_path_f}$ for the nested model considers the release of radionuclides into the fractured rock surrounding the deposition hole. Secondly, $Q_{eq_path_t}$ for the nested model represents the release of radionuclides into both the engineered disturbed zone (EDZ) and the tunnel. Thirdly, a CPM path based on flow through a pure CPM model is calculated for comparison with the type of models used in SR 97.

Radionuclide release into fractured rock for the nested model ($Q_{eq_path_f}$)

$Q_{eq_path_f}$ considers release of radionuclides into the fractured rock surrounding the deposition hole, and hence the particle starts within a DFN canister-scale model and can eventually move into the CPM regional-scale model.

Several fractures may intersect the canister. For reasons of making a conservative assumption, the flux into all fractures that intersect the canister and contribute to advective flow away from the canister are included in the calculation of Q_{eq} . That is, an effective flow rate is calculated for all fractures that cut both the canister and at least one other fracture. These effective flow rates are summed for the canister to give the total Q_{eq} . The equivalent groundwater flow rate for $Q_{eq_path_f}$ (particles starting in the DFN model close to the canister; path_Q1) can be written as:

$$Q_{eq_path_f} = \sum_f \left(2Q_f \sqrt{\frac{4D_w t_{wf}}{\pi}} \right), \quad t_w = \frac{\square \cdot \alpha_t}{Q_f} \quad \text{Equation 5-1}$$

If there are several fractures intersecting a single canister, then a conservative approach to calculate the equivalent groundwater flow rate requires the flow to be summed across all the fractures. Hence, the equivalent Darcy velocity for all fractures intersecting the canister is:

$$U_{0_path_f} = \frac{(\sum_f Q_f)}{W_c} \quad \text{Equation 5-2}$$

where:

- D_w is the diffusivity in water, [$m^2 \text{ year}^{-1}$];
- t_w is the time the water is in contact with the source area, [year];
- L is the length of the fracture intersection with the wall of the deposition hole, [m];
- $U_{0_path_f}$ is the average Darcy velocity in the fracture system around the canister (water flux) [$m^3 \text{ m}^{-2} \text{ year}^{-1}$];
- Q_f is the average flux per unit fracture length in the fracture adjacent to the deposition hole ($m^2 \text{ yr}^{-1}$);
- α_t is the transport aperture adjacent to the deposition hole (m);
- W_c is the canister height.

Radionuclide release into the tunnel and EDZ for the nested model (Qeq_path_t)

Qeq_path_t combines the release of radionuclides into the EDZ and tunnel (used to derive Qeq for path_Q2 and path_Q3). Here the particles are released within the repository some distance from the canister. They therefore start within the small canister-scale CPM part of the model and can move into the canister-scale DFN and then the regional-scale DFN model and so on. It should be noted that travel times and F-quotient contributions associated with parts of any pathway spent in the tunnel have been intentionally removed from the transport PMs. Retention in tunnels is to be handled in future safety assessments.

The equivalent groundwater flow rate for Qeq_path_t (for particles starting in the CPM model, some distance from the canister; path_Q2 and path_Q3) can be written as:

$$Q_{eq_path_t} = 2 \cdot W \cdot U_0 \cdot U_i \cdot \sqrt{\frac{4 \cdot D_w \cdot t_w}{\pi}} \quad \text{Equation 5-3}$$

However,

$$t_w = \frac{L \cdot \varepsilon}{U_0} \quad \text{Equation 5-4}$$

and hence

$$Q_{eq_path_t} = 4 \cdot W \cdot U_i \cdot \sqrt{\frac{D_w \cdot L \cdot \varepsilon}{\pi}} \cdot U_0^{0.5} \quad \text{Equation 5-5}$$

This can be rewritten as:

$$Q_{eq_path_t} = A \cdot U_0^{0.5}, \quad \text{where} \quad A = 4 \cdot W \cdot U_i \cdot \sqrt{\frac{D_w \cdot L \cdot \varepsilon}{\pi}} \quad \text{Equation 5-6}$$

Here:

- U_0 is the Darcy velocity for the advective pathway (water flux), [$\text{m}^3 \text{m}^{-2} \text{year}^{-1}$];
- U_i is a scaling factor to allow for pessimism in the groundwater velocity;
- W is the contact height for the advective pathway, [m];
- D_w is the diffusivity in water, [$\text{m}^2 \text{year}^{-1}$];
- t_w is the time the water is in contact with the source area, [year];
- L is the length of the advective pathway in contact with the source, [m];
- ε is the flowing porosity of the material surrounding the source area, [-].

For $Q_{eq_path_t}$ (path_Q2 and path_Q3), different values of U_i , W , L and ε may be appropriate to calculate the scaling factor A for each path.

Release Path_c for the regional-scale CPM model

Because the CPM model uses a coarse 100 m scale mesh, then there is not the resolution to consider individual canister-scale pathways. The equivalent flow rates for path_Q1, path_Q2 and path_Q3 are all based on the Darcy velocity at the release point. The CPM model considered one case releasing radionuclides into both the fractured rock surrounding the deposition hole (Path_Q1) and into the EDZ (Path_Q2). The equivalent flow rate has been calculated, as above, for the CPM model (Equation 5-6). Note, that a fracture porosity for Forsmark of about 10^{-5} is used based on the DFN model. Also, a flow wetted surface per volume of rock of $0.1 \text{ m}^2/\text{m}^3$ has been used in the rock mass, and 1.0 m^{-1} has been used in a fracture zone to calculate F-quotients for paths in the CPM model. These are values that have been used consistently in the paleo-hydrogeology modelling for both Forsmark and Simpevarp. However, it may be more appropriate to derived vales based on the current fracture concepts in a more self-consistent methodology. One approach would be to use twice the reciprocal of matrix block size MBS derived in Section 2.3.3, although an appropriate fracture length scale cut-off has to be chosen. Based on Table 2-4 and using a fracture length cut-off of 10 m, would indeed support a value for flow wetted surface of about 0.1 to 0.2.

The formula used for calculating the equivalent flow rate in the CPM model is:

$$Q_{eq_path_c} = 4 \cdot W \cdot U_i \cdot \sqrt{\frac{D_w \cdot L \cdot \varepsilon}{\pi}} \cdot U_0^{0.5} \quad \text{Equation 5-7}$$

5.1.4 Parameter distributions

One of the important measures in carrying out canister-scale DFN modelling is the degree of connectivity between the canisters and the fractures. Figure 5-2 shows the distribution of the number of fractures intersecting a canister for two cases. The blue bars show the distribution for a fracture network containing fractures down to a length of 3.5 m. In this case, there are a few canisters (<10) of the 604 that do not intersect a fracture. The remainder intersect between 1 and 12 fractures, with a modal value of 3 intersections. In contrast to this distribution, if the fracture distribution is truncated at a transmissivity of $10^{-9} \text{ m}^2/\text{s}$ (purple bars), well over half of the canisters do not intersect a fracture, and of those that do, the most likely number of intersections is one (maximum 4). This truncation limit of $10^{-9} \text{ m}^2/\text{s}$ is considered since it is about the detection limit for the Posiva flow-log, so all flowing fractures modelled with transmissivities less than this value are in a sense hypothetical.

These cases clearly indicate two very different interactions between the repository and the surrounding fracture network. In the first case (blue bars), >95% of the canisters have an intersection with the network compared with ~45% in the latter case (purple bars). For canisters that do not intersect a fracture, transport from the canisters is most likely to occur via a tunnel and then to the fracture network. (In the combined CPM/DFN canister-scale model, this is the only other transport route. In reality, transport via the rock matrix is possible, but unlikely given the very low permeability of the host rock.)

Fractures Intersecting Canister

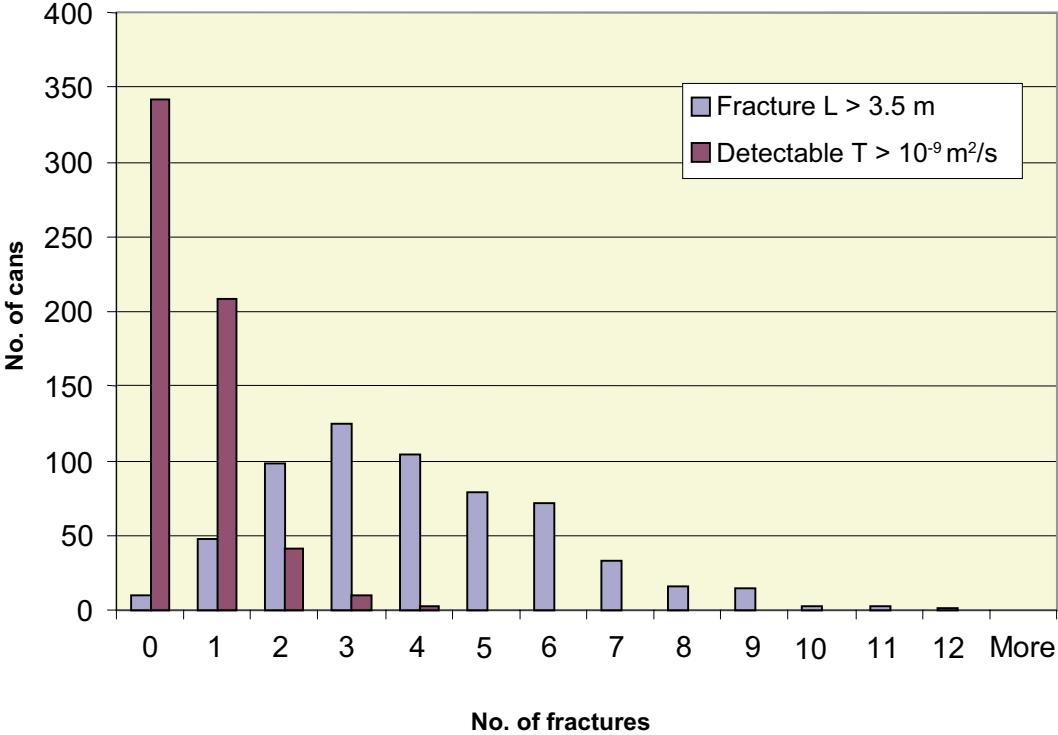


Figure 5-2. Distribution of the number of fractures intersecting a canister in the canister-scale model of 604 canisters. Two cases are shown: based on counting all fractures down to a length of 3.5 m; and only those fractures with transmissivity > 1 10⁻⁹ m²/s (about the detection limit for the Posiva flow-log at Forsmark).

The distribution of flows (Q_{eq}) from the canisters via the fracture network and the tunnels at 2,500 AD is illustrated in Figure 5-3 for both the CPM model and the nested model. For the CPM model, Q_{eq1} is presented only, whereas separate distributions are given for the nested model. (Note that the histogram for the nested model Path_f contains information for only 594 canisters, the remaining 10 having no intersection with a fracture.) The flows in the EDZ (Path_t2) and in the tunnel (Path_t3) have been calculated from U_0 using Equation 5-6 in which the variables have the meanings assigned in subsection 5.1.3 and the values given below:

	Path_t2	Path_t3	Path_c
W (m)	2.0	2.5	5.0
L (m)	2.8	7.0	2.8
D_w (m ² /yr)	0.032	0.032	0.032
ε (-)	10^{-4}	10^{-4}	10^{-5}

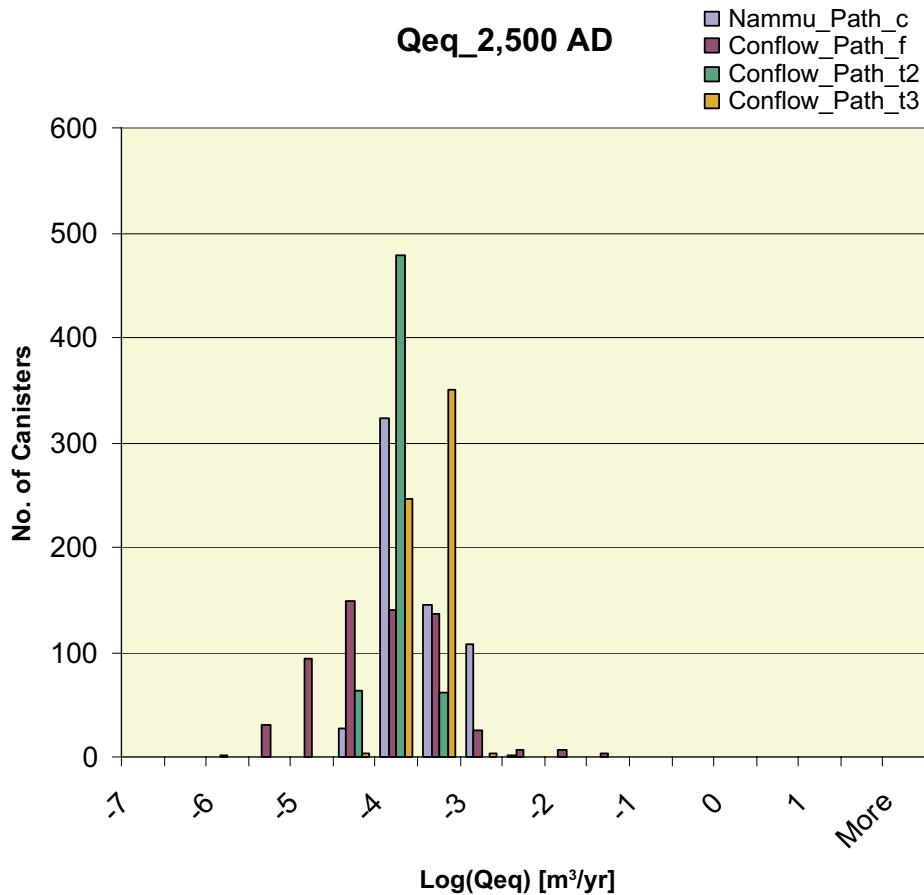


Figure 5-3. Distribution of Q_{eq} in the canister-scale model of 604 canisters for a release of particles at 2,500 AD. The four cases shown are for: the CPM model; the nested model for Path_f (in fractures adjacent to the canister); the nested model for Path_t2 (in the EDZ); the nested model for Path_t3 (in the tunnel).

All the Qeq distributions show a degree of consistency, with the majority of canisters having flows in the range 10^{-3} to 10^{-5} m³/yr, with a mean value close to 10^{-4} m³/yr. The main difference in the data is that the distribution for nested model Path_f is broader than the other three, reflecting the range of fracture sizes/transmissivities into which releases from canisters occur.

Table 5-1. Performance statistics: Distribution of $\log_{10}(\text{Qeq [m}^3/\text{yr]})$ at 2,500 AD for the CPM model (Path_c) and Path_f, Path_t2 and Path_t3 for the nested model.

	CPM model	Nested model		
	Path_c	Path_f	Path_t2	Path_t3
Mean	-3.967	-4.409	-4.251	-3.955
Median	-4.086	-4.454	-4.250	-3.955
5th percentile	-4.494	-5.536	-4.576	-4.281
10th percentile	-4.445	-5.315	-4.507	-4.211
25th percentile	-4.309	-4.923	-4.401	-4.105
75th percentile	-3.707	-3.899	-4.102	-3.806
90th percentile	-3.119	-3.576	-4.000	-3.704
95th percentile	-3.093	-3.378	-3.942	-3.646
Std deviation	0.456	0.726	0.197	0.197
Variance	0.208	0.526	0.039	0.039
Max value	-2.997	-1.558	-3.697	-3.401
Min value	-4.575	-6.276	-4.875	-4.579

Figure 5-4 shows the distribution of Darcy velocity (m/yr) in the CPM and nested models. As in Figure 5-3, distributions for flows via the fracture network and via the tunnels are provided for the nested model. The figure clearly indicates that there is a large degree of overlap in the three distributions, with modal Darcy velocities being of the order of 10^{-4} m/yr. However, it is clear that the distributions for the CPM model and the nested model Path_t (tunnels) are narrower and at a lower range than the distribution for the nested model Path_f (fractures). The highest values for the CPM and Path_t distributions are about 10^{-3} m/yr, whereas about 100 canisters have a Path_f Darcy velocity of about 10^{-2} m/yr, with a few values ranging up to about 10^{-1} m/yr.

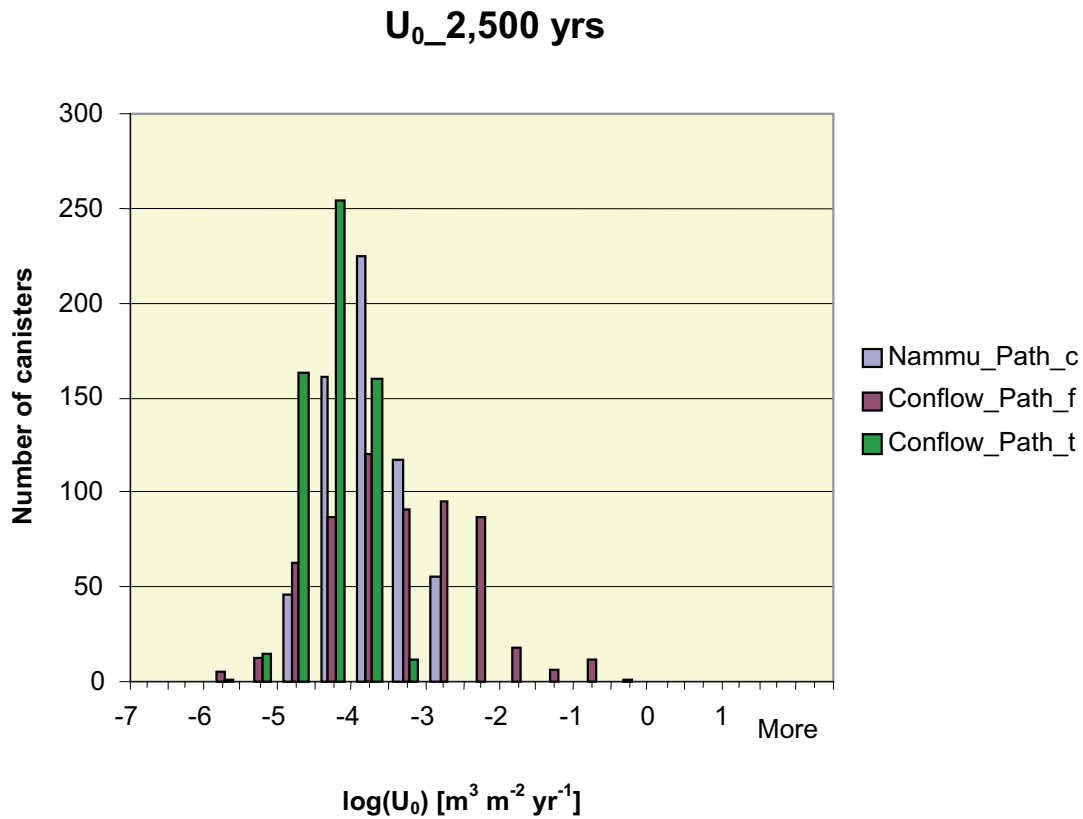


Figure 5-4. Distribution of Darcy velocity (U_0 in the CPM, U_{0f} in the DFN) in the canister-scale model of 604 cans for a release of particles at 2,500 AD. The three cases shown are for: the CPM model Path_c; the nested model for Path_f (in fractures adjacent to the canister); and the nested model for Path_t (in the tunnel).

The distributions of travel time for the CPM and nested models at 2,500 AD (Figure 5-5) show a distinct difference between the two models. The CPM model shows a uni-modal distribution with the vast majority of travel times in the range 1,000 to 10,000 years. However, both sets of paths from the nested model (i.e. via fractures and tunnels) show a bi-modal distribution, with travel times likely to be either in the range 100 to 1,000 years or 10,000 to 100,000 years. The latter distributions clearly fit with the plots of particle tracks given in Figure 4-10 and Figure 4-11 for particles originating in canisters and tunnels respectively. The short travel times correspond to the tracks that discharge in the region above the repository, whereas the long travel times correspond to discharge points on the sea bed to the north of the repository. From Figure 5-5 it is clear that the CPM model does not capture the very short return times (some as short as 10 years) calculated in the nested model (i.e. the fracture network representation provides for short, fast paths to the surface). (See also Figure 5-6, where a similar picture emerges for pathlength.) Statistics for the travel time for the three paths are given in Table 5-2.

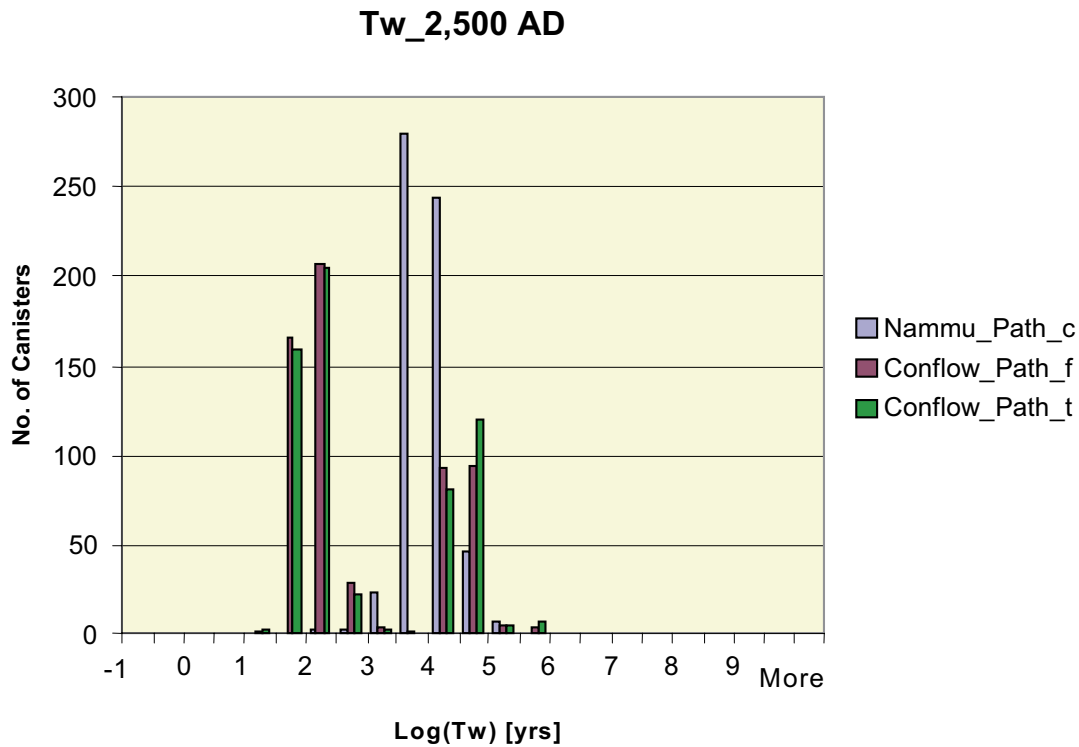


Figure 5-5. Distribution of travel time, t_w , in the nested model with a release from 604 canisters at 2,500 AD. The three cases shown are for: the CPM model (Path_c); the nested model for Path_f (in fractures adjacent to the canister); and the nested model for Path_t (in the tunnel).

Table 5-2. Performance statistics: Distribution of log₁₀(travel time [yr]) for the CPM model and Path_f and Path_t for the nested model at 2,500 AD.

	CPM model	Nested model	
	Path_c	Path_f	Path_t
Mean	3.521	2.418	2.480
Median	3.494	1.751	1.737
5th percentile	3.010	1.244	1.258
10th percentile	3.193	1.336	1.342
25th percentile	3.316	1.482	1.476
75th percentile	3.670	3.956	3.984
90th percentile	3.973	4.148	4.168
95th percentile	4.193	4.226	4.359
Std deviation	0.361	1.202	1.250
Variance	0.130	1.445	1.564
Max value	4.663	5.031	5.026
Min value	1.729	0.833	0.720

Figure 5-6 shows the distributions of pathlength at 2,500 AD for both the CPM and nested models. The picture is very similar to that of Figure 5-5 (travel time), with the CPM model showing a uni-modal distribution, and the nested model showing a bi-modal distribution. For the nested model, the distributions for tracks via the fractures and via the tunnels are very similar, with a cluster of paths between 1,000 and 3,000 m in length and a smaller distinct cluster around 10,000 m in length (corresponding to discharge above the repository and to the sea bed, respectively). The paths in the CPM model tend to fall into the range 3,000 to ~10,000 m and have a correspondingly longer travel time (see Figure 5-5). Statistics for the pathlength are given in Table 5-3.

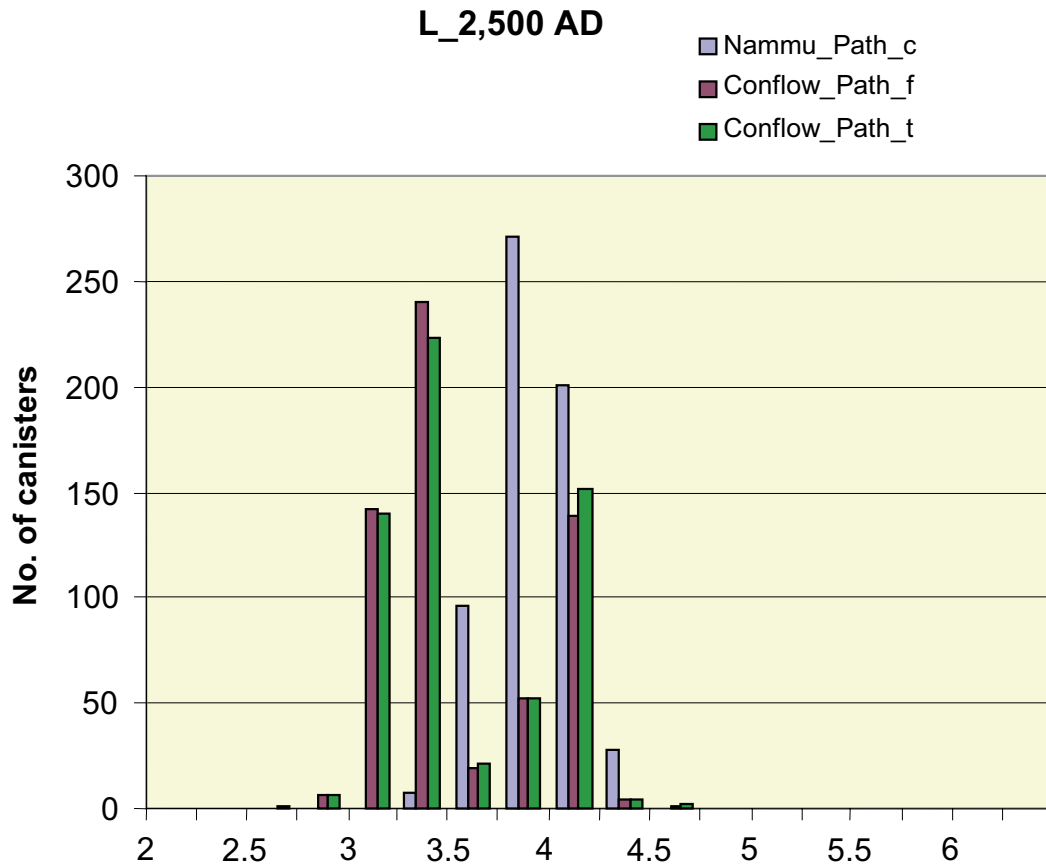


Figure 5-6. Distribution of pathlength, L , in the nested model with a release from 604 canisters at 2,500 AD. The three cases shown are for: the CPM model; the nested model for Path_f (in fractures adjacent to the canister), and the nested model for Path_t (in the tunnel).

Table 5-3. Performance statistics: Distribution of log₁₀ (pathlength [m]) for the CPM model and Path_f and Path_t for the nested model at 2,500 AD.

	CPM model	Nested model	
	Path_c	Path_f	Path_t
Mean	3.686	3.286	3.307
Median	3.694	3.127	3.131
5th percentile	3.468	2.877	2.891
10th percentile	3.483	2.931	2.922
25th percentile	3.531	3.002	3.004
75th percentile	3.820	3.746	3.755
90th percentile	3.906	3.793	3.803
95th percentile	3.993	3.819	3.827
Std deviation	0.188	0.364	0.377
Variance	0.035	0.133	0.142
Max value	4.160	4.380	4.387
Min value	3.022	2.625	2.499

Figure 5-7 illustrates the distribution of the F-quotient in the nested model (Path_f and Path_t) and the CPM model. The corresponding statistics are given in Table 5-4. The mean value for all three distributions is close to 10^7 yr/m, but the range of values is much broader for the two nested model paths. About 40% of each of the paths in the nested model have an F-quotient less than the predominant value range in the equivalent CPM representation (which holds 67% of the CPM sample). Conversely, there are also some 15% of the nested model paths that have an F-quotient greater than or equal to 3×10^8 yr/m, compared with only 1% in the CPM model.

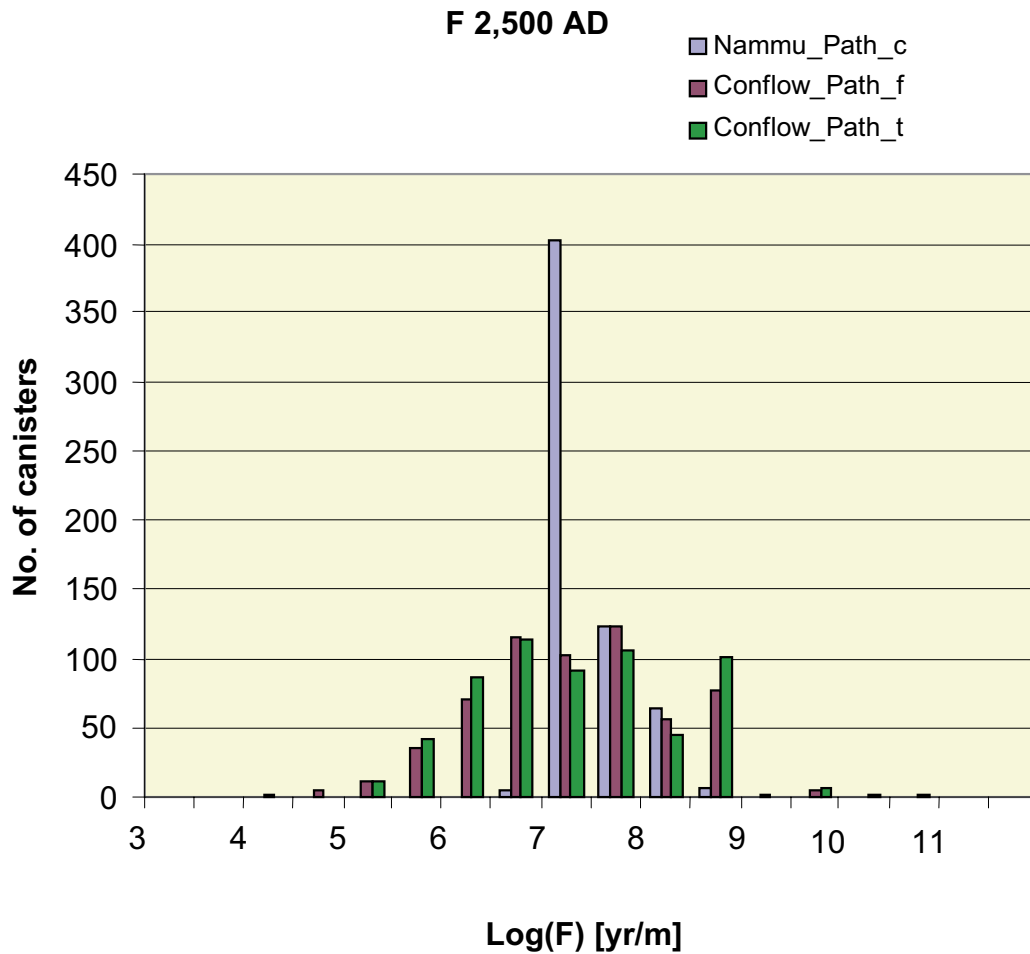


Figure 5-7. Distribution of F-quotient in the nested model with a release from 604 canisters at 2,500 AD. The three cases shown are for: the CPM model; the nested model for Path_f (in fractures adjacent to the canister); and the nested model for Path_t (in the tunnel).

Table 5-4. Performance statistics: Distribution of \log_{10} (F-quotient [yr/m]) for the CPM model and Path_f and Path_t for the nested model at 2,500 AD.

	CPM model	Nested model	
	Path_c	Path_f	Path_t
Mean	6.999	6.791	6.816
Median	6.894	6.791	6.755
5th percentile	6.601	5.265	5.328
10th percentile	6.659	5.567	5.572
25th percentile	6.767	6.114	6.072
75th percentile	7.143	7.454	7.529
90th percentile	7.556	8.056	8.067
95th percentile	7.710	8.089	8.104
Std deviation	0.356	0.943	0.970
Variance	0.127	0.888	0.942
Max value	8.445	9.278	10.119
Min value	6.417	3.781	4.503

Flows in the nested model can be relatively complex, with particle tracks that enter the fracture network potentially entering and leaving the tunnel system at a later time. The distribution of pathlength spent in the tunnels for paths that start in the fractures and in the tunnels is shown in Figure 5-8 for the base case backfill hydraulic conductivity of 10^{-10} m/s. The figure shows that 100% of the tracks that start in tunnels have between 5 and 10% of their pathlength within the tunnel system. For the paths that start in the fractures, >75% of them have 0–5% of their pathlength within tunnels, with the majority of the remainder having 5–10% within tunnels, and a small number having 10–15%. Therefore for a backfill conductivity around or less than 10^{-10} m/s, then the tunnel is not an important transport pathway and so Path_f and Path_t are very similar, at least when taken statistically over many canisters.

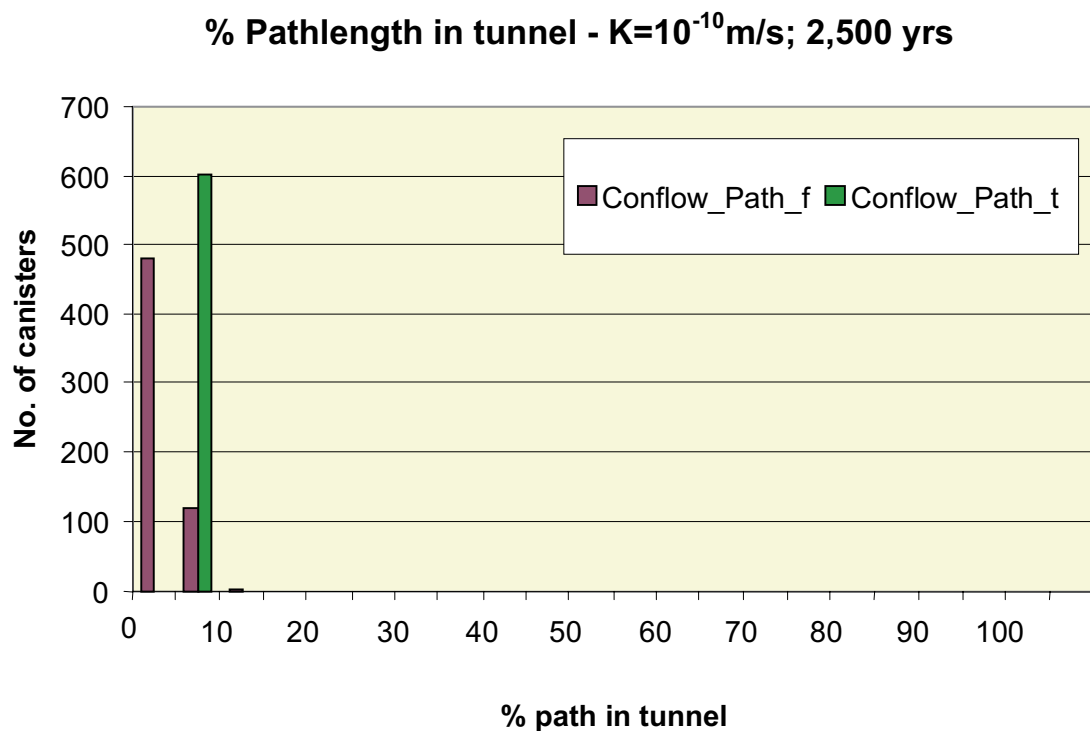


Figure 5-8. Distribution of the percentage of the pathlength in the tunnel compared to the whole pathway for the nested model with a release from 604 canisters at 2,500 AD. The two cases shown are for: the nested model for Path_f (in fractures adjacent to the canister), and the nested model for Path_t (in the tunnel).

Figure 5-9 illustrates the correspondence between the value of Q_{eq} and the travel time for paths in the CPM and nested models at 2,500 AD. Flows into the fractures, EDZ and tunnel are shown for the nested model. The figure clearly shows the split into two sets of travel time data; one between 10 and 100 years, the other between 10,000 and 100,000 years. These correspond to the split in pathways that discharge vertically above the repository, and those that go northwards to the sea. Paths from fractures, EDZ and tunnel all appear in both sets of data, with the last two sets being grouped around a Q_{eq} value of 10^{-4} m³/yr. The range of Q_{eq} values for the nested model fractures is seen to be wider than all others, the great majority being between 10^{-3} and 10^{-6} m³/yr, with a few outliers, especially at higher flows.

In contrast, the Nammu results are grouped between Q_{eq} values of 10^{-3} and 10^{-5} m³/yr, with a distinct banding in the data (i.e. groups with very similar Q_{eq} values) due to the homogenisation of flow due to the low mesh resolution. The travel times range from ~1,000 years up to ~30,000 years in each of these bands. Very few of the Nammu paths have travel times of 100 years or less, indicative of the fact that the paths all head towards the coast in the CPM model and do not discharge on the surface above the repository.

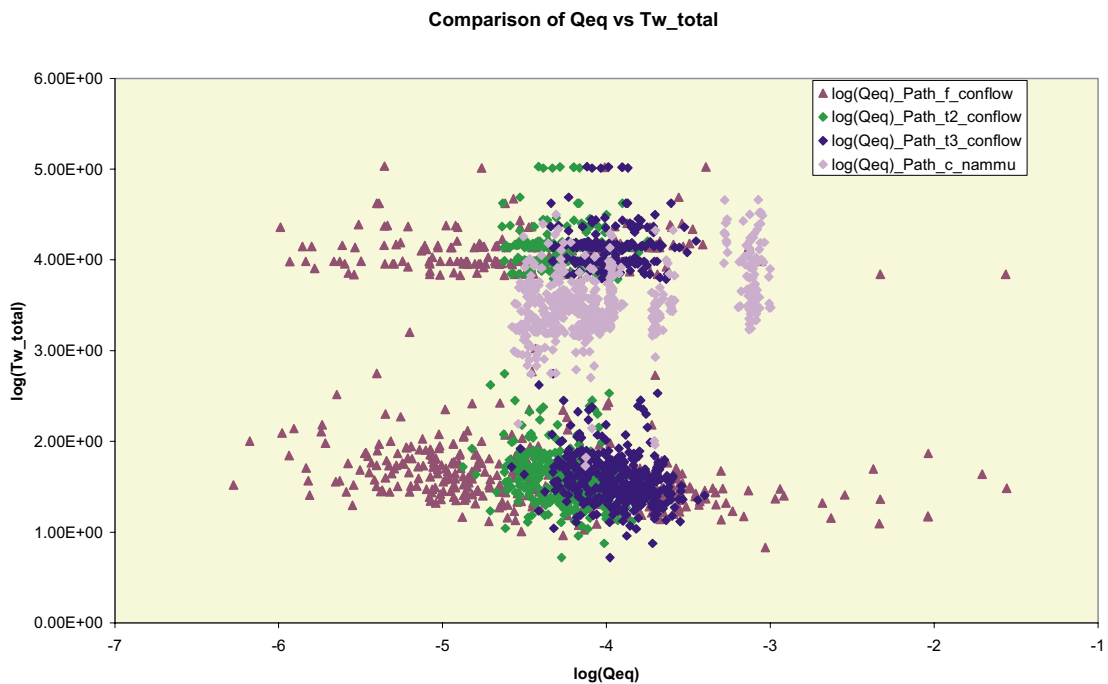


Figure 5-9. Cross-plot of Q_{eq} and travel time, t_w , for pathways in the nested model with a release from 604 canisters at 2,500 AD. The four cases shown are for: the CPM model, the nested model for Path_f (in fractures adjacent to the canister), the nested model for Path_t2 (in the EDZ) and the nested model for Path_t3 (in the tunnel).

The cross-plot of F-quotient against Qeq (Figure 5-10) shows less structure than the previous figure. There is a preponderance of data points in the centre of the graph, with Qeq ranging between 10^{-5} and $3 \cdot 10^{-4}$ m³/yr and the F-quotient in the range 10^5 to 10^8 yr/m. These data belong to all of the paths. A significant group of data points from the Nammu model appear at a Qeq value of $\sim 10^{-3}$ m³/yr and in the F-quotient range 10^7 and 10^8 yr/m. It is noticeable that the F values from the CPM model occupy a smaller range (by several orders of magnitude) than those from the nested model.

The other significant feature of the cross-plot is that the data points at the extremes of the Qeq range are all from the fracture path in the nested model (Path_f). Again, this illustrates the range of fracture sizes/transmissivities that provide the transport path in the nested model.

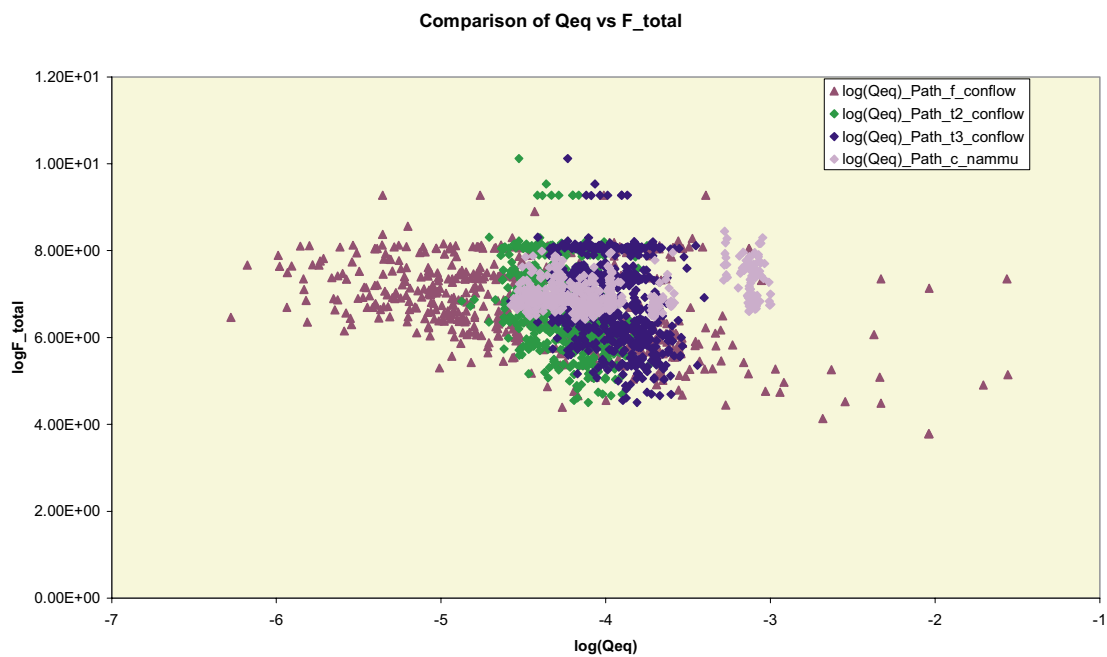


Figure 5-10. Cross-plot of Qeq and F-quotient for pathways in the nested model with a release from 604 canisters at 2,500 AD. The four cases shown are for: the CPM model, the nested model for Path_f (in fractures adjacent to the canister), the nested model for Path_t2 (in the EDZ) and the nested model for Path_t3 (in the tunnel).

Figure 5-11 illustrates the effect of the canister-scale model on the complete transport pathway, i.e. it demonstrates the effect of the first few fractures on transport. In terms of the travel time (upper, blue line), some 30% of the paths have an insignificant proportion of their travel time within the canister-scale model. At the other end of the scale, there are no paths that spend all of their time within the local model. Between the extremes, the graph shows the number of paths gradually diminishing as the proportion of time spent close to the canisters increases.

The behaviour of the F-quotient is quite different, as shown by the lower (pink) line in Figure 5-11. Between values of the F-ratio of 0 and 0.2, there is a rapid rise in the number of paths showing some influence of the local fractures on the F-quotient. However, some 35–40% of the paths have less than 20% of their total F-quotient associated with the fractures local to the canister. For an F-ratio between 0.8 and 1, a further 35–40% of the canisters contribute to the cumulative plot, i.e. 35–40% of the paths have 80% or more of their total F-quotient associated with the fractures in the canister-scale model. Between these extremes the plot is almost linear. Hence, it is hard to make any general conclusion about where most retention occurs and whether approximations can be made e.g. only taking T_w and F from the regional-scale. It is clear that for T_w a significant retention is in the canister-scale (first 50 m here), but for F there are all cases for the canister-scale dominating to the regional-scale. It may be interesting to correlate this ratio to the values themselves (e.g. does the canister-scale only dominate for slower paths?).

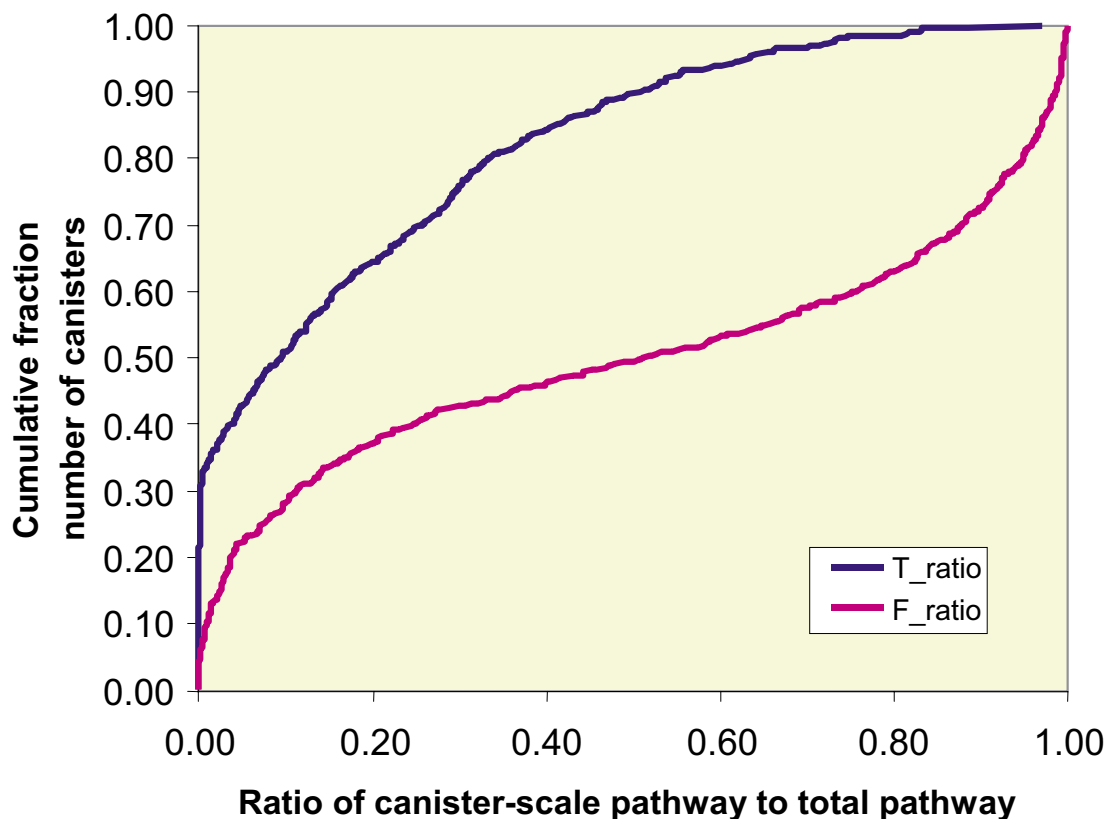


Figure 5-11. Cumulative distribution of the ratios of t_w and F -quotient in the canister-scale model compared to the total values for the nested model for a release from 604 canisters into Path_f at 2,500 AD. A ratio of 0 means there is little retention in the immediate fractures around the canister. A ratio of 1 means all of the retention is in the first few fractures.

Figure 5-12 shows distributions of U_0 for three cases for each of Path_f (fractures) and Path_t (tunnel). The three cases are:

- base case backfill permeability at 2,500 AD;
- base case backfill permeability at 12,000 AD;
- backfill permeability of 10^{-8} m/s at 2,500 AD.

It is clear that the distributions for flows into the fracture network (Path_f) are very similar for all three cases, with a mean U_0 of around 10^{-4} m/yr. The distributions of flows through the tunnel (Path_t) are also very similar for the two cases with base case backfill permeability; in this case the mean flow is of the order of $3 \cdot 10^{-5}$ m/yr. For the more permeable backfill, the mean flow into the tunnels rises to around $3 \cdot 10^{-3}$ m/yr. An increase in the latter value would be expected given a two order of magnitude increase in the backfill hydraulic conductivity and the effect that this would have in focusing groundwater flows through the repository structure.

The distributions of travel time for Path_f and Path_t in the nested model are shown for three cases in Figure 5-13, the cases being for particle releases at 2,500 AD and 12,000 AD for the base-case backfill conductivity, and at 2,500 AD for an increased backfill conductivity. The statistics corresponding to the plots are given in Table 5-5.

The upper plot in Figure 5-13 (Path_f) shows a distinct difference between the travel times for the two cases at 2,500 AD and the case at 12,000 AD. For the earlier release time, the travel times form two groups, one predominantly in the range 10 to 300 years and one predominantly in the range 10,000 to 100,000 years. The distributions are very similar for both the base case and increased backfill permeability, with a mean travel time of about 250 years. As noted earlier, the split in the travel time distribution relates to the existence of two discharge areas in the model, one above the repository (short travel times) and one on the sea bed (long travel times). This split is evident in the cross-plot of Q_{eq} against T_w in Figure 5-9. At 12,000 AD, when the sea has retreated north-east, all discharges are close to the repository location; the distribution of T_w is therefore almost entirely in the range 10 to 300 years, with a mean of ~40 years.

A very similar pattern of travel time distribution is seen in the lower plot of Figure 5-13, for release to the tunnels (Path_t). Again the long travel times evident in the two cases at 2,500 AD do not appear in the distribution for 12,000 AD. Mean travel times are of the order of 300 years for releases at 2,500 AD and 35 years for releases at 12,000 AD.

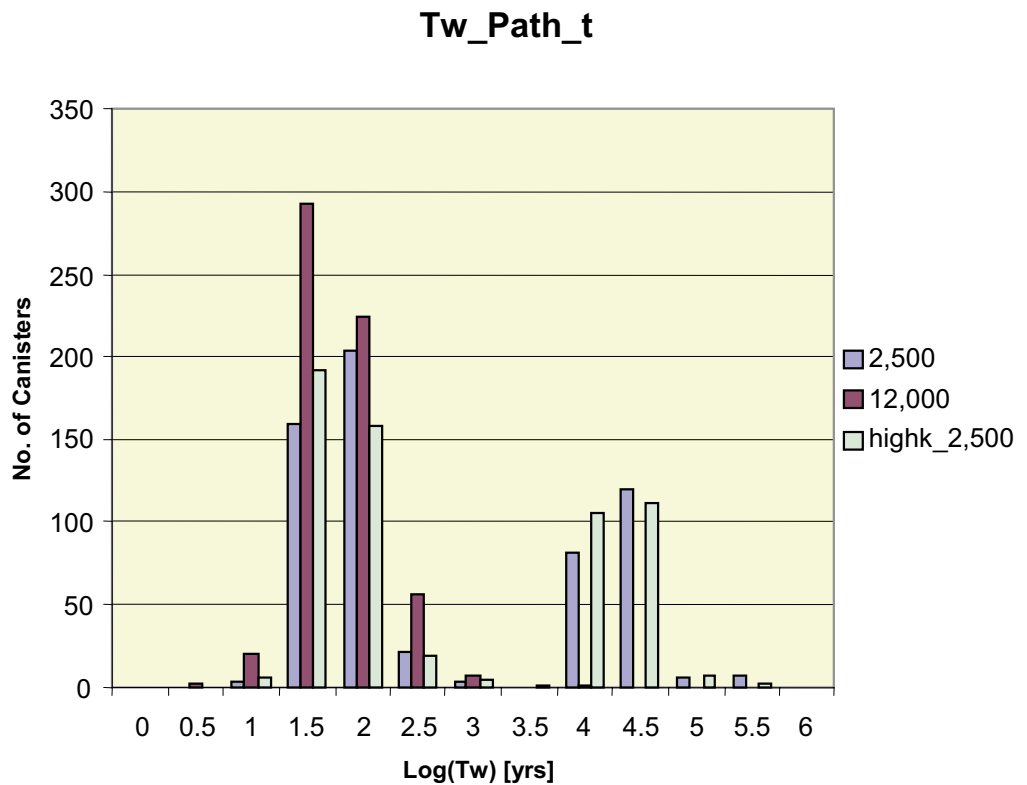
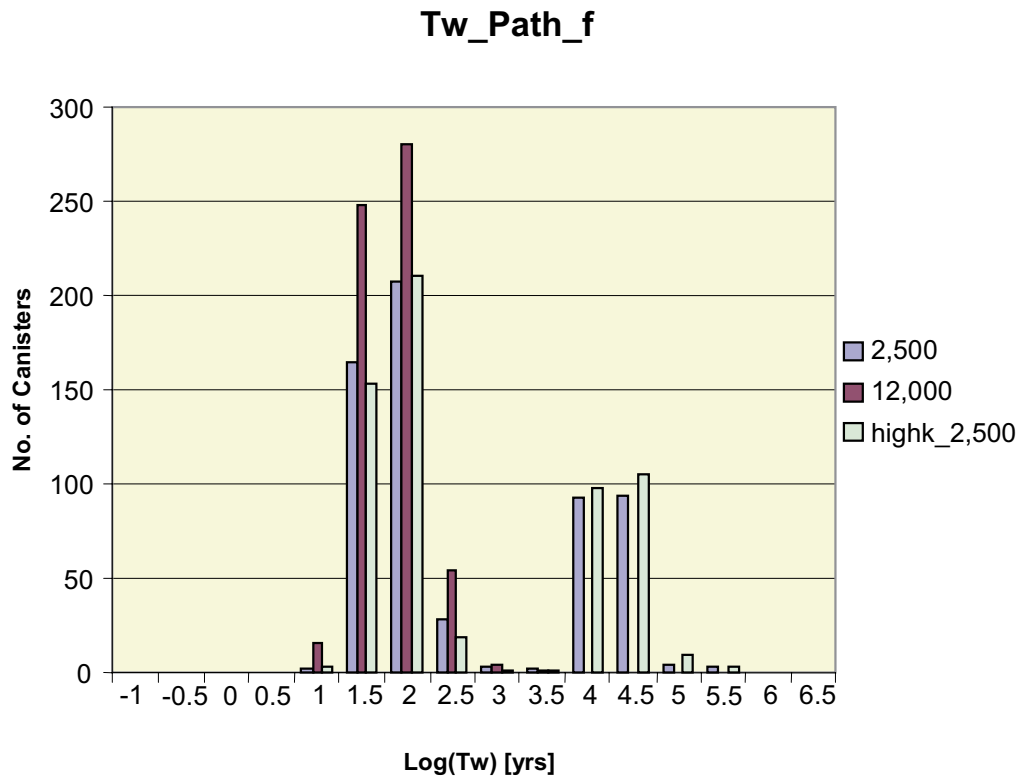


Figure 5-12. Distribution of U_0 in the nested model with a release from 604 canisters into Path_f (top) and Path_t (bottom). Three cases are shown: a release after 2,500 AD; a release at 12,000 AD; and for a backfill conductivity of 10^{-8} m/s for a release at 2,500 AD.

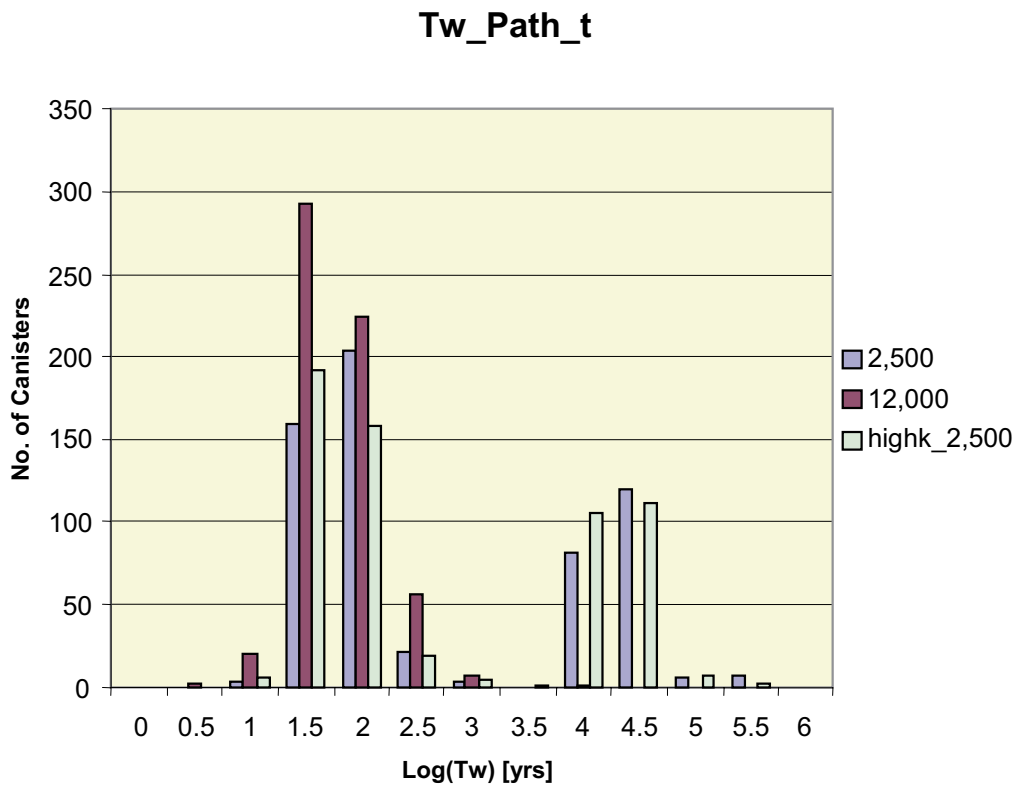
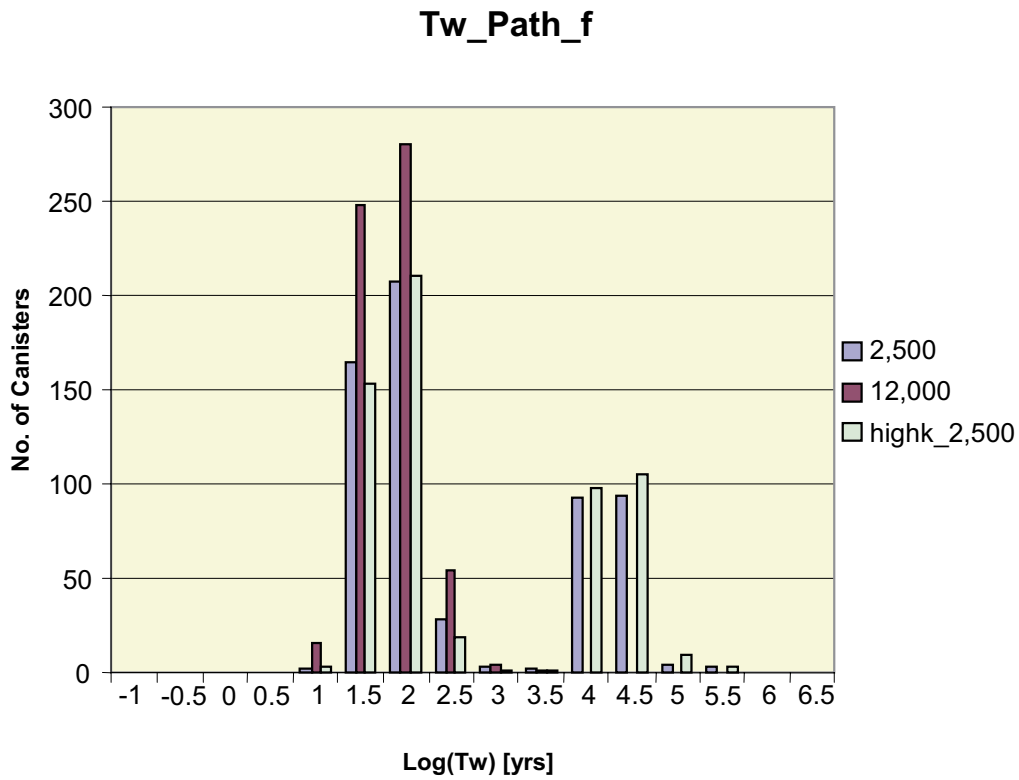


Figure 5-13. Distribution of t_w in the nested model with a release from 604 canisters into Path_f (top) and Path_t (bottom). Three cases are shown: a release after 2,500 AD; a release at 12,000 AD; and for a backfill conductivity of 10^{-8} m/s for a release at 2,500 AD.

Table 5-5. Performance statistics: Distribution of \log_{10} (travel time [yr]) for the nested model Path_f and Path_t at 2,500 AD, 12,000 AD and for an increased backfill hydraulic conductivity at 2,500 AD.

	2,500 AD, base K		12,000 AD		2,500 AD, high K	
	Path_f	Path_t	Path_f	Path_t	Path_f	Path_t
Mean	2.418	2.480	1.574	1.551	2.492	2.501
Median	1.751	1.737	1.552	1.488	1.737	1.708
5th percentile	1.244	1.258	1.114	1.075	1.287	1.192
10th percentile	1.336	1.342	1.189	1.191	1.364	1.304
25th percentile	1.482	1.476	1.350	1.328	1.496	1.449
75th percentile	3.956	3.984	1.731	1.695	3.983	3.983
90th percentile	4.148	4.168	1.992	2.037	4.158	4.160
95th percentile	4.226	4.359	2.291	2.324	4.333	4.341
Std deviation	1.202	1.250	0.343	0.370	1.236	1.267
Variance	1.445	1.564	0.118	0.137	1.527	1.606
Max value	5.031	5.026	3.266	3.789	5.031	5.020
Min value	0.833	0.720	0.638	0.432	0.682	0.734

The pattern of long and short paths, discussed in relation to travel time for Figure 5-13 above, is also evident in the distributions for path length given in Figure 5-15 and Table 5-6. The distributions for paths from releases to fractures (Path_f) at 2,500 AD (two cases, upper plot) show two distinct peaks at around 1,500 m and 10,000 m, with a mean for the distributions of ~2,000 m. The equivalent distribution for releases at 12,000 AD shows a single peak at around 1,500 m, with a mean of ~1,000 m. Again, this fits with the pattern of two discharge zones at 2,500 AD being replaced by a single zone at 12,000 AD. The path length distributions and means for releases to Path_t (lower plot) are almost identical to those for Path_f, as can be seen from the data in Table 5-6.

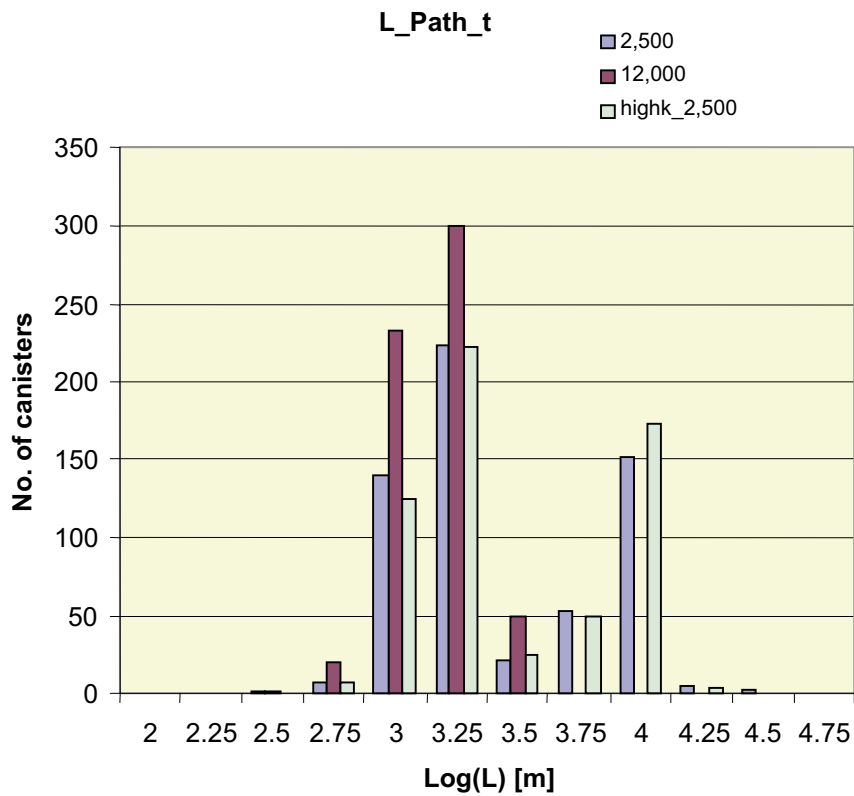
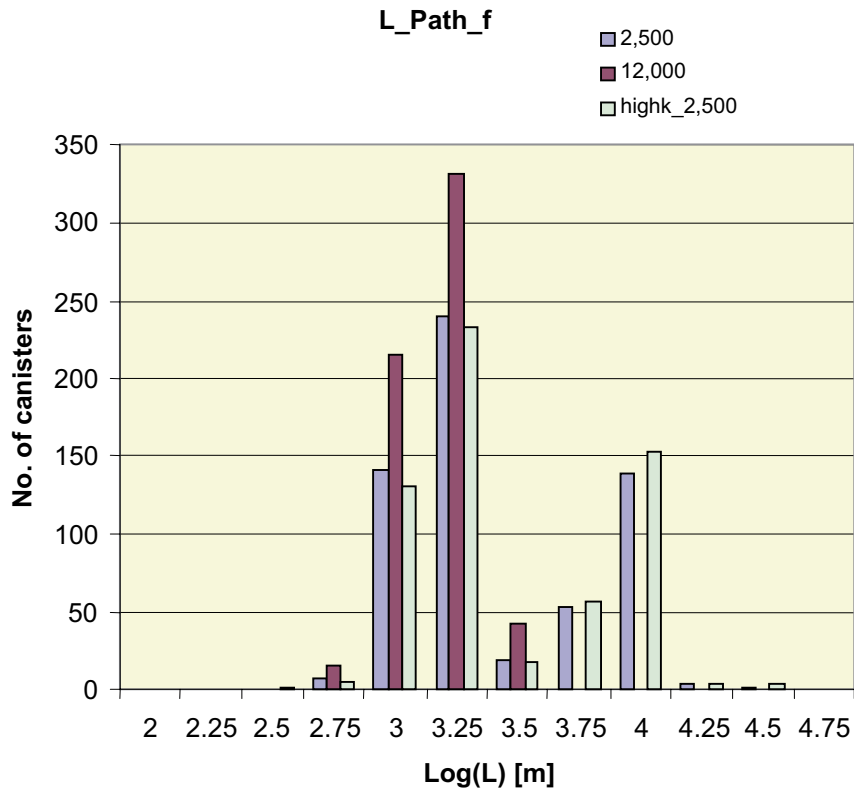


Figure 5-14. Distribution of path length, L , in the nested model with a release from 604 canisters into Path_f (top) and Path_t (bottom). Three cases are shown: a release after 2,500 AD; a release at 12,000 AD; and for a backfill conductivity of 10^{-8} m/s for a release at 2,500 AD.

Table 5-6. Performance statistics: Distribution of $\log_{10}(\text{pathlength [m]})$ for the nested model Path_f and Path_t at 2,500 AD, 12,000 AD and for an increased backfill hydraulic conductivity at 2,500 AD.

	2,500 AD, base K		12,000 AD		2,500 AD, high K	
	Path_f	Path_t	Path_f	Path_t	Path_f	Path_t
Mean	3.286	3.307	3.039	3.034	3.310	3.324
Median	3.127	3.131	3.036	3.028	3.135	3.152
5th percentile	2.877	2.891	2.788	2.773	2.872	2.895
10th percentile	2.931	2.922	2.839	2.847	2.926	2.944
25th percentile	3.002	3.004	2.946	2.931	3.009	3.012
75th percentile	3.746	3.755	3.141	3.139	3.755	3.762
90th percentile	3.793	3.803	3.208	3.211	3.791	3.796
95th percentile	3.819	3.827	3.304	3.318	3.819	3.822
Std deviation	0.364	0.377	0.150	0.153	0.379	0.372
Variance	0.133	0.142	0.023	0.024	0.143	0.138
Max value	4.380	4.387	3.447	3.431	4.386	4.240
Min value	2.625	2.499	2.600	2.431	2.323	2.626

Figure 5-15 shows the distributions of F-quotient for the same three cases as in Figure 5-13. For the releases to fractures (Path_f, upper plot), there is a very broad range of values from $>10^9$ yr/m down to $<10^4$ yr/m, with all three cases falling within this range. However, the two cases for 2,500 AD show a higher proportion of paths at the upper end of this range, as would be expected for paths showing longer path lengths and travel times (Figure 5-13 and Figure 5-14, respectively). The mean F-quotient for all three cases (Table 5-7) is of similar magnitude though, with a value of $\sim 6 \cdot 10^6$ yr/m for the cases at 2,500 AD compared with a value of $\sim 3 \cdot 10^6$ yr/m for the 12,000 AD case. The change in backfill property has a limited impact on F since the F-quotient for parts of the path in the tunnel is not included.

The distributions and means for the releases to Path_t (lower plot) are very similar to those for releases to Path_f discussed above.

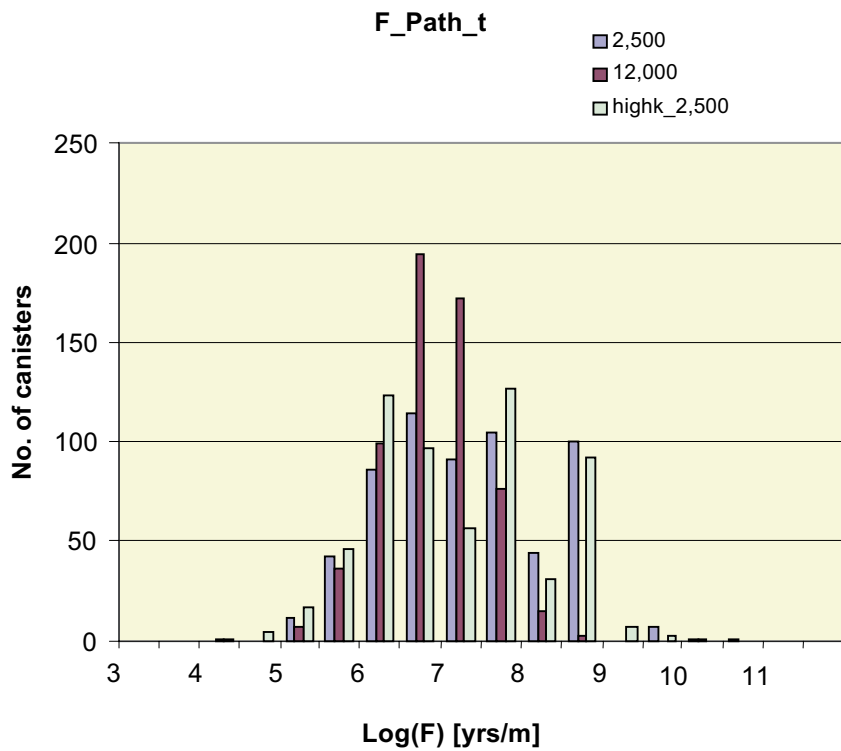
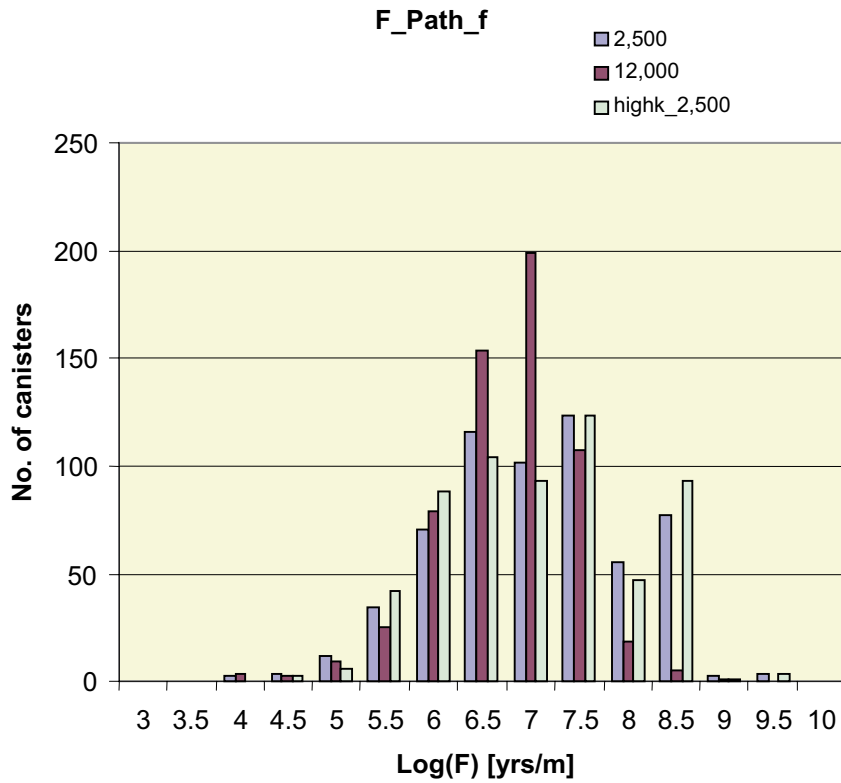


Figure 5-15. Distribution of F-quotient in the nested model with a release from 604 canisters into Path_f (top) and Path_t (bottom). Three cases are shown: a release after 2,500 AD; a release at 12,000 AD; and for a backfill conductivity of 10^{-8} m/s for a release at 2,500 AD.

Table 5-7. Performance statistics: Distribution of \log_{10} (F-quotient [yr/m]) for the nested model Path_f and Path_t at 2,500 AD, 12,000 AD and for an increased backfill hydraulic conductivity at 2,500 AD.

	2,500 AD, base K		12,000 AD		2,500 AD, high K	
	Path_f	Path_t	Path_f	Path_t	Path_f	Path_t
Mean	6.791	6.816	6.508	6.403	6.812	6.691
Median	6.791	6.755	6.581	6.412	6.812	6.617
5th percentile	5.265	5.328	5.345	5.373	5.333	5.177
10th percentile	5.567	5.572	5.653	5.649	5.613	5.463
25th percentile	6.114	6.072	6.122	6.036	6.051	5.809
75th percentile	7.454	7.529	6.950	6.806	7.478	7.439
90th percentile	8.056	8.067	7.247	7.136	8.069	8.063
95th percentile	8.089	8.104	7.452	7.409	8.103	8.095
Std deviation	0.943	0.970	0.671	0.617	0.931	1.024
Variance	0.888	0.942	0.450	0.380	0.867	1.049
Max value	9.278	10.119	8.623	9.748	9.278	9.272
Min value	3.781	4.503	3.661	3.994	4.252	3.838

Figure 5-16 shows the percentage of the path length spent in the tunnels for releases to Path_f (upper plot) and Path_t (lower plot). Three cases are shown for both; base case and increased backfill conductivity at 2,500 AD, and base case backfill conductivity at 12,000 AD. For Path_f, the majority of paths travel <5% of their path length in the tunnels, although the proportion is least for the high backfill conductivity case (59% of releases compared with 80% for the base case at 2,500 AD and 72% of releases at 12,000 AD). Most of the remaining paths travel between 5% and 10% of their path length in tunnels; ~20% for the base case at 2,500 AD, ~27% at 12,000 AD and ~37% for the high backfill conductivity case. Only the last of these cases has a significant proportion of paths travelling for more than 10% of their length in the tunnels (4% of paths with 10–15% of travel time in tunnels), although the highest proportion of time in a tunnel is between 20% and 25% for single paths in the two cases at 2,500 AD.

The picture for Path_t (lower plot of Figure 5-16) is somewhat different. With all paths starting in the tunnels, there are none that spend <5% in the tunnels. The vast majority of paths for all three cases travel for between 5% and 10% of their path length in tunnels (~100% for both cases with base case backfill conductivity, and 85% for the high backfill conductivity case). Of the remaining paths for the latter case, 10% travel for between 10% and 15% of their pathlength in tunnels, with 3% in the range 15–20% and 2% in the range 20–30%. A small number of paths (<1%) from the two base case conductivity simulations travel between 10% and 20% of their path length in tunnels.

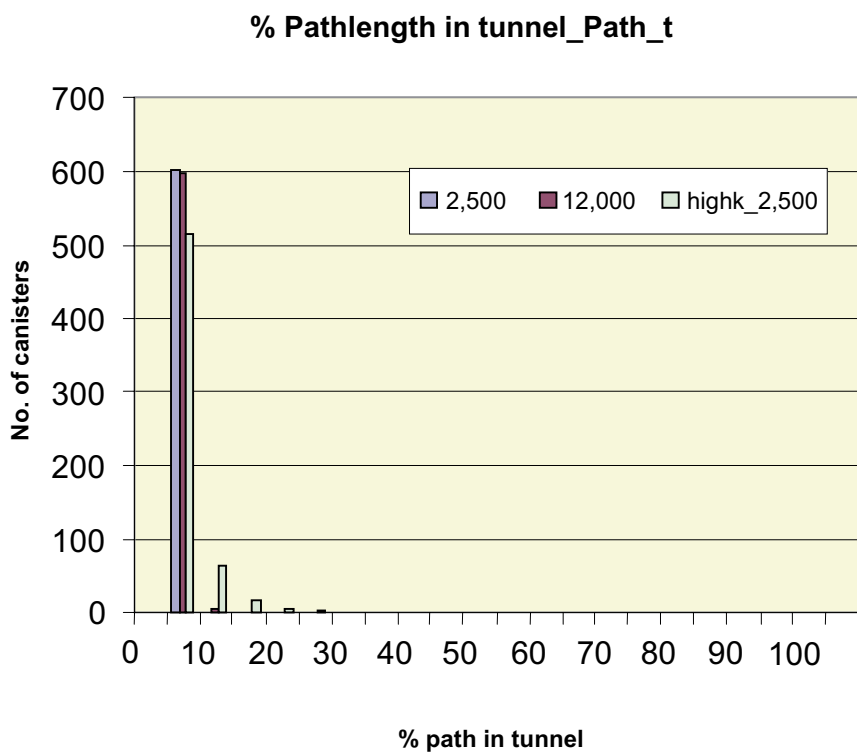
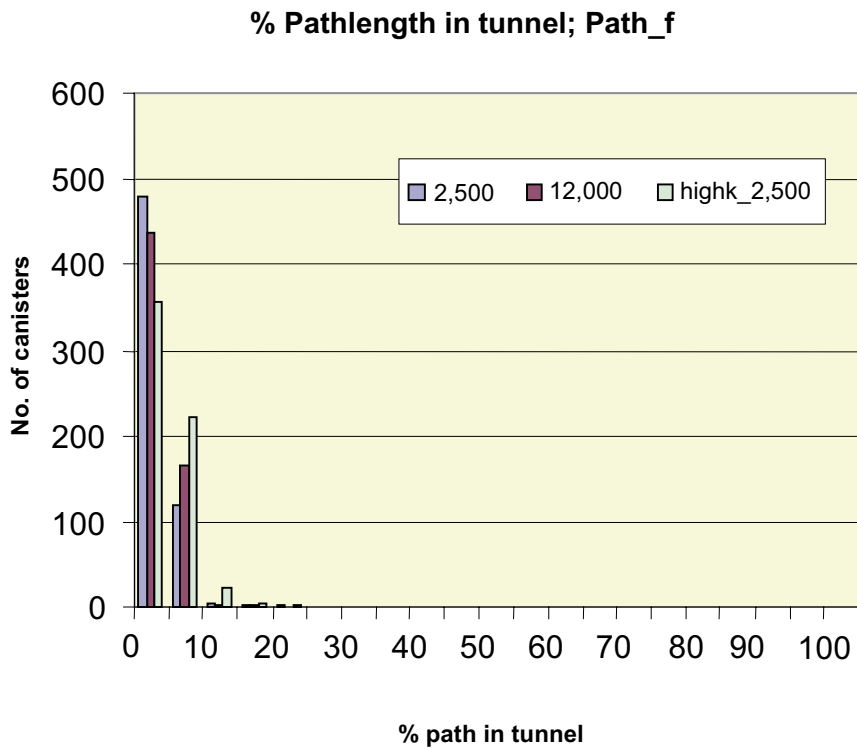


Figure 5-16. Distribution of the percentage of pathlength in the tunnel for the nested model with a release from 604 canisters into Path_f (top) and Path_t (bottom). Three cases are shown: a release after 2,500 AD; a release at 12,000 AD; and for a backfill conductivity of 10^{-8} m/s for a release at 2,500 AD.

The data presented thus far in this section relates to realisation 1 (r1) of the nested model DFN. For the purposes of this study five realisations have been used, although it is recognised that a larger number may be required when undertaking a full assessment rather than as here in developing the methodology. In order to illustrate the differences that can occur between realisations the distributions for Q_{eq} and F-quotient for Path_f are plotted for all five realisations in Figure 5-17.

The upper plot in the figure is for Q_{eq} for the five realisations; statistics for the distributions are given in Table 5-8. The first thing to note about this plot is that none of the distributions stand out as being significantly different from the others. That is, there is consistency of the overall range of values (10^{-6} to 10^{-1} m^3/yr) and of the modal range (10^{-5} to $3 \cdot 10^{-5}$ m^3/yr). Within this overall picture there are differences arising from the stochastic nature of the model. However, the mean value of Q_{eq} for each of the distributions is close to $4 \cdot 10^{-5}$ m^3/yr .

The plot for F-quotient (Figure 5-17, lower plot) also shows a consistent range of values for the five realisations ($3 \cdot 10^3$ to $3 \cdot 10^9$ yr/m), and the means fall within half an order of magnitude of each other at around $3 \cdot 10^6$ yr/m (see Table 5-9). Again there are differences between realisations, for example:

- one and a half orders of magnitude difference in the maximum value of F between realisations 3 and 5;
- a significant number of paths at the upper limit of the distribution for realisation 4, i.e. 48 paths (8%) in the range 10^9 – $3 \cdot 10^9$ yr/m .

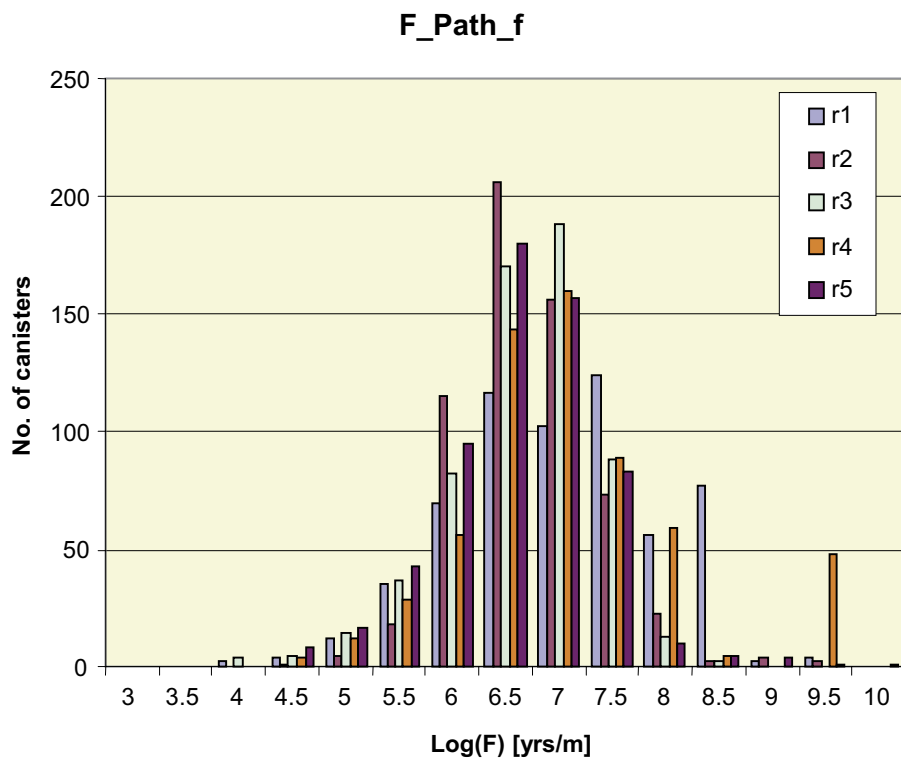
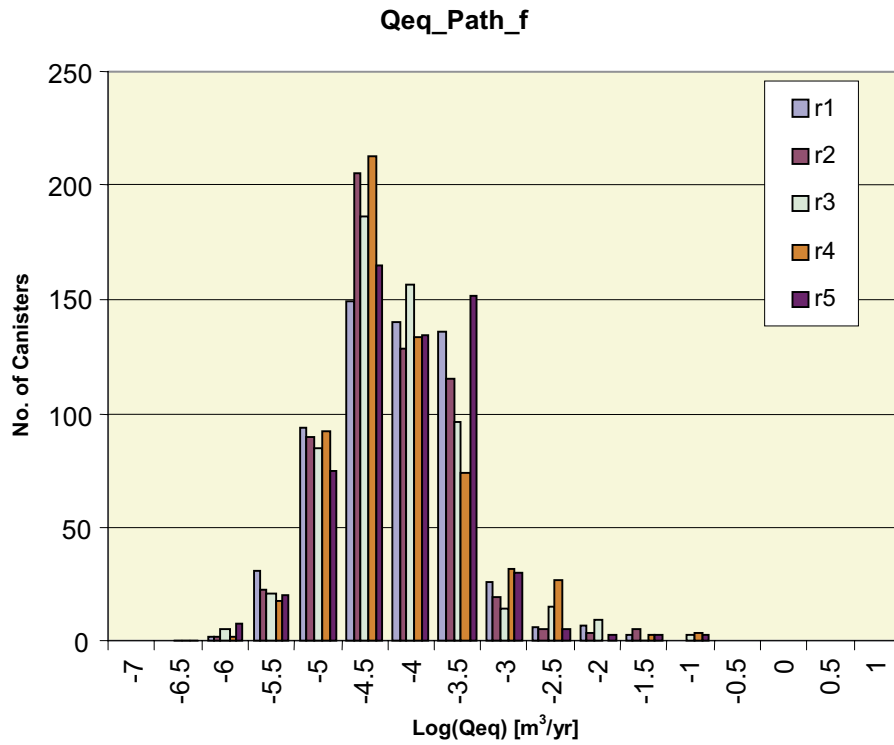


Figure 5-17. A comparison of the distribution of Q_{eq} (top) and F -quotient (bottom) for 5 realisations of the DFN in the nested model for $Path_f$ (particle starting in a fracture adjacent to the canister). The case considered is for a release of a particle from each of 604 canisters in the south-east corner of the repository at 2,500 AD.

Table 5-8. Performance statistics: Distribution of $\log_{10}(\text{Qeq [m}^3/\text{yr]})$ for five realisations of the nested model Path_f at 2,500 AD.

	Realisation number					All paths
	1	2	3	4	5	
Mean	-4.409	-4.454	-4.429	-4.432	-4.368	-4.418
Median	-4.454	-4.569	-4.506	-4.561	-4.386	-4.499
5th percentile	-5.536	-5.397	-5.446	-5.424	-5.478	-5.454
10th percentile	-5.315	-5.204	-5.225	-5.222	-5.178	-5.234
25th percentile	-4.923	-4.889	-4.879	-4.900	-4.857	-4.890
75th percentile	-3.899	-4.012	-4.031	-4.074	-3.838	-3.959
90th percentile	-3.576	-3.657	-3.668	-3.418	-3.597	-3.599
95th percentile	-3.378	-3.469	-3.125	-2.925	-3.418	-3.299
Std deviation	0.726	0.669	0.736	0.741	0.722	0.719
Variance	0.526	0.447	0.541	0.549	0.521	0.517
Max value	-1.558	-1.602	-1.464	-1.450	-1.455	-1.450
Min value	-6.276	-6.042	-6.833	-6.958	-6.843	-6.958

Table 5-9. Performance statistics: Distribution of $\log_{10}(\text{F-quotient [yr/m]})$ for five realisations of the nested model Path_f at 2,500 AD.

	Realisation number					All paths
	1	2	3	4	5	
Mean	6.791	6.447	6.382	6.801	6.366	6.557
Median	6.791	6.398	6.472	6.684	6.390	6.516
5th percentile	5.265	5.587	5.130	5.339	5.119	5.241
10th percentile	5.567	5.684	5.514	5.663	5.424	5.602
25th percentile	6.114	6.042	6.016	6.228	5.938	6.062
75th percentile	7.454	6.817	6.812	7.244	6.827	7.013
90th percentile	8.056	7.218	7.167	7.949	7.177	7.531
95th percentile	8.089	7.489	7.316	9.082	7.409	8.031
Std deviation	0.943	0.629	0.678	0.980	0.742	0.830
Variance	0.888	0.396	0.460	0.960	0.551	0.689
Max value	9.278	9.417	8.074	9.092	9.593	9.593
Min value	3.781	4.436	3.566	4.145	4.012	3.566

6 Updated DFN model for Forsmark SDM 1.1

During the development of the SR-Can methodology problems had been identified in the interpretation of open fractures for the Forsmark V1.1 site description. This prompted a re-interpretation of the fracture core characterisation that lead to significantly lower values of fracture intensity, P32. Since the differences were so great it was felt important to repeat the calculations for the updated DFN to further test the methodology and to see how the results changed for this new and very sparse fracture network. This section describes the results for the updated DFN model.

6.1 Fracture conceptual model analysis

6.1.1 Modifications to fracture parameterisation

The changes made to the DFN parameterisation as a result of the re-interpretation described in the Site Description /4/ are:

- P32 is reduced significantly;
- the relative density of the orientation sets;
- the fracture transmissivity.

In addition, the opportunity was taken to correct the length distribution as described in Section 2.3.2. The change in the transmissivity distribution was necessary to preserve consistency with the transmissivity data from the Posiva flow-logging. That is, since the intensity of fractures, P32, was reduced, then the transmissivity of individual fractures had to be increased to compensate. The change in the relative density between the five orientation sets was resulted also from the re-interpretation of data early in 2004. Table 6-1 summarises the changes in fracture parameterisation for the fractures in the top layer above $z = -300$ m. This actually corresponds to the layer above $z = -400$ m in the site descriptive report, but again an extra layer was inserted between $z = -300$ m and $z = -500$ m to avoid having a step change in properties at the repository. P32 has been reduced by approximately a factor 5, and hence this represents a significantly different scenario to the original DFN.

Table 6-1. P32 (fracture area per unit volume) for fractures above $z = -300$ m for each of the 5 fracture sets. P32 values for different fracture length ranges are also given.

	NE	NW	NS	EW	subH	P32 total
Ratio	0.2868	0.2259	0.0888	0.0863	0.3122	
P32 1 m to 10 m	0.1483	0.0761	0.0298	0.0298	0.1025	0.5171
P32 10 m to 100 m	0.0158	0.0125	0.0049	0.0049	0.0169	0.0554
P32 100 m to 1,000 m	0.0017	0.0013	0.0005	0.0005	0.0018	0.0059
Transmissivity	$T = 1.13 \cdot 10^{-10} L^{1.791}$					

Table 6-5 gives a summary of DFN properties for the repository layer. The base layer is summarised in Table 6-6. Here, the reduction in P32 is only about a factor of 2, but this is still very significant since the original DFN was already close to or below a percolation threshold.

Table 6-2. P32 (fracture area per unit volume) for fractures around the repository $z = -500$ m to $z = -300$ m for each of the 5 fracture sets. P32 values for different fracture length ranges are also given.

	NE	NW	NS	EW	subH	P32 total
Ratio	0.2868	0.2259	0.0888	0.0863	0.3122	
P32 1 m to 10 m	0.0959	0.0761	0.0298	0.0298	0.1025	0.3360
P32 10 m to 100 m	0.0103	0.0082	0.0032	0.0032	0.0110	0.0360
P32 100 m to 1,000 m	0.0011	0.0009	0.0003	0.0003	0.0012	0.0039
Transmissivity	$T = 1.13 \cdot 10^{-10} L^{1.791}$					

Table 6-3. P32 (fracture area per unit volume) for fractures below $Z = -500$ m for each of the 5 fracture sets. P32 values for different fracture length ranges are also given.

	NE	NW	NS	EW	subH	P32 total
Ratio	0.2868	0.2259	0.0888	0.0863	0.3122	
P32 1 m to 10 m	0.0448	0.0355	0.0140	0.0140	0.0476	0.1549
P32 10 m to 100 m	0.0048	0.0038	0.0015	0.0015	0.0051	0.0166
P32 100 m to 1,000 m	0.0005	0.0004	0.0002	0.0002	0.0005	0.0018
Transmissivity	$T = 1.13 \cdot 10^{-10} L^{1.791}$					

6.1.2 Permeability upscaling and fracture length cut-offs

Figure 6-1 shows one realisation of the updated fracture network for the layer above $z = -300$ m depth, and with fracture lengths in the range 10–1,000 m. Clearly the network is predominantly a lot of small fractures with small transmissivity that connect otherwise disjoint large high transmissivity fractures. The equivalent permeability using flux-based upscaling on 100 m blocks is also shown. The permeability is derived as a tensor, but the vertical permeability K_{33} is used here for illustration. This demonstrates that permeability on this scale is very heterogeneous and dominated by the sparse occurrence of large fractures. The background fracturing is sufficiently sparse that some blocks have zero permeability, though quite rare.

The equivalent plots for the updated network for the layer below $z = -500$ m is shown in Figure 6-2. In this case the network is much sparser, and this is reflected in the upscaled permeability which is dominated by blocks with zero permeability. Only where a random fracture larger than 100 m has been sampled is there a non-zero permeability, i.e. the smaller sub-block fractures do not connect to make a network. This has very significant implications for flow and transport since it suggests there will be only occasional and localised flows in the fracture system below $z = -500$ m. Hence, large scale flow pathways at depth are excluded by the fracture data apart from in the regional-scale fracture zones.

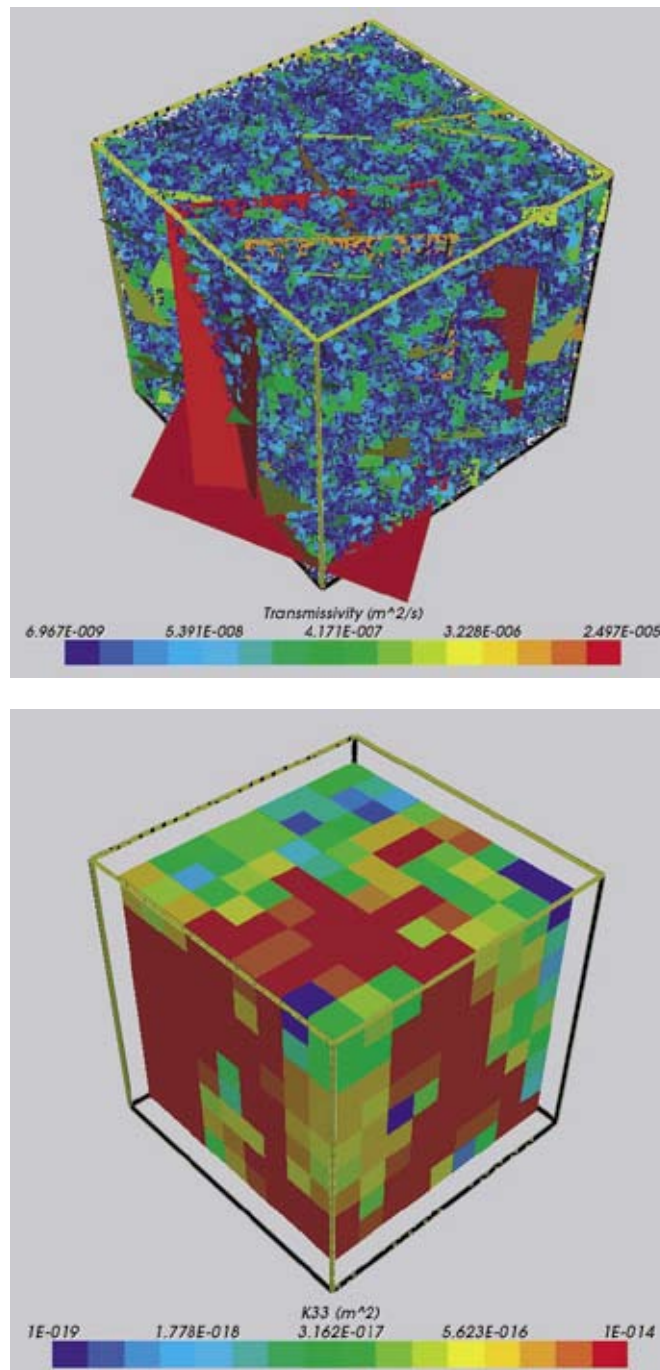


Figure 6-1. Updated fracture network for the zone above -300 m in 1 km block, containing fractures with lengths between 10 m and 1,000 m. Fractures (top) coloured by transmissivity. The equivalent CPM model based on upscaled permeabilities (bottom).

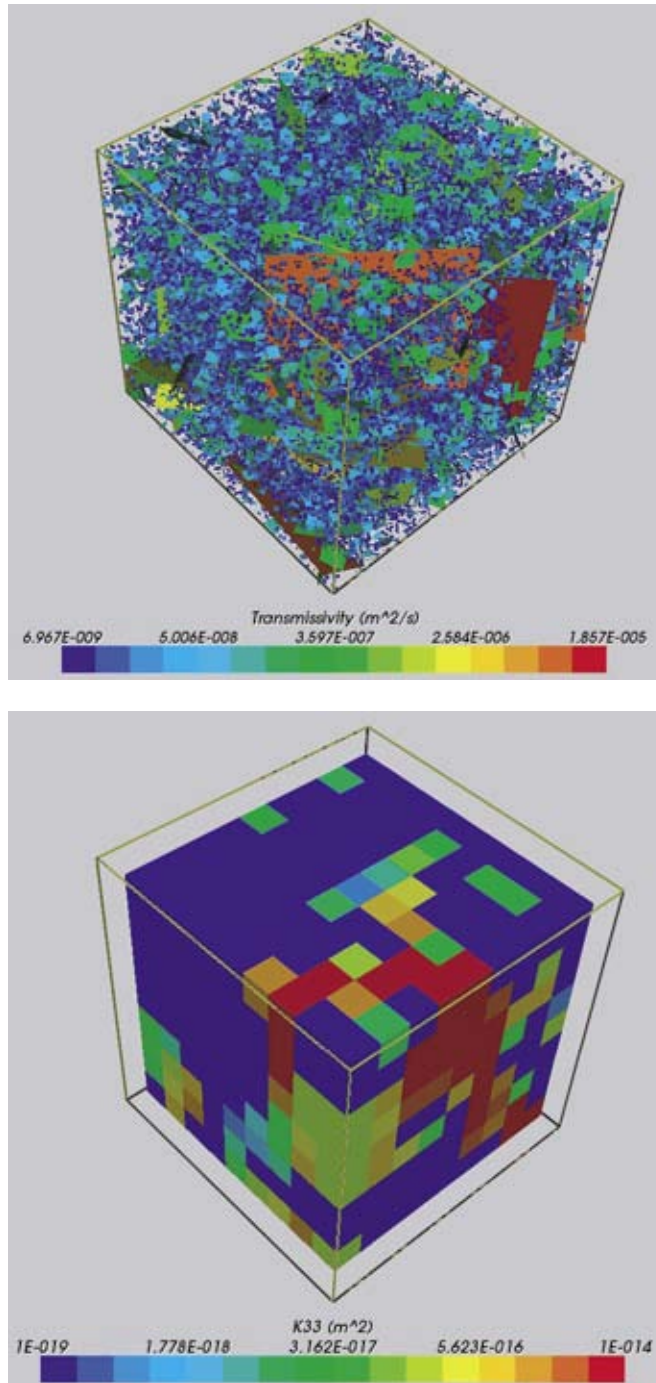


Figure 6-2. Updated fracture network for the zone below -500 m in 1 km block, containing fractures with lengths between 10 m and 1,000 m. Fractures (top) coloured by transmissivity. The equivalent CPM model based on upscaled permeabilities (bottom).

A realisation of the fracture network in the repository layer between $z = -500$ m and $z = -300$ m is shown in Figure 6-3. Here, roughly half the blocks have non-zero permeability suggesting a connected network and the high permeability arises solely from the occasional large random fracture. Again, for this layer flow and transport will only occur where there are either deterministic fractures zones or the occasional random fracture. There are significantly fewer blocks with a non-zero permeability than in the original DFN (Figure 2-7).

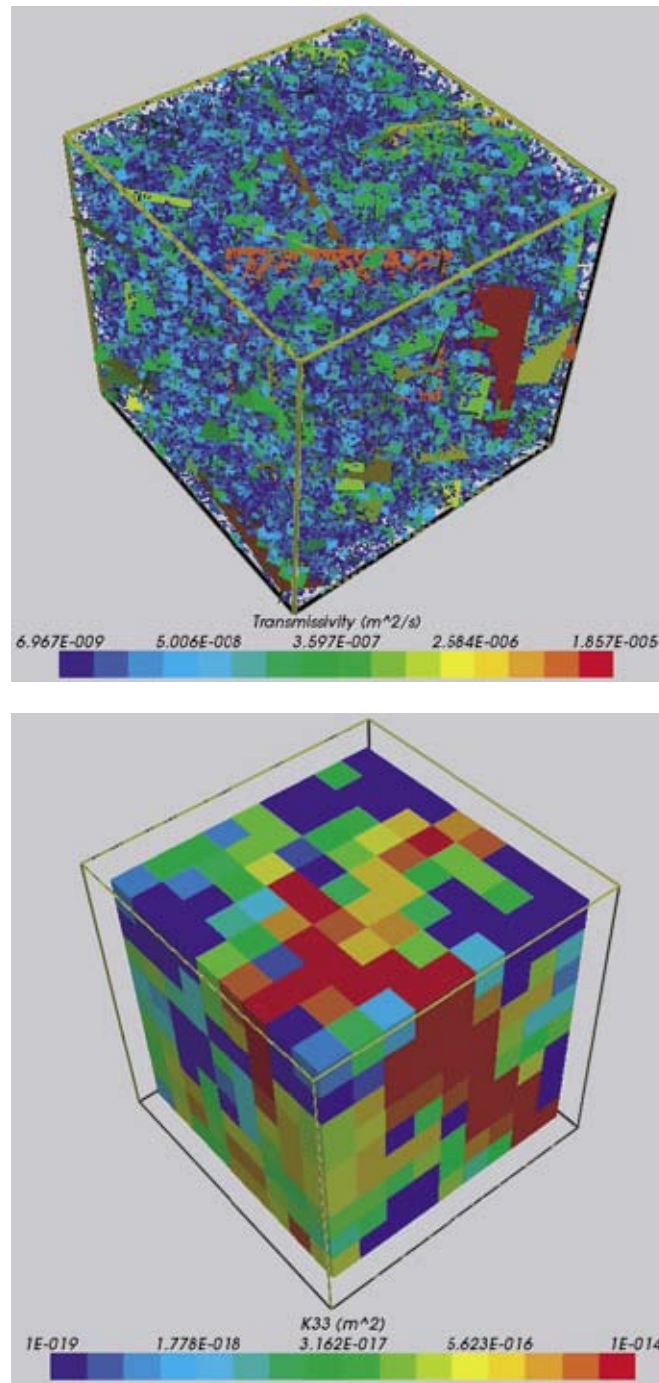


Figure 6-3. Updated fracture network for the repository layer between -500 m and -300 m in 1 km block, containing fractures with lengths between 10 m and 1,000 m. Fractures (top) coloured by transmissivity. The equivalent CPM model based on upscaled permeabilities (bottom).

The results of upscaling the DFN models for 100 m blocks are summarised by histograms and compared with the distributions for the original DFN model. Again, the geometric mean permeability is used as a simple scalar measure of permeability. However, it is noted that for the sparse networks reported in this section, then there is likely to be significant and variable anisotropy. Figure 6-4 shows the distribution of permeability over a $9 \times 9 \times 9$ array of blocks (i.e. 729 blocks in total). The range of values is much greater than for the original DFN and non-Gaussian. High values of permeability, $10^{-13} m^2$, can occur where there is a rare long fracture which have a higher transmissivity than for the original DFN due to

the increase factor in the T versus L correlation used here. A long tail in the distribution arises from the variable connectivity within blocks as the network is around a percolation threshold for the background network. This compares markedly with original DFN which was far more homogeneous in the top layer and had no values below about $3 \cdot 10^{-16} \text{ m}^2$.

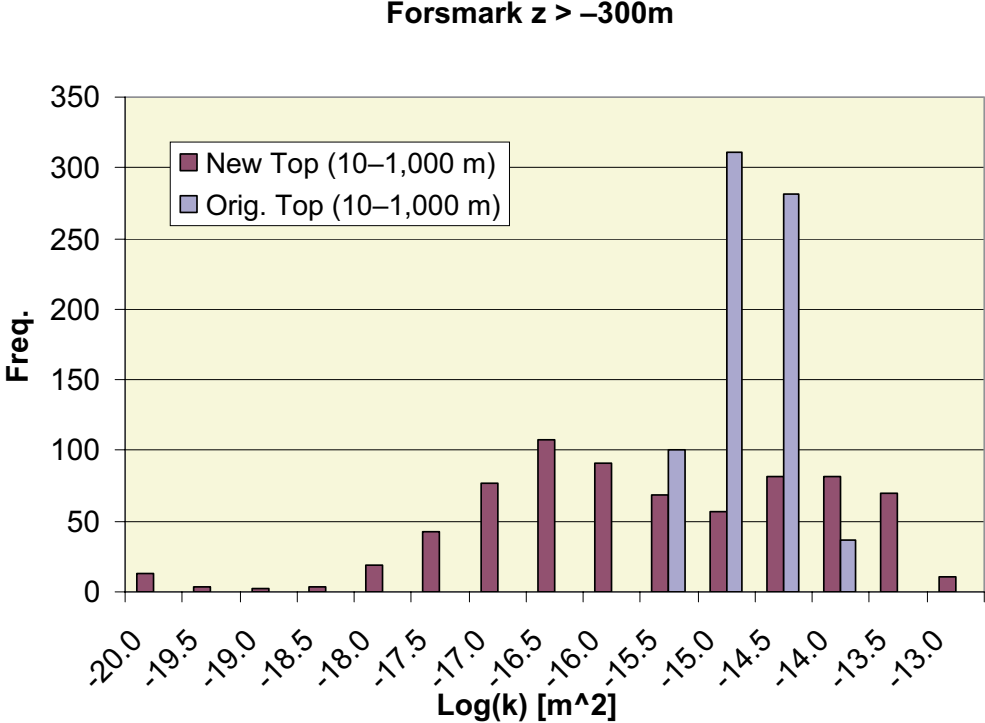


Figure 6-4. Distribution of upscaled permeability for the top DFN model above $z = -300 \text{ m}$ on 100 m blocks (based on a total of 729 blocks). Here, the geometric mean permeability is used as a scalar quantity. The updated DFN model for fractures with lengths between 10 m and $1,000 \text{ m}$ is compared with the equivalent for the original DFN.

The distribution below $z = -500 \text{ m}$ (Figure 6-5) is dominated by blocks with zero permeability with a small peak around 10^{-15} m^2 for the occasional random fracture that is large than the block size. Again, there is a big difference compared to the original DFN which although heterogeneous had a non-zero permeability in about 80% of blocks.

New Forsmark DFN $z \leq -500\text{m}$

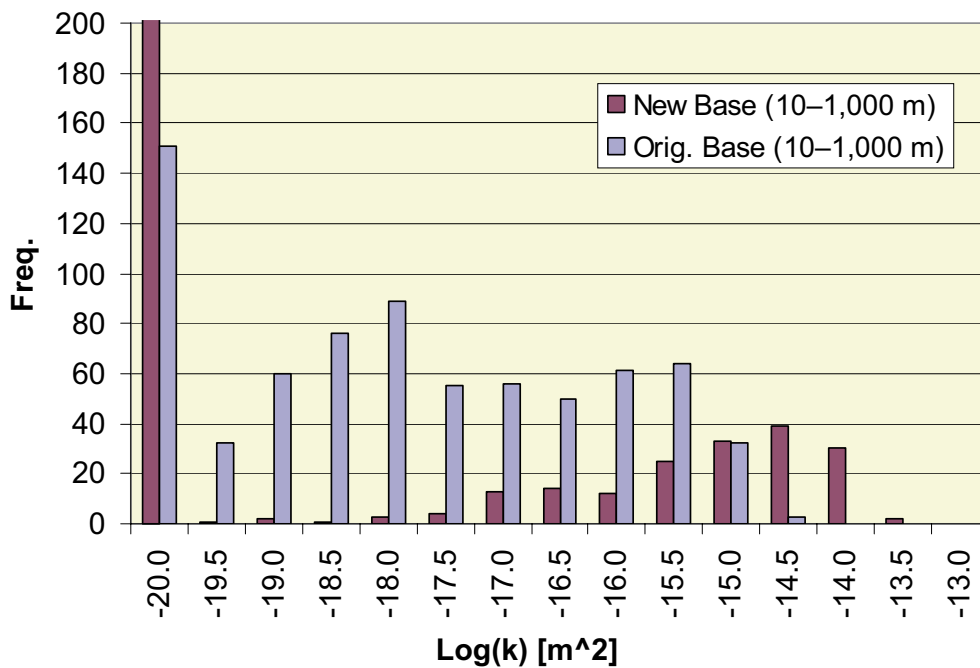


Figure 6-5. Distribution of upscaled permeability for the lower DFN model below $z = -500$ m on 100 m blocks (based on a total of 729 blocks). Here, the geometric mean permeability is used as a scalar quantity. The updated DFN model for fractures with lengths between 10 m and 1,000 m is compared with the equivalent for the original DFN.

For the important repository layer the updated and original DFN models were compared and also the effect of truncating the fracture network according to fracture length was investigated. Figure 6-6 illustrates the wider distribution for the updated DFN compared to the original model. It also demonstrates the permeability distribution is sensitive to truncation of the fracture length distribution for scales less than the block size. It was decided that a truncation of about 20 m was acceptable for permeabilities in the range 10^{-13} to 10^{-17} m² for obtaining realisations of the spatial distribution of permeability on a regional-scale using 100 m finite-elements. A smaller truncation would have lead to a very large number of fractures in the regional-scale.

Forsmark $z = -300$ to -500 m

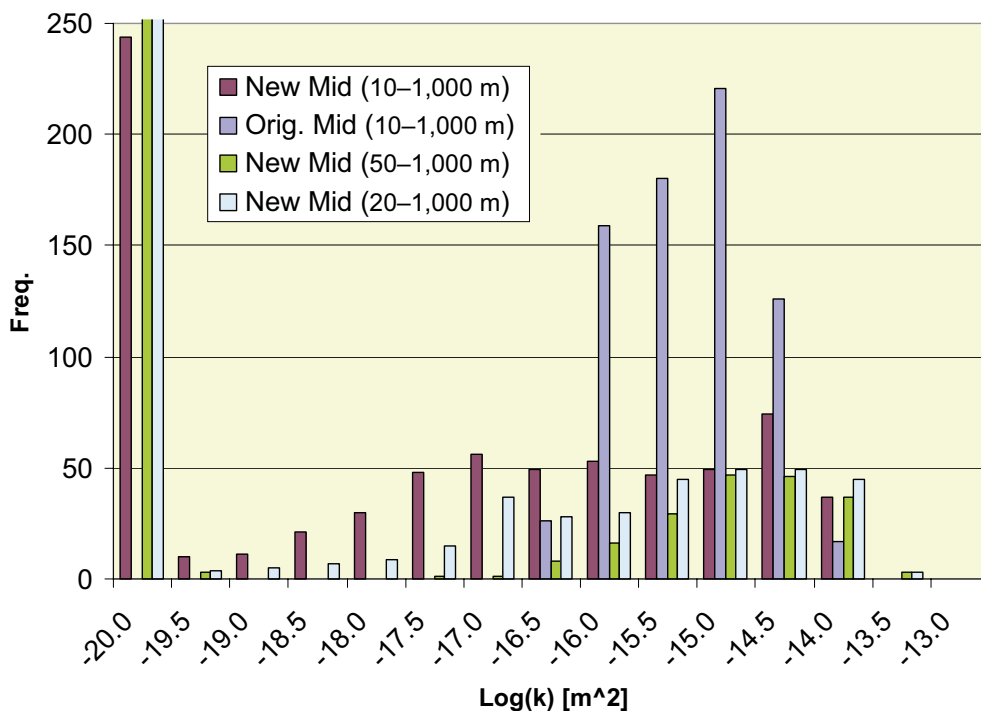


Figure 6-6. Distribution of upscaled permeability for the repository layer DFN model between $z = -500$ m and $z = -300$ m on 100 m blocks (based on a total of 729 blocks). Here, the geometric mean permeability is used as a scalar quantity. The updated DFN model for fractures with lengths between 10 m and 1,000 m is compared with the equivalent for the original DFN.

6.2 Regional-scale CPM modelling

The cycle of paleo-hydrogeological CPM modelling was repeated for the updated DFN model including:

- Generating a regional scale DFN model with fractures between 20 m and 1,000 m;
- Upscaling the permeability tensor for each finite-element in the CPM model;
- A transient groundwater flow and salt transport calculation from 8,000 BC to the current day;
- A transient groundwater flow and salt transport calculation from 2,000 AD to 12,000 AD with the repository included implicitly by modifying properties.

The objective being to supply a realisation of the regional fracture network and supply boundary conditions for the more detailed nested models.

6.2.1 Permeability upscaling

Firstly, a regional scale DFN model was generated that included fractures with length scales ranging from 20 m to 1,000 m. This gave lead to a model with a total of about 4.1 million fractures in the regional domain. Flux-based upscaling was then used to derive an equivalent CPM permeability tensor for each block in the model, which was then

combined with an implicit treatment of the fracture zones. The combined effect is seen in Figure 6-7. One clear feature of this case is the highly visible but rare red streaks on the top surface that correspond to large random fracture of around 1,000 m. These are more pronounced than in the original DFN due to the higher factor in the T versus L correlation. The same is true looking at a slice through the model at repository depth (see Figure 6-8). An average value of permeability in this layer is about 10^{-16} m². Finite-elements coloured blue are likely to be very low permeability due to the absence of a connected network. The permeability in the layer below $z = -500$ m has many cells with very low permeability. As with original DFN, a background permeability for the rock mass a cut-off of 10^{-19} m² was used which is implemented as a minimum permeability used in the model. The porosity and flow wetted surface area was unchanged from the original DFN, although strictly the change in P32 would imply a change in both these transport parameters.

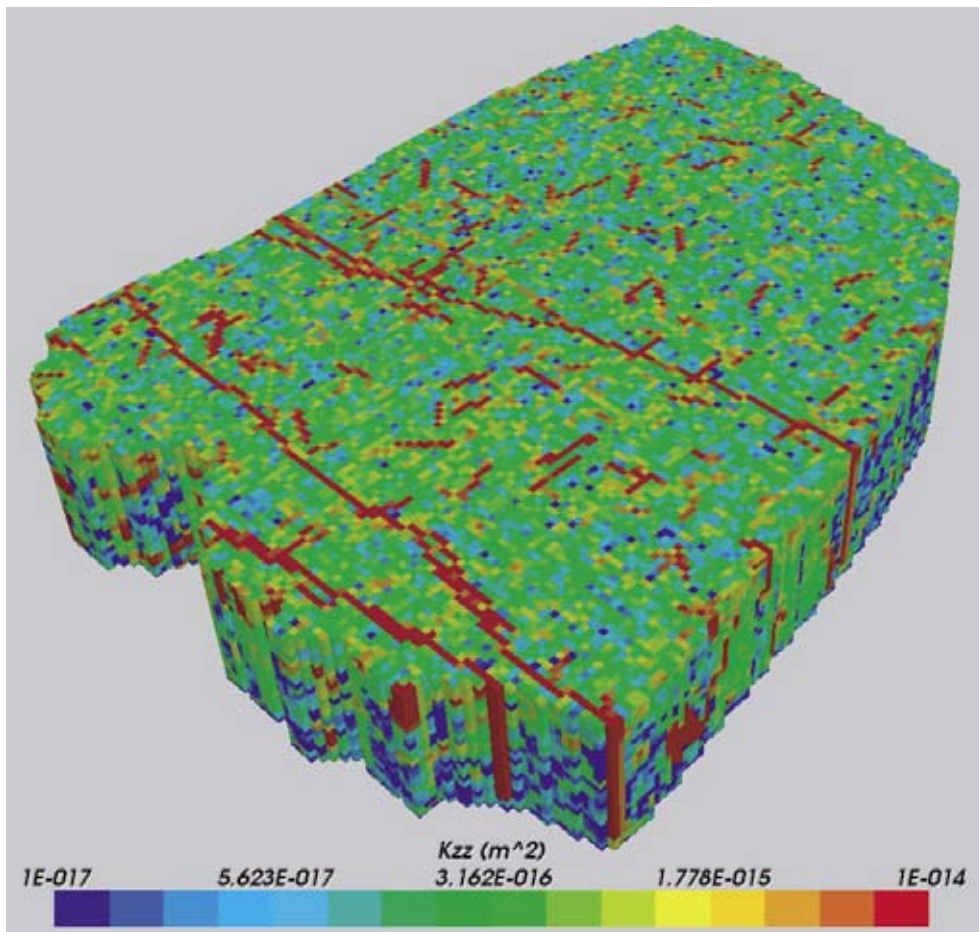


Figure 6-7. Distribution of permeability (vertical component k_{zz}) in the regional model with the top 2 layers removed for the updated DFN.

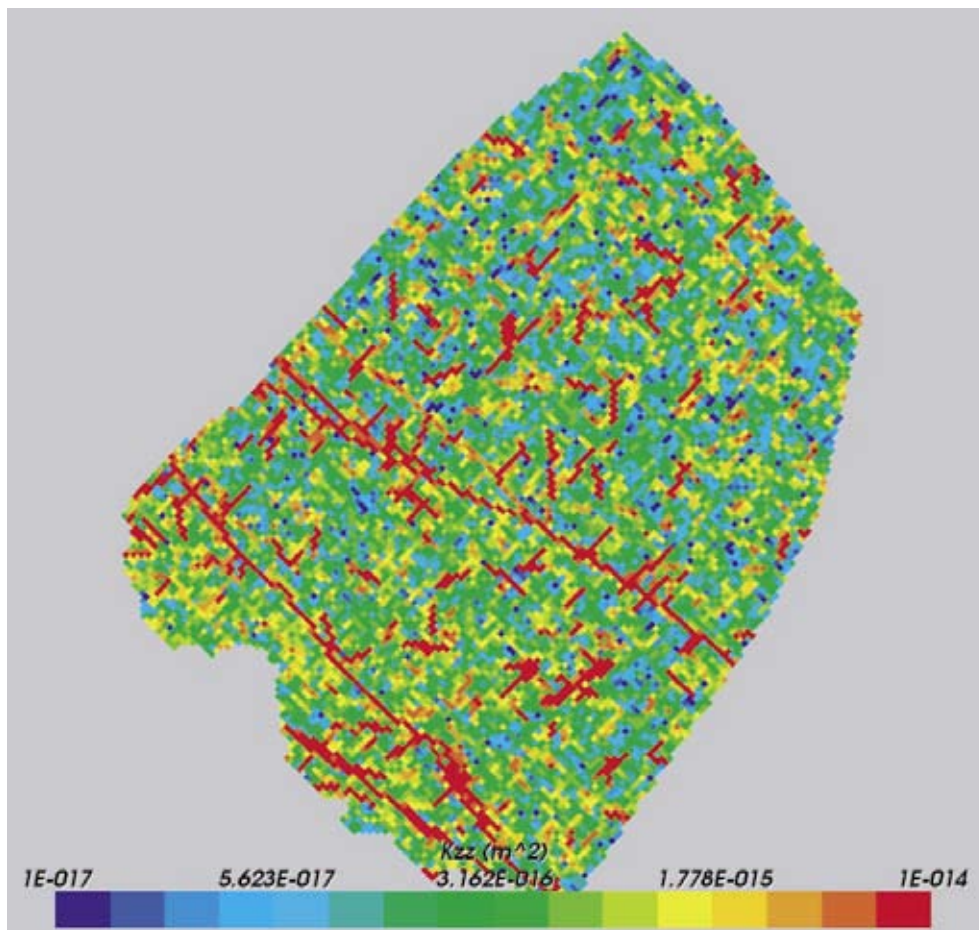


Figure 6-8. Distribution of permeability (vertical component k_{zz}) in the regional model at repository depth $z = -400$ m for the updated DFN.

6.2.2 Pressure and salt transport calculations

The calculations of flow and transport followed the approach described in Section 3.6. The regional-scale CPM results are of interest since they represent a sensitivity study for the Forsmark V 1.1 modelling. Visually, salinity would appear to be flushed earlier from the top layer for the new case. A likely reason is that the lower permeability at depth means that less flow penetrates to depth, but is predominantly in the top 400–500 m, and hence this layer is flushed of salinity earlier than in the original DFN case. The profiles at depth and at 12,000 AD are more consistent with the original DFN. Looking at these profiles, it still can be expected that salinity will have an effect at 2,500 AD, but less so at 12,000 AD.

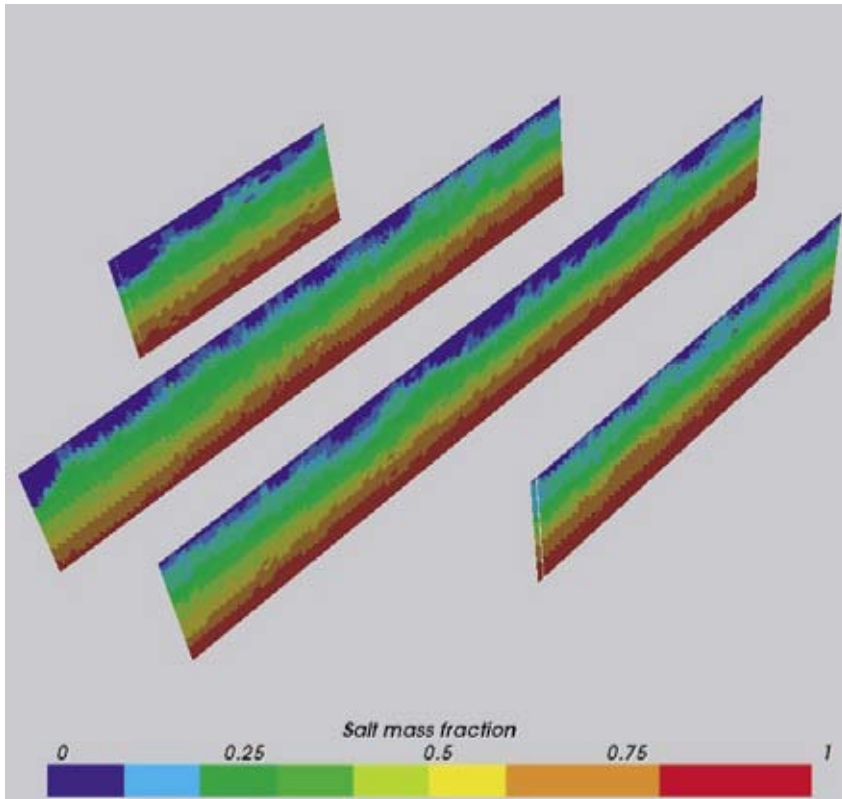


Figure 6-9. Salt mass fraction on 4 vertical slices in the CPM model (based on updated DFN) at 2500 AD.

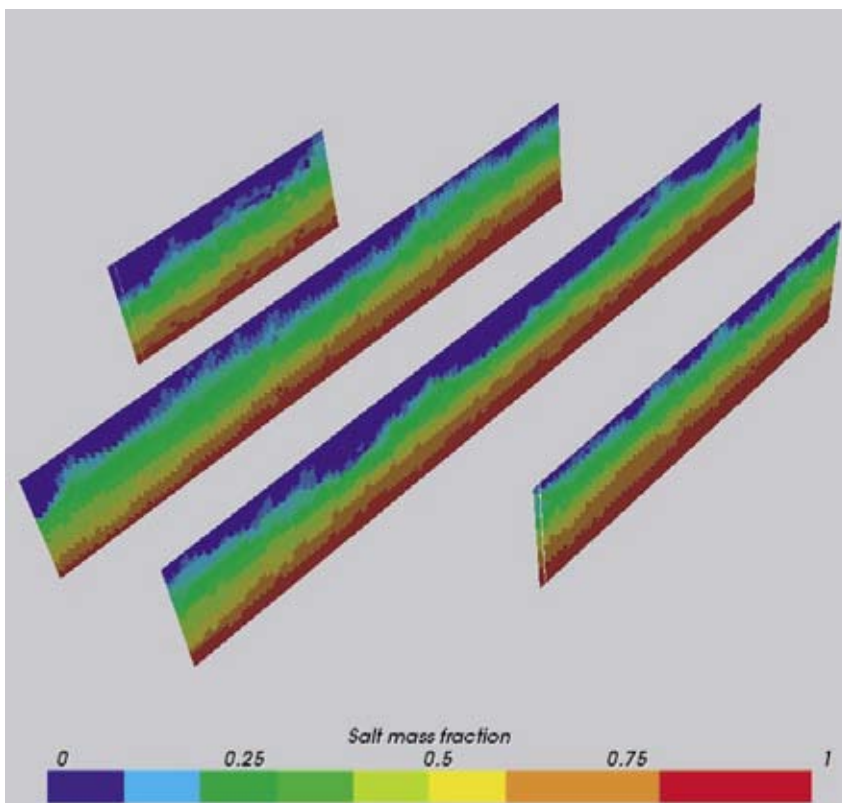


Figure 6-10. Salt mass fraction on 4 vertical slices in the CPM model (based on updated DFN) at 7500 AD.

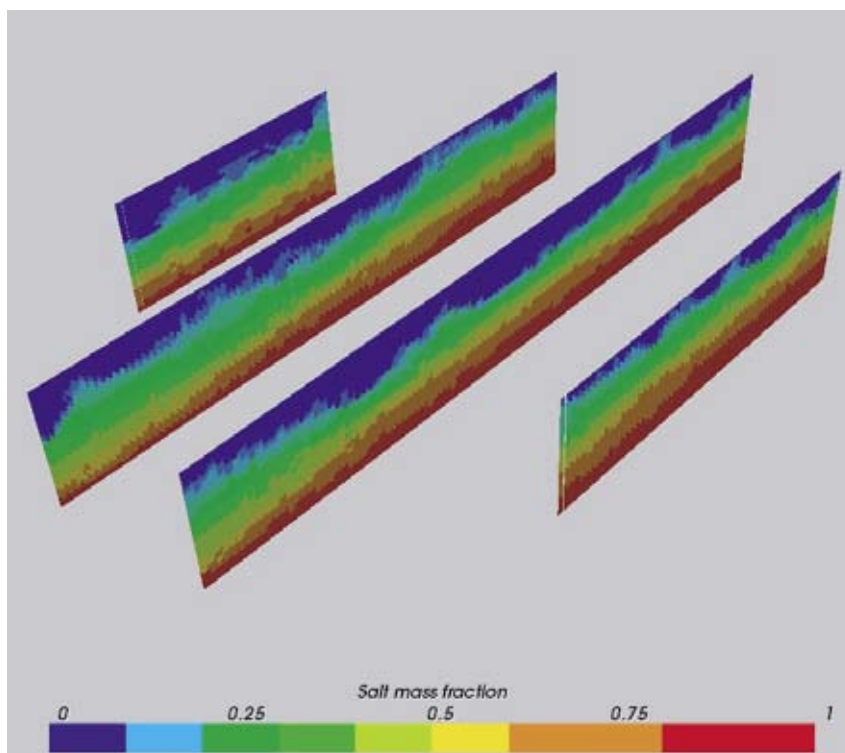


Figure 6-11. Salt mass fraction on 4 vertical slices in the CPM model (based on updated DFN) at 12,000 AD.

6.2.3 Particle tracking calculations

Particle tracking was performed for start positions corresponding to the 604 canisters in the south-east corner of the repository. The exit locations for particles starting at 2,500 AD are shown in Figure 6-12 with exit locations coloured by F-quotient. Most of the paths go NNW toward the sea, but there are a small number that discharge vertically above the repository. Comparing these locations to Figure 3-26 for the original DFN, it is seen that the discharge points are more concentrated with less dispersion in the fracture zones. A plot showing the actual pathlines is given in Figure 6-13 with paths coloured by the cumulative travel time along the path. Figure 6-14 shows the discharge points for a release at 12,000 AD. As for the original DFN, the pathlines seem to be influenced strongly by salinity since there are many more discharge points vertically above the repository for the predominantly freshwater conditions at 12,000 AD. The fact that the CPM model predicts long pathways out to the sea at early times despite the very poor DFN connectivity at depth would suggest that large-scale DFN models are tending to over-predict the connectivity between elements. One way to try and address this would be to look at the sensitivity to the background permeability, and try reducing it so as to break connections between fractures that aren't really there, although this may lead to numerical problems with having ill-conditioned system matrices. Another possibility would be to use finer meshes, but this will raise the computational costs and may need 64-bit machines, for example. Still, it is interesting that the two different releases lead to qualitatively the same behaviour as for the original DFN.

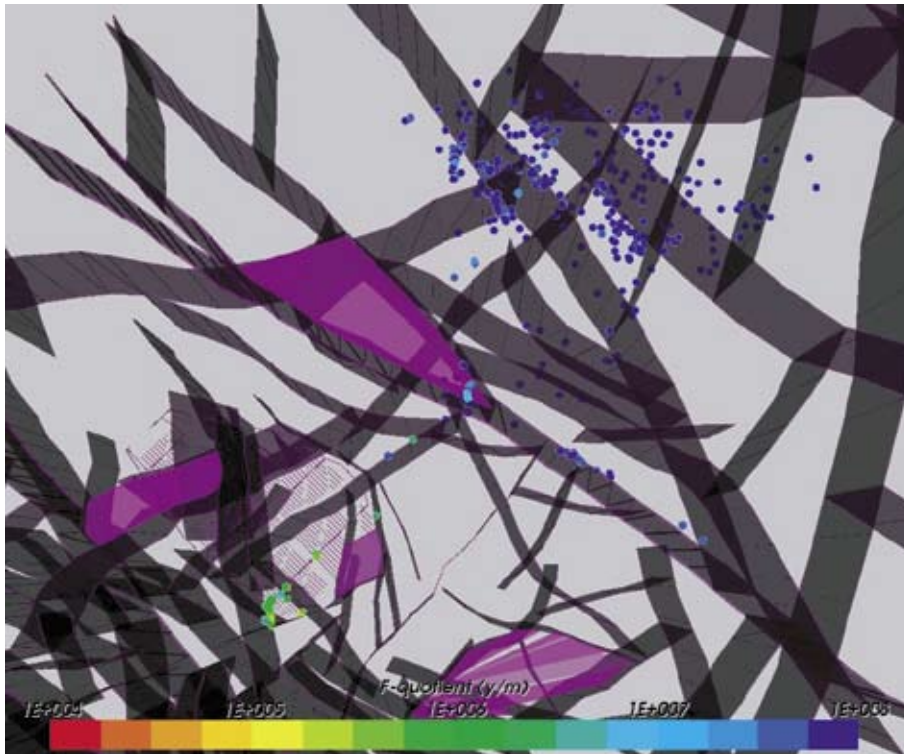


Figure 6-12. Exit locations for particle tracks in the CPM model (based on updated DFN) for the south-east corner of repository. The 604 exit locations are coloured by the total F-quotient for pathlines in the CPM model and tracked through the flow-field at 2,500 AD.

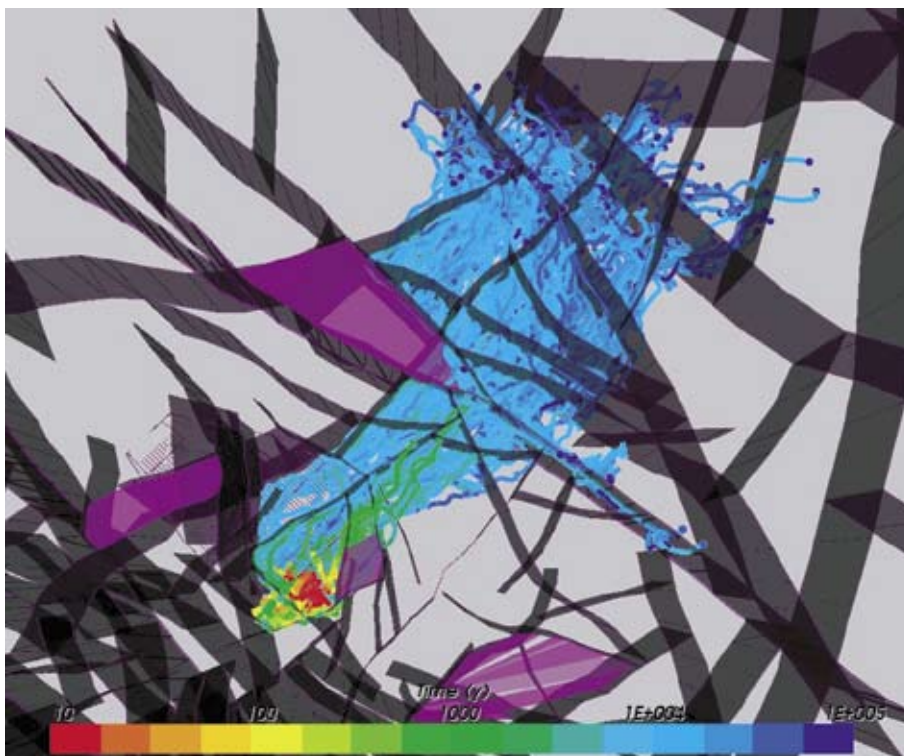


Figure 6-13. Particle tracks in the CPM model (based on updated DFN) for the south-east corner of repository. The 604 pathlines are coloured by the travel time along pathlines in the CPM model and tracked through the flow-field at 2,500 AD.

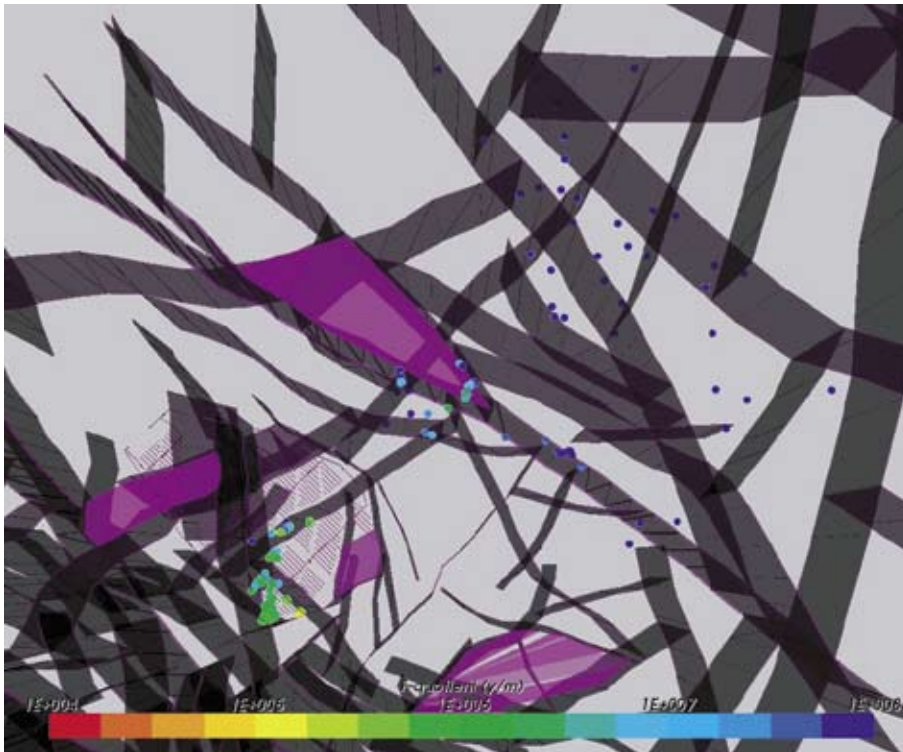


Figure 6-14. Exit locations for particle tracks in the CPM model (based on updated DFN) for the south-east corner of repository. The 604 exit locations are coloured by the total F-quotient for pathlines in the CPM model and tracked through the flow-field at 12,000 AD.

6.3 Regional-scale nested CPM/DFN model

The general approach described in Section 3.7 was repeated for the updated DFN model. However, several changes were necessary due to the sparsity of the network.

6.3.1 CPM/DFN model

In order to represent flow and transport in the regional-scale for the updated DFN it was necessary to include smaller scale fractures to get connectivity of the network. Fractures in the range 20 m–1,000 m are included in the CPM part of the model for upscaling to provide a spatial distribution of permeability. For the DFN part, fractures down to 4 m are included in the repository area which is a 60 m thick slab around the repository at $z = -400$ m. This gave slightly under 0.5 million fractures in the DFN part. The regional-scale model is shown in Figure 6-15. A close-up of the area around the repository is shown in Figure 6-16. This shows the deterministic fracture zones included in the DFN model and the large range of fracture scales.

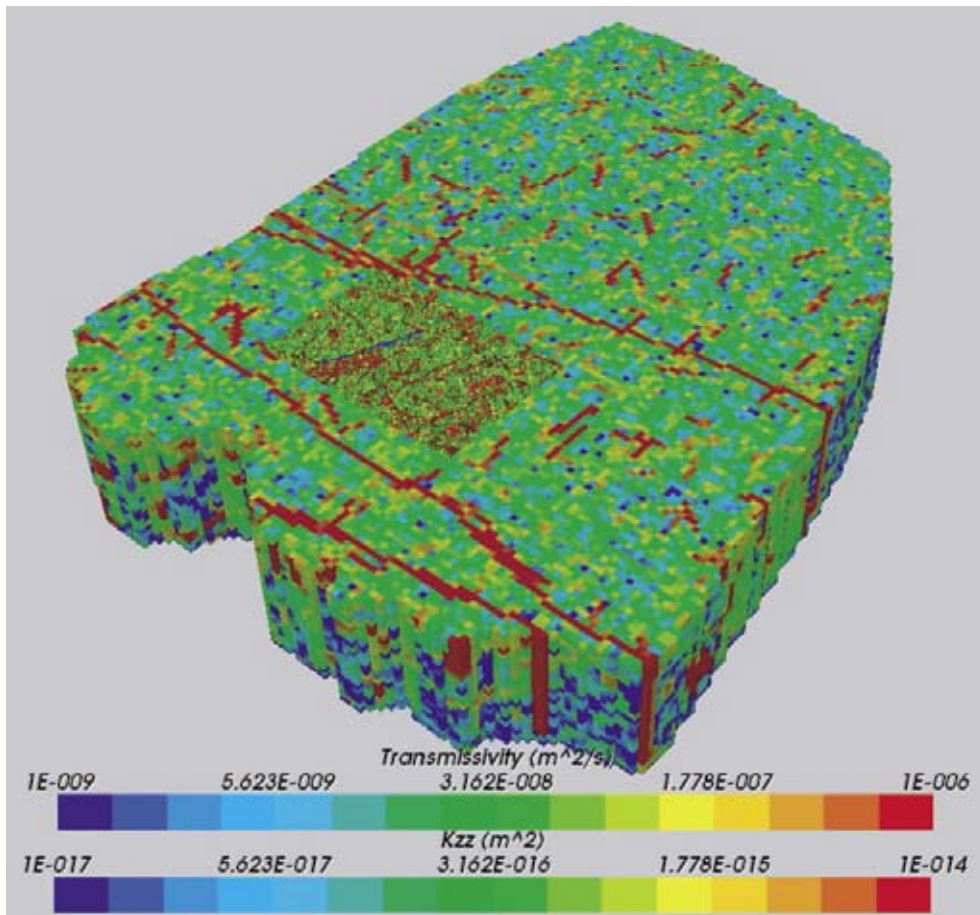


Figure 6-15. The regional nested model (based on updated DFN) with the top 2 layers removed to show the central local-scale DFN sub-area. The CPM model is coloured by vertical permeability (k_{zz}). For the DFN model, fractures are coloured by transmissivity.

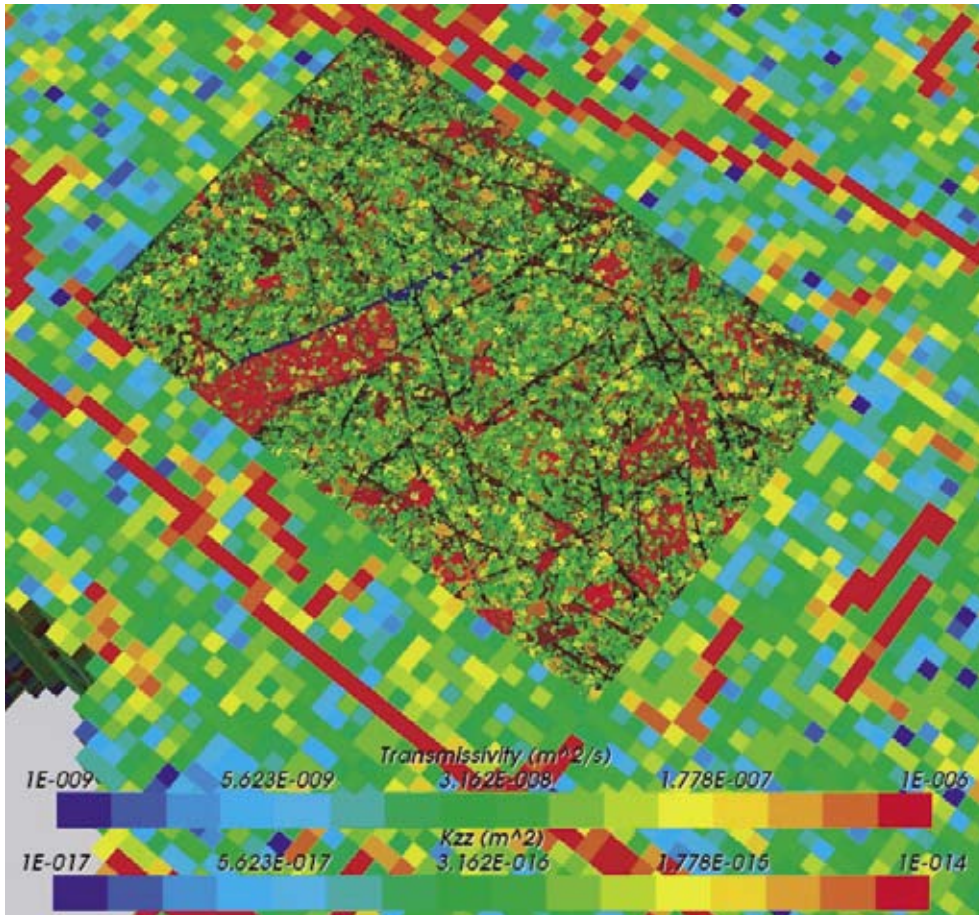


Figure 6-16. The regional nested model (based on updated DFN) with the top 2 layers removed to show the central local-scale DFN sub-area. The CPM model is coloured by vertical permeability (k_{zz}). For the DFN model, fractures are coloured by transmissivity.

The fracturing around the repository (including fractures down to 4 m) is shown on a horizontal slice in Figure 6-17. This indicates that large fractures with high transmissivity are sparse and poorly connected, and even when the extra small-scale fractures around the deposition tunnels are added in, then fractures are still poorly connected. Hence, it can be expected that connectivity will only occur around the large structures, i.e. the fracture zones and depending on backfill quality, the deposition tunnels. Figure 6-18 shows a vertical slice through the nested model showing the traces of fractures cutting the section. This demonstrates the high density of fracturing above the repository and the slab of small-scale fractures that are included around the repository. The deterministic fractures zones appear as vertical red lines running through the entire DFN.

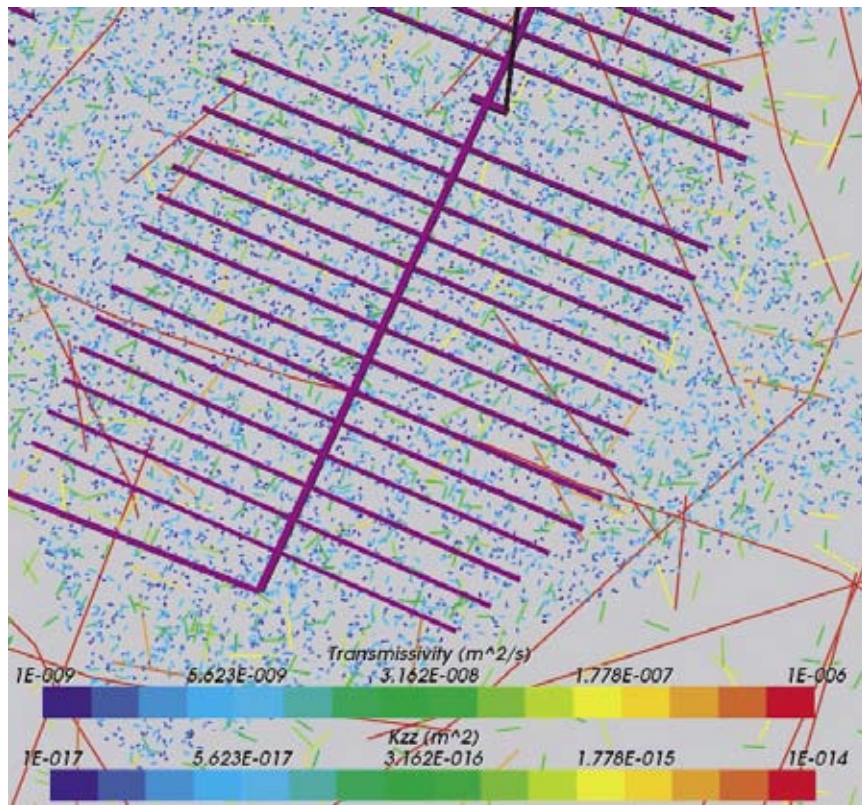
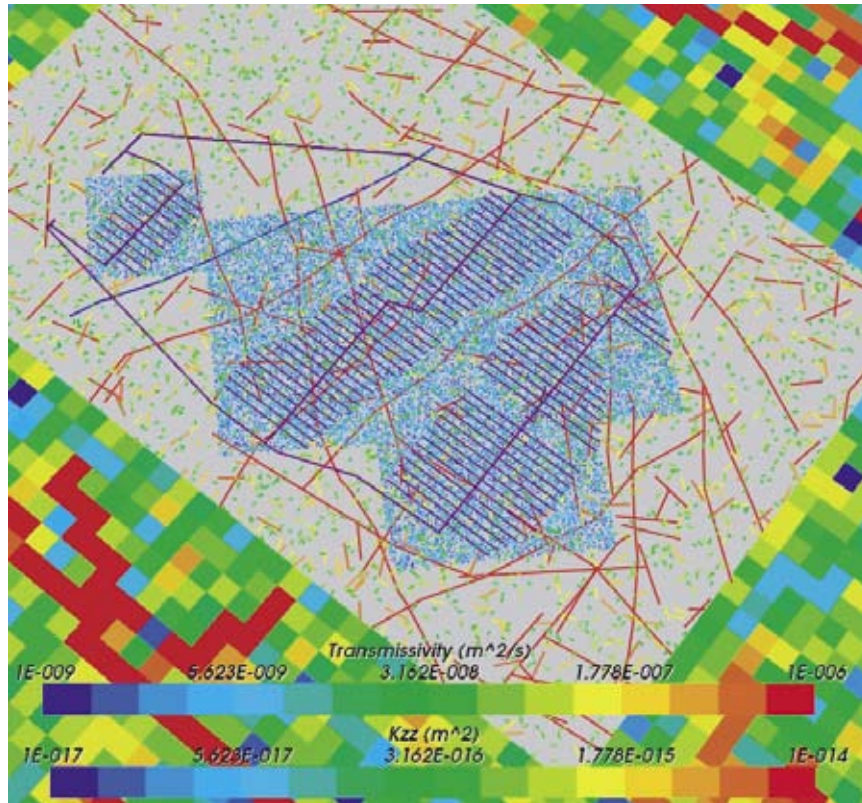


Figure 6-17. A horizontal slice through the regional nested model (based on updated DFN) at repository depth ($z = -400$ m). Showing the DFN area (top) and the south-east corner of the repository (bottom). The CPM model is coloured by vertical permeability (k_{zz}). For the DFN model, fractures are coloured by transmissivity.

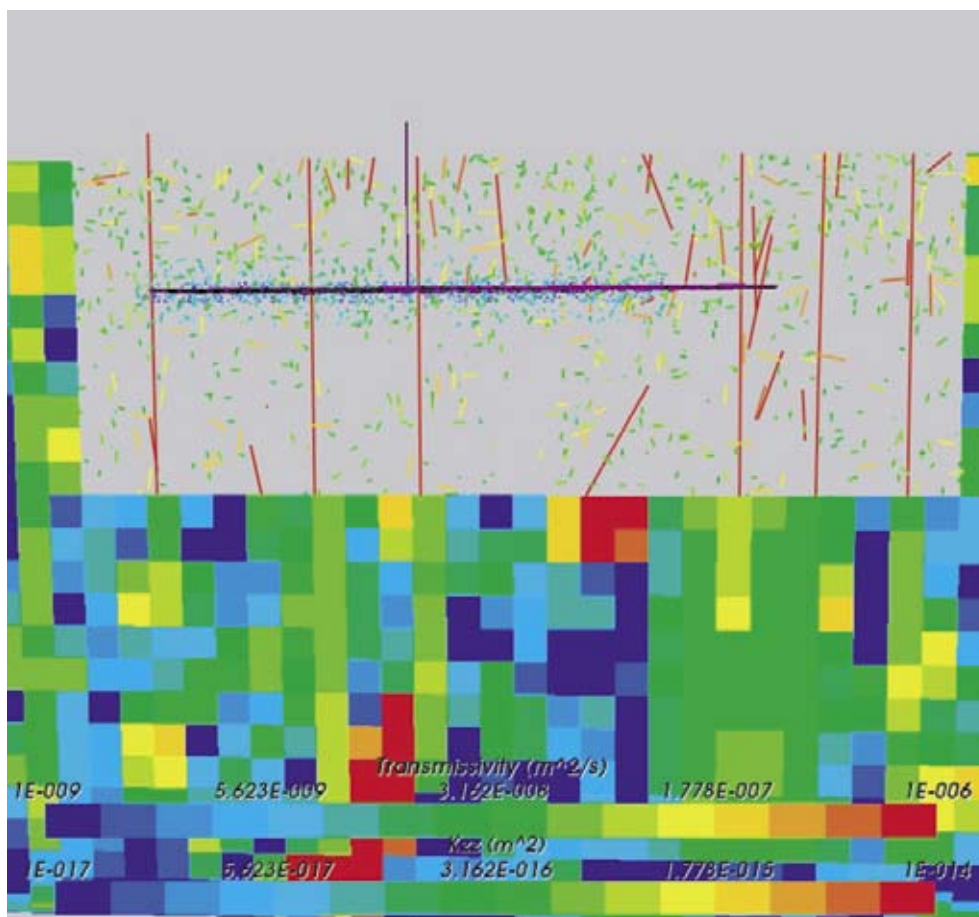


Figure 6-18. A vertical slice through the regional nested model (based on updated DFN) from SW (left) to NE (right). Showing the CPM and DFN area and the extra small-scale fractures around the repository (shown as a purple in the centre). The CPM model is coloured by vertical permeability (k_{zz}). For the DFN model, fractures are coloured by transmissivity. The vertical red lines are fracture zones.

6.3.2 Flow calculations

The distribution of pressure and groundwater flow in the regional-scale nested model was again at times of 2500 AD and 12,000 AD with boundary conditions and the distribution of salinity taken from the updated transient CPM model. The salinity in the CPM part was held fixed and pressure recalculated based on variable density flow with this distribution of groundwater density. It was also used to calculate the environmental pressure in the CPM model on the interface with the DFN to match environmental pressure in the CPM to residual pressure in the DFN. Figure 6-19 shows the distribution of environmental pressure near the top of the regional nested model at 2,500 AD. This demonstrates the continuity in pressure, and near the top surface at least is similar to the pressure distribution shown in Figure 3-41 as would be expected since the top surface boundary condition is set to the current topography. As can be seen many fractures are coloured white. These fractures have no pressure value defined since they belong to isolated clusters not connected to the network. Due to the large degree of heterogeneity in these models, it was found necessary to use a small convergence criterion on the iterative solver used. This resulted in a mass balance of about 10^{-9} .

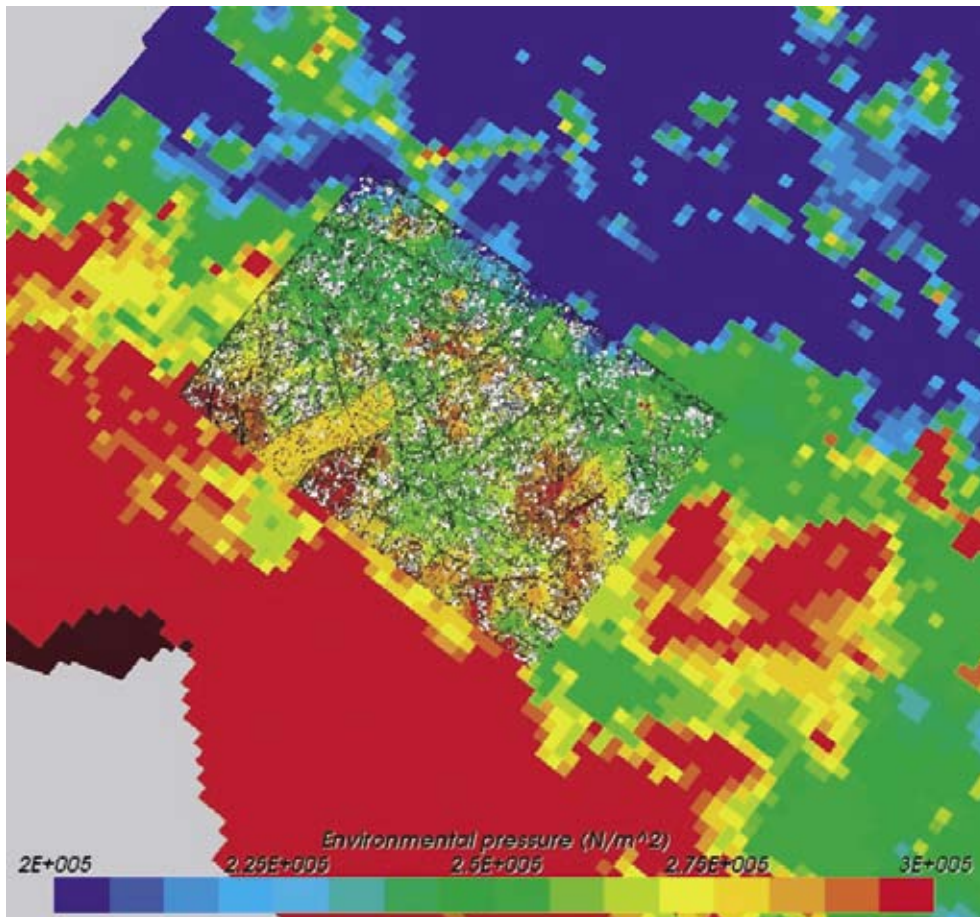


Figure 6-19. Distribution of environmental pressure in the nested regional-scale model (based on updated DFN) near the top of the model with the top two layers removed. For the CPM sub-model, the average environmental pressure in the finite-elements is used. For the DFN sub-model, average residual pressure is used. Fractures coloured white are not connected to the network.

The poor connectivity and its implications for flow and transport are clearly demonstrated in Figure 6-20 which show a horizontal slice through the regional nested model at the repository level $z = -400$ m and at $z = -700$ m. In this case fractures not connected to the network have been removed from the visualisation. At the repository level there are large holes in the DFN model where there is essentially no fracture flow due to the sparsity of the network and connectivity occurs mainly around fracture zones and near the repository tunnel. Hence, the tunnels have a large impact on the potential for flow in fractures by joining up others unconnected clusters of fractures. At $z = -700$ m the repository is superimposed only for reference. Of course it does not affect connectivity at this depth. At this depth connectivity only occurs locally around the fractures zones implying that flow will be heavily channelised into a few discrete fracture zones with little if any flow in the surrounding rock. The distribution of environmental pressure is again shown to be continuous between the DFN and CPM regions. The connectivity in proximity to the tunnels is shown in more detail in Figure 6-21. There are a few areas where clusters of fractures connect adjacent tunnels together while areas away from the tunnels are disconnected. This all suggests that tunnels can potentially play a large role in transport pathways for this sparse network.

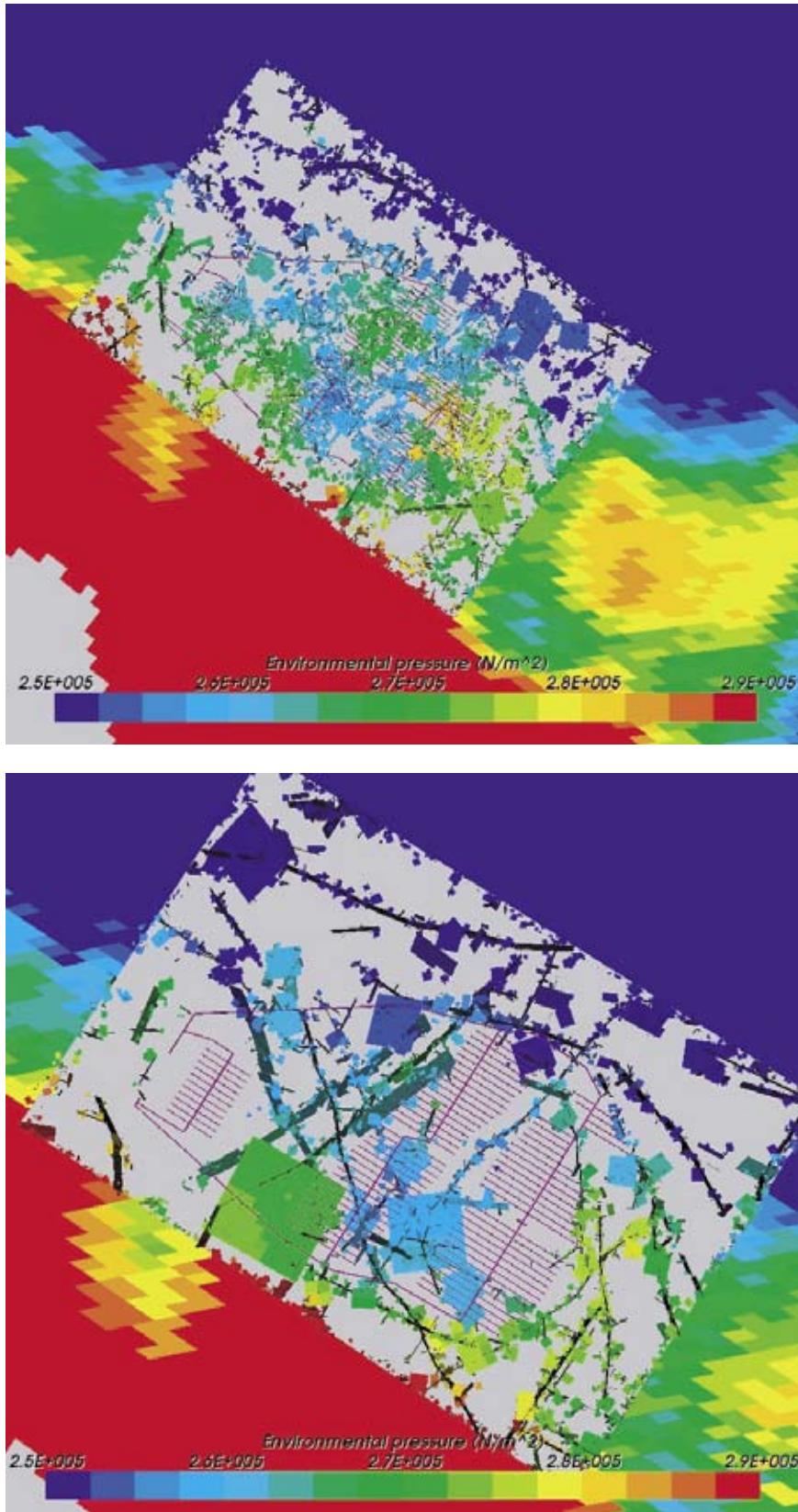


Figure 6-20. Distribution of environmental pressure in the nested regional-scale model at $z = -400$ m (top), and $z = -700$ m (bottom). For the CPM sub-model, the average environmental pressure in the finite-element is used. For the DFN sub-model, the average residual pressure is used. Fractures not connected to the network have been removed.

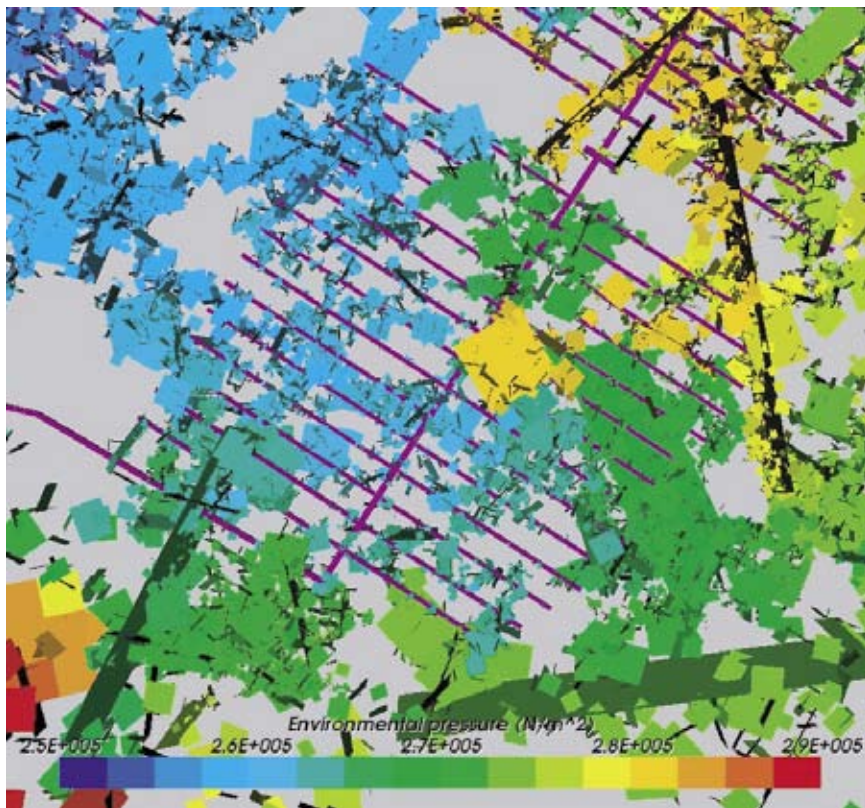
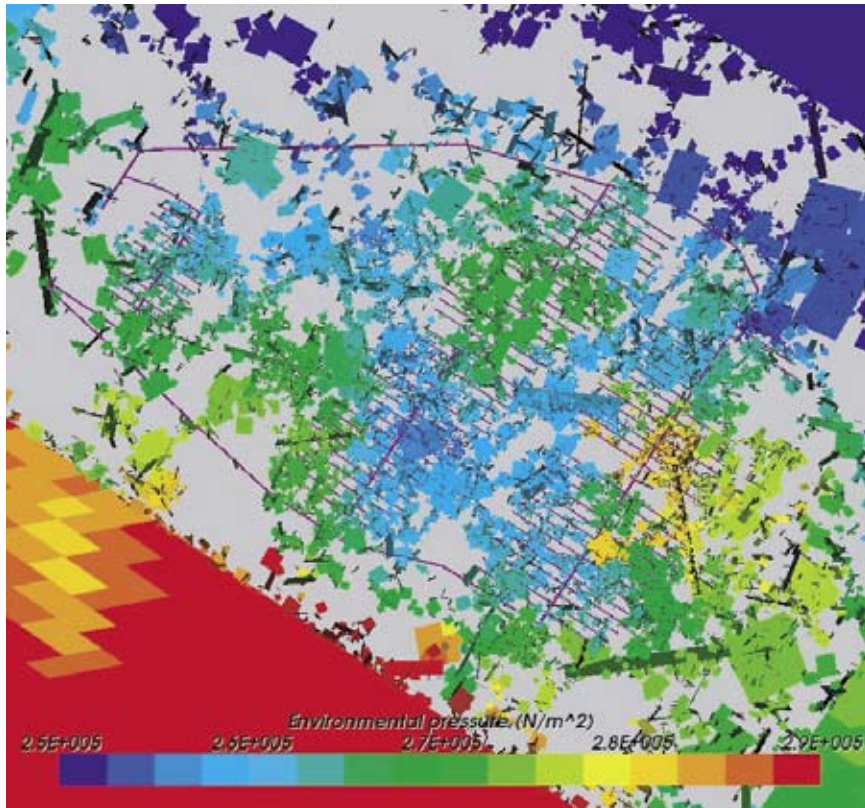


Figure 6-21. Distribution of environmental pressure in the nested regional-scale model at $z = -400$ m for the repository (top), and for the south-east corner (bottom). The average residual pressure in each fracture is used. Fractures not connected to the network have been removed.

6.3.3 Particle tracking calculations

Particle tracks were calculated for all 5026 canisters in the regional-scale model. Note, the deposition tunnels are represented explicitly in the DFN model by vertical fractures with an appropriate transmissivity and transport aperture (though it is set to a very small value to avoid including the travel-time or F-quotient in the tunnel). Since the canisters are not modelled and intersections between canisters and fractures cannot be studied on this scale, a conservative approximation is made to start particles at the nearest connected fracture intersection to the canister. Figure 6-22 shows the start location (nearest fracture intersection) and the exit location. Many of the discharge points are vertically above the repository, although there are a number of longer paths also. Many of the discharge points are associated with large values of F-quotient around 10^8 yr/m. The top picture reveals that the smaller values of F-quotient are almost exclusively associated with canister locations close to deterministic fracture zones.

The process of selecting start locations for particles at the nearest fracture intersection is illustrated in Figure 6-23 where the start points are shown in the top picture, and the start points superimposed on the connected fracture network is shown in the lower picture. Clearly start points coincide with the areas where the tunnels produce clusters of connected local networks. This is thought to be a conservative assumption since particles are moved to the nearest flow channel although there may in fact be no connection between the canister and this flow channel.

Focussing on the main study area in the south-east corner of the repository, Figure 6-24 shows pathlines for particles starting at the nearest fracture. However, it is seen that particles tend to mainly get focussed toward the tunnels and only really enter the network to a significant degree around the fracture zones that runs SE-NW through the repository. This is all for the base case with a low backfill permeability of 10^{-10} m/s, and yet the tunnels dominate the local pathways. Hence, for the updated DFN a lot of attention will have to be paid to the tunnels in the safety assessment.

In performing the transport calculations a numerical problem was identified associated with losing particles in stagnant parts of the network. Up to 10% of particles were lost. This was found to be associated with particles entering dead-ends within the network that although connected act like local circulation cells. Typically these are off-shoots of clusters of small fractures that branch off from large fractures, and result from a combination of the poor connectivity, power-law length distribution and T versus L correlation. A number of approaches were tried to remedy this problem including refining large fractures by subdividing them. Another possible remedy is to remove dead-end clusters along with isolated ones. This would give a pessimistic case, but may remove a retention mechanism of essentially advection/diffusion into stagnant flow areas.

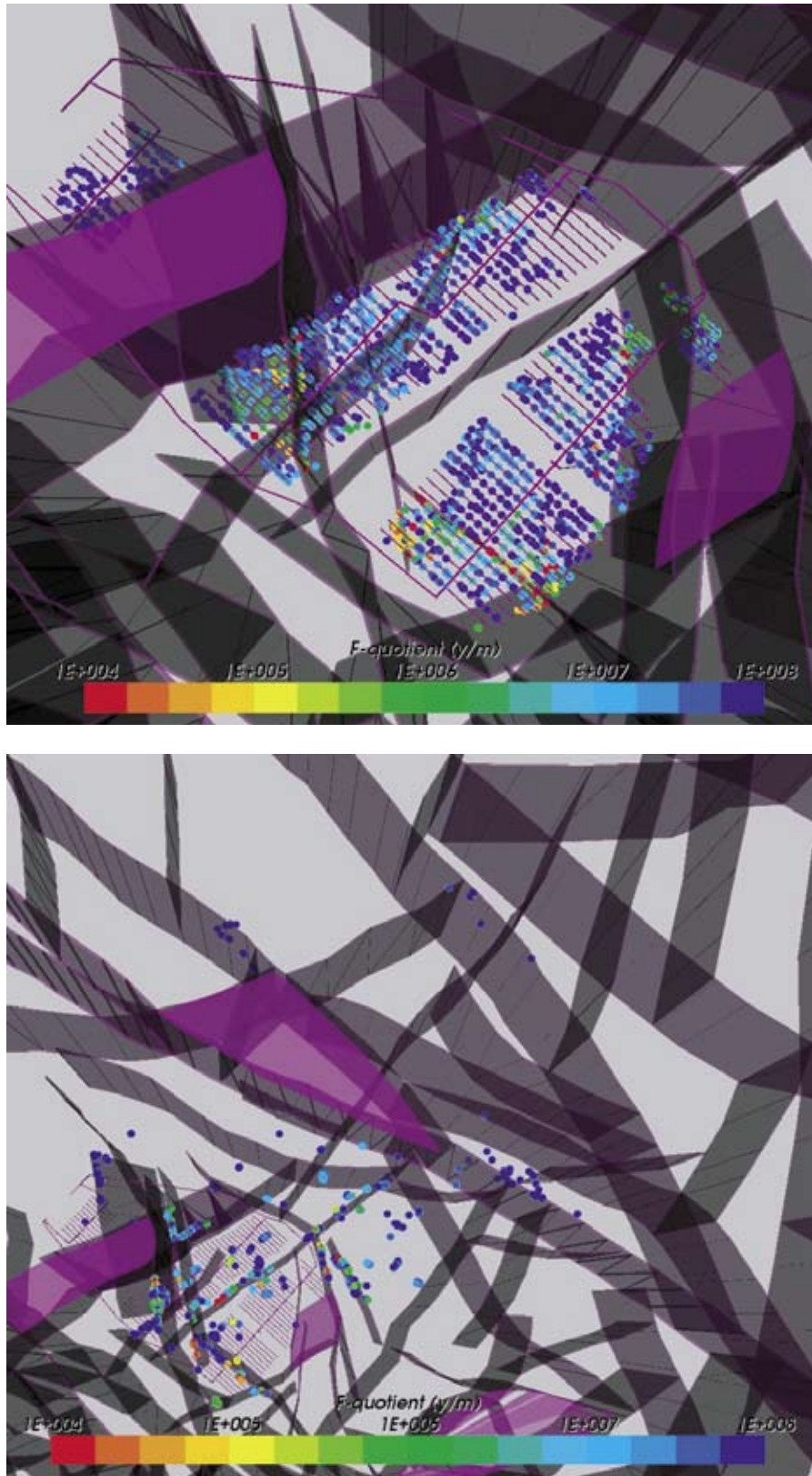


Figure 6-22. Start (top) and exit (bottom) locations for particle tracks in the regional-scale nested model (based on updated DFN) for 5026 canisters. Points are coloured by F-quotient and the fracture zones and repository layout are superimposed. The start points are located at the nearest fracture intersection to the canister.

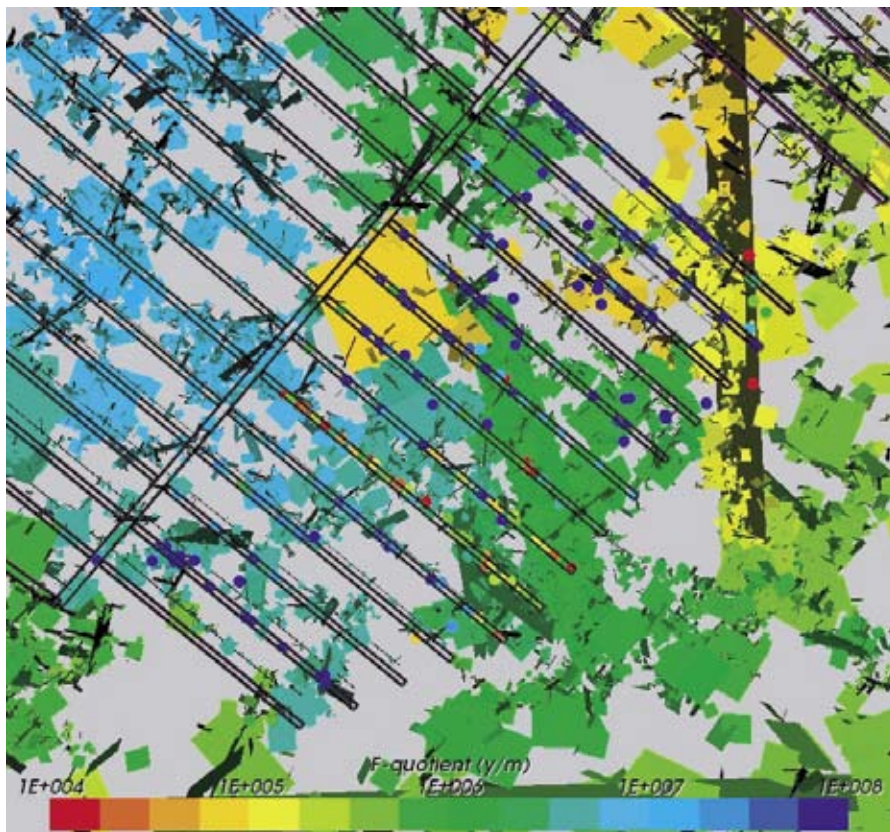
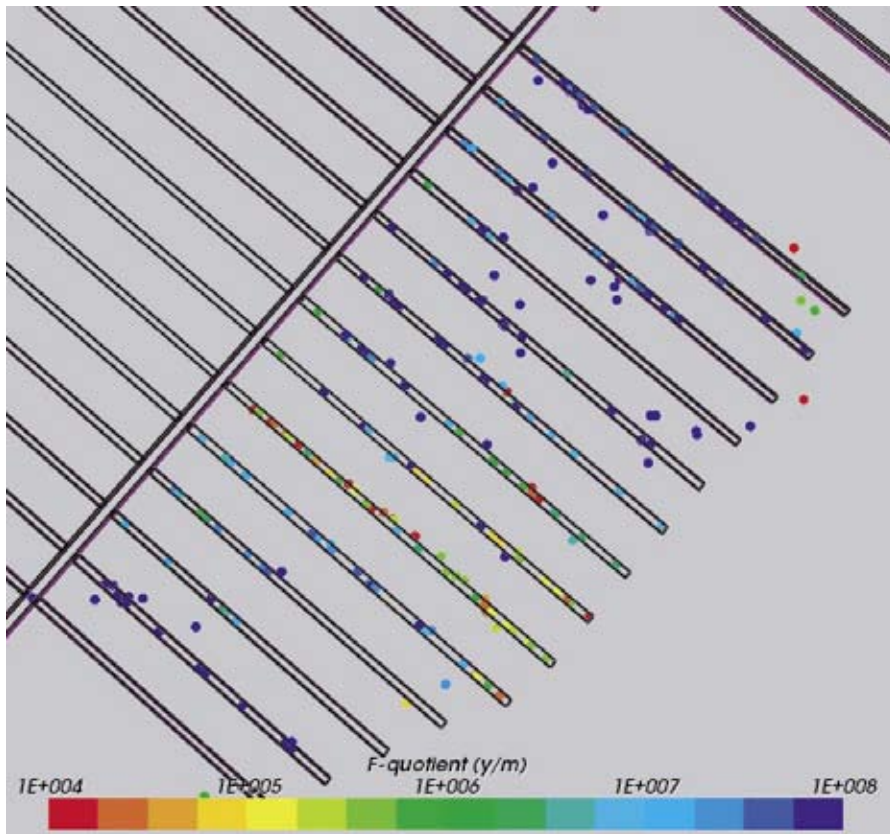


Figure 6-23. Start locations for particle tracks in the regional-scale nested model (based on updated DFN) for 604 canisters in the south-east of the repository. Start points are coloured by *F*-quotient. The start points are located at the nearest fracture intersection to the canister (top), and with the connected fracture network around the repository coloured by head (below).

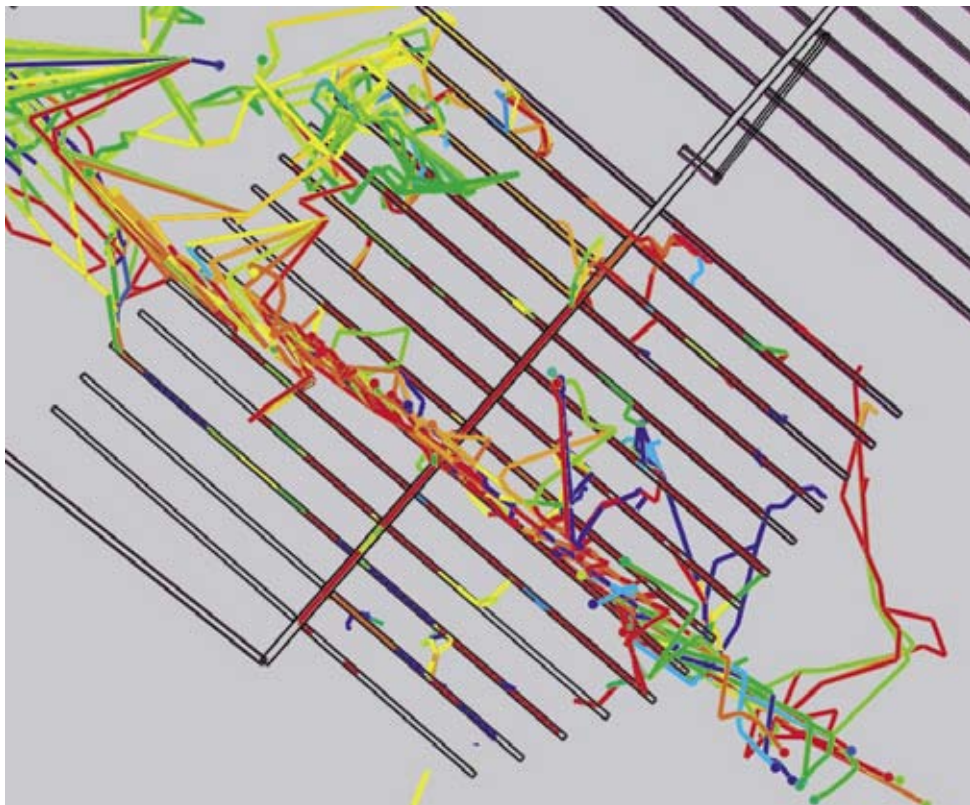
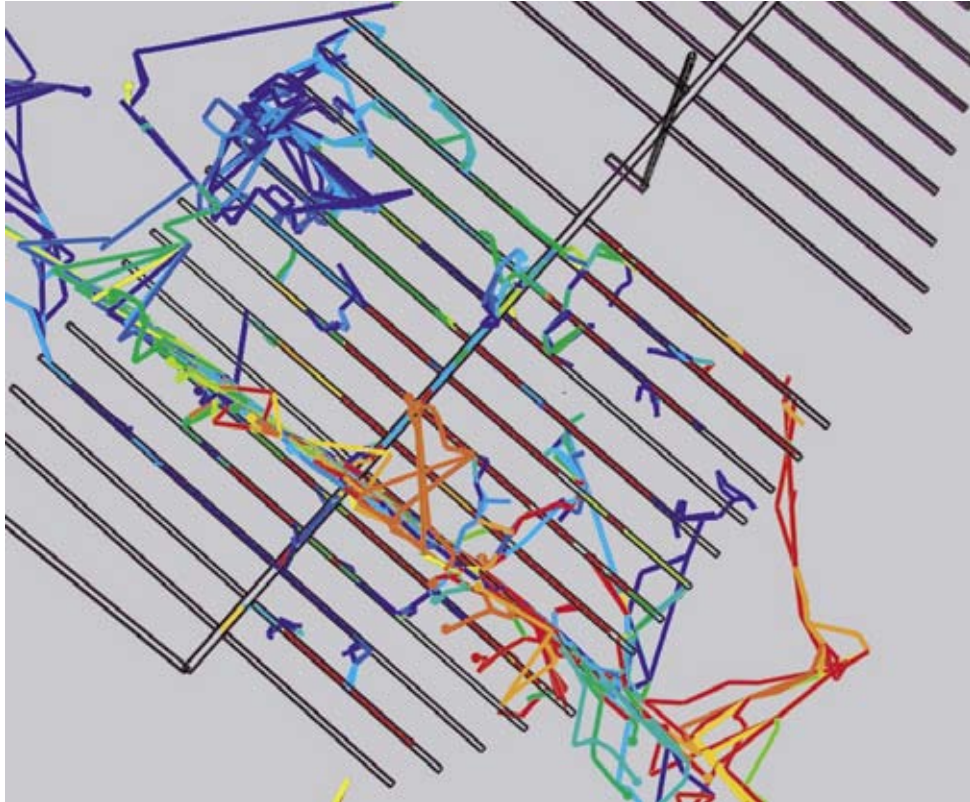


Figure 6-24. Particle tracks in the regional nested model (based on updated DFN) for particles starting in the 604 canisters in the south-east corner of the repository. The paths are coloured by travel time along the path. Particles are released at 2,500 AD. Backfill conductivity is 10^{-10} m/s (top) and 10^{-8} m/s (bottom).

6.4 Nested canister-scale DFN/CPM model

A canister-scale model was constructed for the updated DFN using the 14 deposition tunnels in the same domain as in Section 4 to calculate the flow rates around the canisters and in the deposition tunnels in detail.

6.4.1 CPM/DFN model

The model is 100 m thick. The same larger fractures used in the regional-scale model were imported into this domain (about 30,000 in total) and further small-scale fractures were added around the canisters to try to provide connection between the canisters and a flowing part of the network. This was done by adding fractures on the scale 1.5 m to 4 m in a slab 25 m thick around the tunnels giving about 0.25 million fractures in total. By doing this it was ensured that a fracture intersected every canister hole, but still many of these did not connect to the network. Figure 6-25 shows the fracture network coloured by the calculated head. The boundary conditions were obtained from calculating the environmental pressure in the CPM model at selected times for points on the sides of the nested canister-scale model.

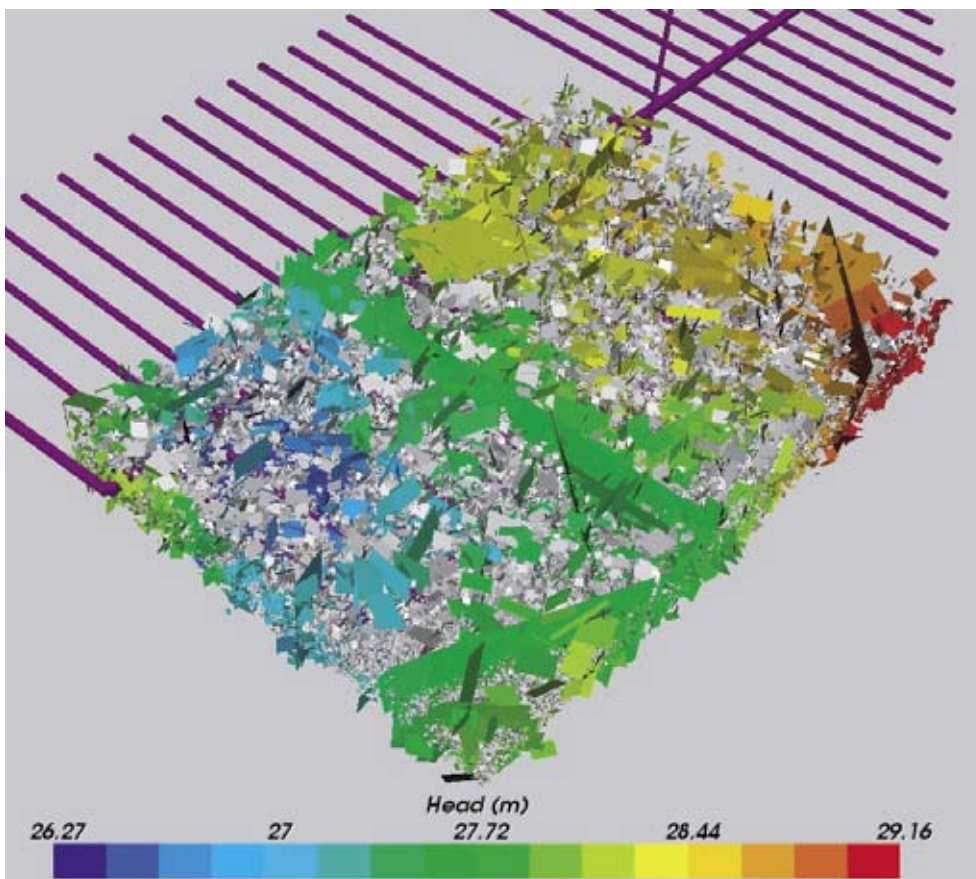


Figure 6-25. The updated DFN model for the nested canister-scale model. The fracture are coloured by head, and part of the repository tunnels is shown in the background.

Figure 6-26 shows a horizontal slice through the network at repository depth showing the distribution of fractures on all scales. Although the small-scale fractures have a high intensity, their connectivity is still poor due to their very limited extent.

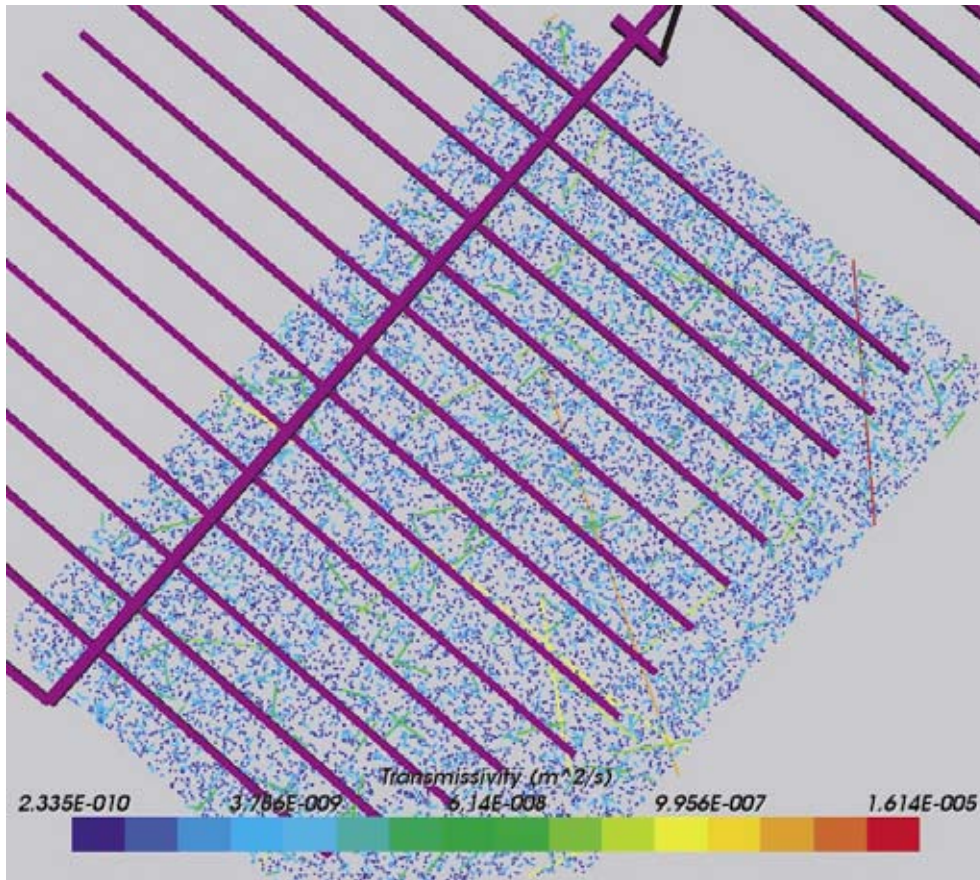


Figure 6-26. The updated DFN model for the nested canister-scale model on a horizontal slice at $z = -400$ m. The fractures are coloured by transmissivity.

6.4.2 Flow calculations

The issue of connectivity is demonstrated in Figure 6-27 which shows the distribution of environmental head around the repository with unconnected fractures removed. It shows the clusters of fractures connected to the tunnels that occasionally connect between adjacent tunnels. The distribution of head suggests a flow from the NE corner to an area of low head in the west. Figure 6-28 shows the connectivity pattern between the tunnels in more detail. Many fractures simply act as dead-end connections spreading out from the tunnel while the occasional larger fracture provides a local network of fractures that joins two tunnels and provides a path for cross flows.

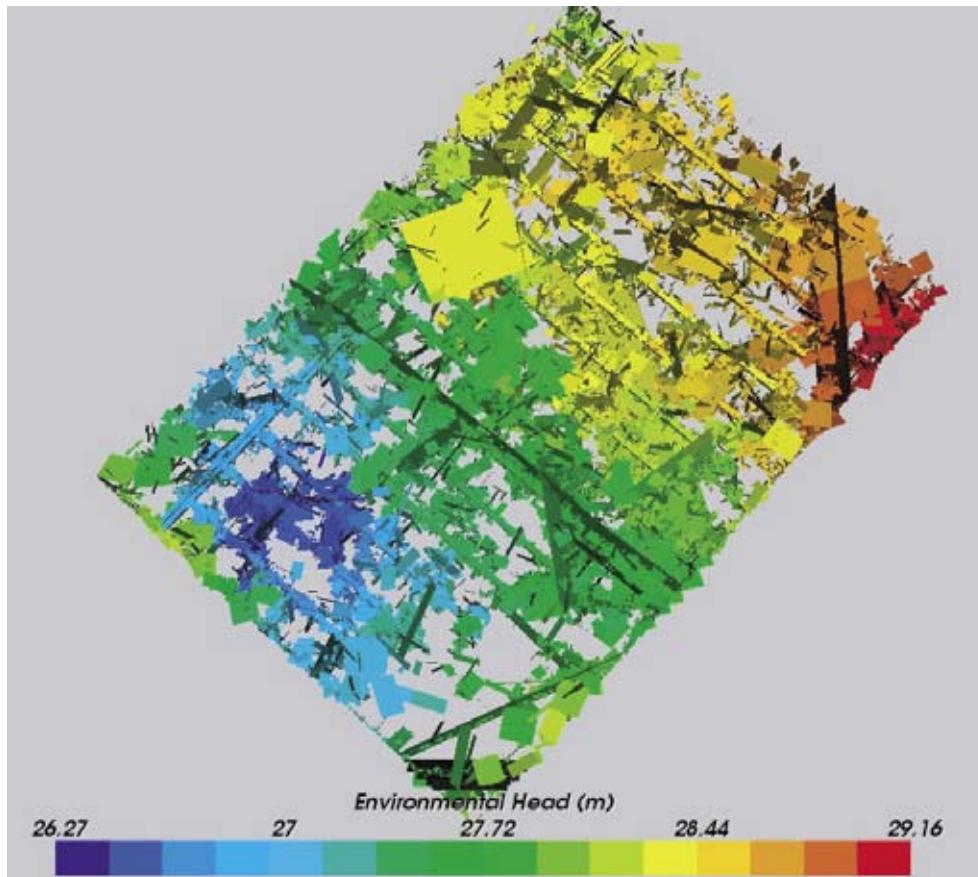


Figure 6-27. The distribution of environmental head in the nested canister-scale model (based on updated DFN). Fractures not connected to the network have been removed. The pressure is continuous between the fractures and CPM tunnels.

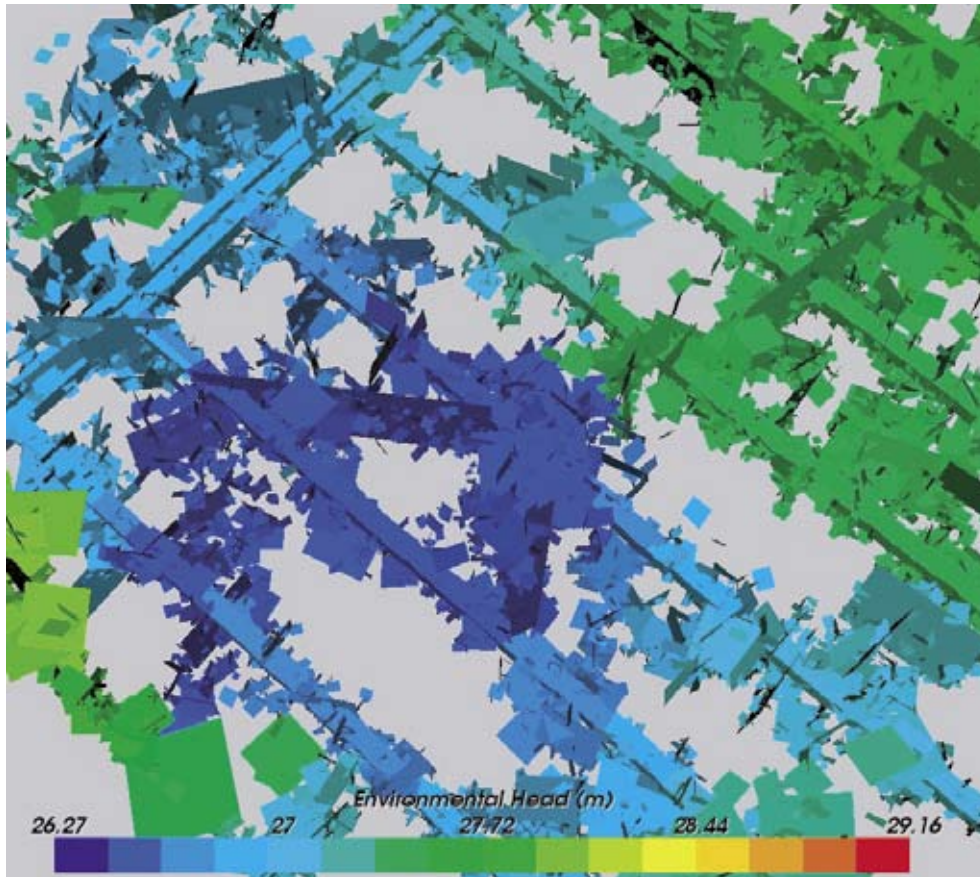


Figure 6-28. The sparsely connected network of fractures around the tunnels. Fractures and tunnels are coloured by a consistent environmental pressure, and fractures not connected to the network are removed.

6.4.3 Particle tracking calculations

It was intended to use a methodology identical to the original DFN in terms of nesting the transport pathways on the canister and regional scales. However, the problem of lost particles (see section 6.3.3) and modelling transport in a system dominated by the tunnels created problems that could not be solved in the timescales available for this updated DFN. These problems could be addressed by removing dead-end clusters and using more refined meshes to represent transport in the tunnels. However, for this methodology development phase it was decided to just calculate the initial flow-rates in the fractures intersecting the canisters and in the tunnels to give the input (Q_{eq}) to the near-field models, and take travel time and F-quotient from the regional-scale nested model.

6.5 Performance measures

- In this section we will consider the performance measures required by safety assessment for three cases:
- A release at 2,500 AD with tunnel backfill with conductivity 10^{-10} m/s;
- A release at 12,000 AD with tunnel backfill with conductivity 10^{-10} m/s;
- A release at 2,500 AD with tunnel backfill with conductivity 10^{-8} m/s.

6.5.1 Base case – low backfill conductivity and release at 2,500 AD

Qeq for the base case is given in Figure 6-29 for the cases of particles starting in a fracture (Path_f), the EDZ (Path_t2), a fracture intersecting the tunnel (Path_t3), and in the CPM model (path_c). For Path_f the distribution is broad with a median value 10^{-5} m³/yr, a standard deviation about 1, and only 366 of the 604 canisters are intersected by connected parts of the network. For the tunnel paths, the median flow rate is over half an order of magnitude higher and is bi-modal. The lower mode corresponds to flows in parts of the tunnel upstream from the first connected fracture cluster to intersect the tunnel i.e. in a stagnant flow end of the tunnel.

The flow-rate in the 100 m porous medium predicts considerably higher flow rates presumably because it tends to over-predict connectivity on this scale. The median flow rate in the CPM is about 4×10^{-4} m³/yr. The results are tabulated in Table 6-1. Comparing with the original DFN the flow rates are lower by about half an order of magnitude than before.

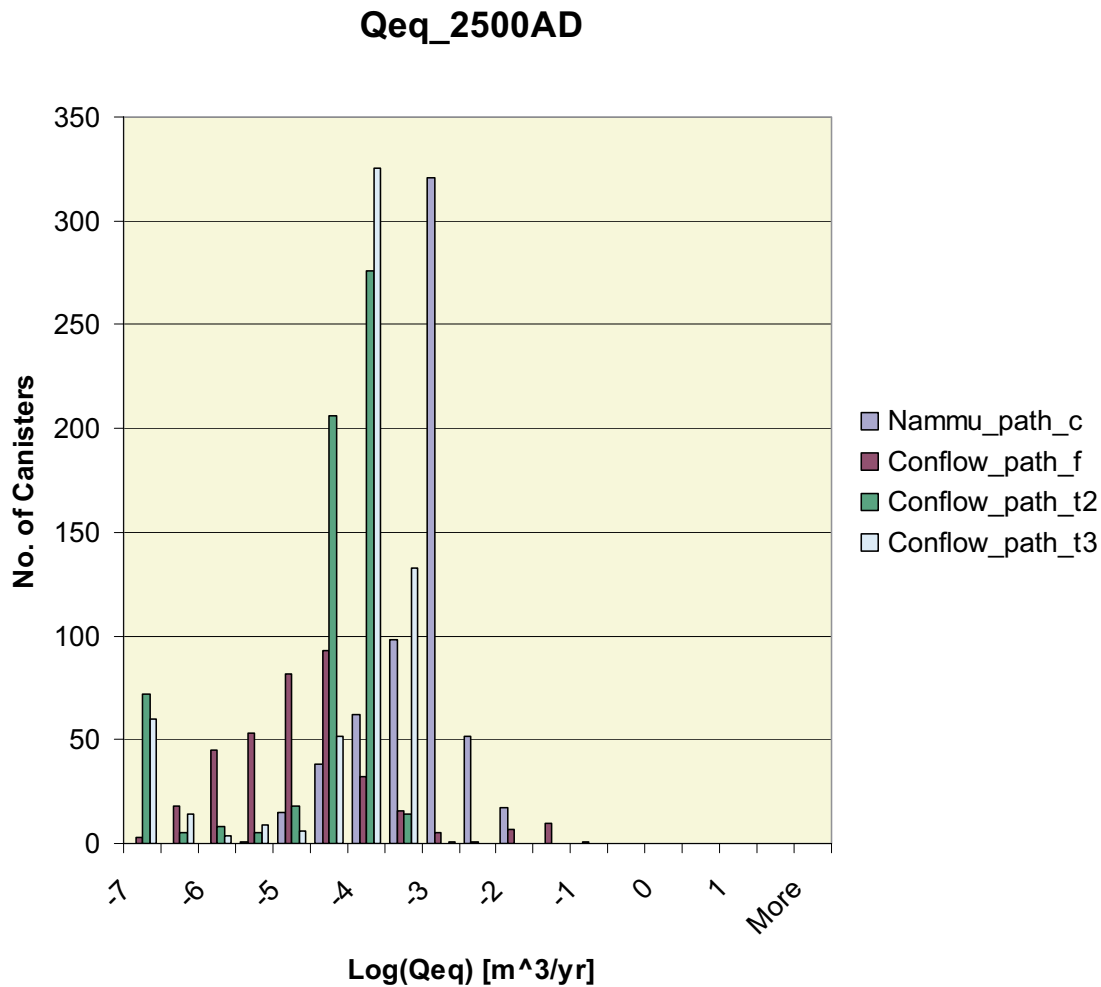


Figure 6-29. Distribution of Qeq in the canister-scale model (based on updated DFN) of 604 canisters for a release of particles at 2,500 AD. The four cases shown are for: the CPM model; the nested model for Path_f (in fractures adjacent to the canister); the nested model for Path_t2 (in the EDZ); the nested model for Path_t3 (in the tunnel).

Table 6-4. Performance statistics: Distribution of $\log_{10}(\text{Qeq} [\text{m}^3/\text{yr}])$ at 2,500 AD for the CPM model (Path_c) and Path_f, Path_t2 and Path_t3 for the nested model (based on updated DFN).

	CPM model	Nested model		
	Path_c	Path_f	Path_t2	Path_t3
Mean	-3.502	-5.058	-4.899	-4.604
Median	-3.338	-5.097	-4.513	-4.217
5th percentile	-4.852	-6.519	-7.763	-7.467
10th percentile	-4.403	-6.224	-7.289	-6.993
25th percentile	-3.892	-5.709	-4.766	-4.470
75th percentile	-3.146	-4.643	-4.316	-4.020
90th percentile	-2.706	-3.929	-4.137	-3.841
95th percentile	-2.638	-2.962	-4.058	-3.762
Std deviation	0.624	1.039	1.100	1.100
Variance	0.389	1.080	1.210	1.210
Max value	-2.153	-1.461	-3.670	-3.374
Min value	-5.645	-7.352	-8.313	-8.017

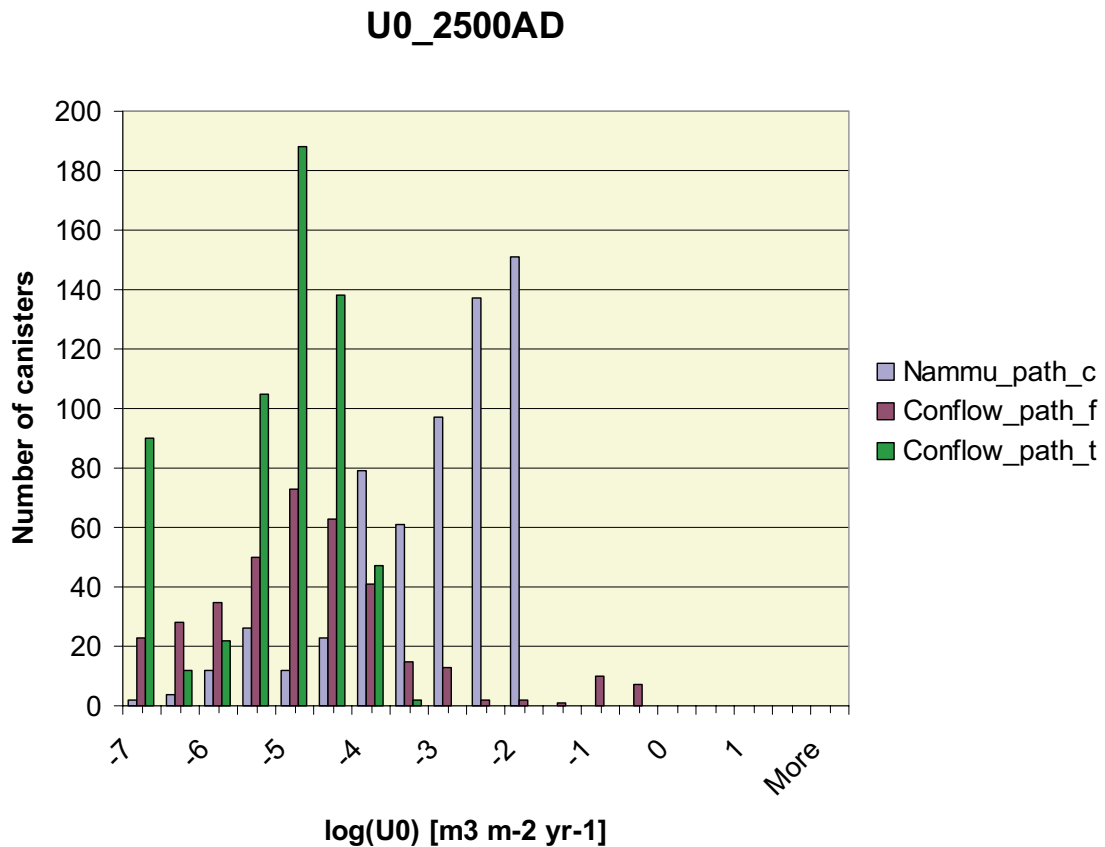


Figure 6-30. Distribution of Darcy velocity (U_0 in the CPM, U_{0f} in the DFN) in the canister-scale model (based on updated DFN) of 604 canisters for a release of particles at 2,500 AD. The three cases shown are for: the CPM model Path_c; the nested model for Path_f (in fractures adjacent to the canister); and the nested model for Path_t (in the tunnel).

The results for the flow velocity U_0 are of course similar as shown in Figure 6-30. The spread of velocities for Path_f is between 10^{-1} and 10^{-7} m/yr with a model value about 10^{-5} m/yr. This is quite distinct from the distribution for the CPM model which has the majority of values between 10^{-4} and 10^{-2} m/yr.

The results for travel time are given as a comparison between paths starting in a fracture, the tunnel or in a CPM model (Figure 6-31 and Table 6-5). The distribution for Path_f and Path_t are very similar as can be expected from the fact that particles starting in a fracture tend to go into a tunnel since they are the main conduits for flow even with low backfill permeability. The median travel time is about 3,000 years with a standard deviation about 1.3. For the CPM model the median is about 20,000 years, but this corresponds to a generally longer path. The standard deviation is much less also, about 0.8. Comparing to the original DFN, travel times are much longer by nearly two orders of magnitude.

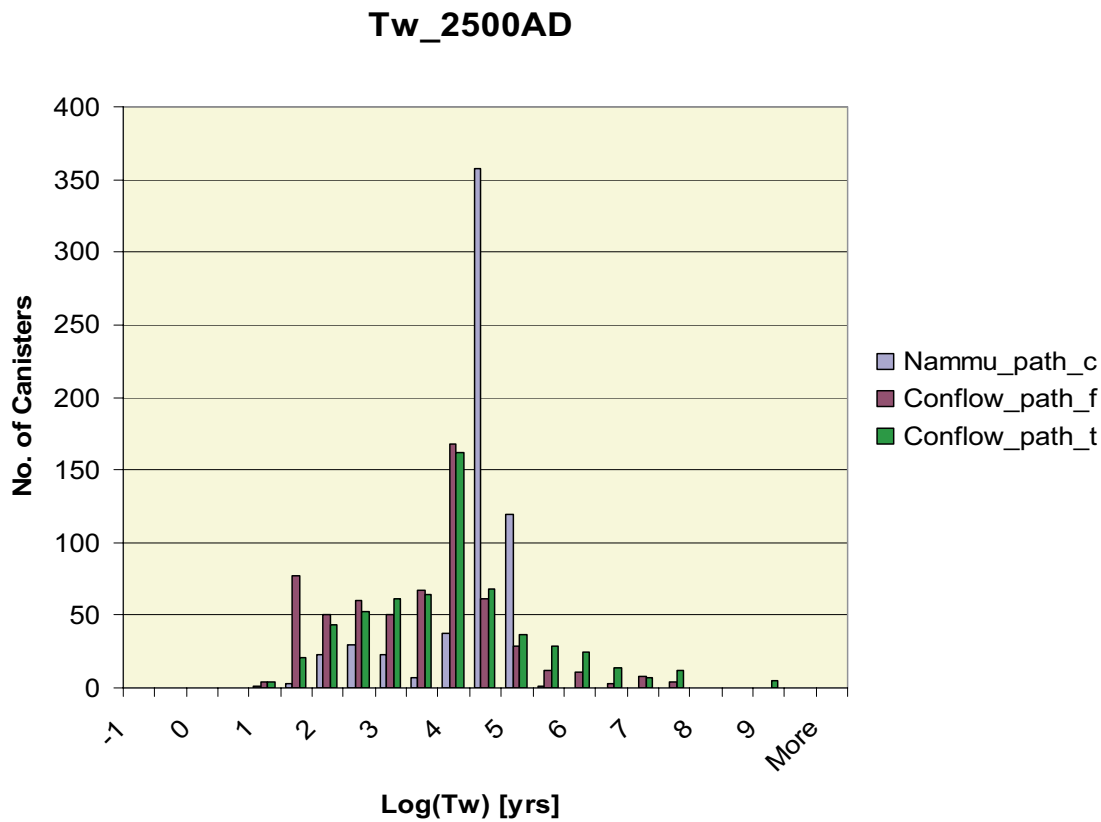


Figure 6-31. Distribution of travel time, tw , in the nested model (based on updated DFN) with a release from 604 canisters at 2,500 AD. The three cases shown are for: the CPM model (Path_c); the nested model for Path_f (in fractures adjacent to the canister); and the nested model for Path_t (in the tunnel).

Table 6-5. Performance statistics: Distribution of \log_{10} (travel time [yr]) at 2,500 AD for the CPM model (Path_c) and Path_f, Path_t nested model (based on updated DFN).

	CPM model	Nested model	
	Path_c	Path_f	Path_t
Mean	4.034	3.180	3.702
Median	4.290	3.471	3.754
5th percentile	2.044	1.261	1.559
10th percentile	2.597	1.384	1.958
25th percentile	4.085	2.149	2.858
75th percentile	4.461	3.922	4.161
90th percentile	4.588	4.508	5.466
95th percentile	4.647	5.200	6.415
Std deviation	0.778	1.276	1.370
Variance	0.606	1.629	1.876
Max value	5.065	7.417	8.574
Min value	0.840	0.885	1.096

For the distribution of pathlengths, as shown in Figure 6-32 and Table 6-6, the median length is about 1,000 m for the nested model since it is predominantly the vertical path upwards to the Lake directly above the repository. The median value for the much longer CPM path to the sea is about 10,000 m. The standard deviations are quite small, about 0.18 for the nested models and 0.38 for the CPM model. This is similar to the original DFN, although the nested model gives a slightly shorter path than before, while the CPM path is longer.

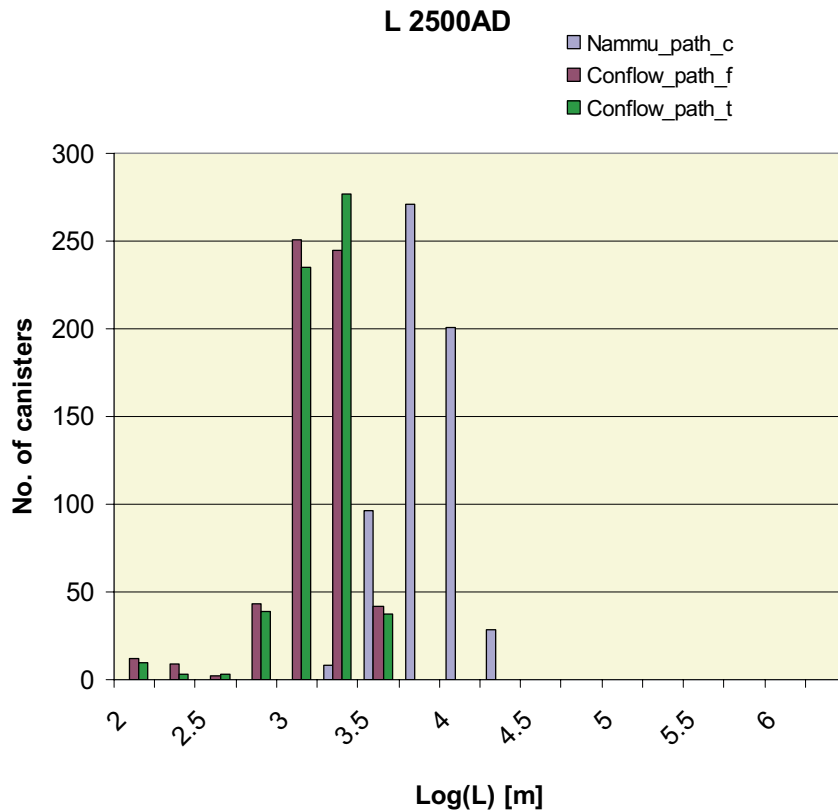


Figure 6-32. Distribution of pathlength, L , in the nested model (based on updated DFN) with a release from 604 canisters at 2,500 AD. The three cases shown are for: the CPM model; the nested model for Path_f (in fractures adjacent to the canister), and the nested model for Path_t (in the tunnel).

Table 6-6. Performance statistics: Distribution of \log_{10} (pathlength [m]) at 2,500 AD for the CPM model (Path_c) and Path_f, Path_t for the nested model (based on updated DFN).

	CPM model	Nested model	
	Path_c	Path_f	Path_t
Mean	3.945	3.001	3.013
Median	4.108	2.987	3.035
5th percentile	2.996	2.724	2.737
10th percentile	3.122	2.764	2.774
25th percentile	3.983	2.852	2.857
75th percentile	4.153	3.169	3.171
90th percentile	4.168	3.236	3.229
95th percentile	4.178	3.265	3.261
Std deviation	0.375	0.184	0.179
Variance	0.140	0.034	0.032
Max value	4.212	3.449	3.361
Min value	2.799	2.460	2.439

Probably the biggest change in the performance measures from the original DFN is in the calculated F-quotient. The distribution for F is given in Figure 6-33 and Table 6-7. It is considerably wider with a median, nearly an order of magnitude higher than for the original DFN, of about 4×10^7 yr/m and a standard deviation of 1.5, which is about double that for the original DFN. The minimum value is about 10^4 yr/m which is similar to the original model.

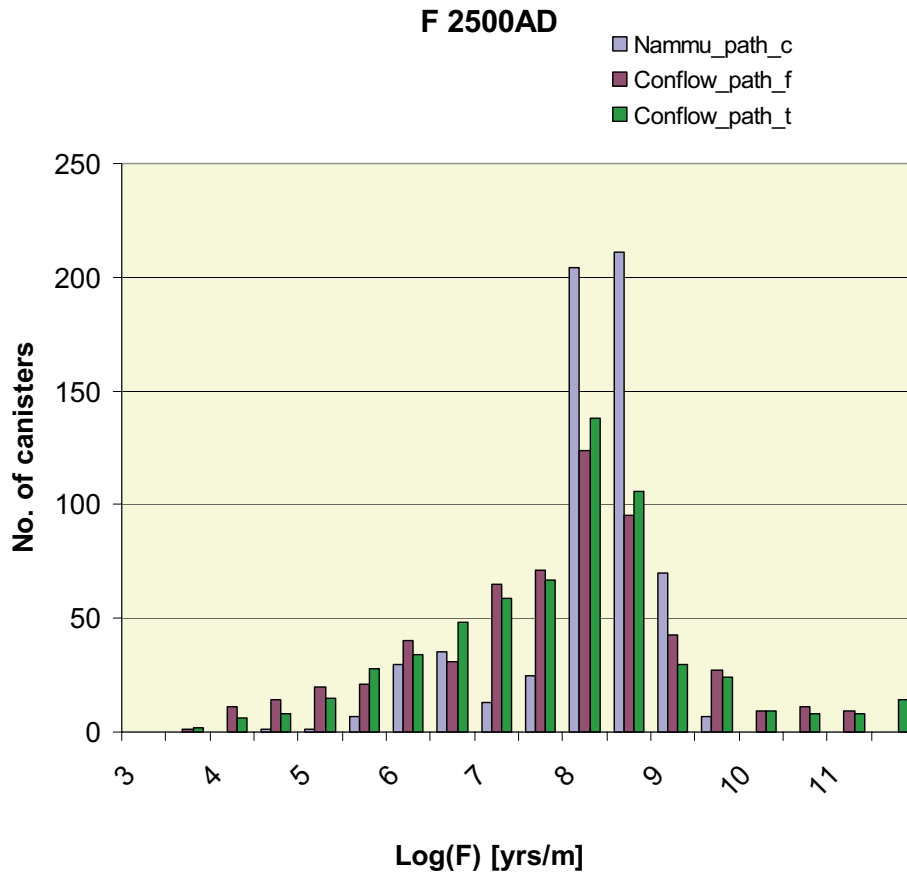


Figure 6-33. Distribution of F-quotient in the nested model (based on updated DFN) with a release from 604 canisters at 2,500 AD. The three cases shown are for: the CPM model; the nested model for Path_f (in fractures adjacent to the canister); and the nested model for Path_t (in the tunnel).

Table 6-7. Performance statistics: Distribution of \log_{10} (F-quotient [yr/m]) at 2,500 AD for the CPM model (Path_c) and Path_f, Path_t for the nested model (based on updated DFN).

	CPM model	Nested model	
	Path_c	Path_f	Path_t
Mean	7.794	7.435	7.488
Median	7.967	7.635	7.699
5th percentile	5.949	4.856	5.040
10th percentile	6.184	5.259	5.637
25th percentile	7.646	6.628	6.653
75th percentile	8.330	8.227	8.186
90th percentile	8.564	9.063	8.914
95th percentile	8.760	9.698	9.685
Std deviation	0.828	1.492	1.402
Variance	0.685	2.225	1.965
Max value	9.154	11.727	11.727
Min value	4.344	3.719	3.764

% Pathlength in tunnel - K=1E-10m/s; 2500 AD

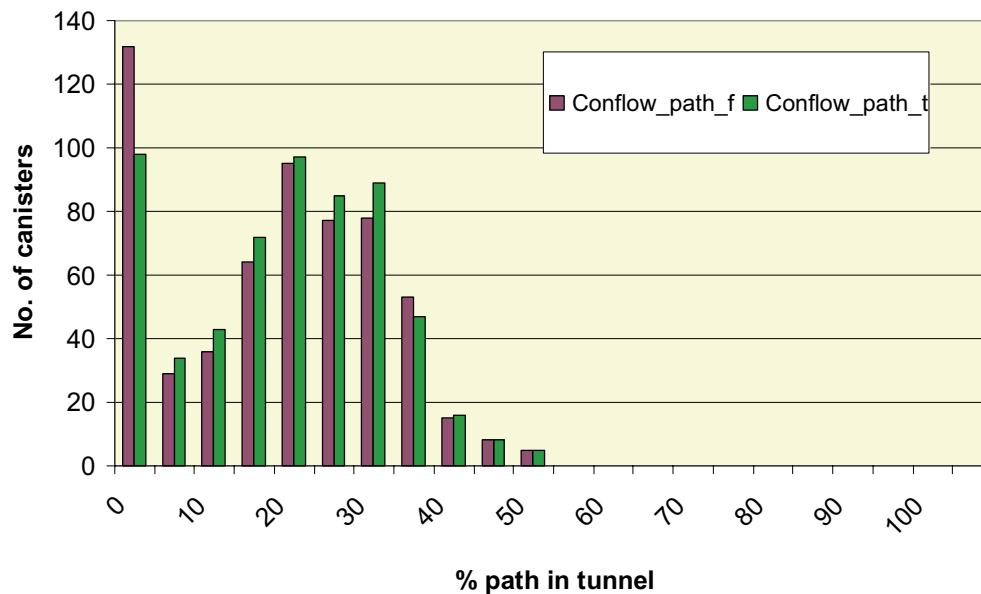


Figure 6-34. Distribution of the percentage of the pathlength in the tunnel compared to the whole pathway for the nested model (based on updated DFN) with a release from 604 canisters at 2,500 AD. The two cases shown are for: the nested model for Path_f (in fractures adjacent to the canister), and the nested model for Path_t (in the tunnel).

The rise in importance of the tunnel as a significant transport pathway is evident in the distribution of % of pathlength spent in the tunnel. For both Path_f and Path_t, many pathways spend a significant distance in the tunnel with a modal value of about 20% and maximum of about 50% which would suggest pathways either entering several tunnels or a deposition tunnel and the access tunnel. This is markedly different to Figure 5-8 where hardly any paths spent more than 10% of their distance in the tunnel.

Figure 6-35 illustrates the correlation between flow-rate Q_{eq} and travel time for the various paths. Path_f is a bit of a ‘shot-gun’ distribution with large spread in both Q_{eq} and to a slightly lesser extent travel time. For Path_t2 and Path_t3 the bi-modal behaviour is apparent with a cluster of points with high Q_{eq} and low travel time for particles starting in parts of the tunnel with some through-flow, while the second cluster of points with high travel time and low Q_{eq} correspond to particles starting in stagnant areas of the tunnel. The Path_c case is a very concentrated set with little variation in travel time and moderate spread in Q_{eq} toward the higher end of values seen in the nested model.

Figure 6-36 seeks correlations between Q_{eq} and F . For all paths the correlation is quite weak, although for Path_f, high values of Q_{eq} do tend to be associated with lower values of F . Path_t does not suggest any clear correlation between Q_{eq} and F . Again, the scatter for the nested model paths is much greater than that for the CPM model, although there is a spread in F -quotient of about four orders of magnitude for F in the CPM model.

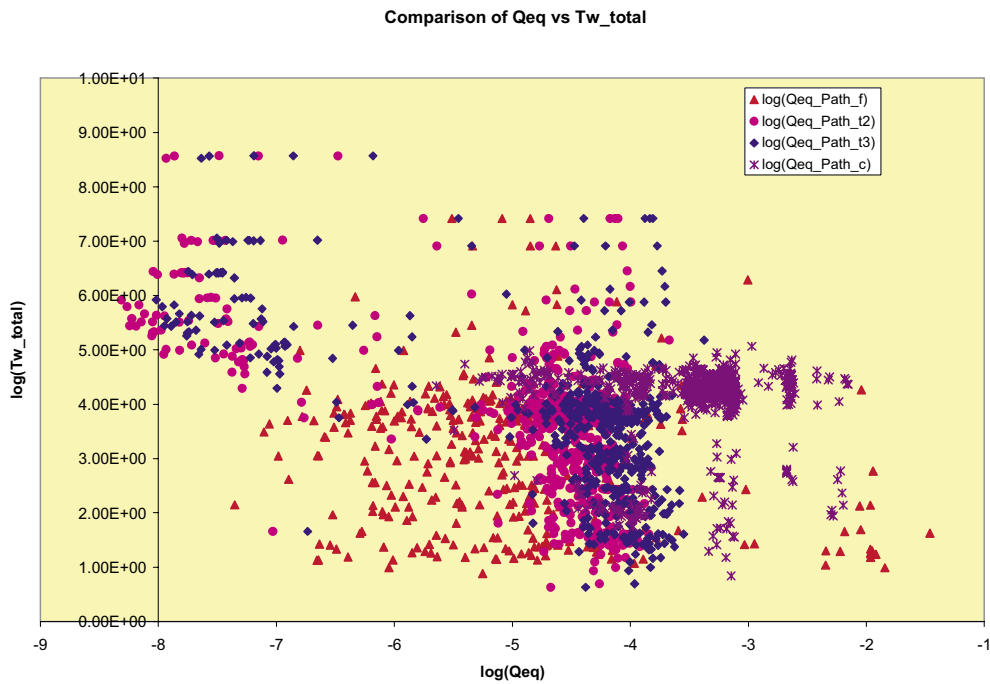


Figure 6-35. Cross-plot of Q_{eq} and travel time, t_w , for pathways in the nested model (based on the updated DFN) with a release from 604 canisters at 2,500 AD. The four cases shown are for: the CPM model, the nested model for Path_f (in fractures adjacent to the canister), the nested model for Path t2 (in the EDZ) and the nested model for Path_t3 (in the tunnel).

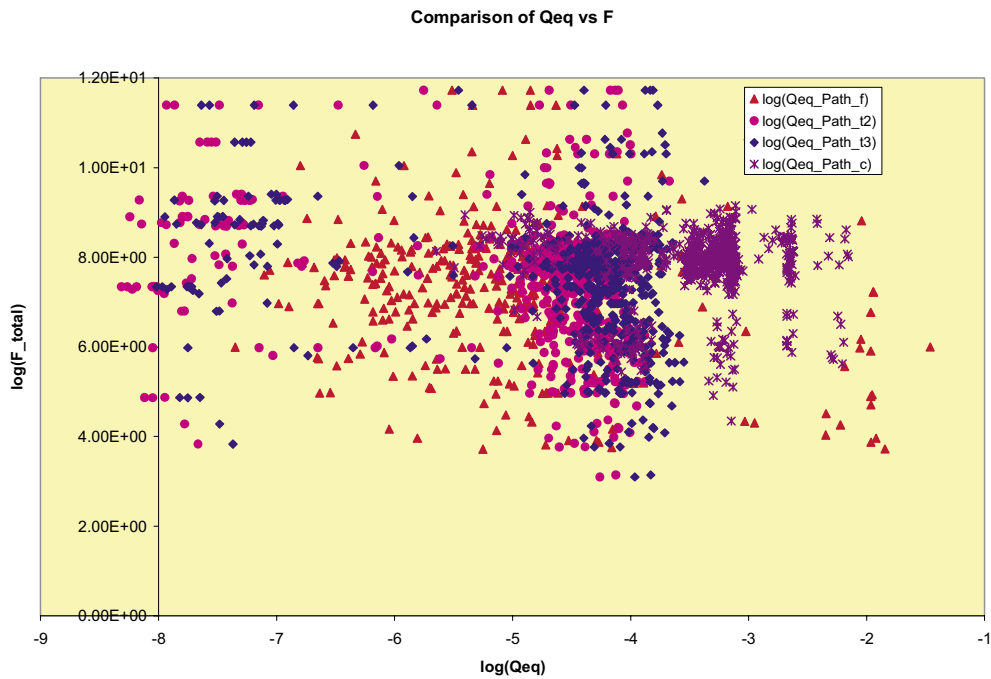


Figure 6-36. Cross-plot of Q_{eq} and F -quotient for pathways in the nested model (for updated DFN) with a release from 604 canisters at 2,500 AD. The four cases shown are for: the CPM model, the nested model for Path_f (in fractures adjacent to the canister), the nested model for Path_t2 (in the EDZ) and the nested model for Path_t3 (in the tunnel).

Due to time constraints and the problem with stuck particles in the updated DFN case, only the first realisation is reported here. Due to the sparsity of the updated DFN it is likely that there will be more variation between realisations than was seen in the original DFN, and hence for the final SR-Can more realisation will be required once solutions have been found for dealing with the stagnant dead-end fracture clusters.

For the single realisation performed the scenarios for a release at 12,000 AD and a higher conductivity backfill case were calculated. In a sense, the higher backfill conductivity case is probably less of a distinct scenario than it was for the original DFN since the tunnels are already an important pathway for a backfill conductivity of 10^{-10} m/s.

Equivalent flow-rates, Q_{eq} , for Path_f and Path_t are compared for the three scenarios in Figure 6-37. For Path_f the results are all very similar. Possibly this suggests that the flow in the fracture system is mainly controlled by the variations in fracture connectivity around the canisters than the exact details of the boundary conditions/pressure gradients. For Path_t there is a slight decrease in Q_{eq} for a release at 12,000 AD and large increase of about two orders of magnitude for the higher conductivity backfill. This is entirely expected since the conductivity is increased by two orders of magnitude. Interestingly, the second mode of Q_{eq} for Path_t around 10^{-7} m³/yr is unchanged by the change in conductivity. This is presumably because this second mode corresponds to flow in stagnant ends of the tunnel which are insensitive to changes in backfill properties and pressure gradients.

The sensitivities of travel time are shown in Figure 6-38 for both paths in the nested model. The two paths are very similar and there is little difference between the two release times. However, changing the backfill conductivity has quite a profound change by narrowing the distribution toward shorter travel times centred on about 100 years. This is a consequence of the higher conductivity tending to focus even more flow on the tunnel and particles having a higher proportion of the pathlength in the tunnel overall. Remember that time spent in the tunnel is excluded from the transport PMs.

The effects on the F-quotient are similar as seen in Figure 6-39. Path_f and Path_t are similar and the different release times have little effect. For the higher conductivity the F-quotient distribution is narrower and has a modal value about two orders of magnitude lower than for the base case backfill around 10^6 yr/m. Again, this can be explained by having more of the path in the tunnel where F-quotient is intentionally excluded from the PMs. The change in the % of pathlength spent in the tunnel for the high backfill conductivity is illustrated in Figure 6-40. The profiles are similar for the two different release times, but there is a general shift to the right for the higher conductivity backfill. Since travel time and F-quotient have been excluded from portions of the path in the tunnel then there is no explicit retention in the tunnel, and hence the sensitivity to this scenario demonstrated in the previous two figures. Clearly, in the safety assessment the methodology needs to account for retention in the tunnel for very sparse networks such as this.

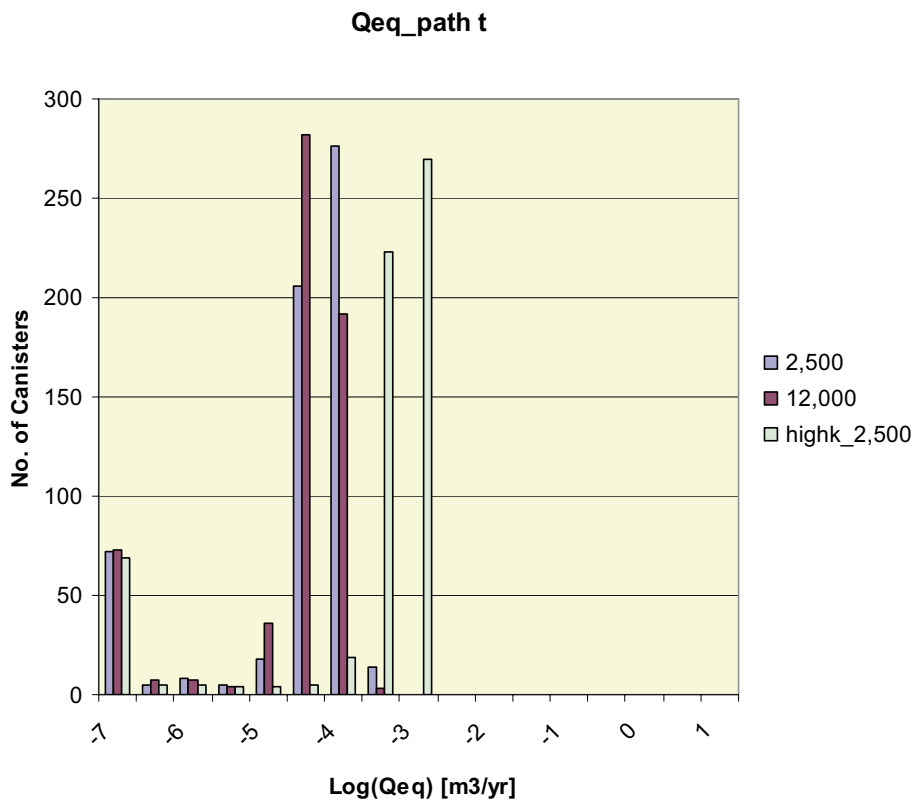
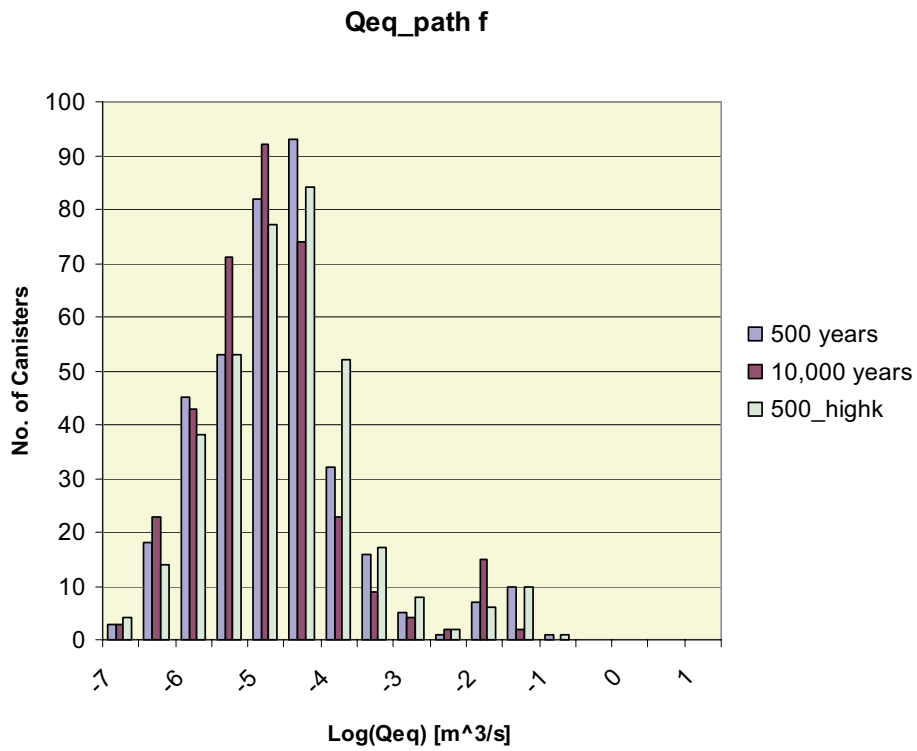


Figure 6-37. Distribution of Q_{eq} in the nested model with a release from 604 canisters into Path_f (top) and Path_t2 (bottom). Three cases are shown: a release after 2,500 AD; a release at 12,000 AD; and for a backfill conductivity of 10^{-8} m/s for a release at 2,500 AD.

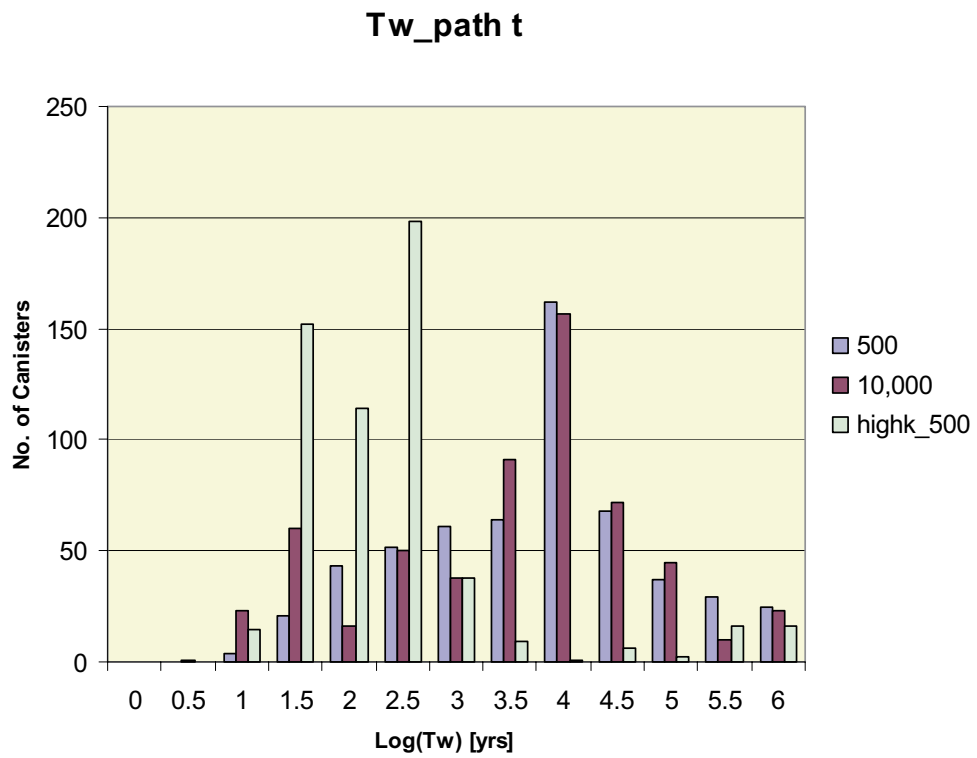
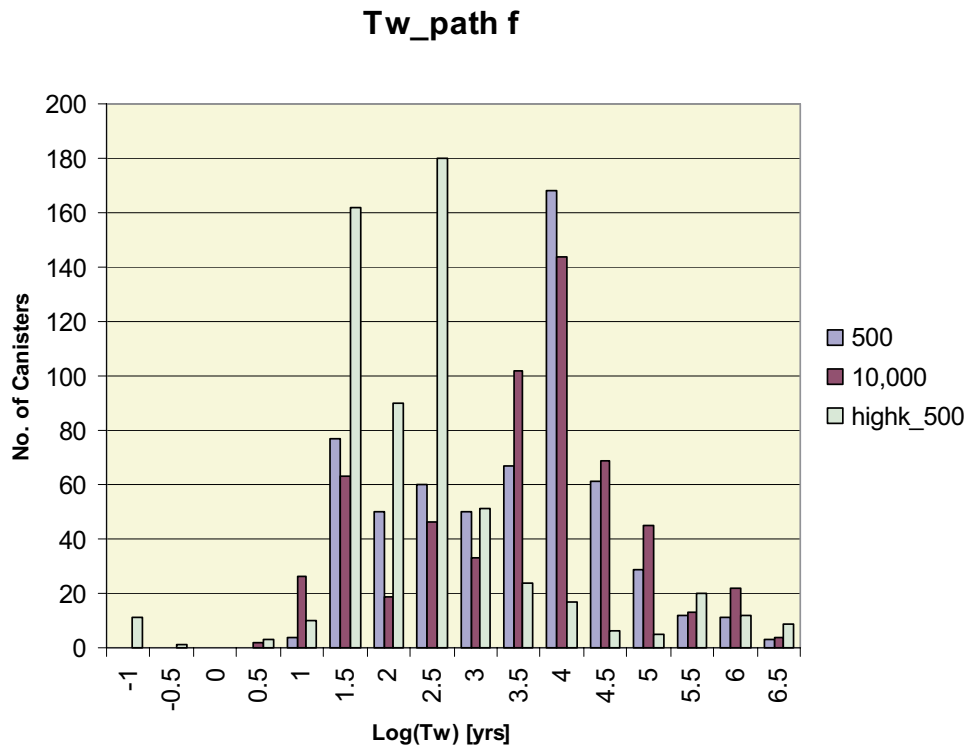


Figure 6-38. Distribution of T_w in the nested model with a release from 604 canisters into Path_f (top) and Path_t2 (bottom). Three cases are shown: a release after 2,500 AD; a release at 12,000 AD; and for a backfill conductivity of 10^{-8} m/s for a release at 2,500 AD.

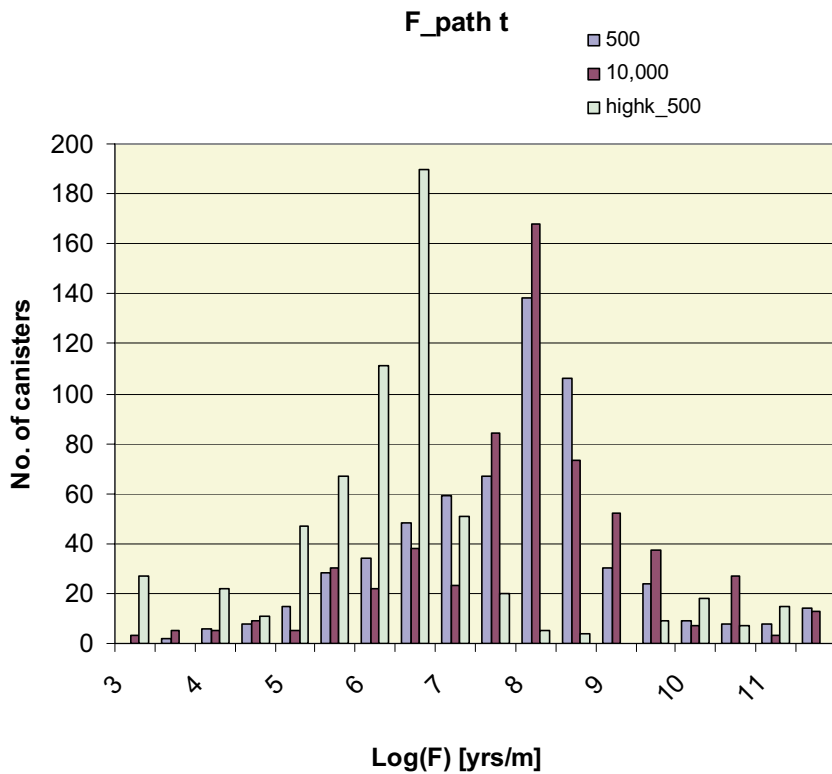
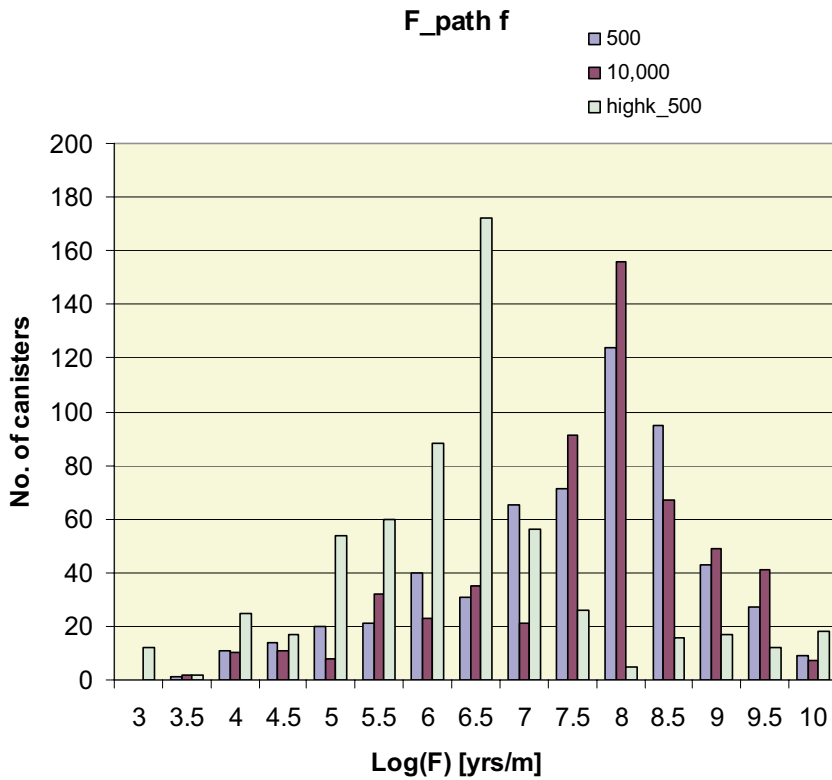


Figure 6-39. Distribution of F-quotient in the nested model with a release from 604 canisters into Path_f (top) and Path_t2 (bottom). Three cases are shown: a release after 2,500 AD; a release at 12,000 AD; and for a backfill conductivity of 10^{-8} m/s for a release at 2,500 AD.

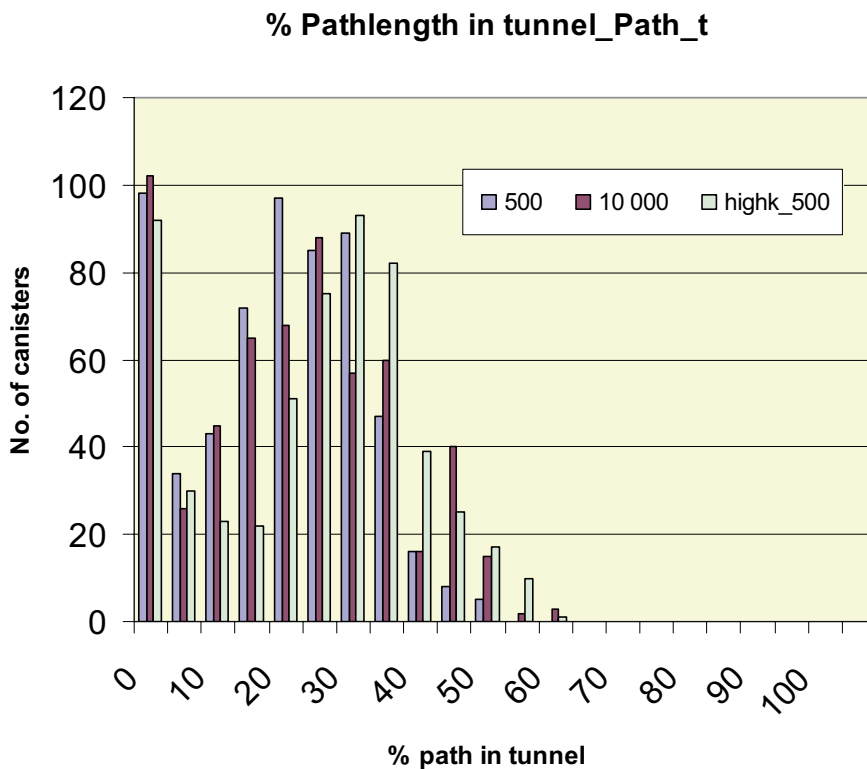
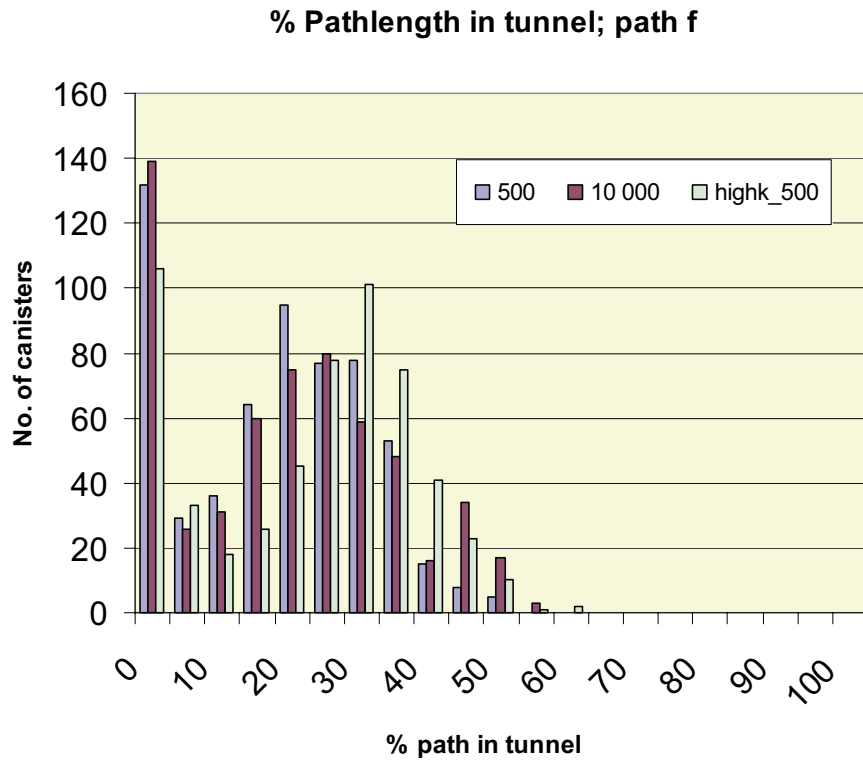


Figure 6-40. Distribution of percentage of pathlength in the tunnel for the nested model with a release from 604 canisters into Path_f (top) and Path_t2 (bottom). Three cases are shown: a release after 2,500 AD; a release at 12,000 AD; and for a backfill conductivity of 10^{-8} m/s for a release at 2,500 AD.

7 Conclusions

The methodology proposed in SKB Technical Report TR-03-08, 'Planning Report for the Safety Assessment SR-Can' /3/ has been illustrated with alternative interpretations of the fracture network data from Forsmark Version 1.1. This has shown the development of the complete model chain from fracture network data, fracture conceptual model analysis, regional-scale paleo-hydrogeology to the use of detailed nested models to obtain performance measures for the near-field, far-field and biosphere as required by safety assessment. The methodology has shown to be tractable and to yield more realistic and detailed distribution of PMs than has been possible in the past. A number of scenarios have been considered including release from canisters at different times, different backfill properties, and quite distinct interpretations of the underlying fracture network data. This demonstrates the robustness and flexibility of the approach.

For the original DFN interpretation the fracture network connectivity is relatively good and may be analogous to the situation at Oskarshamn to some extent. The general conclusions for this data are:

- A cut-off in fracture length about 50 m can be used for deriving the equivalent CPM permeability distribution for 100 m blocks;
- Fractures down to about 3 m have to be included on the canister-scale to consider the near-field flows;
- Natural transients have a significant affect on PMs due to differences in head and salinity at 2,500 AD and 12,000 AD. Future freshwater conditions imply shorter paths and hence greater risk;
- At 2,500 AD paths discharge vertically above repository or on the sea bed for nested model, whereas in the CPM the longer paths towards sea dominates;
- At 12,000 AD all paths in the nested model discharge close to the repository (coast retreated to NE);
- DFN modelling gives greater probability of many canisters being in 'safe' areas away from high-K features. CPM uses average properties and hence all canisters are in an 'averagely safe' area. Generally lower equivalent flow-rates, Q_{eq} , for the nested model;
- Far-field PMs for Path_f (starting in the fracture) and Path_t (starting in the tunnel) are similar. Presumably this is because for the base case, fractures are the dominant pathway and so particles starting in the tunnel tend to enter the fracture system after only a short distance;
- Five realisations of the DFN model show no major differences in path behaviour;
- Higher hydraulic conductivity backfill focuses more flow through repository, reflected in higher Q_{eq} values for Path_t, and hence higher risk.

For the updated DFN interpretation the fracture network connectivity is relatively poor and represents a distinct case. The general conclusions for this data are:

- A cut-off in fracture length about 20 m can be used for deriving the equivalent CPM permeability distribution for 100 m blocks;

- Fractures down to about 1 m have to be included on the canister-scale to consider the near-field flows;
- Natural transients have a secondary effect on PMs. Flow-rates and pathways are more dominated by the local fracture connectivity around the deposition tunnels;
- The tunnel provides a dominant local pathway for transport even with a low backfill conductivity of 10^{-10} m/s. As well as providing a major conduit for flow, the tunnels also connect up localised fracture clusters that would otherwise be inaccessible to site-scale flows;
- Only about 60% of canisters are intersected by the connected fracture network;
- There is little difference between Path_t and Path_f in terms of the far-field PMs for the opposite reason to the original DFN. That is, now the tunnel pathway dominates so particles entering the fracture system tend to enter a tunnel;
- DFN modelling gives greater probability of many canisters being in ‘safe’ areas away from high-K features compared to a low-resolution CPM model. CPM uses average properties and hence all canisters are in an ‘averagely safe’ area. Generally lower equivalent flow-rates, Q_{eq} , for the nested model;
- Higher hydraulic conductivity backfill focuses more flow through repository, reflected in higher Q_{eq} values for Path_t, and significantly lower travel times and F-quotients;
- The dominance of the tunnels as a pathway in this case demands an explicit treatment of retention in the safety assessment for this case.

The methodology as developed should not be viewed as entirely complete. A number of issues have arisen as the project has proceeded and some approximations were made during this initial phase. It is suggested that in the next phase of SR-can the following issues should be addressed:

- The EDZ should be modelled explicitly in the canister-scale model and greater mesh resolution should be used to resolve transport in the tunnels especially for poorly connected networks where the tunnel dominates. Other repository design features such as plugs could be considered also;
- The canister-scale models should include all canisters explicitly;
- Consideration has to be given to alternative fracture conceptual models and interpretations;
- The sensitivity to the structural model in terms of confidence of structures needs to be addressed;
- A verification of the pathways and transport statistics against a refined CPM model of the local-scale would be valuable to support the approximation of solving for constant density in the DFN model but coupled to environmental pressure;
- The effects of channelisation of transport within fractures needs to be modelled more explicitly;
- An approach needs to be found that is more robust for handling transport in dead-end fracture clusters that occur for sparse networks;
- If CPM models are still to be propagated through the safety assessment then the spatial distribution of fracture porosity and flow-wetted surface area should be derived from upscaling DFN models in a similar way to permeability.

References

- 1 **SKB, 1999.** SR 97 – Post-closure Safety. SKB TR-99-06. Svensk Kärnbränslehantering AB.
- 2 **SKB, 2002.** Preliminary Safety Evaluation, Based on Initial Site Investigation Data, Planning Document. SKB TR-02-28, Svensk Kärnbränslehantering AB.
- 3 **SKB, 2003.** Planning Report for the Safety Assessment SR-Can. SKB TR-03-08. Svensk Kärnbränslehantering AB.
- 4 **SKB, 2004.** Preliminary Site Description: Forsmark area – Version 1.1. SKB R-04-15. Svensk Kärnbränslehantering AB.
- 5 **S Follin and I Rhén, 2003.** Task Description 1.1 for Forsmark Version 1.1, file: TD-PFM_V1-1_031013.doc.
- 6 **S Follin, 2003.** Data delivery file: PFM_V.1.1_Data_Delivery_SP1.xls.
- 7 **S Follin, 2003.** Addendum to Task Description PFM V1.1, file: Addendum_to_TD_031118.ppt.
- 8 **C P Jackson, A R Hoch and S J Todman, 2000.** Self-consistency of a Heterogeneous Continuum Porous Medium Representation of a Fractured Medium, Water Resources Research Vol 36, No 1, Pages 189–202.